Morphology of

Poly(3,4-ethylene dioxythiophene) (PEDOT)

Thin Films, Crystals, Cubic Phases, Fibers and Tubes

by

Jinghang Wu

A dissertation submitted in partial fulfillment

Of the requirements for the degree of

Doctor of Philosophy

(Macromolecular Science and Engineering)

In The university of Michigan

2011

Doctoral Committee:

Associate Professor Jinsang Kim, Co-Chair

Adjunct Professor David C.Martin, Co-Chair

Professor Peter F.Green

Associate Professor Joerg Lahann

2011

To my parents

And

To my beloved wife, Xiaomei Zhang

Acknowledgements

I am very grateful for having Professor David C. Martin as my thesis advisor. He inspires me both in research and life with his intelligence, resourcefulness, passion for research and constant helps to others. I am not only thankful for all the encouragement, guidance he gave me through my research and his helps on moving me along with my career, and I also thank him for all his supports for overcoming the difficulties in my life during this period. He sets a good example for me in both my future research and life.

I would like to thank the rest of my thesis committee, Professor Jinsang Kim for his kindness of picking up the role of co-chair, Professor Peter F. Green and Professor Joerg Lahann, for their guidance and review of my work. I would also like to thank Dr. Kai Sun, Dr. Haiping Sun and Yin Qi at the University of Michigan Electron Microbeam Analysis Laboratory (EMAL) and Dr. Chaoying Ni and Frank Kriss at the university of Delaware (UD) KECK lab for their help on the facilities and equipments. All the valuable advice and helps from Professor Thomas W. Smith at Rochester Institute of Technology are appreciated. All the helps got from the faculty and staffs at both Michigan and UD are appreciated.

I learned a lot from all the past and current Martin research group members. They all contributed to my study in many ways. Helps and friendship from the students and friends at Michigan and UD are appreciated. I want to specially thank Nonna Hamilton. The life and study during my Ph.D period would have been a lot more difficult without her help.

Last but not least, I would like to thank my family members. My parents, Xiangju Wu and Xiumei Zhang and my Parents-in-law, Huijun Zhang and Ruifeng Zhao for all their support and love for me in so many years. I owe many thanks to my beloved wife,

Xiaomei Zhang for her love and support without which I would never have reached this point.

This work was supported in part by the National Science Foundation (NSF), Ford company and the ACS Petroleum Research Fund (PRF).

Table of Contents

List of Figures

List of Tables

Chapter I

Overview

Background and motivation

Organic electronic devices such as memory, photovoltaics, and light-emitting diodes (OLEDs) have received considerable recent interest (Kelley et al., 2004). Conjugated polymers have been widely studied for organic electronic applications due to their relatively high conductivity and chemical stability (Martin et al., 2010; Baughman, 1996; Schmidt, Shastri, Vacanti & Langer , 1997; Kuhn, Child, Skotheim, Elsenbaumer & Reynolds, 1998; Bar-Cohen, 2001). Conjugated polymers have an overlap of pi-molecular orbitals to allow the formation of delocalized electron wave functions along the molecular backbone.

The properties of conducting polymers are strongly dependent on the morphology of the material in the solid-state. Of particular interest is the degree of crystallinity and the size and shape of the crystalline domains. In our laboratory, the use of conducting PEDOT coatings for improving the long-term performance of microfabricated neural prosthetic devices that are directly implanted into the central nervous system has been investigated. Soft, low impedance, and biologically active conducting PEDOT coatings can be prepared by electrochemical deposition directly on the electrode sites (Cui & Martin, 2003; Yang & Martin, 2006).

Microfabricated silicon-based neural prosthetic devices have been used to facilitate the functional stimulation of and recording from neurons of the central nervous system. Glial cell inflammation is a common problem when these prosthetic devices are implanted in living tissue. The more than 7-order of magnitude difference between the mechanical properties of silicon (~170 GPa) and brain tissue (~100 kPa) leads to chronic problems at the interface between the hard, inorganic substrate and the soft, organic tissue (Buchko, Slattery, Kozloff and Martin, 2000). To temper this issue, conductive polymers have been used to improve the long-term performance of these devices (Martin

et al., 2010) Poly(3,4-ethylene dioxythiophene). PEDOT has received particular interest because of its better electrical conductivity and long term chemical stability (Figure 1.1) (Kirchmeyer & Reuter, 2005; Groenendaal, Jonas, Freitag, Pielartzik & Reynolds, 2000; Nguyen, Rendu, Long & De Vos,2004; Kros, van Hövell, Sommerdijk & Nolte, 2001; Smela, 2003; Yamato, Ohwa & Wernet, 1995).

In Chapter II, we critically review recent work from our laboratory and elsewhere to investigate the morphology of PEDOT in the solid state. We discuss the importance of oxidative chemical and electrochemical polymerization, as well as the critical role of the counterion used during synthesis and film deposition. We have obtained information about the morphology of PEDOT from a number of different complimentary techniques including X-ray diffraction, optical microscopy, scanning electron microscopy, transmission high-resolution electron microscopy, and low-voltage electron microscopy.

Electron microcopy has been widely used in studying morphologies and structures of polymers and organic molecular crystals. Low contrast and beam damage issues of polymeric and organic molecular samples have been major limiting factors for studies using Transmitted Electron Microscopy (TEM), as compared to inorganic samples. High Resolution Electron Microscopy (HREM) has been developed to directly image the crystal packing of organic samples, especially using low dose techniques to minimize the beam damage. A novel low voltage (~5 kV) electron microscope (LVEM) has been developed to address the issue of low contrast of organic samples and other samples with low atomic number elements (Figure 1.2). Recent progress about HREM and LVEM in our research group and by other researchers has been reviewed. Strengths and problems of these techniques are detailed discussed in Chapter III.

When using bromine as a counterion during electrochemical deposition, we have found that extraordinarily large single crystals are reproducibly formed. A detailed study of these unique crystals is discussed in Chapter IV. Optical micrographs show highly birefringent, needle-shaped crystals that are hundreds of micrometers in size (Figure 1.3). This ordered microstructure is quite different than the limited order typically seen when polymerizing PEDOT with other counterions. The crystals are highly textured with a

preferred growth plane parallel to the substrate surface. They have well-defined, distinct facets and show sharp melting points in the DSC. FTIR and UV-Vis spectroscopy show characteristic absorptions similar to those seen in PEDOT. XPS has also confirmed the presence of peaks characteristic of PEDOT, confirming that at least oligomers have formed. SEM images show a fibrillar surface texture oriented perpendicular to the long axes of the needle-shaped crystals, indicating anisotropic organization of the molecules in the solid-state. X-ray diffraction, electron diffraction, and FFTs of high-resolution TEM images all show sharp, highly oriented reflections consistent with large, highly ordered single crystals. We hypothesize that these large crystals may have formed due to simultaneous crystallization of the EDOT during electrochemical oligomerization or polymerization in the presence of bromine. This process is somewhat similar to the crystallization-induced transesterification reactions that have been observed in certain types of polyesters (Lenz & Go, 1973; Lenz & Go, 1974).

Surfactant, oil and water ternary systems can produce many different nanostructures depending on composition ranging from micellar, hexagonal, lamellar and cubic phases (Figure 1.4) (Allen & Thomas, 1999). PEDOT has been templated into hexagonally ordered fibrillar structures (Hulvat & Stupp, 2003; Hulvat & Stupp, 2004). PEDOT bicontinuous phase had not been successfully developed. Templating of conductive polymers into bicontinuous cubic phases which divide 3D space into discrete regions that are both continuous and mutually interconnected would provide many advantages that present important limitations with current generation materials due to its high surface area and volume to mass ratio. The performance of drug-releasing systems is expected to be improved with such small, well-defined, and interconnected channels. The characteristic response times of chemical sensors or electrochromic devices made from conducting polymers could be significantly reduced by decreasing the diffusion distances of the analyte, and by coupling to the conjugated backbones in the bicontinuous cubic structure (Swager, 1998; Kim, McQuade, Rose, Zhu & Swager, 2001). Figure 1.5 is an illustration showing some of the potential benefits of these conductive bicontinuous cubic phases. Chapter V investigated the templating of PEDOT into these bicontinuous

cubic phase structures by surfactant, oil and water ternary systems. Mesophase structures could be controlled by varying the composition and temperature.

The electrical properties of these bicontinuous conducting polymer cubic phases are expected to be quite sensitive to their solid-state structure. In Chapter VI, we studied the in-situ electrical property changes associated with structural transitions of these phases induced by temperature changes by simultaneous measurements of impedance spectroscopy and microstructural evolution by small angle X-ray scattering (Figure 1.6).

Nerve injuries are a significant cause of disability. They may be treated more effectively using nerve guidance channels and scaffolds containing aligned fibers (Corey, et al., 2007). In Chapter VII, we present two novel approaches to electrospin aligned PEDOT fibers and tubes using different biocompatible polymers such as PLGA and PCL as fiber templates by electrospinning onto either a rotating wheel or an insulating gap between two conductive metallic strips. This technique is novel in terms of combining different methods of electro-spinning aligned nanofibers of polymer-conjugated monomer blends, and the subsequent template-assisted creation of nanotubes by oxidative polymerization. It opens an avenue to the cost-effective, large scale and facile processing of PEDOT into aligned fibers and tubes with nanoscale diameters (Figure 1.7).

Dissertation outline

Chapter II of this thesis describes the morphology of PEDOT. Structure and properties of electrochemically polymerized PEDOT was studied. Crystal packing of PEDOT film is investigated in detail. The typical length scale of the predominant (100) intermolecular crystal planes in these PEDOT crystals is one to two nanometers.

Chapter III reviews the low dose high resolution and low voltage electron microscopy used in studying the morphology of organic samples including PEDOT. Low dose high resolution TEM tackles the beam sensitivity issue of organic and polymeric

crystals, while the 5 kV table-top TEM resolves the low contrast issue of organic materials in electron microscopy.

Chapter IV discusses the development of highly oriented crystalline PEDOT-LiBr crystals. This is counterintuitive to the semicrystalline, relatively disordered nature of typical PEDOT films. The length scale of interest here is around one nm.

Chapter V investigated the development of templating PEDOT into bicontinuous cubic phases using surfactant, water and oil ternary systems. The monomer was loaded in the aqueous part of the surfactant, oil and water ternary system. The important length scales here are a couple of nanometer to tens of nanometers.

In Chapter VI, the thermal stability and the electric property changes of the bicontinuous cubic phase PEDOT were studied by simultaneous X-ray scattering and impedance spectroscopy at different temperatures.

In Chapter VII, two novel methods for fabricating aligned PEDOT fibers and tubes using electrospinning are presented. A rotating wheel or a dielectric gap was used to align biocompatible polymer-EDOT monomer blend nanofibers that were then used as templates for the subsequent polymerization of the EDOT monomer. The final PEDOT nanofiber and nanotube diameters could be tailored from 100 nanometers to a couple of microns. The aligned fibers have been shown to direct neural cell growth.

The Conclusions of this work are presented in Chapter VIII together with some possible future directions following these studies.

Figures:

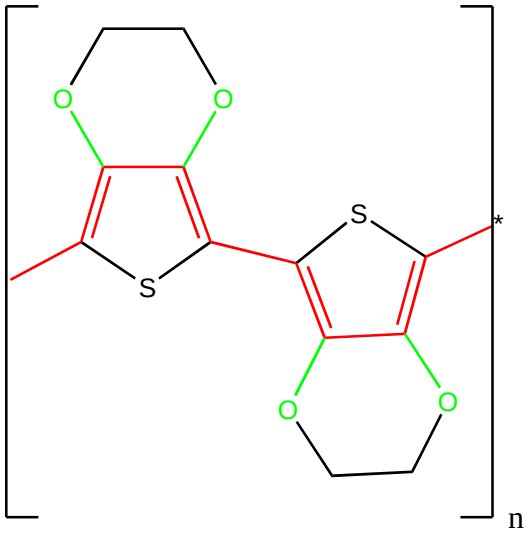

Figure 1.1. Chemical structure of conjugated conductive polymer poly(3,4-ethylene dioxythiophene) (PEDOT)

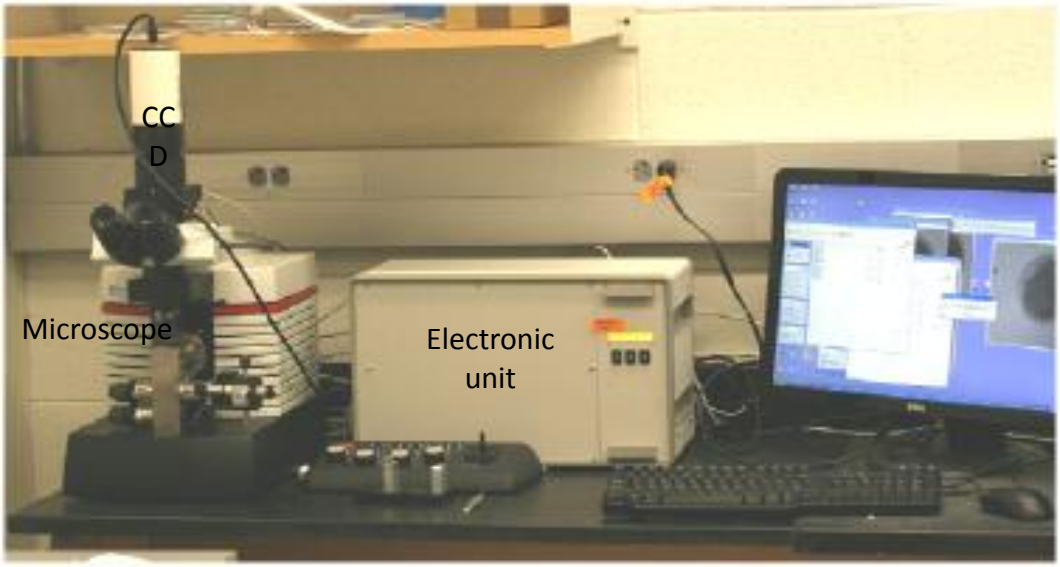

Figure 1.2. Picture of a table-top sized 5 kV LVEM5 electron microscope by Delong USA that can be operated in TEM, STEM, SEM or electron diffraction mode.

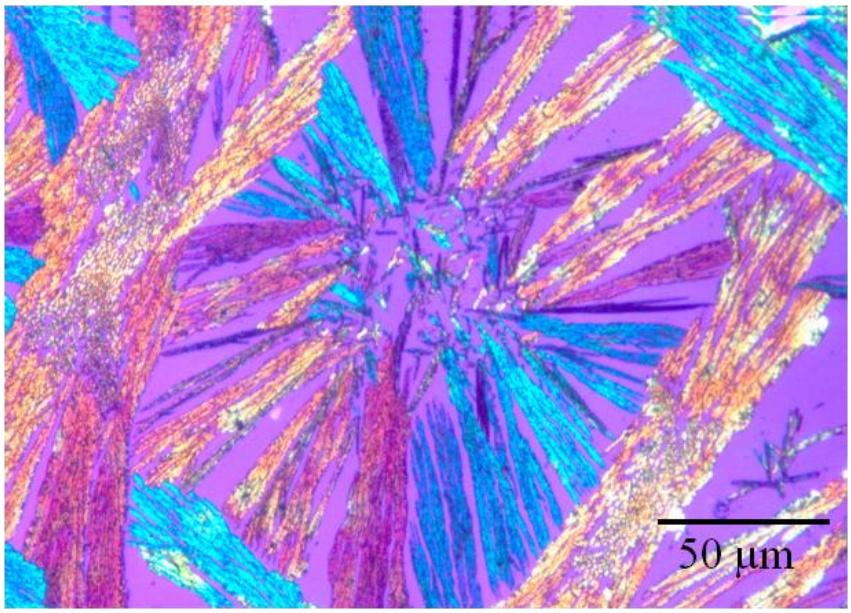

Figure 1.3. Optical micrograph of electrochemically deposited PEDOT film, using bromine as a counterion in polarized light with a full-wave red filter. The films have highly regular, birefringent, faceted crystals that are tens of micrometers in size.

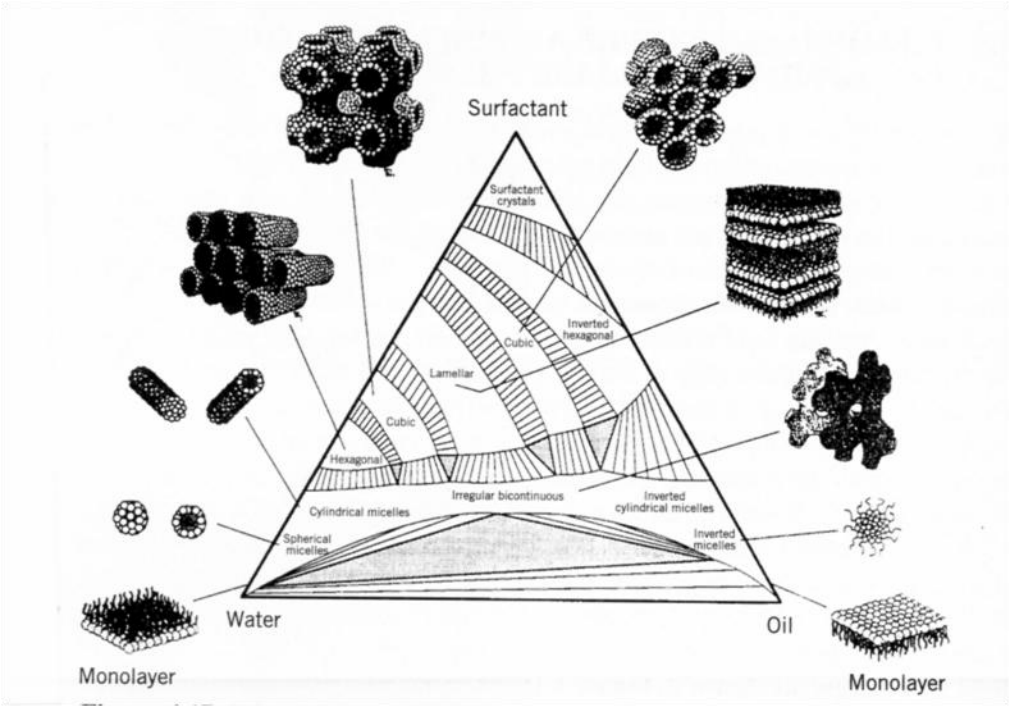

Figure 1.4. Schematic of a ternary surfactant-oil-water phase diagram showing compositional ranges expected for different ordered phases (Allen & Thomas, 1999).

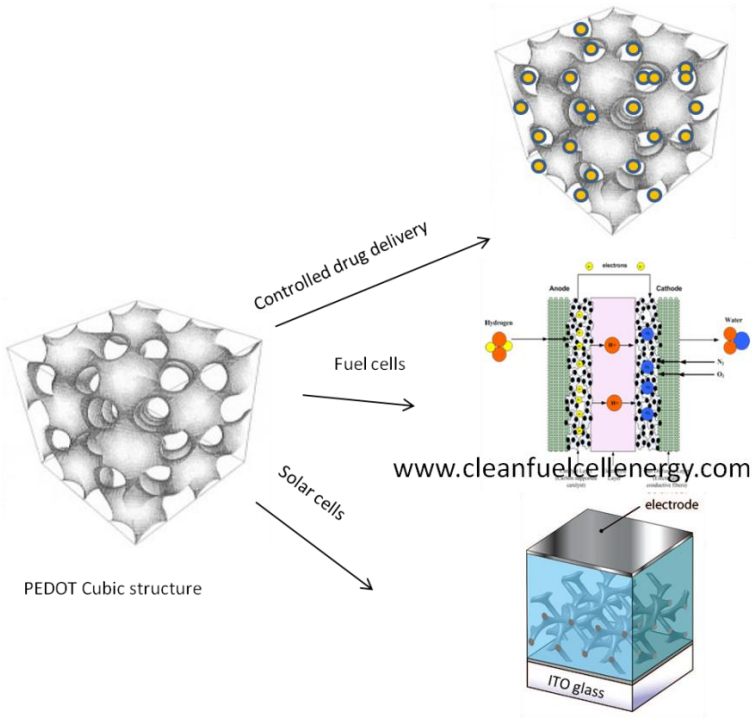

Figure 1.5. Schematic of potential applications for PEDOT bicontinuous cubic structures

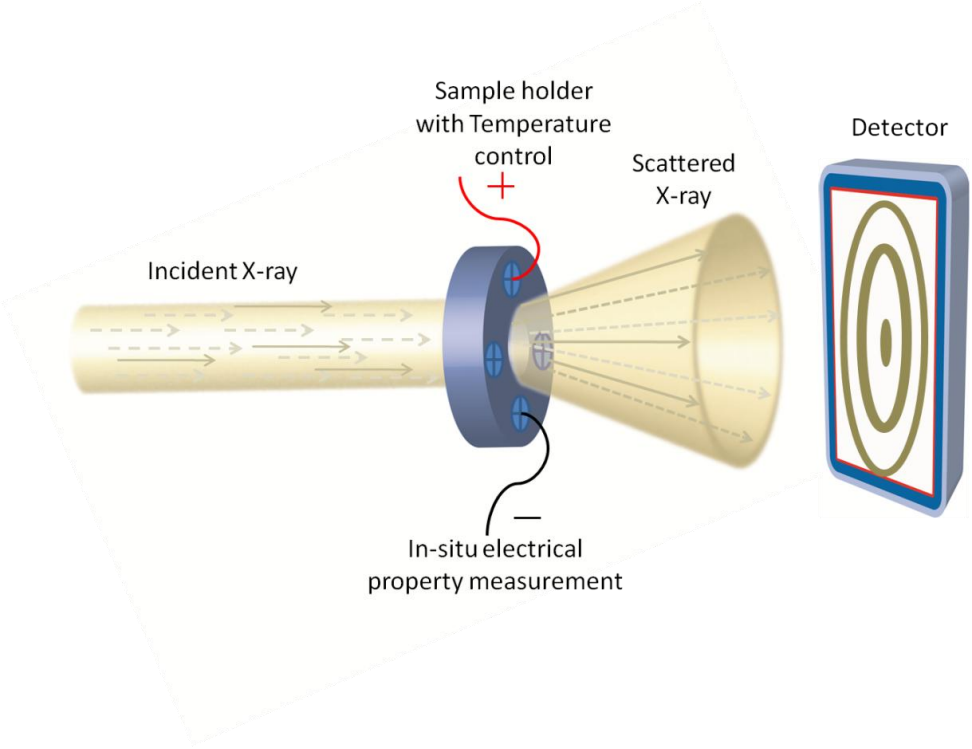

Figure 1.6. Schematic illustration of in-situ electrical property measurements at different temperatures while simultaneously monitoring the structure by SAXS

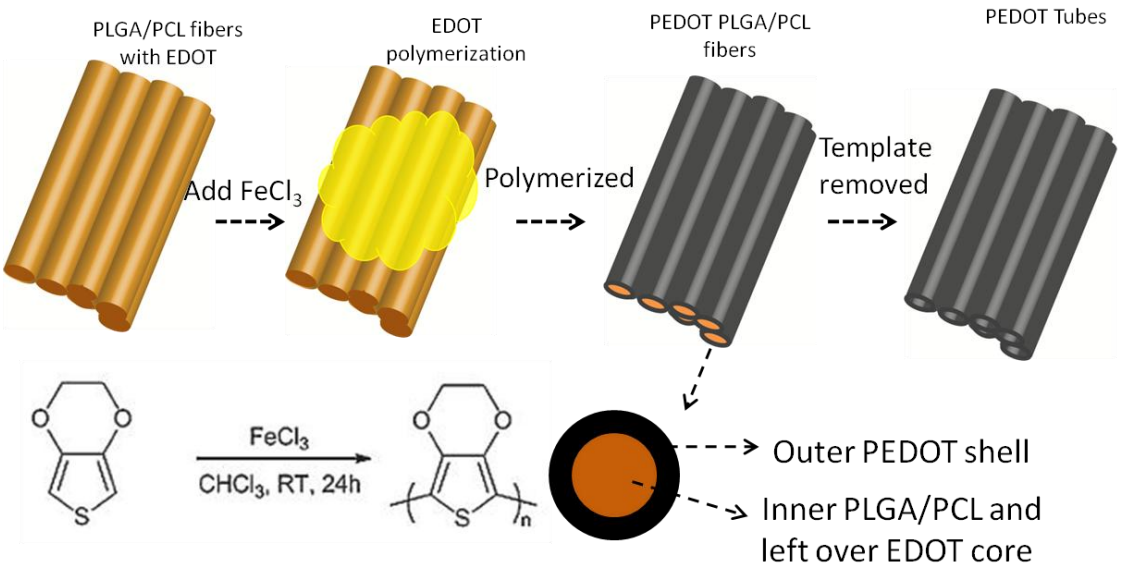

Figure 1.7. Schematic illustration of methods for preparing aligned PEDOT nanofibers and PEDOT nanotubes by the oxidative polymerization of EDOT monomer incorporated into oriented assemblies of electrospun PLGA/PCL nanofibers.

References

Allen, S. M., and Thomas, E. L. *The Structure of. Materials.* New York, NY : John Wiley,. Chapter **4**,(1999), 237

Bar-Cohen, Y. *Bellingham, Wash.: SPIE Press.* (2001).

Baughman, R. H. *Synthetic Metals,* **78,** (1996). 339- 353.

Buchko, C.J., Slattery, M.J., Kozloff, K.M. and Martin, D.C. *J. Mater. Res*. **15**, (2000). 231.

Cui, X.Y. and Martin, D.C. *Sens. Actuators B Chem*. **89**, (2003),92.

Corey, J.M., Lin, D.Y., Mycek, K.B., Chen, Q., Samuel,S., Feldman, E. L.and Martin,D.C. *Journal of Biomedical Materials Research Part A,* **83A**, (2007), 636-645.

Groenendaal L., Jonas F., Freitag D., Pielartzik H. and Reynolds J.R., *Adv Mater* **7** (2000), 481–494.

Hulvat, J. F. and Stupp, S. I. *Angewandte Chemie-International Edition*, **42**, (2003), 778-781.

Hulvat, J. F. and Stupp, S. I. *Advanced Materials*, **16**, (2004). 589-592.

Kelley, T. W.; Baude, P. F.; Gerlach, C; Ender,D. E.; Muyres, D.; Haase, M. A.; Vogel, D. E. and Theiss, S. D. *Chem. Mater*. **16.** (2004), 4413-4422

Kirchmeyer, S. and Reuter, K. *Journal of materials chemistry*., **5**, (2005), 12077-2088

Kros, A., van Hövell, S.W.F.M., Sommerdijk, N.A.J.M. and Nolte, R.J.M. *Adv. Mater.* **13**, (2001),1555 .

Kuhn, H. H. & Child, A. D. In T. A. Skotheim, R. L. Elsenbaumer, & J. R. Reynolds (Eds.), *Handbook of Conducting Polymers(Second Edition)*. New York: Marcel Dekker, Inc. (1998). 993-1013 New York: Marcel Dekker, Inc.

Lenz, R. W. and Go, S. *Journal of Polymer Science Part A: Polymer Chemistry*, **11,**(1973), 2927

Lenz, R. W.and Go, S. *Journal of Polymer Science Part A: Polymer Chemistry*, **12,** (1974), 1–10.

Martin, D.C; Wu, J; Shaw, C.M; King, Z; Spannigga, S.A; Rcihardson-Bruns, S; Hendricks, J and Yang, J; *Polymer Reviews*, **50**, (2010), 340–384

Nguyen, T P., Rendu, P., Long, P D. and De Vos, S A. *Surface and coatings technology*, **180-181**, (2004), 646-649

Schmidt, C. E., Shastri, V. R., Vacanti, J. P., & Langer, *R. Proc. Natl. Acad. Sci. USA*, **94**, (1997) 8948-8953.

Smela,E. *Adv. Mater*. **15**, (2003), 481.

Swager, T. M. *Accounts of Chemical Research*, **31**, (1998). 201-207.

Yamato, H. Ohwa, M. and Wernet, W. *J. Electroanal. Chem*. **397**, (1995),163.

Yang, J., Martin, D C. *J. Mater. Res.* **21,** (2006), 1124-1132

Chapter II

The Morphology of Poly(3,4-Ethylenedioxythiophene)

Note: much of the content in this chapter has already appeared in press in: Polymer Reviews, 50(3), 340-384, (2010).

Abstract

Poly(3,4-ethylene dioxythiophene) (PEDOT) is a chemically stable, conjugated polymer that is of considerable interest for a variety of applications including coatings for interfacing electronic biomedical devices with living tissue. Here, we describe recent work from our laboratory and elsewhere to investigate the morphology of PEDOT in the solid state. We discuss the importance of oxidative chemical and electrochemical polymerization, as well as the critical role of the counterion used during synthesis and film deposition. We have obtained information about the morphology of PEDOT from a number of different complimentary techniques including X-ray diffraction, optical microscopy, scanning electron microscopy, and transmission high-resolution electron microscopy.

PEDOT is a relatively rigid polymer that packs in the solid state at a characteristic face-to-face distance (010) of ~0.34 nm, similar to graphite. These sheets of oriented PEDOT molecules are separated from one another by ~1.4 nm laterally, with the (100) distance between layers quite sensitive to the choice of counterion used during sample preparation. The order in the films is typically modest, although this also depends on the counterion used and the method of film deposition. The films can be organized into useful structures with a variety of nanoscale dissolvable templates (including fibers, particles, and lyotropic mesophases). When PEDOT is electrochemically deposited in the presence of bromine counterions, highly ordered crystalline phases are observed. The crystallinity and surface morphology of electrochemically polymerized PEDOT films can be controlled by changing deposition conditions.

Introduction

There has been considerable interest in the development of conjugated polymers because of their potential use in flexible organic electronic devices such as photovoltaics, light-emitting diodes, sensors, actuators, and thin-film transistors (Forrest, 2004). The conjugated polymer backbone, consisting of alternating carbon–carbon double bonds, provides for π-orbital overlap along the molecule. This leads to a number of useful properties including relatively easy charge transport and the ability to tailor the absorption and emission spectrum (Batchelder, 1988). Conjugated polymers that have been investigated in some detail include poly(acetylene), poly(phenylene vinylene), poly(pyrrole), as well as poly(thiophenes) and their various derivatives.

Conjugated polymers are typically synthesized by oxidative polymerization using chemical, electrochemical, or chemical vapor deposition methods (Groenendall, Jonas, Freitag, Pielartzik & Reynolds, 2000; Groenendaal, Zotti, Aubert, Waybright & Reynolds, 2003). During the reaction covalent bonds are established between the constituent monomers, removing hydrogens from the aromatic phenyl, pyrrole, or thiophene rings depending on the structure of interest. Irregularities in the chemical structure can arise when the monomers have more than one reactive hydrogen present on the conjugated ring (Schlenoff & Xu, 1992).

One conjugated polymer that has been of particular recent attention is the diethoxysubstituted thiophene poly(3,4-ethylene dioxythiophene), or PEDOT (Groenendall, et al., 2000; Kirchmeyer & Reuter, 2005; Kirchmeyer, Reuter & Simpson, 2007). As shown in Figure 2.1, the EDOT monomer consists of a five-membered thiophene ring with the hydrogens at the 3 and 4 positions replaced with a dioxy-ethyl substituent group. Note that because the EDOT monomer has only two reactive hydrogens (at the 2 and 5 positions), it is not in principle possible to have chemical defects in the PEDOT chain (other than from variations in the monomer purity). This regularity in the molecular structure has been associated with its outstanding chemical

stability (Cui & Martin, 2003).The polymer is typically used in its oxidized state where the molecular backbone is loaded with mobile carriers (holes) and thus is electrically conductive. PEDOT can be doped with many different types of anions including smaller molecules ($ClO4^-$, heparin), as well as macromolecular polyanions such as poly(styrene sulfonate) (PSS) (Asplund, von Holst & Inganäs, 2008). At equilibrium it is usual to find a charge density of about one extra positive charge per every three EDOT monomer units (Groenendall, et al., 2000). It is therefore necessary to have one charge-balancing anion per every three EDOT units (Figure 2.1). Because of resonance structures that arise from the conjugated backbone, it is expected that the PEDOT chains will be fairly stiff and extended and ought to remain reasonably linear locally. The PEDOT molecule is locally rigid and extended, with the planar thiophene rings alternating back and forth along the nearly linear molecular trajectory. Although PEDOT itself is not soluble in water, it is possible to form an aqueous suspension by complexing it with PSS. Given the substantial difference in rigidity between PEDOT and the more globular PSS, it is expected that several PSS coils will be associated with a given PEDOT molecule (Kirchmeyer & Reuter, 2005; Kirchmeyer, Reuter & Simpson, 2007).

A number of other functionalized thiophene monomers have been synthesized that are chemically similar to EDOT, including 3,4-propylenedioxythiophene (ProDOT) and 3,4-butylenedioxythiopene (BuDOT) (Groenendall, et al., 2000). It is also possible to modify the EDOT monomer with side groups to tailor the surface properties, including designing specific interactions with solid substrates or with living tissue. Examples include hydroxy-methylated EDOT (Ng, Chan & Yu, 1997) and alkoxy-functionalized EDOT (Lima, Schottland, Sadki & Chevrot, 1998; St ́ephan, et al., 1998). The synthesis of an EDOT monomer functionalized with a carboxylic acid (EDOT-acid) has recently been reported (Povlich, Cho, Spanninga, Martin, & Kim, 2007), as well as EDOT-thiol (Balog, Rayah, Le Derf & Salle, 2008).

Bifunctional molecules linking together two monomers of EDOT and EDOT derivatives have been created (Reeves, Thompson, Abboud, Smart & Reynolds, 2002). Other interesting examples include PEDOT variants with pendant crown ethers, attached

either onto the side of the thiophene ring directly or via a more flexible side chain (Bäurle & Scheib, 1995; Rimmel & Bäurle, 1999). The backbone chemistry of PEDOT is quite similar to that of eumelanin, the dark brown–black pigment common in nature. Eumelanin is derived from 3,4-dihydroxy-lphenylalanine, or l-DOPA. Melanins are, of course, abundant as natural pigments in skin and hair, where they serve to absorb light, presumably providing a measure of ultraviolet (UV) protection. However, it is interesting to consider that they are also found in electronically and ionically active living tissues including the retina, the inner ear, and the brain. Indeed, there is a component of the brain stem called the *substantia nigra* (Latin for *black substance*), which is dark because of a high local concentration of neuromelanin. The loss of pigmentation in the substantia nigra is known to be correlated with Parkinson's disease (PD). Autopsies of patients with PD show a much lighter color of the substantia nigra than healthy individuals. Melanin is also highly expressed in the cochlea (inner ear), particularly in the region between the scala media (a chamber filled with a potassium-enriched fluid called *endolymph*) and the scala tympani (filled with a sodium-enriched fluid called *perilymph*). This local variation in ionic composition leads to a relatively large voltage difference (the endocochlear potential) of the order 80–100 mV (von Bekesy, 1952).

The purpose of this article is to describe recent efforts from our laboratory and elsewhere to characterize the morphology of PEDOT in the solid state. We have been particularly interested in the development of PEDOT as a soft, functional material for interfacing hard, electronically conducting metallic and semiconducting biomedical devices with wet, ionically active living tissue.

When considering the design of materials for interfacing electronic biomedical devices with living tissue, it is necessary to consider and optimize many different performance requirements. Electronic biomedical devices are typically engineered from solid inorganic metals (platinum, gold, iridium) or semiconductors (silicon). They are also inert and conduct current electronically. On the other hand, living tissue is organic, wet, and conducts charge ionically. Furthermore, engineered components typically have a relatively flat, uniform surface, whereas surfaces in biological systems are complicated

and may facilitate active transport from the interior to exterior of a cell. In order to create materials that are better suited for biomedical device–tissue interface applications, it is important to match both the electrical and mechanical properties of the materials used with those of the living systems.

Figure 2.2 dramatically demonstrates the scale of this design problem, plotting the electrical properties (as resistivity in units of ohm/m) of known engineering materials as a function of their mechanical properties (as modulus in units of Pa), using the CES Selector software version 4.6.1 by Granta Design, Cambridge, UK. The resistivities vary over 30 orders of magnitude, from highly conducting (10−9 ohm/m) to highly insulating (1018 ohm/m). Likewise, there are over 12 orders of magnitude of differences in mechanical response, from extremely soft (with moduli of a few Pa) to extremely stiff (1012 Pa). Classes of chemically similar materials (metals, ceramics, polymers) tend to cluster together when plotted in diagrams of this sort. (Ashby, 2005) In this particular diagram the upper right corresponds to the highly insulating, stiff ceramics, and the lower right is the highly conductive inorganic metals and semiconductors. Polymers are much softer than metals or ceramics and are usually insulating. However, solid, fully dense polymers are still much softer than low density foams or liquid-swollen gels. PEDOT is an example of a conductive polymer with a resistivity approaching that of common metals. Tissue itself is a relatively soft, gel-like material that is swollen with an electrolyte, making it an ionic conductor. The use of soft, organic, conducting polymers like PEDOT seems to be a reasonable way of interfacing tissue with hard, inorganic conductors, because they can help to bridge these large gaps in performance. There is likely to be significant potential in the direct integration of PEDOT into hydrogels with mechanical properties similar to tissue.

We have used a variety of different microscopic characterization methods to interrogate the structure of PEDOT in these studies. Here, we will summarize some of these results and in the process demonstrate how these different techniques provide complimentary information, leading to a detailed understanding of the morphology of this particularly important and interesting polymeric material. Our laboratory has been

actively developing a variety of methods for the detailed microstructural characterization of ordered polymers and organic molecular crystals. In particular, we recently reported on the refinement and application of low-dose high-resolution electron microscopy (HREM) (Martin, Chen, Yang, Drummy & Kübel, 2005). This chapter focuses on the use of different microscopy techniques, along with X-ray diffraction, electrochemical impedance spectroscopy (EIS) and cyclic voltammetry (CV) to elucidate the morphology of PEDOT.

Results and discussion

Mechanisms of EDOT Polymerization

During polymerization of EDOT, the monomer is oxidized to a radical cation in a zone adjacent to the electrode (for electrochemical polymerization) or the reactive oxidant species (for chemical vapor deposition [CVD] or chemical polymerization) (Sadki, Schottland, Brodie & Sabouraud, 2000). It has been hypothesized that this radical cation then reacts with another radical cation to form a dimeric dication (Schuhmann, 1998). The dimeric dication subsequently loses two protons, leading to the formation of dimers and then eventually higher oligomers and polymers. In the electrochemical method, deposition of PEDOT onto the metal anode is promoted by the relative insolubility of the polymer in the reaction media. We have found that significant local changes in the pH near the electrode can be detected by using indicator dyes during the reaction.

Although the molecular weight of electropolymerized films of PEDOT is difficult to measure because of their insolubility, it has been demonstrated that neutral PEDOT can be solubilized in common organic solvents by careful control of the stoichiometry of the iron (III) chloride oxidant during the reaction (Kirchmeyer & Reuter, 2005). The PEDOT prepared in this manner can evidently be solubilized in chloroform, dichloromethane, or tetrahydrofuran (THF) and has a number average molecular weight

of 1,000 to 1,500 g/mol, corresponding to 7–10 EDOT units (the monomer molecular weight is 144 g/mol) (Kirchmeyer & Reuter, 2005).

In order to create films of PEDOT of interest for practical devices, at least four different methods have been employed. The first is to use an oxidant such as iron chloride to polymerize the monomer and a counterion such as PSS to keep the PEDOT molecules in suspension. These PEDOT/PSS suspensions can be readily spun-cast into thin films with reasonable electrical properties and are the basis for the Baytron/Clevios materials that have been commercialized by H. C. Starck, Leverkusen, Germany. The conductivities of these films are modest, presumably because the PSS forms a shell around the PEDOT that prevents good contact between chains after the films are formed. The second method is to use electrochemical deposition, causing the polymer to be formed on the anode. Electrochemical deposition can be readily done on patterned metallic surfaces and provides films with better electrical properties than chemical polymerization. Because charge transport is required for the films to form, this method ensures that the PEDOT is electrically connected to the conductive substrate. The last two methods involve oxidative polymerization on solid surfaces. Vapor-phase polymerization (VPP) involves the polymerization of EDOT from a surface that has been previously coated with a layer of oxidant. The last technique is oxidative CVD. This method requires fairly specialized high-vacuum equipment.

To date the most ordered and crystalline thin films of PEDOT have been seen using the VPP and CVD techniques. Chemical polymerizations in solutions or suspensions and electrochemical polymerizations onto metal surfaces have usually led to film with much less crystallinity. However, it is possible to create nanometer-scale structures in PEDOT using templates such as polymer latex spheres or liquid-crystalline mesophases. In addition, extremely highly ordered films, with faceted, optically birefringent crystals many hundreds of micrometers in size, have been observed when electrochemically depositing PEDOT with bromine counterion.

Vapor-Phase Polymerized PEDOT

In the vapor-phase polymerization of PEDOT, the surface of a solid sample is first coated with an Fe(III) salt and then exposed to an atmosphere of EDOT monomer (Kim, Kim, Won, Lee & Suh, 2003; Winther-Jensen, Breiby &West, 2005). The technique results in uniform, relatively thin (submicron) films of PEDOT (Winther-Jensen, Breiby &West, 2005; Winther-Jensen & West, 2004).

Grazing incidence X-ray diffraction of these films has shown high degrees of order, with the PEDOT chains packing into sheets (Winther-Jensen, et al., 2008). The chains were oriented parallel to the substrate surface, and the chain–chain edge-to-edge packing distance d100 was around 1.4 nm. The face-to-face packing dimension d010 was about 0.34 nm, as expected for close packed, nearly planar conjugated molecules. Evidence for an order–disorder transition was seen near 130 ℃ by DSC and XRD; however, this did not lead to dramatic changes in the conductivity of the film, suggesting that the efficiency of electrical transport was not directly related to the degree of crystallinity alone (Winther-Jensen, et al., 2008).

The unit cell for PEDOT was proposed from earlier studies on more weakly ordered films by Aasmundtveit et al (Aasmundtveit, 1999). The essential picture of PEDOT in the solid state is one in which the oriented, rigid, and linear PEDOT chains are packed into close-packed layers. The PEDOT molecules are organized with the chain parallel to the *c* direction (as is usual for polymers). The repeat distance along *c* is 0.78 nm or 0.39 nm per monomer unit. The *a*-axis spacing (~1.4 nm) corresponds to the distance between chains side to side and, as discussed, this fluctuates from system to system depending on the dopant. The *b*-axis (0.68 nm) corresponds to twice the distance from molecule to molecule face to face (0.34 nm). Because of the alternating arrangement of the EDOT monomers along the PEDOT backbone, the minimum energy configuration is for two neighboring chains to pack so that these side groups alternate positions, with the monomer units on a given chain lining up over gaps between the monomers in the chain next to it.

Figures 2.3 and 2.4 show schematically the arrangement of PEDOT chains in the condensed state. A single chain is formed with the alternating EDOT monomers along the backbone. A second chain placed on top of this chain has its minimum energy position so that the monomer side group is placed between the monomers on the lower chain. By stacking many chains like this, a sheet of PEDOT molecules is created (Figures 3 and 4). These sheets then stack at different distances from one another depending on the dopant (Figure 4).

Chemically Vapor-Deposited PEDOT

Gleason et al. have described the preparation of thin films of PEDOT using CVD (Lock, Im & Gleason, 2006; Im & Gleason, 2007; Im, Olivetti & Gleason, 2007). In this case the films are deposited in a vacuum chamber, and the iron (III) chloride oxidant is introduced by sublimation. CVD can presumably produce films that are substantially thicker than VPP; however, relatively specialized vacuum equipment is required, and the end result is a film that conformally coats the target entirely. It is thus somewhat difficult to locally pattern the films onto specific locations (such as the electrodes themselves) for a given device geometry**.**

Chemically Polymerized PEDOT

The most common method of preparing PEDOT is to use oxidative chemical polymerization with a catalyst such as iron chloride and then stabilize the resulting suspension with a hydrophilic counterion such as poly(styrene sulfonate). The resulting aqueous suspension can then be cast into films of interest for a wide variety of applications. Studies of the morphology of these films by XPS and ultraviolet photoelectron spectroscopy (UPS) revealed local phase segregation of PEDOT and PSS and were interpreted to correspond to "grains" of about 3–4 nm with a PSS-rich shell and a PEDOT-rich core (Greczynski, Kugler & Salaneck, 1999). This general picture was confirmed by scanning tunneling microscopy studies, although the size of the grains can be somewhat larger (30–50 nm) (Timpanaro, Kemerink, Touwslager, de Kok & Schrader,

2004). The size of these grains has been associated with the particles formed in the processing of suspension and the filtering processes during preparation. The current understanding is that the particles are deformed into pancake-shaped plates during the drying processes involved in film formation (Lang, Müller, Naujoks & Dual, 2009). Recent efforts have generally been consistent with this picture, suggesting that the individual grains of PEDOT are formed from "tangles" involving the association of several PEDOT molecules with larger, more flexible PSS strands, and that the grains themselves are composed of several tangles into larger clusters (Lang, Müller, Naujoks & Dual, 2009).

Electrochemically Deposited PEDOT

Like other conducting polymers such as polypyrrole, PEDOT can be readily deposited onto metal surfaces using oxidative electrochemical deposition. Both water and acetonitrile can be used as solvents. Certain organic ionic liquids have also proven to be useful as solvent for PEDOT electrochemical deposition (AhmadDeepa & Singh, 2007; Döbbelin, et al., 2007). Electrochemical deposition can be done under constant current (galvanostatic) or constant voltage (potentiostatic) modes. This can also be done by cycling the potential through the oxidation point. The PEDOT films are deposited directly onto a conductive electrode and can have precisely tailored structures by using dissolvable templates such as particles (Yang & Martin, 2004a; Yang & Martin, 2004b) or nanofibers (Abidian, Kim & Martin, 2006; Abidian & Martin, 2009).

Wide-angle X-ray scattering from electrochemically deposited PEDOT films typically shows only a limited degree of structural order, although this is a function of the dopant used during deposition and the charge density used in the process. Figure 2.5 shows a series of two-dimensional (2D) XRD patterns with different dopants (including PSS, NaCl, LiF, and $CaCl_2$). The lower panel shows azimuthally averaged scans showing the peak near 6–7 degrees 2θ (corresponding to a *d*-spacing of ~1.4 nm), showing that the NaCl sample has the highest intensity and sharpest peak, whereas the other dopants have significantly weaker and somewhat broader peaks (Figure 2.4).

Figure 2.6 shows a powder XRD pattern from PEDOT using NaCl as the dopant. The peak near 6–7 degrees 2θ is associated with the (100) spacing, corresponding to the average distance between the ladder-like PEDOT molecules. The face-to-face packings between chains are in the 0.3–0.4 nm range, but the limited degree of order in typical PEDOT samples has not made it possible to be any more definitive about the nature of the packing in the solid state. When different dopants are used to prepare PEDOT, it is found that there are systematic variations in the position of the low-angle XRD peak, corresponding to variations in the average d100 distance between the stacks of PEDOT chains. Table 2.1 shows a listing of the observed d100 spacings, ranging from 1.52 nm (with poly(acrylic acid) [PAA] as the dopant) to 1.15 nm (for F- as dopant). This variation in morphology is shown schematically in Figure 2.4.

Electrochemical deposition makes it possible to deposit PEDOT directly onto a microfabricated metal electrode. We have found that the deposition of PEDOT films onto metal electrodes leads to a dramatic decrease in the impedance for the biologically important frequencies near 1,000 Hz corresponding to the characteristic width of a neural pulse (1 ms) (Cui & Martin, 2003). This drop in net impedance has been associated with the development of increased surface area that facilitates charge exchange between the electrons in the metallic and semiconducting engineered substrate, the holes along the conducting polymer backbone, and the ions in the dopant and surrounding electrolyte.

We have been quite interested in developing methods for increasing the effective area of interaction between the conducting polymer and the surrounding electrolyte to reduce the impedance of these electrodes as much as possible. Rather than create flat films, we focused on methods to make the surface as fuzzy and furry as possible, such as using poly(acrylic acid) as a counterion. We have found that with a molecular weight of PAA near 500K, concentration near 0.5 wt%, and current density near 0.5 mA/cm^2, it is possible to reproducibly create nanofibrillar morphologies (Yang, Lipkin & Martin, 2007). It has been shown that these nanofibrils are mechanically compliant, and the soft mechanics of the films correlates with their high surface area and hence good electrical

properties (Yang & Martin, 2006). Figure 2.7 shows scanning electron microscope (SEM) images of PEDOT nanofibrils produced over large areas on a gold-palladium-coated epoxy substrate.

Cross sections of these fuzzy, nanofibrillar films can be obtained by embedding them in epoxy and microtoming. Figure 2.8 shows a side-by-side set of such thin sections of PEDOT shown in both the transmission electron microscope (TEM) and in the optical microscope. Direct correlations of images such as this make it possible to compare the optical properties of the PEDOT films with their electron scattering behavior (predominantly mass thickness contrast). Brightfield (BF) TEM images of the PEDOT films are shown in Figure 2.9. The dark ~20-nm layer at the bottom is the polycrystalline gold-palladium thin film used as the conductive substrate for depositing the PEDOT. The PEDOT film itself has a nominal thickness of 500 nm for this sample. The rough outer surface of the film seen in the SEM is readily evident, as well as the local thickness and uniform density of the underlying PEDOT film. Elemental mapping of the cross-sectioned sample can be done with energy dispersive spectroscopy (EDS) in the STEM. The Z-contrast scanning transmission electron microscopy (STEM) image shows that most of the scattering comes from the gold-palladium thin support film, and sulfur maps out the position of the PEDOT film itself (Figure 2.10).

Transmitted-light optical images (Figure 2.11) of microtomed samples were used to locate PEDOT film. At a thickness of 60 nm, PEDOT doped with different counter-ions all show light blue color which is a characteristic color of PEDOT film. Cross sections were taken at similar magnifications under both optical and TEM micrograph and compared. Upon electron beam exposure, the films tend to split along the interface between gold-palladium substrate and epoxy which indicates a stronger adhesion between PEDOT film and the conductive substrate.

Bright field TEM images of PEDOT with PSS, LiF and NaCl were shown in Figure 2.12. It shows that the films are dense and smooth close to the substrate. As the film grows thicker, it becomes more open and less dense. This confirms our previous illustration about the PEDOT growth that PEDOT film forms a loose open structure on

the electrode sites and then become dense and smooth with further polymerization and is consistent with the impedance and stiffness change with different film thickness or deposition charge.

Electrical properties were investigated by EIS and CV using bare ball electrodes (Figure 2.13). The phase plot of the impedance spectroscopy reveals phase angles of 75–85 ° for the bare at frequencies of <10 kHz indicating that the electrode is primarily functioning as a capacitor. Coating with PEDOT with different counter ions all dramatically drop the phase angle to <20 °making the electrode more resistive as opposed to capacitive at frequencies above 0.1 kHz.

PEDOT coated electrodes all result in lowering of electrode impedance 1–2 orders of magnitude across frequencies between 0.01–100 Hz, with a ranking of PEDOT Pss, PEDOT Paa LiClO4, PEDOT LiF and Pedot NaCl from low impedance to high. This shows that lower of impedance is largely due to increase in effective surface area of the electrode. The more ordered PEDOT NaCl has the highest impedance comparing to the less ordered PEDOT Pss whose impedance is the lowest.

CV was used to assess the charge transfer capacity of the PEDOT with different counter ions. The charge transfer capacities for PEDOT with the polymeric counter ions (Pss and Paa) are evidently larger than that of the smaller counter ions (Cl^-, F^-).

Crystallinity and morphology control of electrochemically deposited PEDOT

The relative high packing order of PEDOT NaCl has been chosen to do the deposition current density study. The deposition current densities are ranged from 5 $\mu A/cm^2$ to 180 $\mu A/cm^2$. The deposition time is varied with the current densities as to make the same amount of charge passing through the substrate or form the same film thickness. The higher the deposition current densities, the higher the crystallinity as can been seen from the Figure 2.14. The center of the diffraction peaks are not influenced by varying different deposition current density. The crystallinity ranges from 20.5 wt % to 35 wt % (Table 2.2) as the current increased from 5 $\mu A/cm^2$ to 180 $\mu A/cm^2$. The color of the film changed from black to light blue to blue to light purple and to purple as the

deposition current densities varied from 5 $\mu A/cm^2$ to 10 $\mu A/cm^2$ to 50 $\mu A/cm^2$ to 100 $\mu A/cm^2$ and to 150 $\mu A/cm^2$ (Figure 2.15). The surface morphology of these PEDOT with different crystallinities were studied by SEM (Figure 2.16). The lower crystalline PEDOT film showed granular surface while the higher crystalline PEDOT film assumed chunks of fibrillar textures on the surface.

HREM of PEDOT

Like other ordered, conjugated polymers, PEDOT can be imaged using HREM techniques using low-dose methods. However, the limited crystallinity of most PEDOT preparation has meant that there is relatively little order in most cases. An example of some HREM images from PEDOT crystals using low-dose techniques is shown in Figure 2.17. This image is shown with local digital fast fourier transforms (FFTs) superposed on the image, revealing that there is a single predominant spacing corresponding to the ~1.4-nm side-to-side packing of the rigid PEDOT molecules. The HREM images show that the PEDOT molecules are evidently locally quite rigid in solid state, with little or no evidence yet for the molecular bending that has been observed in other conjugated polymers like poly(nonylbithiazole) and poly(nopthalene benzobisoxazole) (Kübel, Gonzalez-Ronda, Drummy & Martin, 2000; Gonzalez-Ronda & Martin, 2004).

Liquid-Crystalline PEDOT

It has been shown the PEDOT can be polymerized in surfactant mesophases, leading to templating of the liquid-crystalline structure on the resulting polymer (Hulvat & Stupp, 2003; Hulvat & Stupp, 2004; Yang, Kim, Hendricks & Martin, 2005). Figure 2.18 is an optical micrograph of a diffusion couple between NP9 surfactant and a PEDOT solution, showing the different characteristic textures that develop, depending on the local symmetry of the most stable mesophase. We have recently reported on the polymerization of PEDOT into bicontinuous cubic phases, resulting in the formation of structures that presumably have both electronic and ionic transport capabilities (Martin, et al., 2009).

Highly Ordered PEDOT Phases

When using bromine as a counterion during electrochemical deposition, extraordinarily large crystals are reproducibly formed. Optical micrographs show highly birefringent, needle-shaped crystals that are hundreds of micrometers in size (Figure 2.19). This ordered microstructure is quite different than the limited order seen when polymerizing PEDOT with other counterions. The crystals are highly textured with a preferred growth plane parallel to the substrate surface. They have well-defined, distinct facets and show sharp melting points in the DSC. FTIR and UV-Vis spectroscopy show characteristic absorptions similar to those seen in PEDOT. XPS has confirmed the presence of peaks characteristic of PEDOT, confirming that at least oligomers have formed. SEM images show an anisotropic fibrillar surface texture oriented perpendicular to the long axes of the needle-shaped crystals. We hypothesize that the large crystals may have formed due to simultaneous crystallization of the EDOT during electrochemical polymerization in the presence of bromine. This process is somewhat similar to the crystallization-induced transesterification reactions that have been observed in certain types of polyesters (Lenz & Go, 1973; Lenz & Go, 1974).

Conclusions

It has been hard to prepare TEM cross section sample of electro chemically deposited PEDOT films. We have developed an effective way of preparing cross section of electro chemically deposited PEDOT for TEM study using microtome with a vibrating diamond knife. PEDOT film is densest near substrate, and is less dense and open near the polymer film surface away from the substrate, which confirms our former founding that the impedance increases initially and then drops after reaching a maximum. This indicates that the minimum impedance correlates well with the surface microstructure and our illustration about PEDOT film growth on electrode sites which the initial growth is dense and smooth and become porous and fuzzy with lots of water content incorporated as the film grows thicker. Some of the fibrillar structure observed in SEM images was collapsed upon microtome. The hairy PEDOT PAA $LiClO_4$ were mostly doped with PAA.

The d_{100} scattering intensity is very strong, while the d_{010} scattering intensity is weak. Different counter-ions of the dopants produce PEDOT with different d_{100} spacing. The simple inorganic counter-ions seem to produce smaller d_{100} spacing than complex polymeric counter-ions. The cations of the dopants have limited effect on d_{100} spacing. The deposition current density plays a significant role in the crystallinity of PEDOT and has no effect on the size of d_{100} spacing.

Experimental

Sample preparation

Baytron P® , obtained from Bayer company, TEM sample was made by dissolving it into water forming a 0.1wt% solution. A drop was deposited onto copper grid with freshly made thin carbon film. Bright field Electrochemical polymerized PEDOT was prepared as follow:

EDOT(Aldrich) was dissolved in water forming a 0.01M solution. Different counter ions, PSS (Aldrich), NaCl (Sigma®), LiF (Aldrich) and poly acrylic acid (PAA) (Aldrich) LiClO4 (Aldrich) were dissolved in the solution forming a 0.01M solution. PEDOT films were grown on ITO or on 35 nm gold-palladium film at a current density of 0.5mA/cm^2 on an Autolab galvanostat/potentiostat with Frequency Response Analyzer (FRA) system.

EIS and CV were collected by the autolab. PEDOT with different counter-ions are polymerized on bare ball electrodes with a diameter of about 400 μm at a deposition current of 2 μA for 300 seconds.

PEDOT doped with different counter ions were made by electrochemical polymerization onto substrates with 35nm thick gold-palladium thin film on them. Structures of the films were studied by Wide angle x ray scattering (WAXS) on a Bruker D8 Discover diffractometer with a fine-focused beam and x-y-z translation stage.

Microtomed samples were prepared as follows:

Thin PEDOT film was deposited onto an epoxy substrate with 35nm Au-Pd film with a current density of 0.5mA/cm^2 for 15minutes. The film was then embedded in epoxy. 60nm thick TEM samples were cut by Reichert FC4 ultramicrotome with a Diatome oscillating knife under room temperature. LVEM samples were cut into 20nm thick slices.

Hairy PEDOT film was prepared by the previous method reported by our lab (Yang, Lipkin & Martin, 2007). It was then examined under WAXS. The SEM sample was coated with 10nm thick gold film to improve the conductivity of the PEDOT film. The microtomed sample was examined by TEM.

PEDOT-NaCl films were prepared under different current density ranging from 5 μA/cm^2 to 180 μA/cm2 with the same amount of deposition charge by varying different polymerization time. Conductivity of the PEDOT films were evaluated by a four point probe.

Optical micrograph of Mictrotomed sample was taken by a Nikon Optical Scope. Bright field images were taken by JOEL 3011. Scanning transmission electron microscope (STEM) dark field images and elemental mappings were taken by JOEL 2010F.

Equipments

Optical microscopy was done on a Nikon Optiphot-POL (Mager Scientific, Dexter, Michigan, USA) in transmitted or reflected light. The microscope was also equipped with polarizers and analyzers and a full-wave red filer. Digital images were acquired with a SPOT-RT camera (Diagnostic Instruments; Mager Scientific, Dexter, Michigan, USA).

Wide-angleX-ray diffraction patternswere acquiredwith a BrukerD8Discover system (Bruker AXS Inc., Madison,Wisconsin, USA), equipped with a 2D position-sensitive wire array detector. Samples were typically oriented in a near-grazing incidence geometry, with the film plane horizontal and the Cu Kα X-ray source at an incoming

angle of ~2 degrees, and the detector collecting the diffracted X-rays from ~5 to 40 degrees 2θ.

TEM imaging was performed with a 200 kV JEOL 2010F STEM and a JEOL 3011 at the EMAL at the University of Michigan. We have recently described the use of low-dose HREM techniques for beam-sensitive polymers. The estimated critical dose of PEDOT has been determined to be ~0.1 C/cm^2. This correlates with the established relationship between electron beam sensitivity and thermal stability (Martin, Chen, Yang, Drummy & Kübel, 2005; Kumar & Adams, 1990). Digital images were acquired using a CCD.

Figures and tables

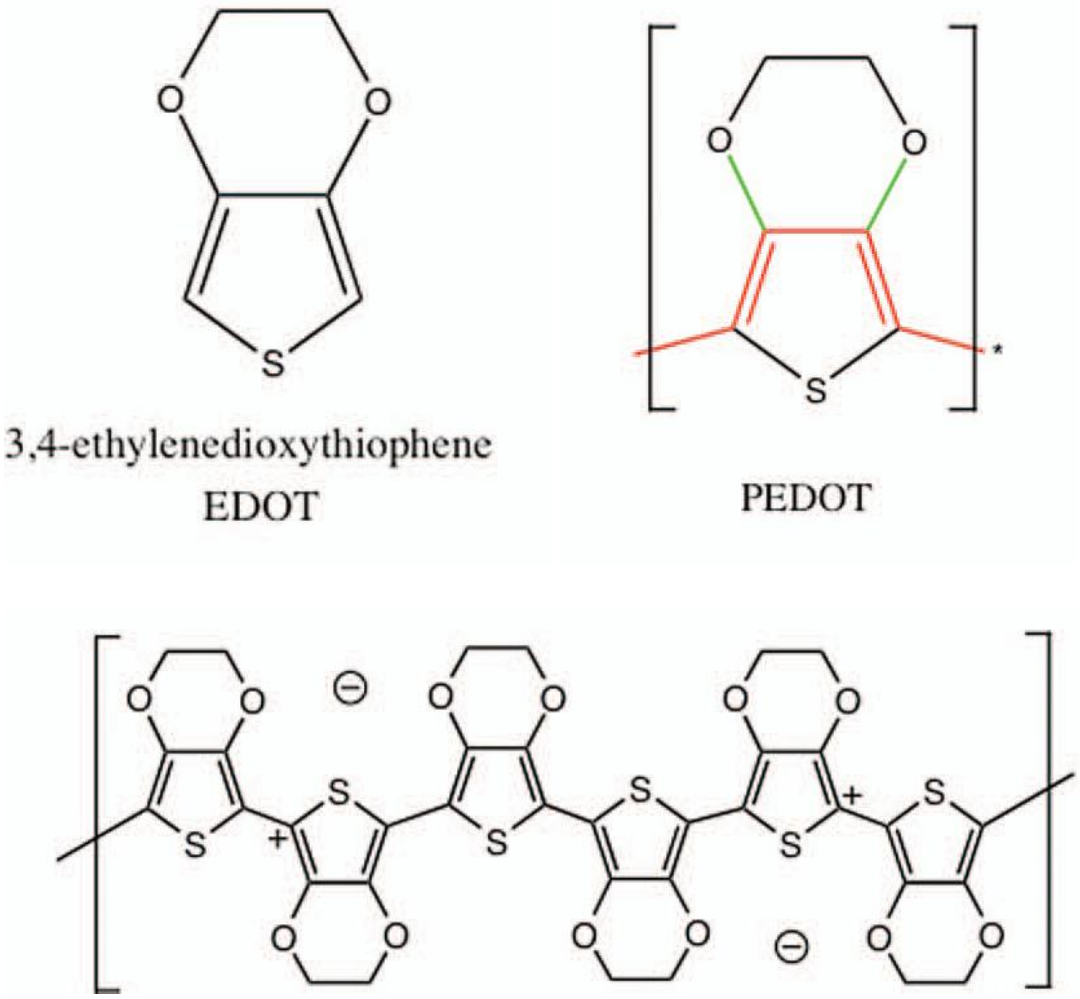

Figure 2.1. Top: Chemical structures of 3,4-ethylene dioxythiophene (EDOT) and poly(3,4-ethylene dioxythiophene) (PEDOT) Bottom: In the electrically active, oxidized state, there is one positive charge on the PEDOT molecule per every three EDOT units. This charge on the backbone is balanced with an anion that may be either a small molecule or a macromolecular anion such as poly(styrene sulfonate) (PSS).

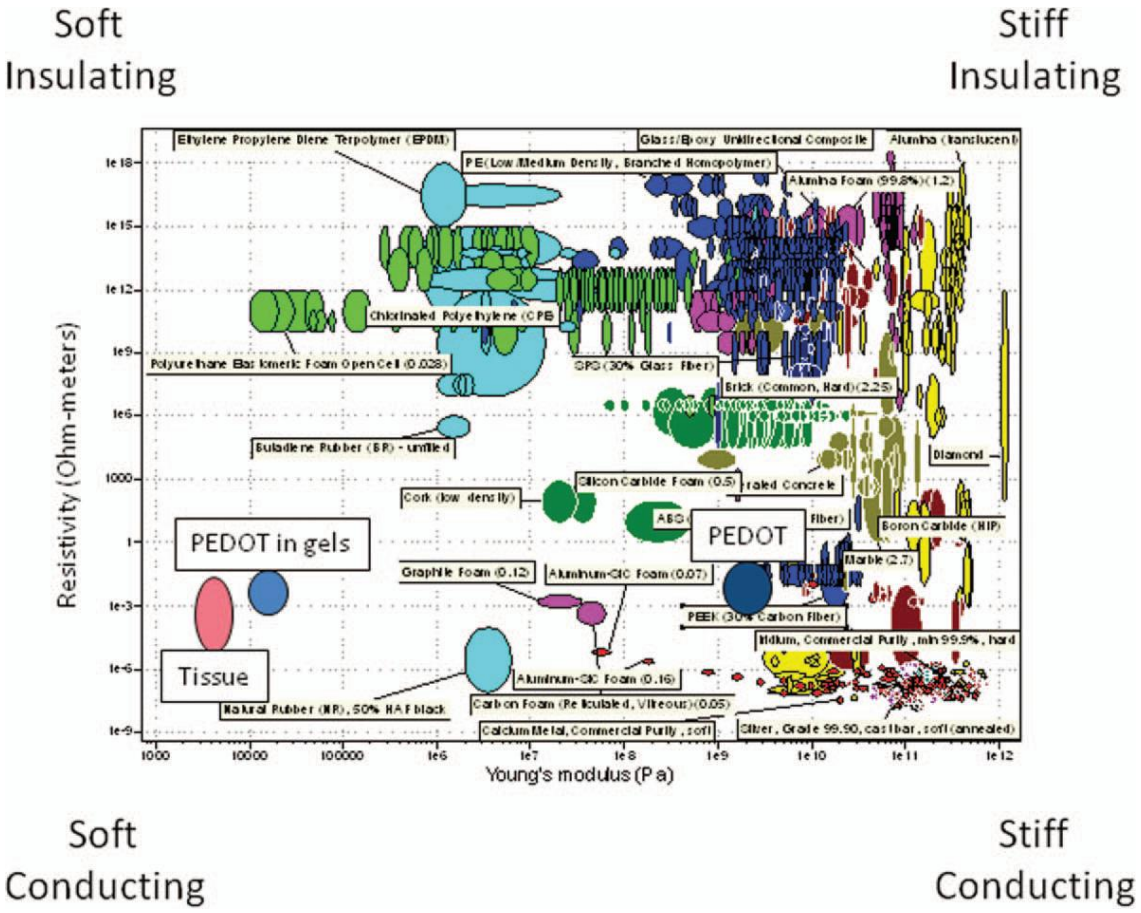

Figure 2.2. Plot of the electrical properties of materials (resistivity in ohm/m) as a function of their mechanical properties (Young's modulus in Pa) for known engineeringmaterials. Plot generated using CES Selector software version 4.6.1 by Granta Design. The upper right shows the stiff insulating ceramics, and the lower right shows the stiff, conducting inorganic metals and semiconductors. Polymers are typically insulating and are softer than ceramics but not nearly as soft as gels and foams. Tissue is quite soft and is also conducting because it is an electrolyte. There is a need for soft, conducting materials that can interface between the living tissue and the hard, electrically conducting materials typically used in biomedical devices.

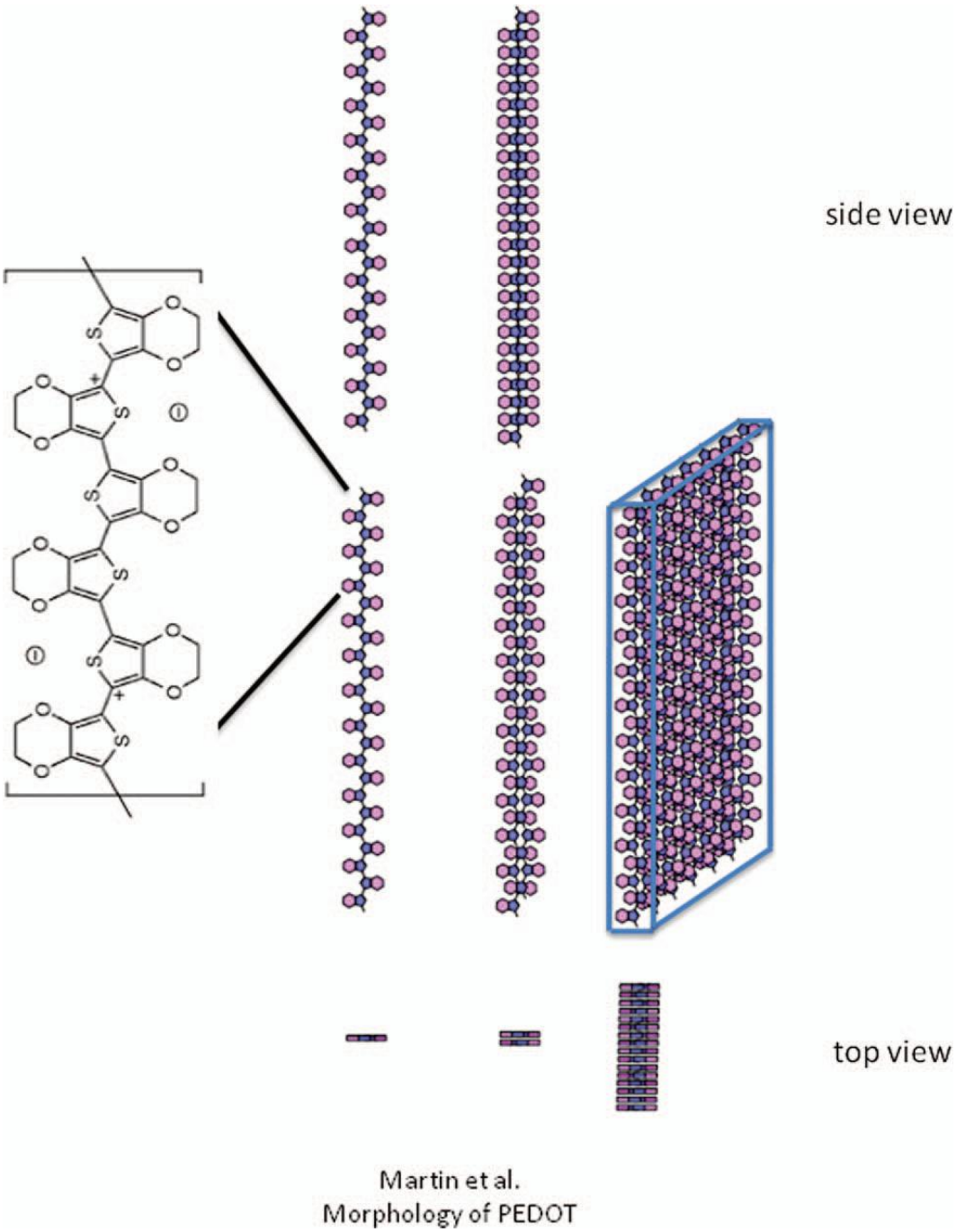

Figure 2.3. Schematic diagrams showing the geometry and assembly of single PEDOT chains, twochain PEDOT molecular complexes, and PEDOT sheets. Top: Side view ([010] projection), middle: oblique view, bottom: top view ([001] projection).

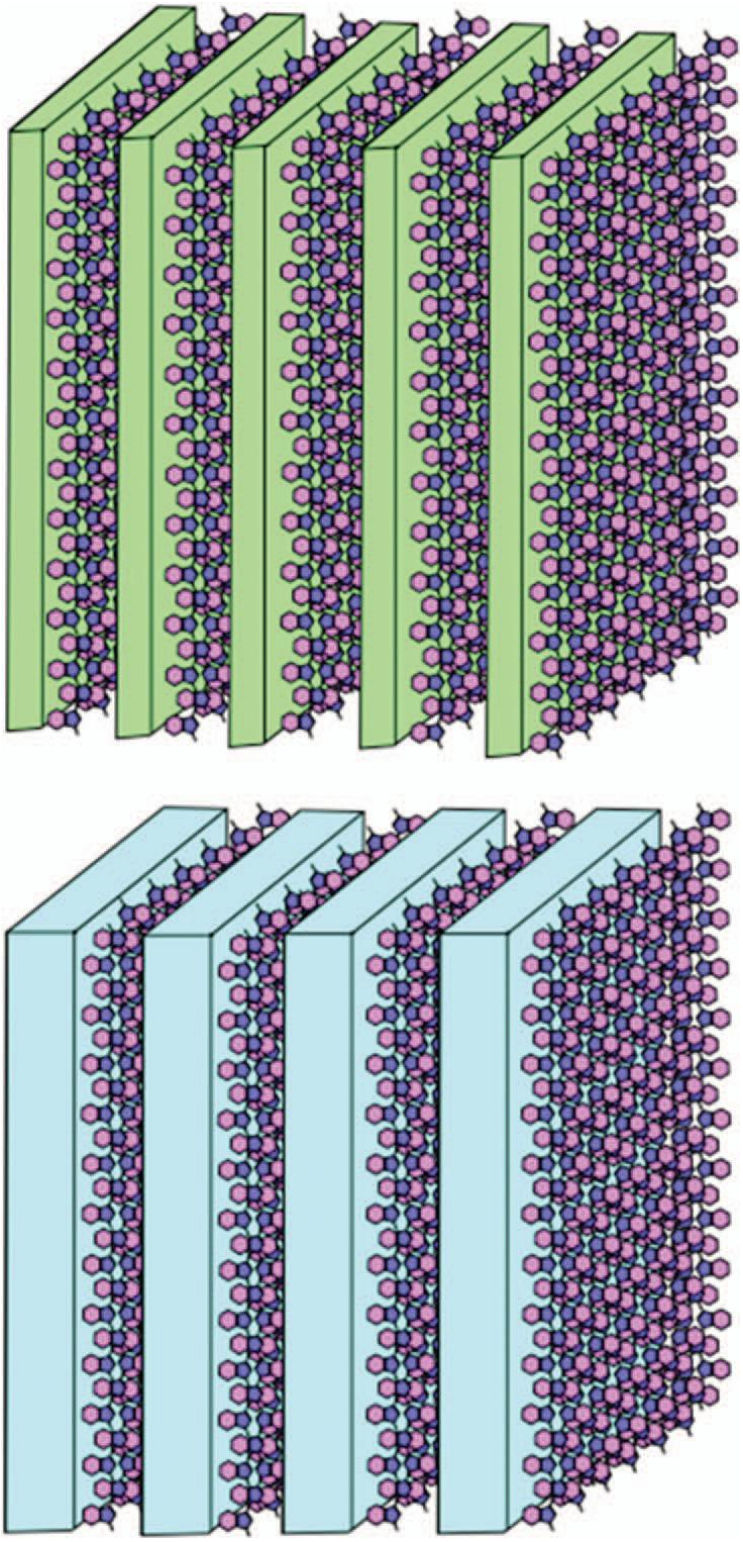

Figure 2.4. Schematic of the variation in microstructure of crystalline PEDOT with different dopants causing the (100) sheets of PEDOT chains to be closer together (green) or farther apart (blue) depending on the chemistry of the counterions used.

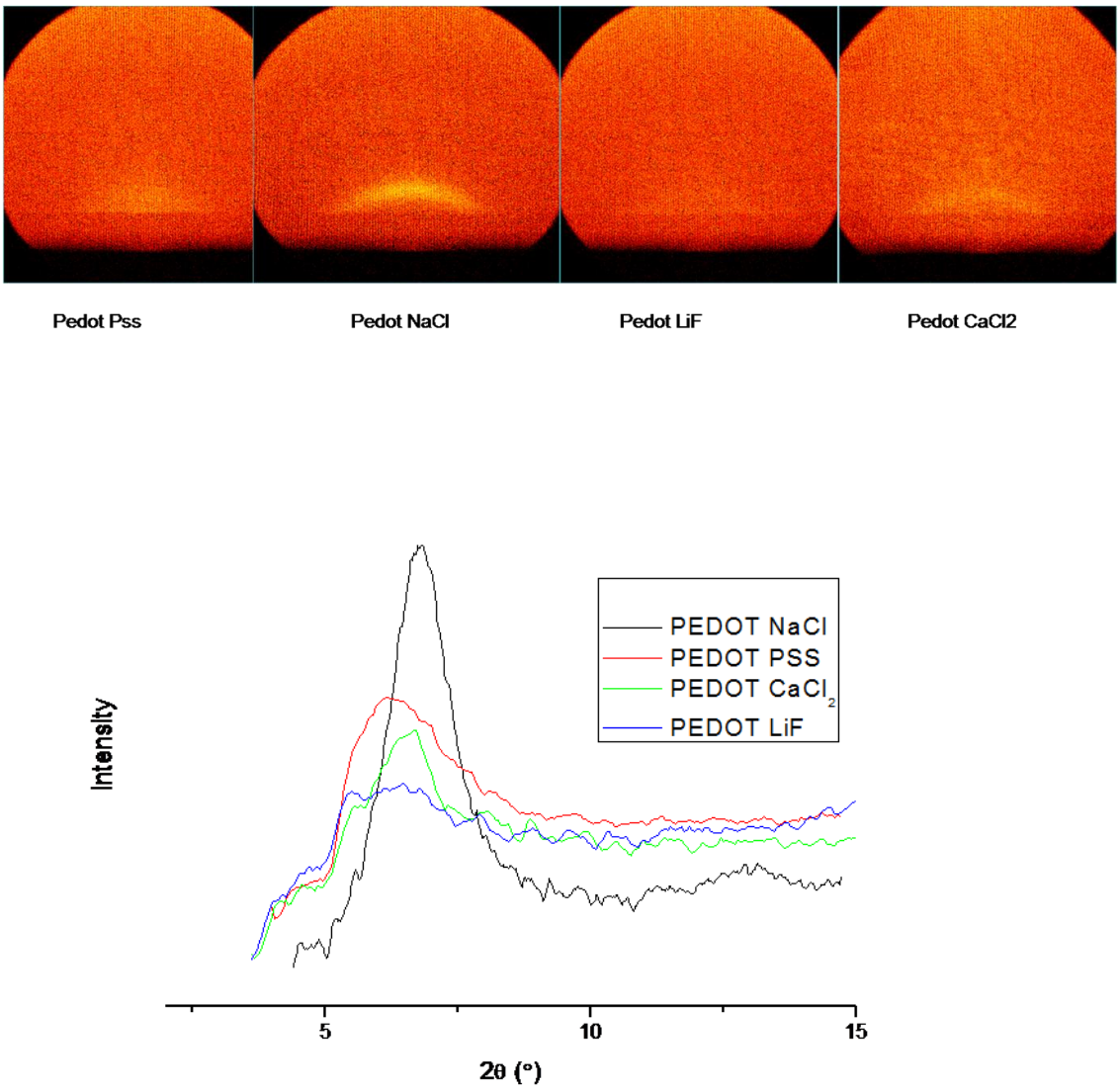

Figure 2.5. Top: 2D wide-angle x-ray scattering (WAXS) of scattering from PEDOT with different counterions: PSS, NaCl, LiF, and CaCl2. Bottom: Azimuthally averageWAXS scans of the scattering below 20 degrees showing the development of the ~1.4 nm (100) intersheet peak with different counterions.

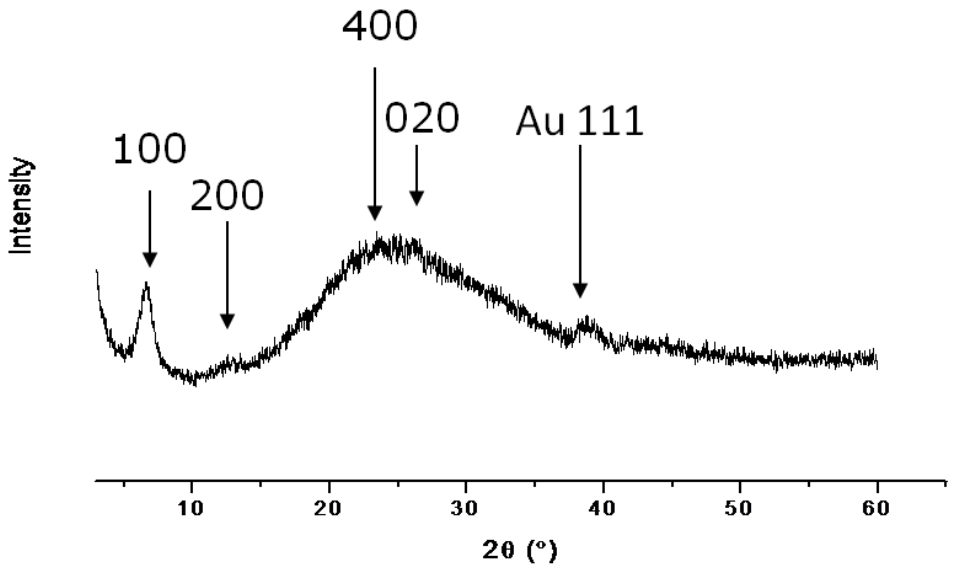

Figure 2.6. Powder WAXS from PEDOT films showing the (100), (200), (400), and (020) peaks for crystalline PEDOT. There is also a peak from an underlying Au(111) film used for electrochemical deposition and diffraction pattern calibration.

Table 2.1

(100) *d*-Spacings of PEDOT as a function of counterion chemistry

Counterion	d_{100} (nm)
PAA^-	1.52
PSS^-	1.46
PTS	1.39
Cl^- (NaCl)	1.39
C_{14} SO_3	1.37
Cl^- ($CaCl_2$)	1.33
EBS	1.32
CSA	1.29
F^-	1.15

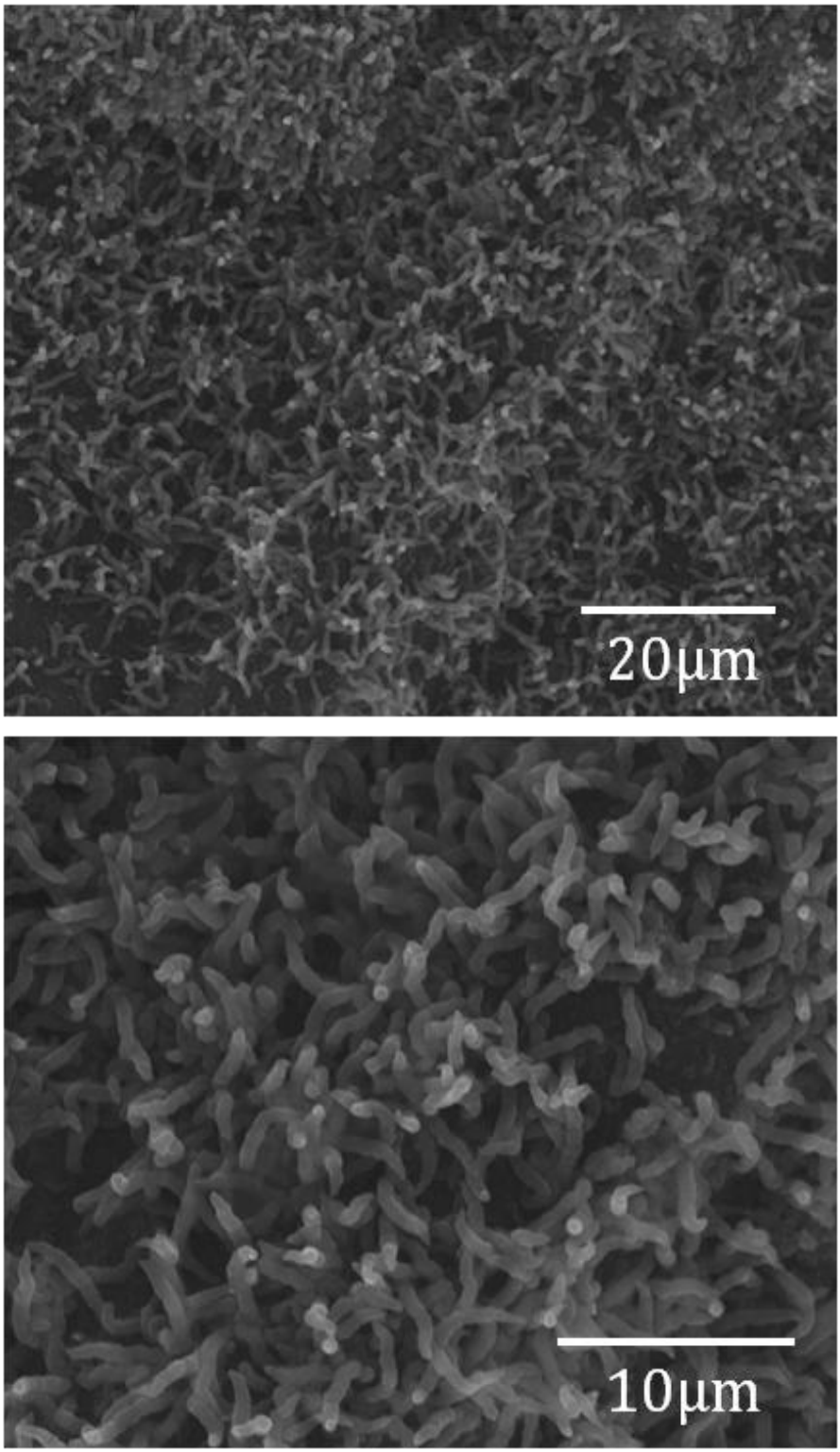

Figure 2.7. SEM images of PEDOT nanofibrils deposited over an extended flat electrode. The nanofibrillar structure is obtained when poly(acrylic acid) is used as a counterion.

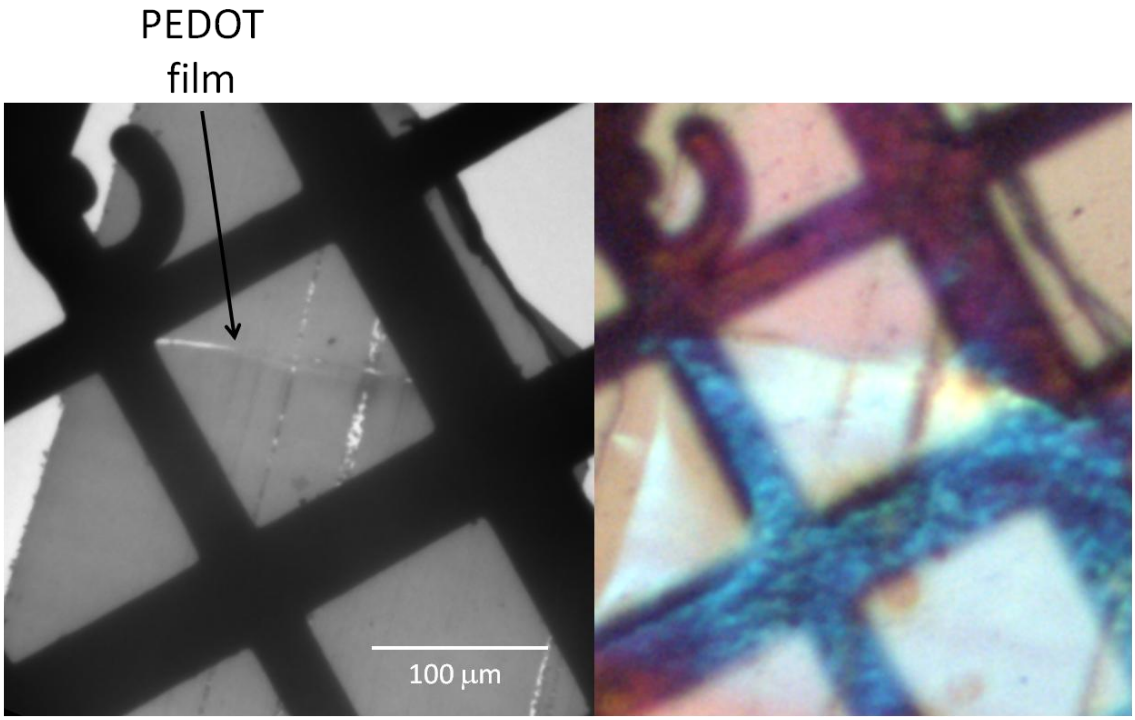

Figure 2.8. Left: Low-magnification TEM image of the cross section of a PEDOT film embedded in epoxy. Right: Optical microscope image of the same PEDOT film taken in reflected light.

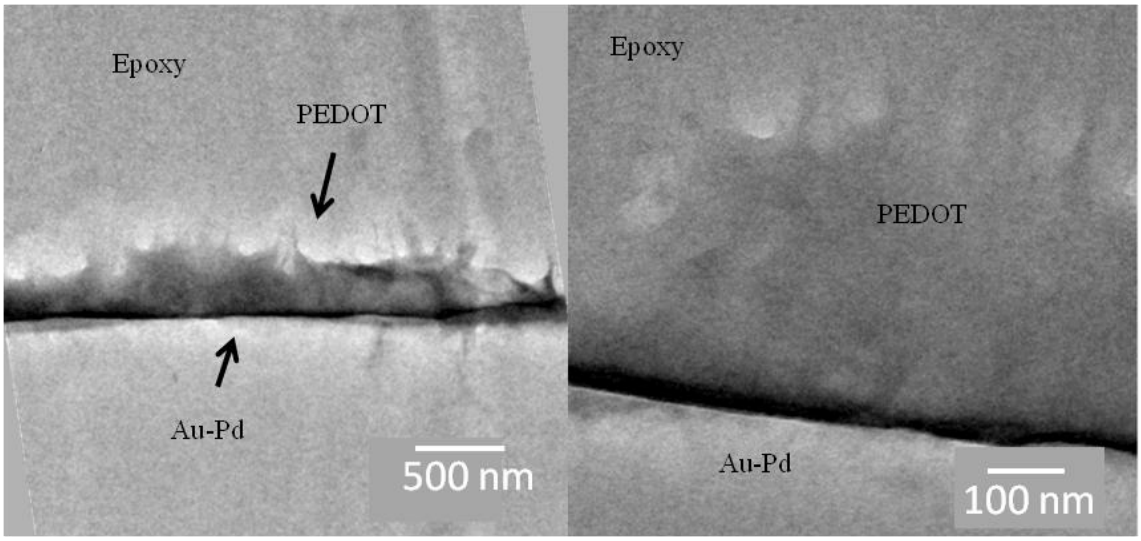

Figure 2.9. Brightfield TEM images of the cross section of a ~400-nm PEDOT thin film grown on a thin Au-Pd sputter-deposited polycrystalline metal film. The PEDOT is relatively uniform in density with an extremely rough surface texture.

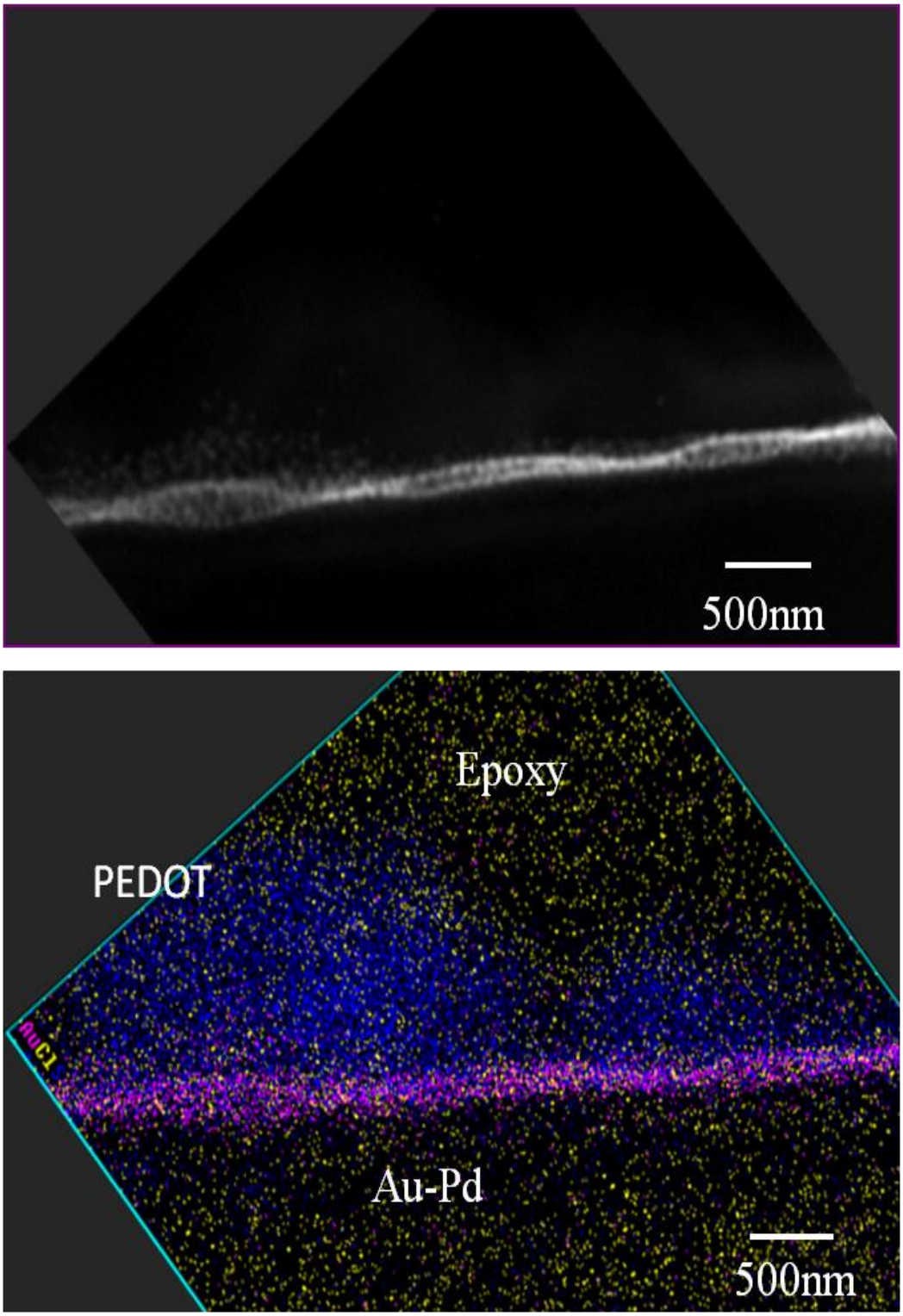

Figure 2.10. Top: STEM Z-contrast of a PEDOT film on an Au-Pd substrate. Bottom: EDS elemental mapping of the same region of the sample. In this image purple is gold, blue is sulfur, and yellow is chlorine.

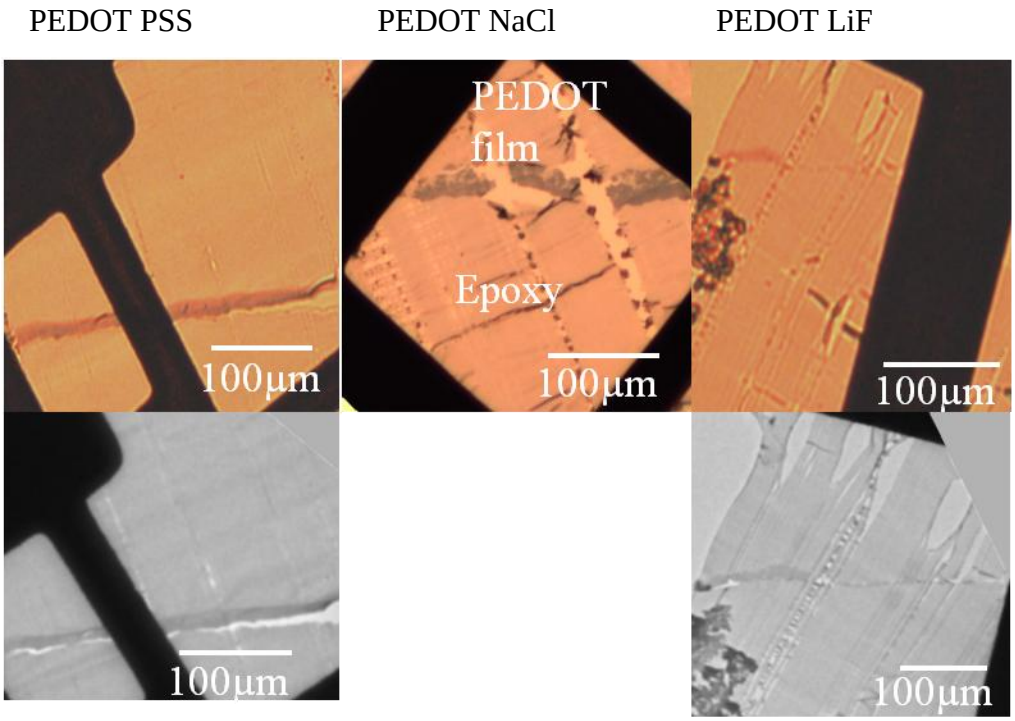

Figure 2.11. Microtomed TEM sample of PEDOT film (top: transmitted light optical images, bottom: low magnification bright field TEM images)

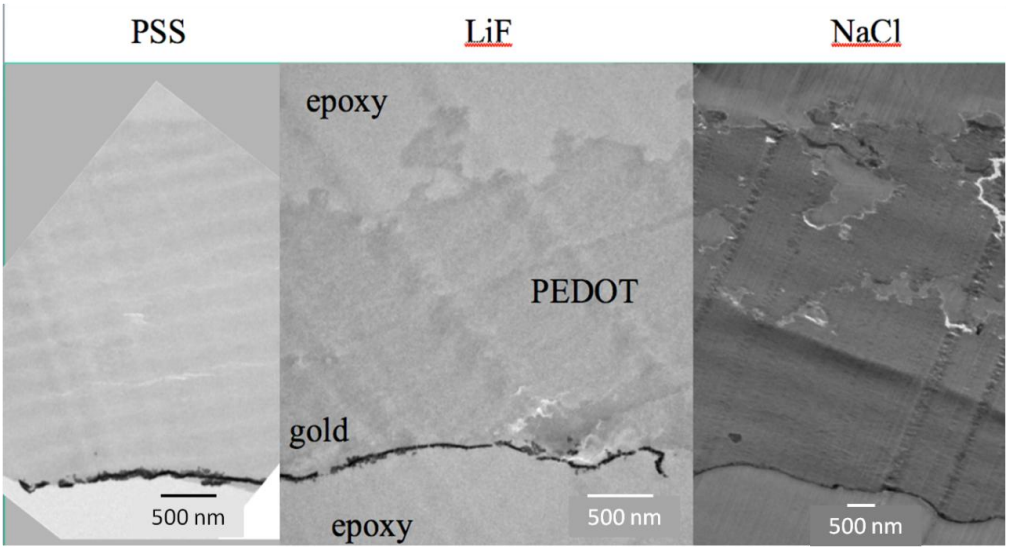

Figure 2.12. Bright field TEM images of cross sections of electrochemically deposited PEDOT film with different counter-ions.

EIS Impedance of PEDOT

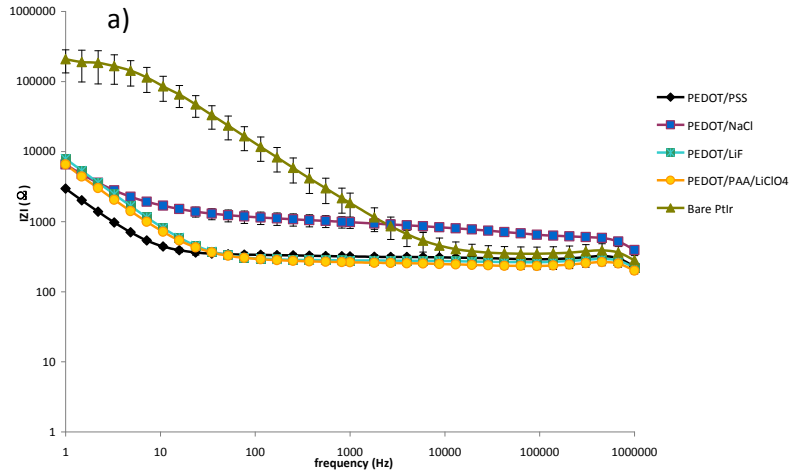

EIS Phase Angle of PEDOT

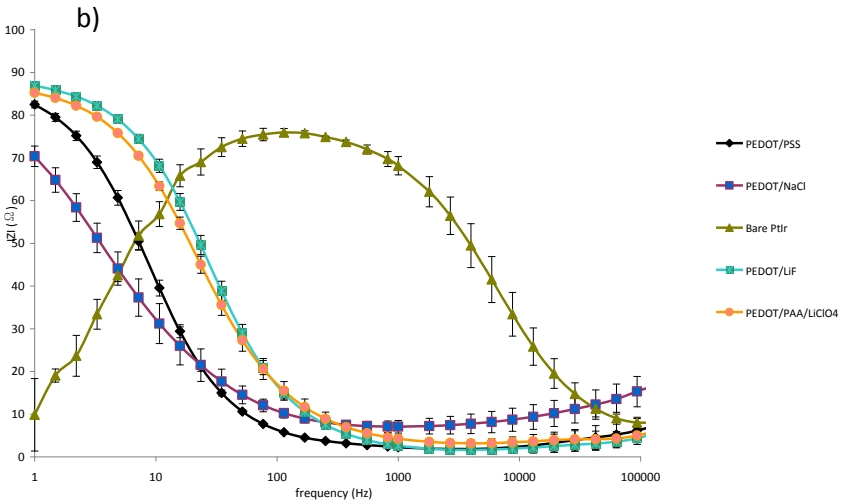

c)

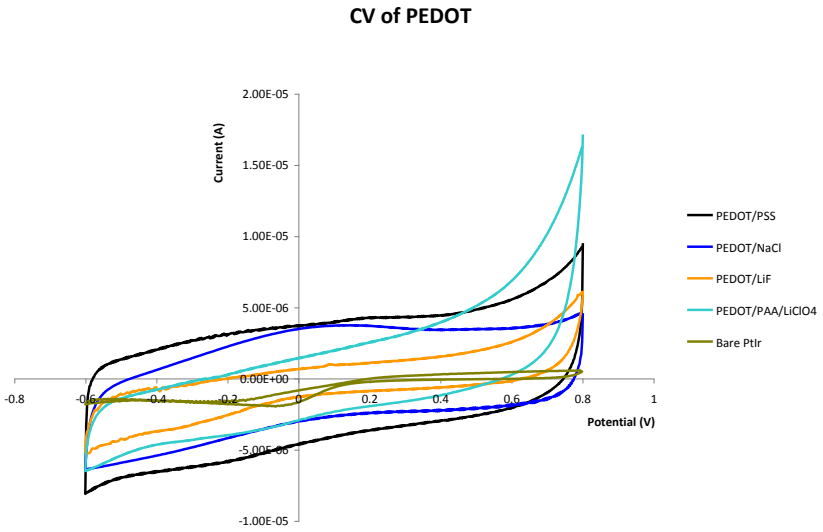

d)

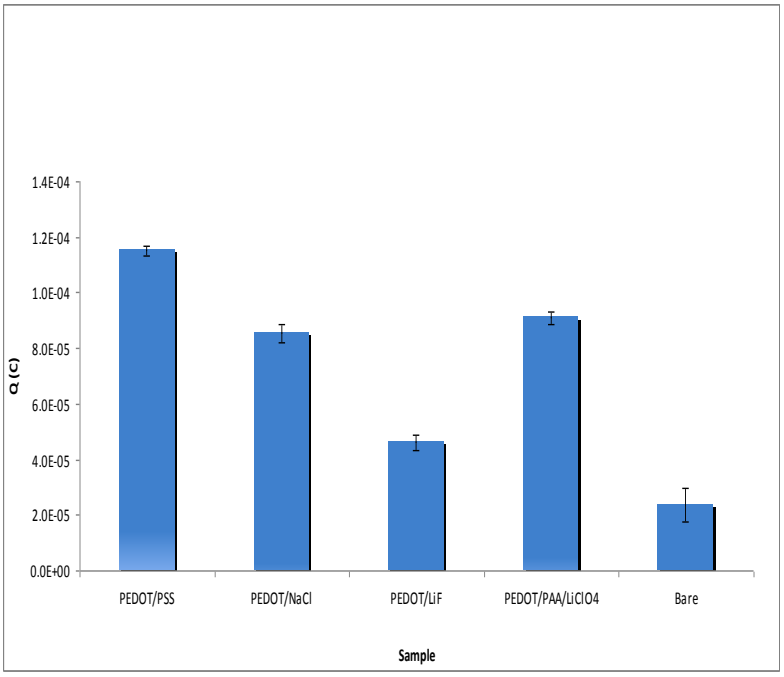

Figure 2.13. EIS and CV of electrochemically deposited PEDOT film with different counter-ions (a. Impedance plot of electrochemical deposited PEDOT with different counter-ions, b. Phase angle plot of electrochemical deposited PEDOT with different counter-ions, c. CV of electrochemical deposited PEDOT with different counter-ions, d. Charge capacities of electrochemical deposited PEDOT with different counter-ions)

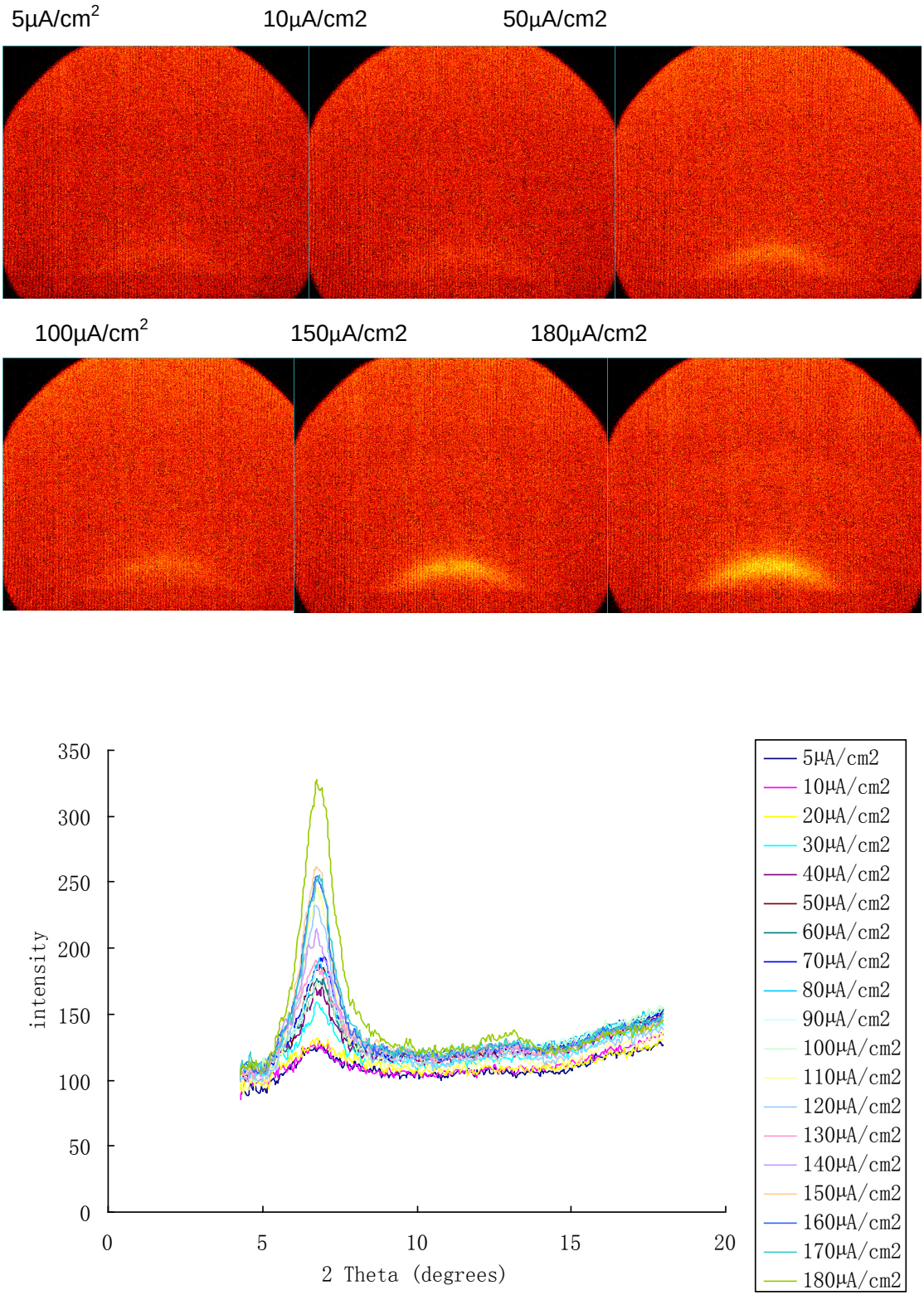

Figure 2.14. WAXS of PEDOT NaCl electrochemical polymerized under different deposition current densities showing control of crystallinity by the sharpness of the diffraction pattern (top: 2-D Scan, bottom: 1-D Scan).

Deposition current ($\mu A/cm^2$)	Crystallinity (fraction)
5	0.205
10	0.21
50	0.23
100	0.27
150	0.32
180	0.35

Table 2.2. Crystallinity of PEDOT-NaCl with different deposition current density (calculated from WAXS)

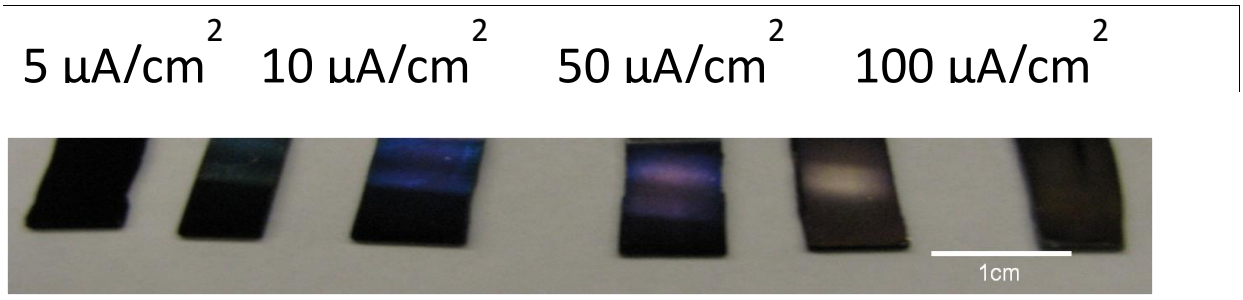

Figure 2.15. Different colors of PEDOT NaCl with different deposition current densities .

5 μA/cm^2 10 μA/cm^2 50 μA/cm^2

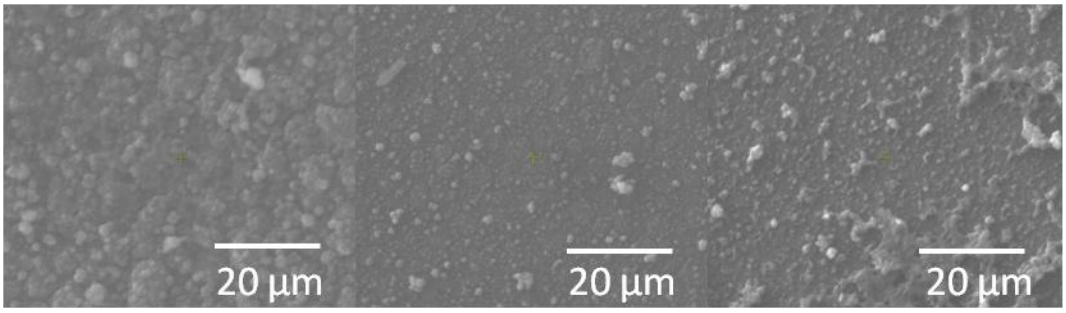

100 μA/cm^2 150 μA/cm^2 180 μA/cm^2

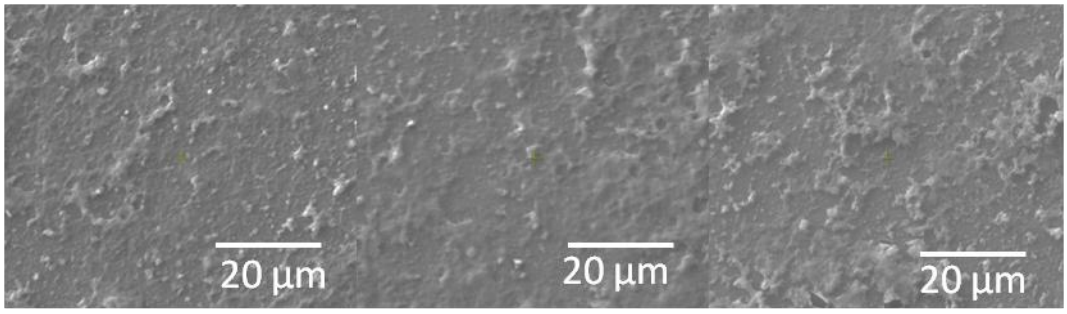

Figure 2.16. Different colors of PEDOT NaCl with different deposition current densities (the units are μA/cm^2).

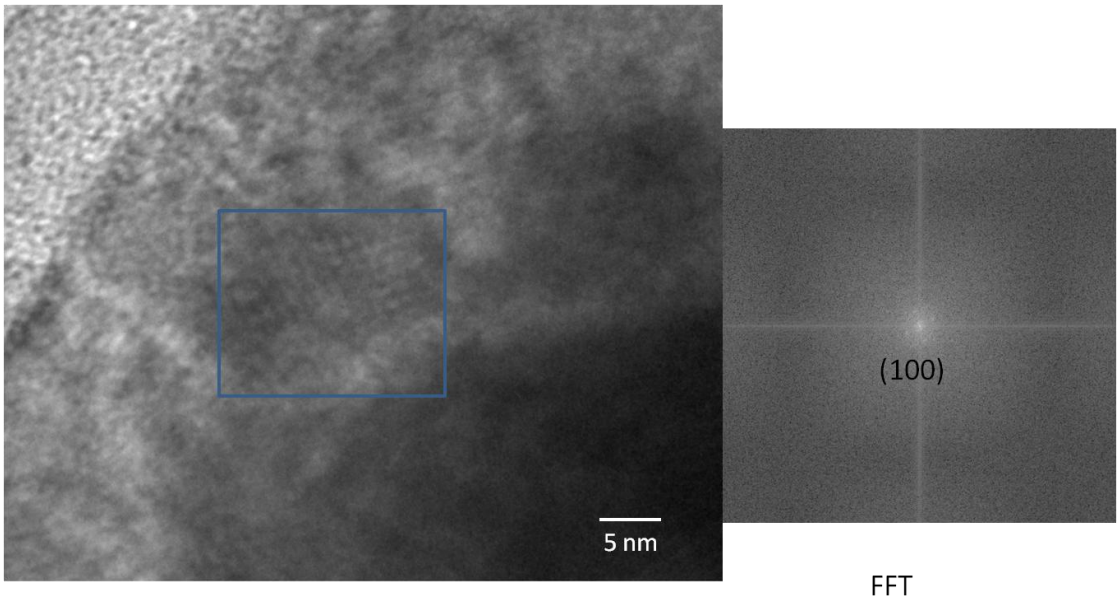

Figure 2.17. Low-dose HREM image of PEDOT film. There is only weak order in the film, although some regions have evidence for crystallites with ~1.4 nm (100) fringes corresponding to stacks of PEDOT chains arranged into layers, consistent with the XRD results. Right FFT shows ~1.4-nm (100) fringes in different regions of the image.

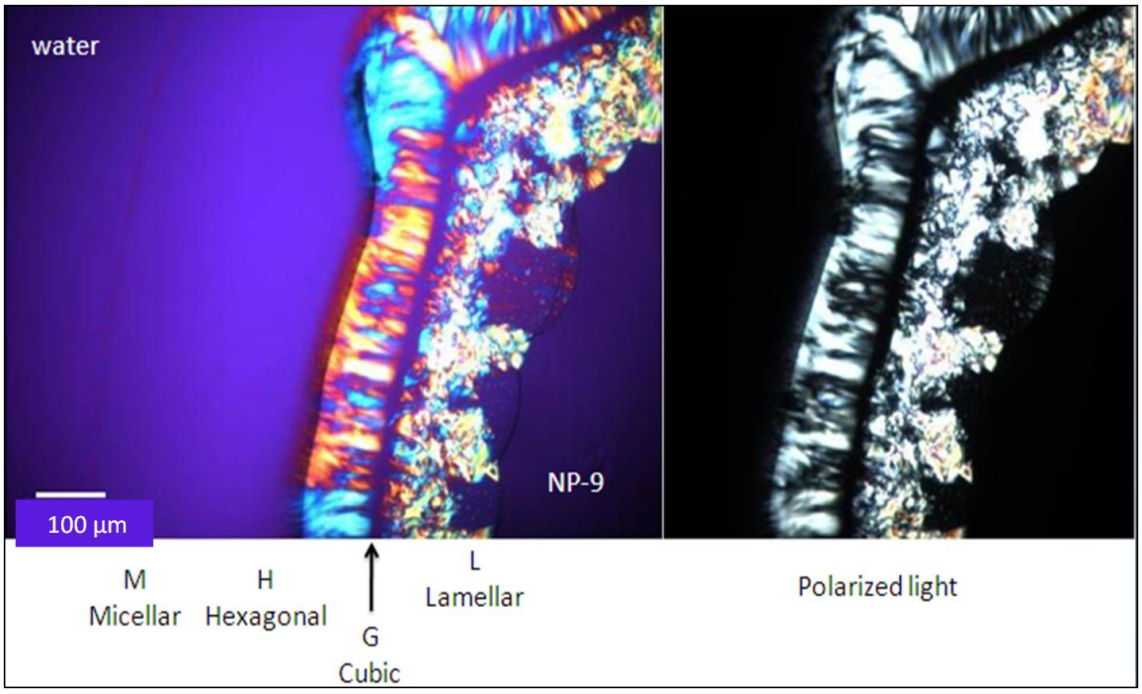

Figure 2.18. Optical micrograph of a diffusion couple formed between water and the nonionic surfactant NP-9. The concentration of nonionic surfactant increases from left to right, corresponding to the formation of a number of different phases with different characteristic textures including M (micellar), H (hexagonal), G (bicontinuous cubic), and L (lamellar). The texture is shown in cross-polarized light (right) and with a full-wave red filter (left).

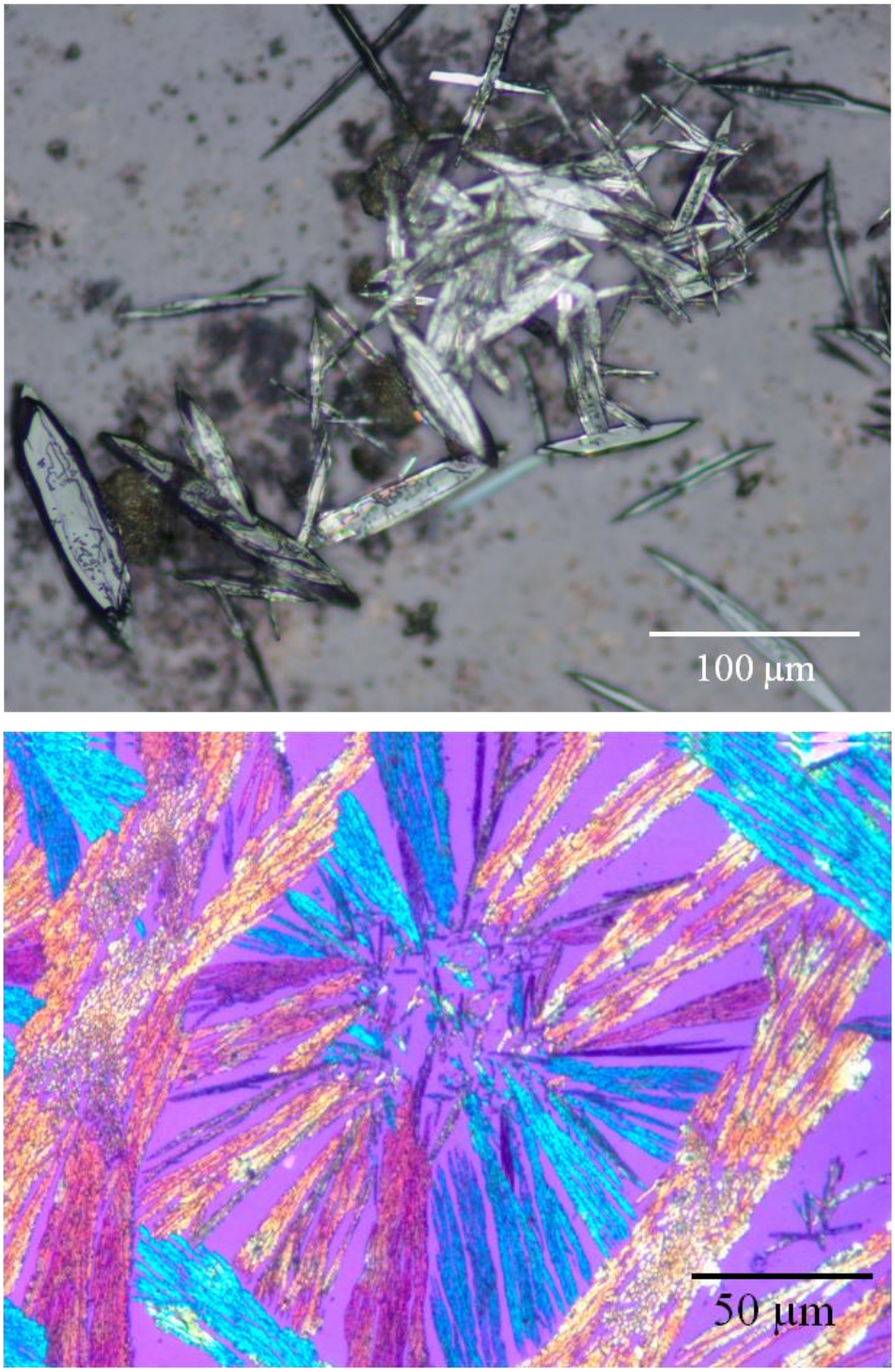

Figure 2.19. Optical micrographs of electrochemically deposited PEDOT film, using bromine as a counterion. Top image: Brightfield; lower image: in polarized light with a full-wave red filter. The films have highly regular, birefringent, faceted crystals that are tens of micrometers in size.

References

Aasmundtveit, K. E.; Samuelsen, E. J.; Pettersson, L. A. A.; Ingan ̈as, O.; Johansson, T.; Feidenhans'l, R. *Synthetic Metals*, **101**, (1999), 561–564.

Abidian, M. R.;Martin,D. C. *Advanced Functional Materials*, **19**, (2009), 573–585.

Abidian, M. R.; Kim, D.-H.; Martin, D. C. *Advanced Materials*, **18**, (2006), 405–409.

Ahmad, S.; Deepa, M.; Singh, S. *Langmuir*, **23**, (2007), 11430–11433.

Ashby, M. F. Materials selection in mechanical design; Elsevier Butterworth-Heinemann: Burlington, MA, (2005).

Asplund, M.; von Holst, H.; Ingan ̈as, O. *Biointerphases*, **3**, (2008), 83–93.

Balog, M.; Rayah, H.; Le Derf, F.; Salle, M. *New Journal of Chemistry*, **32**, (2008), 1183–1188.

Batchelder, D. N. *Contemporary Physics*, **29**, (1988), 3–31

Bäurle, P.; Scheib, S. *Acta Polymerica*, **46**, (1995), 124.

Cui, X.; Martin, D. C. *Sensors and Actuators B: Chemical*, **89**, (2003), 92–102.

Döbbelin, M.; Marcilla, R.; Salsamendi, M.; Pozo-Gonzalo, C.; Carrasco, P. M.; Pomposo, J.A.; Mecerreyes, D. *Chemistry of Materials*, **19**, (2007), 2147–2149.

Forrest, S. R. *Nature*, **428**, (2004), 911–918.

Gonzalez-Ronda, L.; Martin, D. C. *Macromolecules*, **37**, (2004), 2872–2879.

Greczynski, G.; Kugler, T.; Salaneck, W. R. *Thin Solid Films*, **354**, (1999), 129–135.

Groenendall, L. B.; Jonas, F.; Freitag, D.; Pielartzik, H.; Reynolds, J. R. *Advanced Materials*, **12**, (2000), 481–494.

Groenendaal, L. B.; Zotti, G.; Aubert, P.-H.;Waybright, S.M.; Reynolds, J. R. *Advanced Materials*, **15**, (2003), 855–879.

Hulvat, J. F.; Stupp, S. I. *Angewandte Chemie International Edition*, **42**, (2003), 778–781.

Hulvat, J. F.; Stupp, S. I. *Advanced materials*. 16, (2004), 589–592.

Im, S. G.; Gleason, K. K. *Macromolecules*, **40**, (2007), 6552–6556.

Im, S. G.; Olivetti, E. A.; Gleason, K. K. *Surface and Coatings Technology*, **201**, (2007), 9406–9412.

Kim, J.; Kim, E.; Won, Y.; Lee, H.; Suh, K. *Synthetic Metals*, **139**, (2003), 485–489.

Kirchmeyer, S.; Reuter, K. *Journal of Materials Chemistry*, **15**, (2005), 2077– 2088.

Kirchmeyer, S.; Reuter, K.; Simpson, J. C. in *Conjugated polymers: theory, synthesis, properties and characterization*; Skotheim, T. A. and Reynolds, J. R., Eds.; Taylor and Francis: Boca Raton, FL, (2007). Chapter 10, pp. 10-1–10-22.

Kübel, C.; Gonzalez-Ronda, L.; Drummy, L. F.; Martin, D. C. *Journal of Physical Organic Chemistry*, **13**, (2000), 816–829.Lang, U.; M ¨uller, E.; Naujoks, N.; Dual, J. *Advanced Functional Materials*, **19**, (2009), 1215–1220.

Kumar, S.; Adams, W. W. *Polymer*, **31**, (1990), 15–19.

Lenz, R. W.; Go, S. *Journal of Polymer Science Part A: Polymer Chemistry*, **11**, (1973), 2927.

Lenz, R. W.; Go, S. *Journal of Polymer Science Part A: Polymer Chemistry*, **12**, (1974), 1–10.

Lima, A.; Schottland, P.; Sadki, S.; Chevrot, C. *Synthetic Metals*, **93**, (1998), 33.

Lock, J. P.; Im, S. G.; Gleason, K. K. *Macromolecules*, **39**, (2006), 5326– 5329.

Martin, D. C.; Chen, J.; Yang, J.; Drummy, L. F.; K ¨ubel, C. *Journal of Polymer Science: Physics*, **43**, (2005), 1749–1778.

Martin, D. C., Shen, Y., Wu, J., Povlich, L., Leach, M., Spanninga, S., and Shaw, C., *PMSE Preprints*, Proceedings of the American Chemical Society Meeting, Salt Lake City, UT, March (2009).

Ng, S. C.; Chan, H. S. O.; Yu, W.-L. *Journal of Materials Science Letters*, **16**, (1997), 809.

Povlich, L. K.; Cho, J. C.; Spanninga, S.; Martin, D. C.; Kim, *J. Polymer Preprints*, **48**, (2007), 7–8.

Reeves, B. D.; Thompson, B. C.; Abboud, K. A.; Smart, B. E.; Reynolds, J. R. *Advanced Materials*, **14**, (2002), 717–719.

Rimmel, G.; B ¨aurle, P. *Synthetic Metals*, **102**, (1999), 1323.

Sadki, S.; Schottland, P.; Brodie, N.; Sabouraud, G. *Chemical Society Reviews*, **29,** (2000), 283–293.

Schlenoff, J. B.; Xu, H. *Journal of the Electrochemical Society*, **139**, (1992), 2397–2401.

Schuhmann, W. in *Immobilized biomolecules in analysis: A practical approach*; Cass, T. and Ligler, F. S., Eds.; Oxford: New York, (1998); 198.

St ́ephan, O.; Schottland, p.; Le Gall, P. Y.; Chevrot, C.; Mariet, C.; Carrier, M. *Journal of Electroanalytical Chemistry*, **443**, (1998), 217–226.

Timpanaro, S.; Kemerink, M.; Touwslager, F. J.; de Kok, M. M.; Schrader, S. *Chemical Physics Letters*, **394**, (2004), 339.

von Bekesy, G. *Journal of the Acoustical Society of America*, **24**, (1952), 72–76.

Winther-Jensen, B.; Breiby, D. W.; West, K. *Synthetic Metals*, **152**, (2005), 1–4.

Winther-Jensen,B.; Forsyth, M.;West, K.;Andreasen, J.W.; Bayley, P.; Pas, S.;MacFarlane,D.R. *Polymer*, **49**, (2008), 481–487.

Winther-Jensen, B.; West, K. *Macromolecules*, **37**, (2004), 4538–4543.

Yang, J.; Kim, D.; Hendricks, J.; Martin, D. C. *Acta Biomaterialia*, **1**, (2005), 124–136.

Yang, J.; Lipkin, K.;Martin, D. C. *Journal of Biomaterials Science—Polymer Edition*, **18**, (2007), 1075–1089.

Yang, J.; Martin, D. C. *Sensors and Actuators A: Physical*, **113**, (2004a), 204–211.

Yang, J.; Martin, D. C. *Sensors and Actuators B: Chemical*, **101**, (2004b), 133–142.

Yang, J.; Martin, D. C. *Journal of Materials Research*, **21**, (2006), 1124– 1132.

Chapter III

High resolution and low voltage electron microscopy of polymers and organic molecules: a review of recent development

Abstract

Electron microcopy has been widely used to study the morphology of polymers and organic molecular crystals. The low contrast and beam sensitivity of polymeric and organic samples have been major limiting factors in studies using Transmitted Electron Microscopy (TEM), as compared to inorganic samples. High Resolution Electron Microscopy (HREM) has been developed to directly image crystal packing of organic samples using low dose techniques to minimize beam damage. A novel low voltage (~5 kV) electron microscope (LVEM) has been developed to address the issue of low contrast of organic samples and samples with low atomic number elements in electron microscopy. Recent progress about HREM and LVEM in our research group and other researchers has been reviewed. Strengths and problems of these techniques are detailed and discussed.

Introduction

The properties of polymers and organic molecular materials are largely dependent on their molecular structures, architecture and processing history. Electron Microscopy (EM) is a powerful tool to study structure-property correlations of homopolymers, copolymers, blends, and composites over a variety of length scales. The most common EMs include transmission electron microscopes (TEM) and scanning electron microscopes (SEM) (Adhikari & Michler, 2009; Sawyer, Grubb & Meyers, 2008; Egerton, 2005).

Figure 3.1 shows a schematic of the interactions of different types of electron and ion beams with a sample, and the various types of signals that can be generated. In a

TEM, the electron beam is defocused and uniformly illuminates a relatively thin sample. The image is collected from the transmitted beam, and contrast develops due to interactions with the local variations in density, thickness, or crystallographic orientation. HREM refers to imaging in TEM mode by phase contrast at a resolution sufficient to see the regular intermolecular packing arrangements of the crystal lattice directly (Voigt-Martin, Krug & Dyck, 1990), and so is also often referred to as "lattice imaging" (Martin & Thomas, 1995; Martin, Chen, Yang, Drummy & Kübel, 2005).

In an SEM the beam is focused down to a small spot and then rastered across the sample surface. An image is formed by collecting either secondary electrons (SE) or backscattered electrons (BSE), and then plotting the intensity of this signal as a function of the position of the beam on the sample I(x,y). The SE image mode is quite sensitive to the angle of inclination of the surface, and thus primarily provides information about the topography of the sample. The BSE intensity is more a function of atomic number, and thus the BSE image mode produces images with compositional contrast. For thin enough samples, the beam can penetrate through the samples, making it possible to do Scanning Transmission Electron Microscopy (STEM). STEM imaging combines aspects common to both SEM and TEM (Egerton, 2005).

Specific interactions with the sample make it possible to obtain analytical information about the local chemistry, including atomic number and electron bonding states. When the electron beam interacts with the atoms in the material there can be energy lost due to collective excitations (plasmons, with typical energies of 10-30 eV) or specific energetic transitions within the atom (characteristic loss edges, from 100-1000 eV). By quantifying the energy of the transmitted electron beam, it is possible to perform electron energy loss spectroscopy (EELS) (Egerton, 1986; Libera & Egerton, 2010). Photons can also be emitted from the sample, and these may have energies in the characteristic X-ray range (enabling energy dispersive spectroscopy, or EDS), or they may also be in the visible range (cathodoluminescence). Finally, Auger electrons with characteristic low energies (50 eV – 3 kV) can be emitted from the near surface of the sample (few nm), facilitating sensitive measurements of surface composition.

The energy of the electron beam depends on the accelerating voltage of the microscope and the mode of imaging used. The emission filaments themselves are made from either a tungsten hairpin wire or a LaB_6 single crystal. State-of-the-art instruments use a cold source, field emission gun with a sharp tungsten needle (FEG) to get the ultimate brightness and beam coherence. In TEM, conventional instruments are typically operated from 80 kV-1000 kV, with 100-300 kV the most common (Williams & Carter, 1996). An SEM is usually operated from about 30 kV down to 1 kV and below. Recently, a table-top sized low voltage electron microscope (LVEM) has been developed that operates near 5 kV, and can be used in either TEM, SEM, or STEM modes (Drummy, Yang, & Martin, 2004).

In more recent years new generations of microscopes have become available that also use focused ion beams (FIBs) such as gallium (Ga) (Sugiyama & Sigesato, 2004) or helium (He) (Sijbrandij, Thompson, Notte, Ward, & Economou, 2008). The development of these FIB systems now makes it possible to do local machining and etching of the sample to create trenches (for imaging the resulting sidewalls) or thin sections (that can later be removed from the FIB, mounted a support grid, and then examined in a TEM) (Loos, Duren, Morrissey, & Janssen, 2002). In a single-beam FIB, the ion beam itself generates secondary or backscattered electrons that are then used to create an image as in an SEM. Often, these instruments also have an additional electron column installed so that they can be operated in a dual beam FIB/SEM mode. Another relatively recent development is the use of STEM-in-SEM mode (Bogner, Jouneau, Thollet, Basset, & Gauthier, 2007). If a given sample can be milled into a thin enough section by the FIB, it is possible to install a STEM detector that can provide images similar to those obtained in a dedicated STEM, albeit with somewhat more modest resolution.

Electron microscopy techniques for organic molecular and polymer materials are always complicated by the strong interactions of the electron beam with the sample. The weak intermolecular interactions, organic composition, soft mechanical properties, and low thermal stability of organic materials typically make EM studies of their structure more challenging than for inorganic materials. However the ability to obtain local

information about the nature and extent of organization means that EM remains an important method for the analysis of this important class of compounds.

Our research group has had continued interest in studying the local packing and organization of polymers and organic molecules into ordered assemblies using low dose HREM techniques. Most of the low dose HREM in our lab has been done with a 400 kV JEOL 4000EX and a 300 kV JEOL 3011 with a LaB_6 filament in the North Campus EMAL laboratory at the University of Michigan. Our group is now at University of Delaware and are continuing our HREM research using a 200 kV JEOL 2010 FEG-STEM in the W. M. Keck Electron Microscopy facility. The review presents an overview of the method along with some recent developments, with particular attention to the role of processing in controlling the organization of polymers in the solid-state.

Discussion

Sample preparation

Regardless of the type of instrument used, well-defined sample preparation techniques are essential for obtaining high quality, reliable, and reproducible results. For TEM, the sample thickness should be small in comparison to the electron mean free path in order to prevent significant multiple electron scattering which can introduce difficulties in interpreting images and spectroscopic data. This usually means less than 75 nm for conventional TEM, and perhaps less than 25 nm for LVEM. Thin polymer samples can be prepared by depositing a solution onto substrate, spin coating, substrate dipping, ultramicrotoming, or FIB slicing depending on the properties of the sample. For polymer samples with low glass transition temperatures, sectioning at cryogenic temperatures is often necessary. For the best sections, it is usual to use a diamond single crystal knife with a 45-degree included angle. Oscillating the diamond knife edge parallel to the sample surface during sectioning can significantly reduce the amount of distortion seen during ultramicrotomy, and also makes it possible to obtain much thinner samples (Studer & Gnaegi, 2000).

Beam sensitivity of polymer and organic samples

There are many different mechanisms of radiation damage in organic materials, including electrostatic charging, ionization damage (radiolysis) and displacement damage (Grubb, 1974). Polymer thin films under electron beam exposure can be torn due to the mechanical forces produced from charging. Atomic displacement is caused by high angle scattering from interactions between the incoming electrons and the atomic nucleus, and can be minimized by lowering the sample temperature (Fryer, 1983). It has been reported that cooling samples to liquid nitrogen temperatures can reduce sample mass loss by factors between 3 and 100 depending on their composition.

The beam sensitivity of the sample can be characterized by observing the fading of electron diffraction pattern under controlled current conditions. The dose required to cause significant fading of a given Bragg reflection is called the critical dose (with units of C/cm^2) for that spacing. Although the mechanisms of degradation are not exactly the same, it has been found that there is a general correlation with thermal stability and electron beam damage resistance (Kumar & Adams, 1990; Martin & Thomas, 1995; Martin et al., 2005).

Electron Beam Induced Structural Transitions in Organic Molecular Crystals

Although sensitivity to the electron beam limits the dose that organic molecular samples can be exposed to in the TEM, it is possible to examine the structural changes induced during irradiation and obtain interesting and useful information about the material. It has long been known that polyethylene undergoes a transition from an orthorhombic to hexagonal symmetry when exposed to high-energy electrons (Orth & Fischer, 1965). Lovinger examined the electron beam-induced transition of crystalline PVDF from an initially somewhat defective ferroelectric phase, through a more ordered, less defective paraelectric phase before final amorphization (Lovinger, 1985). We have examined the electron-beam induced transition from monomer to polymer for the diacetylene 1,6-di(N-carbazolyl)-2,4 hexadiyne (DCHD) (Liao & Martin, 1993).

The critical dose for TIPS-pentacene was determined to be 0.05 C/cm^2 at 300 kV, compared with 0.2 C/cm^2 at 100 kV for pentacene. Coupled with Fast Fourier Transform (FFT), Low dose HREM of TIPS-pentacene showed no obvious reorganization around lattice fringes near the crystal edges and grain boundaries indicating a lack of local

structural distortions accommodation around grain boundaries. This is a main barrier for carrier transport (Chen & Martin, 2007).

A series of pentacenes with different alkyl side chains were studied by our research group, and critical electron dose of beam damage for the most stable 3-Si was 0.045 C/cm^2. The much lower electron beam stability of pentacenes with different alkyl side chains came from the lower aromatic content which is more stable under electron beam than aliphatic compounds, because aromatic rings are stronger and have π- eletrons with high resonance energy which scatters inelastic scattering energy over many electrons preventing bond breakage (Voigt-Martin, Krug & Dyck, 1990; Chen, et al., 2008).

Low dose HREM

Detailed techniques and reviews of low dose HREM have been previously reported. A system that we have studied in some detail is the diacetylene 1,6-di(N-carbazolyl)-2,4 hexadiyne (DCHD) (Wilson & Martin, 1992a; Wilson & Martin, 1992b; Wilson, 1994) . The DCHD monomer crystals has a monoclinic structure with a=1.76 nm, b=1.36 nm, c=0.455 nm, γ=94 °, and a P21/c space group, whereas the polymer the same space group symmetry but different unit cell parameters (a=1.739 nm, b=1.289 nm, c =0.490 nm, and γ=108.3 °). Polymerization of DCHD can be induced by electron beam exposure through a quasi-homogeneous phase transition (Liao & Martin, 1993). Electron diffraction patterns taken down the [001] axis during the course of the polymerization show the angle γ between (200) and (010) increasing through a continuous series of crystalline intermediate structures all the way from 94 ° for the monomer to 108 ° in polymer state (Figure 3.2) (Liao & Martin, 1999).

DCHD can be grown into long single crystals by slow crystallization from solution (Figure 3.3). The monomer crystals are clear or slightly blue, whereas after polymerization they have a shiny metallic golden color. Figure 4.3 shows cms-long DCHD crystals grown over an extended period of time at room temperature. Optical micrographs of DCHD crystals obtained from acetone solution are fairly large, typically hundreds of microns long and around 10 microns in width (Figure 3.4). Cracks often develop along the [001] (chain) direction (Liao & Martin, 1996). Solvents having high DCHD solubility and slow evaporation rate produce larger DCHD diacetylene single

crystals. TEM samples are readily prepared by depositing DCHD acetone solutions onto a copper grid with amorphous carbon (Figure 3.5). Figure 3.6 is an enlarged image from the selected area in Figure 4.5, and is a typical high resolution image of a single crystal of DCHD in the [010] zone orientation showing lattice fringes corresponding to the (200), (101) and (-101) planes. The 1.2 nm (010) lattice fringes were shown in Figure 3.7. These lattice fringes correspond to the spacing between chains. Electron diffraction of polyDCHD samples prepared from solution droplets showed extra reflections which suggest fiber-texturing of the sample. The diffraction pattern is consistent with the fiber-textured diffraction simulation (Figure 3.8) (Wilson & Martin, 1992; Apgar & Yee, 1978).

Under more rapid evaporation conditions, single crystals of DCHD can be created that have large amounts of internal porosity (Liao & Martin, 1996). HREM images make it possible to extract detailed information about crystal orientation distributions and crystal sizes both parallel and perpendicular to the chain backbone direction. Even though the pores themselves are large and relatively poorly oriented, the local crystal structure is highly organized and uniformly aligned (Liao & Martin, 1996).

By evaporating DCHD solutions into droplets deposited on surfaces, we were able to establish that boundary conditions can lead to significant distortions of the crystal lattice planes during solidification (Wilson & Martin, 1992b). A phenyl-acetylene foldamer that was deposited into an isolated droplet on a solid surface, and then solidified by solvent evaporation was studied (Kübel, Mio, Moore, & Martin, 2002). Conventional TEM images and electron diffraction revealed a high degree of molecular orientation (with characteristic spacings of 2.62 nm (100), 1.51 (110) between molecules and 0.36 (001) along the stacking direction) and a peculiar banded structure of unclear origin within individual droplets. HREM of the (100) and (110) spacings revealed the local distortions that arose during the solidification process in detail.

Poly(3,4-ethylene dioxythiophene)(PEDOT or PEDT) is a widely used π-π conjugated polymer. The rigid conformation of PEDOT facilitates charge transport and favors crystallization that reduces its solubility and processability. Our group has been investigating PEDOT coatings onto electrodes of bionic devices to improve desired properties. We have recently reviewed the PEDOT morphology elsewhere (Martin et al.,

2010). PEDOT is only modestly crystalline, and has an orthorhombic structure with lattice parameters a, b and c of 1.4 nm, 0.68 nm and 0.78 nm respectively. Figure 3.9. is an X-ray scattering data of an electro chemically deposited PEDOT-NaCl onto a gold-palladium film. The lattice parameters a, and b were calculated to be 1.33 nm and 0.68 nm respectively. Chain stacks along b-axis forming face to face layers with a stacking distance of b/2, which is also the π-π stacking. π-π stacking of different conjugated polymers have been imaged under TEM. One functional thiophene polymer, Poly (2,6-bis(3-alkylthiophen-2-yl)dithieno-[3,2-b;2′,3′-d]thiophene) (PBTDT), has been reported to have a π-π stacking distance of 3.8 Å after annealed at 160 °C (Li, et al., 2008). polypyrrole (PPy) which is another π-π conjugated polymers with a 3.8 Å π-π stacking distance (Lee, et al., 2008). PEDOT prefers to organize into sheets, and the (100) spacing thus varies depending on the identity of the counter-ion to prepare a given sample.

A commercially available PEDOT associated with poly(styrene sulfonate) counterion (PSS), Baytron® P was studied before and after annealing at 150 ℃. Baytron® P consists PEDOT chemically polymerized by using the oxidant $FeCl_3$ and residual amounts of $FeCl_3$ are often found in HREM images. The semicrystalline PEDOT itself is much more beam sensitive, and more poorly ordered than the inorganic $FeCl_3$. Figure 3.10 shows high resolution TEM images of a Baytron® P sample which were actually images of $FeCl_3$ existing in the sample. The 10 Å lattice fringes of $FeCl_3$ can easily be misinterpreted as d 100 fringes of PEDOT which ranges from 11.5 to 15.2 Å depending on the counter-ions associated with it (Studer & Gnaegi, 2000). The critical dose of the PEDOT has been determined to be around 0.1 C/cm^2. The (100) lattice spacing for PEDOT-PSS has been estimated to be 1.4 nm from HREM images (Figure 3.11). Under certain conditions we have also been able to obtain low dose HREM images of the (020) π-π stacking distance in PEDOT before and after annealing. These (020) fringes show an increase from 0.34 nm (as cast) (Figure 3.12) to 0.39 nm after annealing at 150 ℃ (Figure 3.13); these observations are generally consistent with previous studies showing an expansion in the lateral packing of PEDOT on heating. However the degree of order in PEDOT is relatively modest, indicative of its limited degree of crystallinity.

Poly(3-hexylthiophene) (P3HT) and its derivatives are another class of π-conjugated polymeric semiconductors that have received wide interest due to their relatively facile processability and high charge carrier mobilities. The electrical properties of these materials can be controlled by many factors such as their intrinsic chemistry, processing conditions, and quality of device contacts. It has been reported that samples with larger molecular weights have higher mobilities, but the detailed reasons for this have not been determined. Detailed studies of P3HT films are thus important to understand their corresponding transport properties and their relationship to processing and chemical structure.

Brinkmann et al. studied the structure of regioregular head-to-tail (HT)-coupled poly(3-hexylthiophene-2,5-diyl)s (Rr-P3HT)s with different molecular weight by low dose HREM (Brinkmann, Contal, Kayunkid, Djuric, & Resel, 2010). Edge-on lamella and flat-on lamella, two typical oriented domains of Rr-P3HT with M_w=7.3 kDa, had been identified both in underfocused BF TEM and low dose HREM micrographs. The P3HT chains preferentially tilt to certain well-defined angles in the crystalline lamellae. From HREM micrographs of Rr-P3HT with these three different molecular weights, the thickness of the crystalline lamellae were independent of the molecular weight, while the thickness of the interlamellar amorphous zones increased with molecular weight. The packing disorder of P3HT chains in the crystalline domains also increased with the increase of molecular weight. The crystalline lamellae was observed to be strongly interconnected by a few modestly-ordered π-stacked Rr-P3HT polymer chains that may account for the higher carrier mobility in Rr-P3HT with higher molecular weights.

Kayunkid et al. studied highly oriented and nanotextured P3HT on the surface of an aromatic salt (potassium 4-bromobenzonate)(K-BrBz) (Kayunkid, Uttiya, & Brinkmann, 2010). The nanotextured P3HT films developed highly oriented crystalline domains connected by amorphous interlamellar zones. Coupled with electron diffraction and molecular modeling, the P3HT chains were found to be preferentially oriented along two in-plane directions [0 ±2 1] corresponding to rows of bromine atoms on the surface of K-BrBz substrate. The unit cell of this highly crystalline P3HT was determined by a

trial-and error method combining molecular modeling and calculation of electron diffraction patterns to be a monoclinic unit cell with space group $P2_1/c$ and two chains per cell (a=1.6 nm, b=0.78 nm, c =0.78 nm and γ=86.5 deg). Interplanar stacking distances of 0.34 nm between successive poly-thiophene backbones were observed that were comparable to those of other conjugated polymers.

Stacking faults in and crystal structure of β-form single crystals of syndiotactic polystyrene with an orthorhombic unit cell and planar-zigzag conformation have been studied by HREM supplemented by dark field TEM and electron diffraction (Tosaka et al., 1998; Tosaka, Tsuji, Kohjiya, Cartier, & Lotz, 1999). Stacking faults were indicated by the shift or kink of (210) lattice fringes observed in the HREM images. Monoclinic domains in the single-crystal-like lamellae of β'–modification and twin plane between the domain boundaries were identified by HREM.

Molecular simulations

It is often useful to correlate experimental HREM results with simulations of images. In order to better understand the relationship between disorder and expected changes in dynamic electron diffraction and HREM images, Kübel and Martin used multislice simulations for polyDCHD showing that significant changes in the intensities in dynamic diffraction can result from small changes in the molecular geometry, leading to large variations on the expected contrast of the HREM images (Kübel & Martin, 2001). HREM images were simulated for different crystallographic zone and annealing temperatures which reduced symmetry by inducing local disorder within a monomer unit. Pendellosung plots of the amplitude or phase of selected diffracted beams make it possible to predict the expected contrast of HREM images as a function of sample thickness. For samples with smaller thickness (50-70 nm), dynamic scattering and HREM images showed less dependence on thickness; whereas for samples with larger thickness, the dynamic scattering and HREM images showed larger influences of thickness. These simulations made it possible to estimate the sample thickness needed to image characteristic displacements of a given magnitude. As anticipated, with a larger degree of disorder, the samples must be thinner to maintain a particular value of the expected HREM image intensity variation. For a sample thickness of 100 nm, errors of 40% in

the predicted diffraction intensity were observed for average displacements of only 0.05 nm.

LVEM

The mass thickness contrast in TEM is a strong function of the atomic number Z. Conventional TEMs operate from 200 to 400 kV and give little contrast to samples with low atomic number elements (including organic and polymeric samples). Staining by heavy metals is a common process to enhance the contrast of organic materials in EM. One way to increase contrast is to operate at lower voltages, where the interactions of the electron beam with the carbon atoms in the organic samples are even stronger. A Low Voltage Electron Microscope (LVEM) with a field emission gun that operates near 5 kV has been developed by Delong Instruments in Brno, Czech Republic (www.dicomps.com). The LVEM has the capability of producing good contrast on low-Z organic and polymer samples even without staining (Drummy, Yang, & Martin, 2004). The LVEM can be operated in TEM mode, STEM mode, Electron Diffraction mode and SEM mode. The schematics of different operation modes of LVEM has been shown in Figure 3.14. It has been reported that there is about twenty times more image contrast in the LVEM at 5 kV than a conventional TEM with a 100 kV electron source. The contrast for a 10 nm thick section with a density difference of just 0.075 g/cm^3 imaged by the 5 kV LVEM is around 5%.

Polyethylene single crystals, showing the typical faceting and screw dislocation overgrowths near the edges were studied by LVEM (Drummy, Yang, & Martin, 2004). The LVEM beam is able to penetrate through about 4-5 layers of these 10 nm thick hydrocarbon crystals. Other examples of LVEM images of low contrast samples include the imaging of individual, 8 nm diameter unstained Generation 7 (G7) PAMAM dendrimers (Drummy, Yang, & Martin, 2004). Texter et al. studied nanoscilica formation in a thermoreversible block copolymer gel. They were able to image nanoparticle agglomerations on the 10 to 30 nm length scale and were able to see certain features brought by the high contrast of LVEM, which would be missed by conventional TEM (Texter, Schwarz & Stepan, 2007).

Unfortunately, the low voltage also decreases the critical electron beam dose required to damage organic crystalline structures. The mean free path for total electron scattering was calculated to be 15 nm for organic samples at 5 kV. Because of the ultrathin sample requirement (<25 nm), it is even more challenging to prepare samples for LVEM than for normal TEM. We have found that a convenient way to prepare LVEM samples is to deposit them by atomizing from dilute sample solution onto a 3 mm diameter copper TEM grid covered with a thin carbon film (<10 nm). For dry samples, microtomy is challenging below 50 nm at room temperature. Our group uses an oscillating diamond knife that has proven to be able to section samples as thin as 10 nm at room temperature (Studer & Gnaegi, 2000).

Our lab has determined the critical dose for polycrystalline pentacene thin film by electron diffraction on the LVEM to be 0.035 ± 0.01 C/cm^2 at 5 kV, whereas this value is 0.25 ± 0.05 C/cm^2 at 300 kV. Stary et al has simulated the critical thicknesses for elastic, inelastic and combined elastic and inelastic scattering at 5 kV beam energy (Stary & Nebesarova, 2008). With a sample of 1.6 g/cm^3, the elastic, inelastic and combined transparent thickness are 21.4, 12.8 and 7.9 nm respectively. Drummy et al. used LVEM to study the crystal size of a 25 nm thick silk sample (Drummy, Farmer & Naik, 2007). This is consistent with what we saw in our lab that transparent thickness for microtomed epoxy sample with a density of 1.11 g/cm^3 is around 20 nm (Figure 3.15). Significant size distribution of crystallites has been determined by the LVEM images although electron diffraction and high-resolution images were not possible because of the extreme beam sensitivity of the silk at 5 kV.

We have templated PEDOT into bicontinuous cubic phase with nm size features using nonionic surfactants (Martin, et al., 2009). Figure 3.16. showed pieces of PEDOT bicontinuous cubic phase after it was collapsed due to phase transition induced by surfactant removal or varying temperatures (Wu, Shim & Marin, 2010). The left LVEM image which was a sample without staining clearly showed that 3 to 5 nanometer pores formed in the film. The right image is the same sample after staining with osmium tetroxide for an hour, which is a common practice to enhance contrast of organic materials by introducing heavy metals into the sample. The pores after staining were gone,

a clear indication of structure damage in the process of staining. This highlighted the benefit of avoiding staining polymer and organic samples under LVEM.

Dispersed Carbon nanotubes (CNs)

Single wall carbon nanotubes (SWCNs) have received wide interest for a variety of applications. Its self-aggregation problem has been an obstacle for its use in composite materials. Shim et al, have incorporated SWCNS into nanocomposite films using a layer by layer (LBL) method (Shim et al., 2007). SWCNs in an LBL film were imaged by a conventional JEOL 3011 TEM with a 300 kV lanthanum hexaboride (LaB_6) thermoelectric emission gun. The contrast of SWCN is low under conventional TEM due to its small thickness, all carbon composition, and diameters around 1 to 2 nm. The SWCNs were dispersed by sodium poly(styrenesulfonate) (PSS) in aqueous solution or Nafion® in ethanol solution. LVEM images of the dispersed SWCNs show them to be well exfoliated into single strands in both dispersion systems indicating that no SWCN agglomerations formed in the system (Figure 3.17).

Multiwall carbon nanotubes (MWCN) were dispersed into sodium poly(styrene sulfonate) (PSS) aqueous solutions and then imaged both under a conventional JEM-2000FX TEM with a 200 kV LaB6 gun and LVEM (Figure 3.18). The diameter of the MWCNs was around 20 nm. Higher contrast was obvious in the LVEM when compared to conventional TEM.

LVEM images of PEDOT/PSS (Baytron P®) on a thin (~2.5 nm) amorphous carbon substrate have been reported (Martin et al., 2010). The resulting films are composed of highly extended, randomly oriented filaments that are seemingly insensitive to the forces present during the de-wetting of solvent droplets. This indicates the formation of aggregates of filaments in the suspension that do not separate simply on dilution. These filaments are somewhat longer than would be expected for 4.75 kg/mol PEDOT chains from MALDI experiment, though are so thin that few chains could be present in each filament. The extended nature of these filaments clearly indicates the presence of PEDOT, however, as PSS is quite flexible and would form coiled—rather than linear—deposits on the support film. Thus these filaments are likely formed by a

small number of linear PEDOT chains, each individually complexed with PSS for charge neutrality. The occasional observation of seemingly branched filaments also supports this model, as both EDOT and styrene-sulfonate have a functionality of two. Persistence length calculations of these filaments arrive at a value of approximately 27 nm (corresponding to 68 EDOT monomer units along the chain). While not precisely a persistence length for PEDOT itself, this value must be largely dominated by the PEDOT, given the flexibility of PSS. Furthermore, this value should be interpreted as something of an underestimate of PEDOT flexibility, as the likely presence of several PSS-coupled PEDOT chains in a single filament implies the presence of several points of uncharacteristic flexibility, i.e. joints in the otherwise rigid filament. The fact that these images were collected without the use of stains or an objective aperture indicate the possibility of determining the persistence length of this and other sufficiently rigid polymers by direct observation, provided sufficient separation of individual molecules can be achieved.

LVSEM

Butler et al. studied low-voltage scanning electron microscopy (LVSEM) of polymers (Butler, Joy, Bradley, & Krause, 1995). The LVSEM with a field emission gun (FEG) operating at low accelerating voltages (normally 1-2 kV) produces topographical contrast secondary electron micrographs at higher magnifications than conventional SEM with added benefit of producing contrast based on chemical composition differences in the sample, minimizing beam damage and lowering charging effects. These advantages are brought by the high brightness of FEG gun which can be focused down to extremely fine focused (~2.5 nm) probes yet still maintaining enough intensity to produce usable signal levels.

There are two SEM operating contrast modes including materials signal and relief mode in LVEM with a BSE detector. The annular BSE detector is broken in to two individual signals A and B corresponding to scattering to either side of the electron beam chamber. The combined signals (A+B) produces materials contrast mode and the

subtracted signals (A-B) give relief contrast mode respectively. More morphology information can be obtained from these two complemented contrast modes. Studies using both of these modes together on the same sample have shown local variations in both composition and structure. An LVSEM micrograph showing both topographical and compositional contrast from a given area of an electrochemically deposited PEDOT film has been reported in previous paper (Martin et al., 2010).

Electrospun nanofibers

Our group has been actively investigating polymer fibers and tubes with diameters in different length scale using electrospinning with application in drug release and directing neural cell growth (Abidian, Kim & Martin, 2006; Corey, 2008). We have shown in previous report of imaging electrospun Nylon 6,6 beaded fibers (Drummy, Yang, & Martin, 2004). Figure 3.19. shows micrographs of the same electrospun polycaprolactone (PCL) fibers sample in SEM, TEM and STEM modes. The straight PCL fibers were around 200 nm thick and microns in length with relatively smooth surfaces. The LVEM provides complementary information through different modes on the same sample in microstructural and morphological analysis.

Focused Ion Beam imaging of polymers on inorganic substrates

One of the advantages of the dual beam FIB/SEM systems is the ability to make cross-sections through thin layers of soft polymers deposited onto hard, inorganic substrates (White et al., 2001; Loos et al., 2002) . Figure 3.20 shows a cross section of an electrochemically deposited film of PEDOT deposited onto a microfabricated neural electrode using an FEI Helios NanoLab 600. The FIB is able to make a clean cut down through the fuzzy polymer coating, and reveal contrast due to variations in the composition and crystallinity of the underlying inorganic device. These cross sections make it possible to insure that the coatings are in intimate adherence with the metal electrode, and facilitate detailed analysis of the surface roughness variations. Thin sections can be extracted and examined using locally using EDS in a STEM. Reflected light optical micrographs and SEM images of the sample surfaces are shown in each case.

The two sections shown here correspond to different methods of electrochemical deposition used to create either a fibrillar, open texture (left) or a more compact, yet still lumpy surface (right).

Cryo-TEM Techniques

For many samples, it is of interest to investigate their structure in the wet or swollen state. To accomplish this, Cryo-TEM methods have been developed (Bellare, Davis, Scriven, & Talmon, 1988). In Cryo-TEM, the sample is wicked from an aqueous suspension onto a holey carbon grid, and then rapidly quenched into a cryogen such as liquid ethane. The cooling rapid is enough to vitrify the water, providing a uniform matrix for imaging the organic particles or supramolecular assemblies of interest (Bellare, Davis, Scriven, & Talmon, 1988). Cryo-TEM was once limited to a relatively few laboratories who had developed the instruments and methods required (vitrification system, cryo-transfer stage); however in recent years the method has become somewhat more widespread due to the improvements and refinement of commercially available instruments (Zhong & Pochan, 2010).

Pochan et al. have recently discussed the use of Cryo-TEM to look at a variety of polymer and organic materials including peptides and block copolymers (Zhong & Pochan, 2010). An emerging technique is the use of cryogenic stages in the FIB/SEM to machine thin samples that can be later be imaged by TEM and STEM (Marko, Hsieh, Moberlychan, & Frank, 2006; Marko, Hsieh, Schalek, Frank, & Mannella, 2007). This method of sample preparation may allow for thicker samples to be examined, but the details of this methodology are still under active development and the equipment itself is not yet widely available.

Aberration-corrected microscopy

The limiting resolution of an electron microscope is related to spherical aberrations in the objective lens. These aberrations are associated with a spherical aberration coefficient Cs, that is typically of order 1-3 mm. Scherzer long ago predicted

that spherical aberrations would be inevitable in microscopes that use a cylindrically symmetric lens (Scherzer, 1949).

In recent years it has been shown to be possible to eliminate the spherical aberration of an electron microscope altogether by using a multipole lens that breaks the cylindrical symmetry of the magnetic focusing field (Rose, 1990). Aberration correction has been demonstrated in TEM (Haider, Braunshausen, & Schwan, 1995), SEM (Zach & Haider, 1995) and STEM (Krivanek, Dellby, & Lupini, 1999) imaging modes. Aberration-corrected microscopes are now commercially available that correct the beam both before (for improved beam collimation) and after (for improved resolution) the sample (Kirkland, Chang, Haigh, & Hetherington, 2008; Ziegler et al., 2009).

Although there have been few studies of beam-sensitive samples by aberration-corrected TEMs, it was recently reported that paraffin crystals could be imaged, albeit at modest resolution (Evans et al., 2008). Nam et al. recently reported the aberration-corrected imaging of thin films of peptoid polymers, however the samples in this study were exposed to high doses of irradiation (Nam et al., 2010). It is thus likely that these HREM results correspond not to the original, pristine structure of the material but rather to the structures obtained after extended beam exposures.

Dynamic TEM

The ability to use rapidly image structural transitions in the TEM is of interest in a number of laboratories (Bostanjoglo & Otte, 1993) . Such systems combine a TEM column with a time-resolved laser system that can control the exposure of the sample sample (LaGrange et al., 2006; Evans et al., 2008; Reed et al., 2009). These methods have recently been used to image extremely rapid events such as the in-situ reaction of intermetallic nanolaminates. If it is possible to expose the sample to high current at time scales less than those required for the structural reorganization that occurs during exposure, then techniques such as this may one day make it possible to improve imaging of beam-sensitive organic samples (Martin & Thomas, 1995).

Conclusions

Electron microscopy continues to provide valuable information about the morphology of beam sensitive polymer and organic molecular materials. A wide variety of complimentary methods are now available, including SEM, TEM, HREM, STEM, FIB, STEM-in-SEM, Cryo-TEM, and LVEM. Active areas of research include the use of aberration corrected instruments, dynamic imaging modes, and dual beam methods. As these methods continue to improve, it will be possible to have a more complete understanding of the relationship between the microstructure of these interesting materials and their macroscopic properties.

Experimental

Baytron P® samples

Baytron P®, obtained from Bayer company, TEM sample was made by dissolving it into water forming a 0.1wt% solution. A drop was deposited onto copper grid with freshly made thin carbon film. Samples before and after annealed at 150 ℃ were studied under a JEOL 3011.

Epoxy samples

Epoxy samples (Pelco Expoxy, TED Pella,Inc) with a density of 1.11 g/cm^3 were cut into different thickness from 10 nm to 25 nm by Reichert FC4 ultramicrotome with a Diatome oscillating knife under room temperature.

SWCNs and MWCNs samples

The samples of single wall carbon nanotube (SWCN) and multiwall carbon nanotube (MWCN) (www.nano-lab.com) were dispersed into poly(sodium 4-styrene sulfonate) (PSS) (SigmaAldrich) aqueous solutions or Nafion® (SigmaAldrich) ethanol solutions and then nebulized onto copper grids with nanometer thick amorphous carbon film.

DCHD samples

DCHD samples were made by depositing a 0.1 wt% DCHD acetone solution onto copper grids with carbon film.

PEDOT bicontinuous cubic phases sample

Method of preparing PEDOT bicontinuous cubic phases was described in previous report. (Martin, et al., 2009)LVEM samples were made by depositing a drop of the bicontinuous cubic phase PEDOT-acetone suspension onto copper grids with thin carbon film. The stained sample was prepared by exposing the pristine sample under Osmium tetroxide vapor for an hour.

Electrospun fibers

Poly caprolactone was dissolved in THF forming a 11 wt% solution. 15 kV potential was applied onto the electrospinning apparatus. Fibers were spun onto copper grids with thin carbon films. Distance between tip of needle and copper grides was 12 cm.

Optical microscopy was done on a Nikon Optiphot-POL in reflected light. The microscope was also equipped with polarizers and analyzers and a full-wave red filer.

High resolution TEM images of the sample before and after annealing at 150 ℃ for 10 hours were taken on JEOL 3011. Selected area electron diffraction and low dose high resolution images were taken with a 200 kV JEOL 2010F at Keck lab at the University of Delaware.

LVEM images were obtained in SEM, STEM, and TEM modes on a table-top-sized LVEM-5 from DeLong Instruments (Brno, Czech Republic). The operating voltage was ~5 kV, and TEM images were acquired using a charge-coupled detector (CCD) camera from the YAG screen of the LVEM. An objective aperture was not required for sufficient contrast and was not employed in the images shown.

Figures

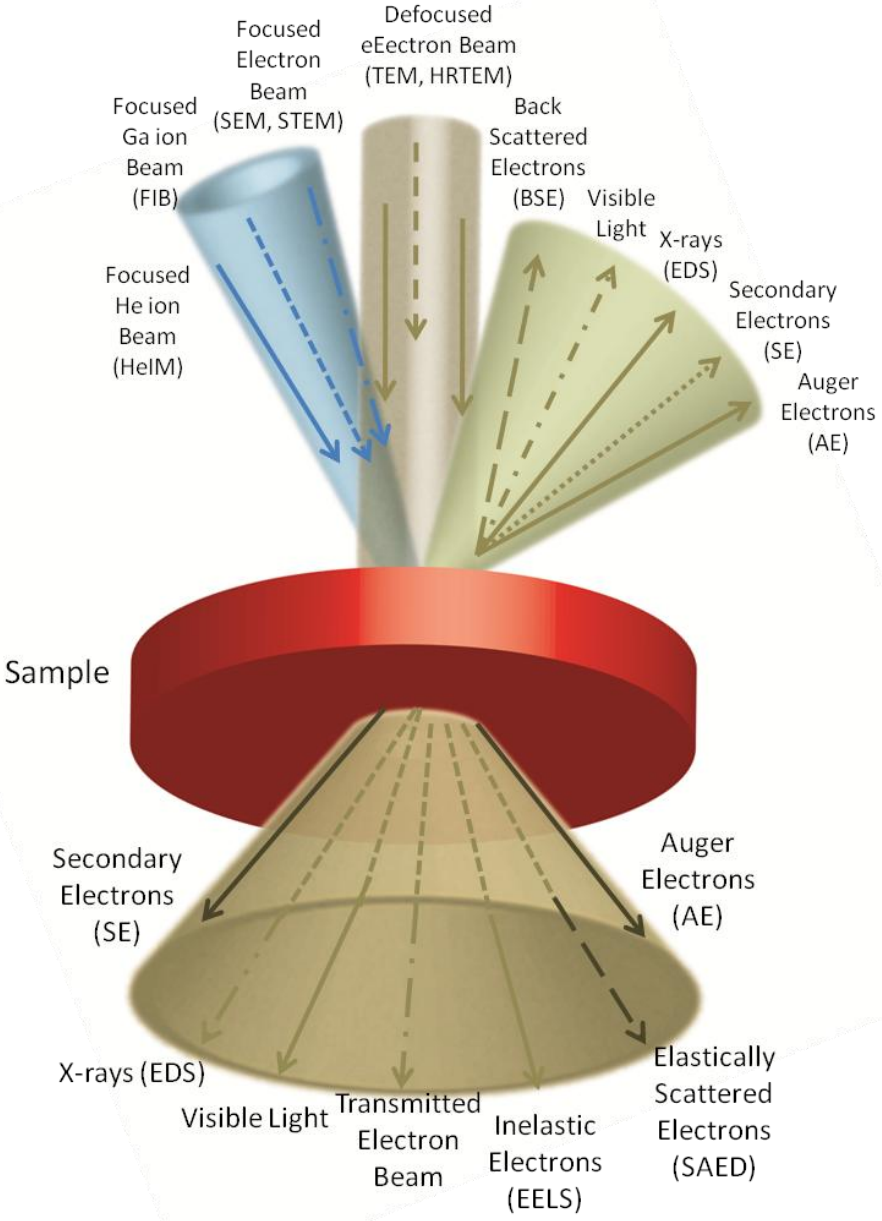

Figure 3.1: Schematic showing the various types of interactions that can occur when a sample is exposed to an electron beam or a focused ion beam.

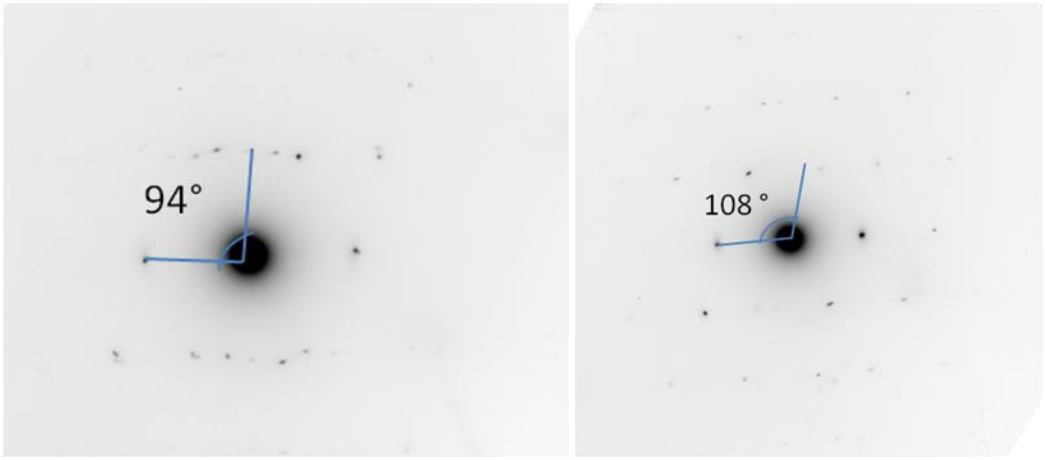

Figure 3.2. Electron diffraction of DCHD monomer corresponding to the [001] zone

Electron diffraction of DCHD polymer corresponding to the [001] zone

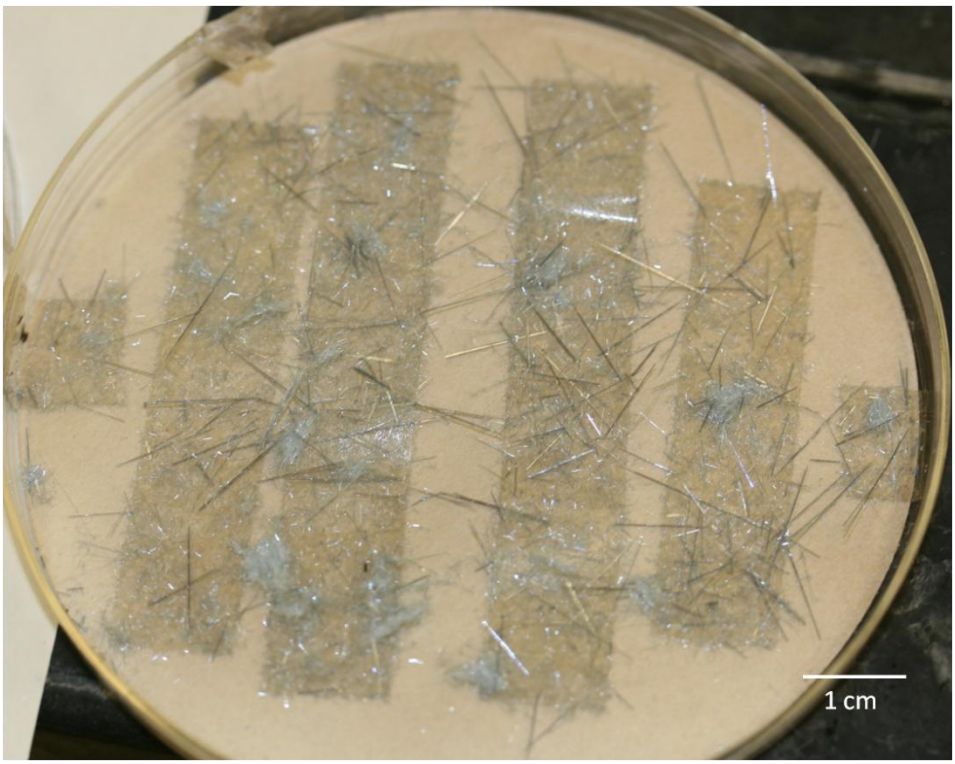

Figure 3.3. Single crystals of DCHD diacetylene grown at room temperature.

Figure 3.4. Transmitted light optical micrograph of DCHD single crystals (little amount of cracks developed along the [001] (chain) direction)

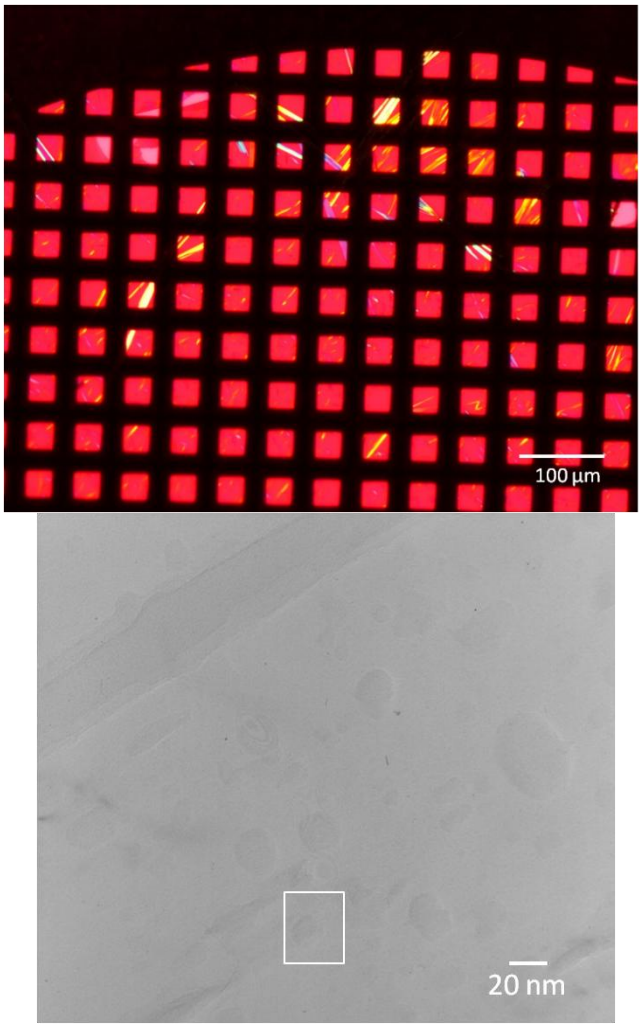

Figure 3.5. TEM samples of DCHD crystals prepared from acetone solution onto copper grid with amorphous carbon film (left: optical image, right: TEM image showing the area of high resolution blow out of Figure 6)

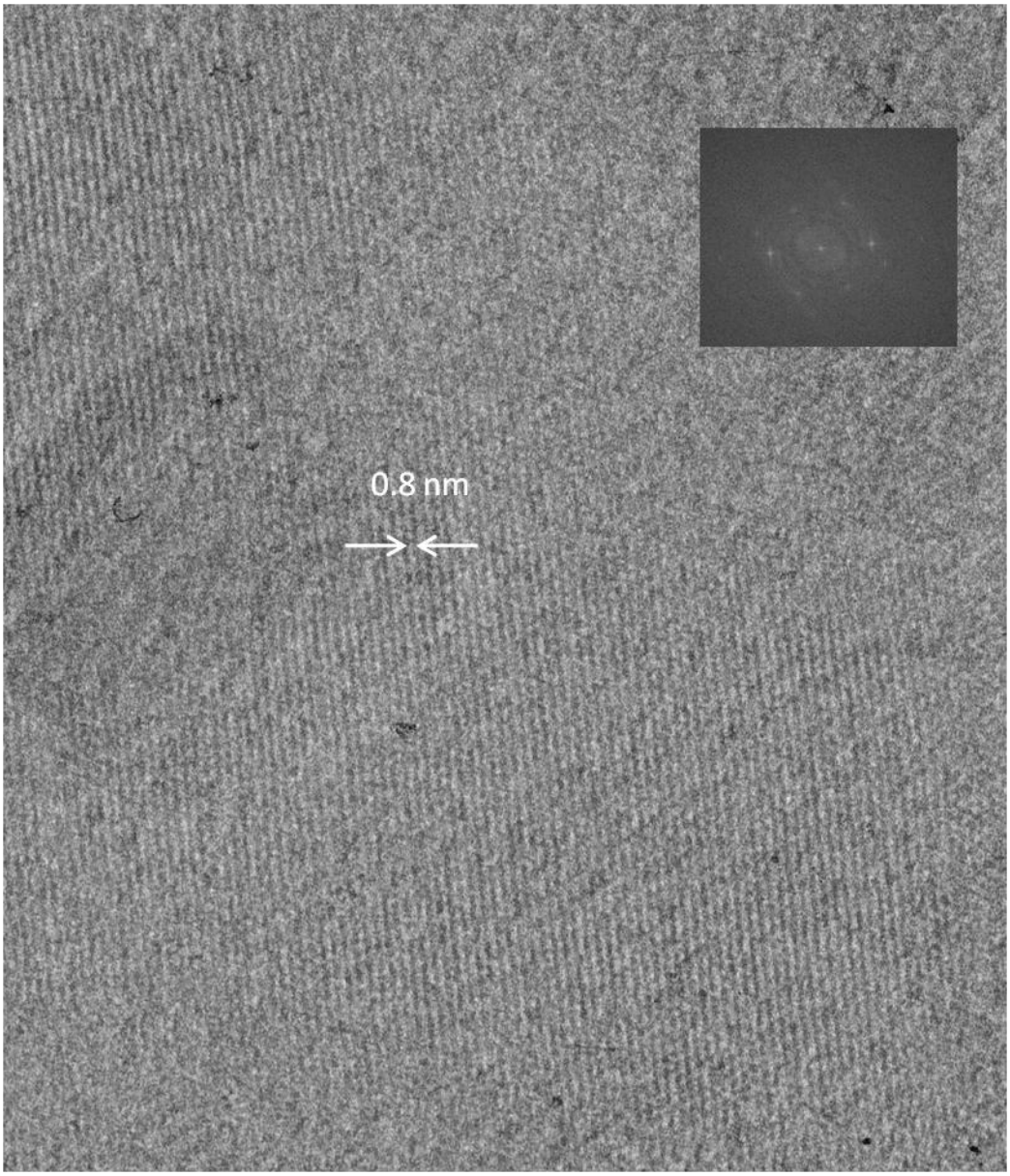

Figure 3.6. Low dose high resolution image of DCHD crystals showing highly ordered fringes of the lateral side-to side packing distance between polymer chains (FFT analysis showed small amounts of misorientation)

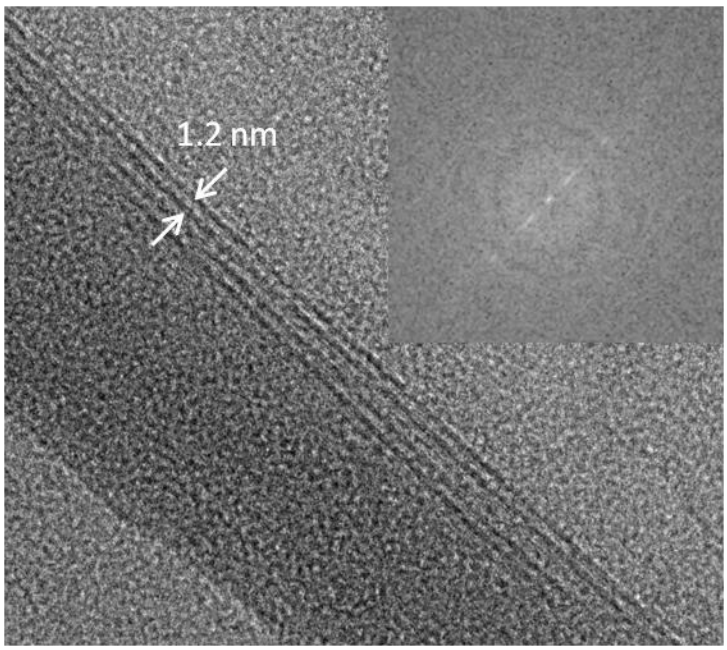

Figure 3.7. HREM image of DCHD crystal showing 1.2 nm spacing lattice fringes of the (010) planes corresponding to the spacing between chains

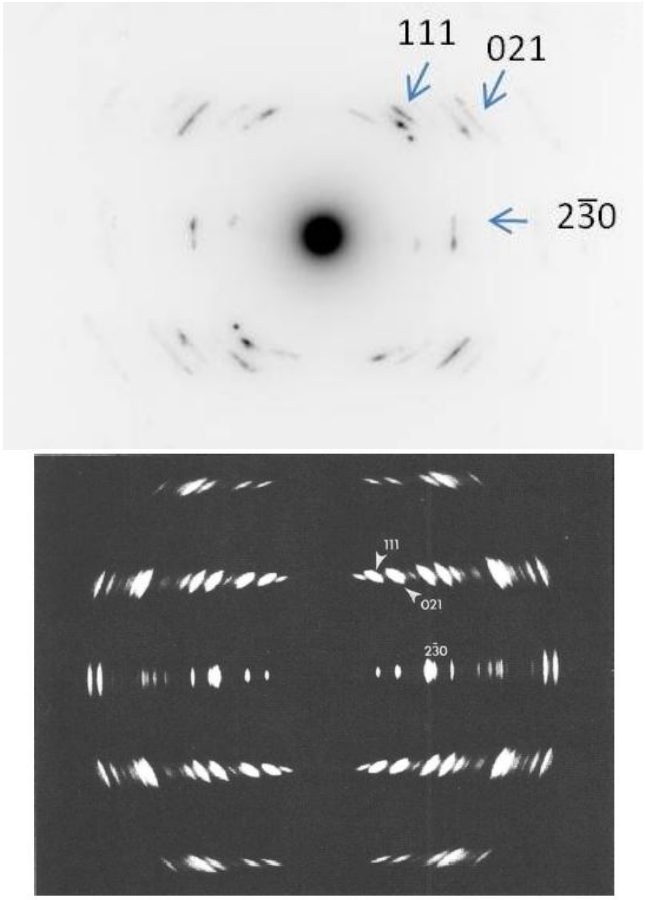

Figure 3.8. Left:SAED of poly(DCHD) prepared from acetone solution droplet . Right: simulation of SAED pattern using fiber texture geometry (CERIUS) (Wilson & Martin, 1992)

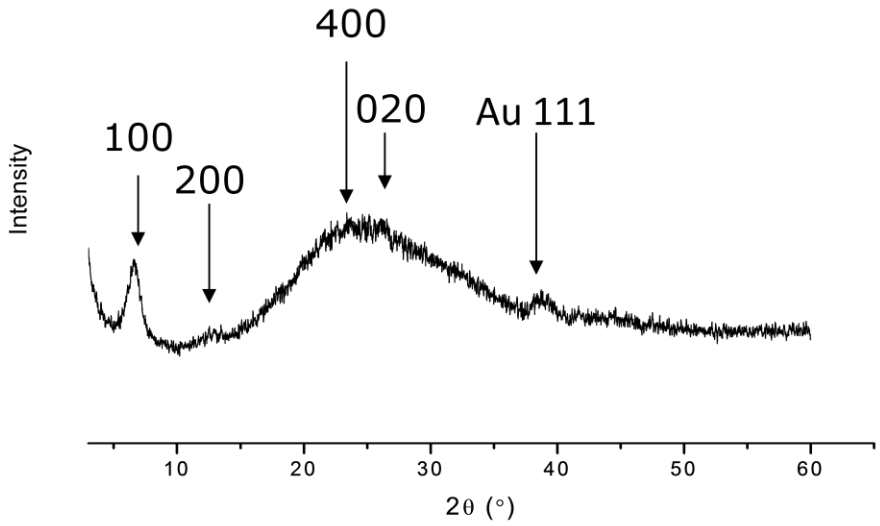

Figure 3.9. 1 D X-ray scattering of electrochemically deposited PEDOT-NaCl

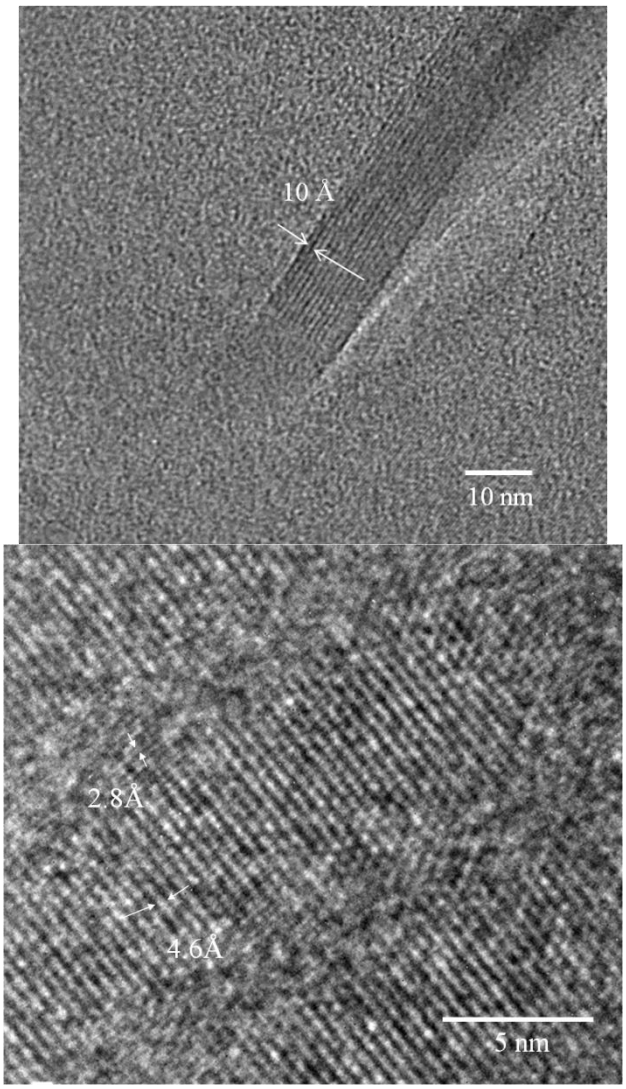

Figure 3.10. High resolution images of leftover FeCl3 in Baytron® P

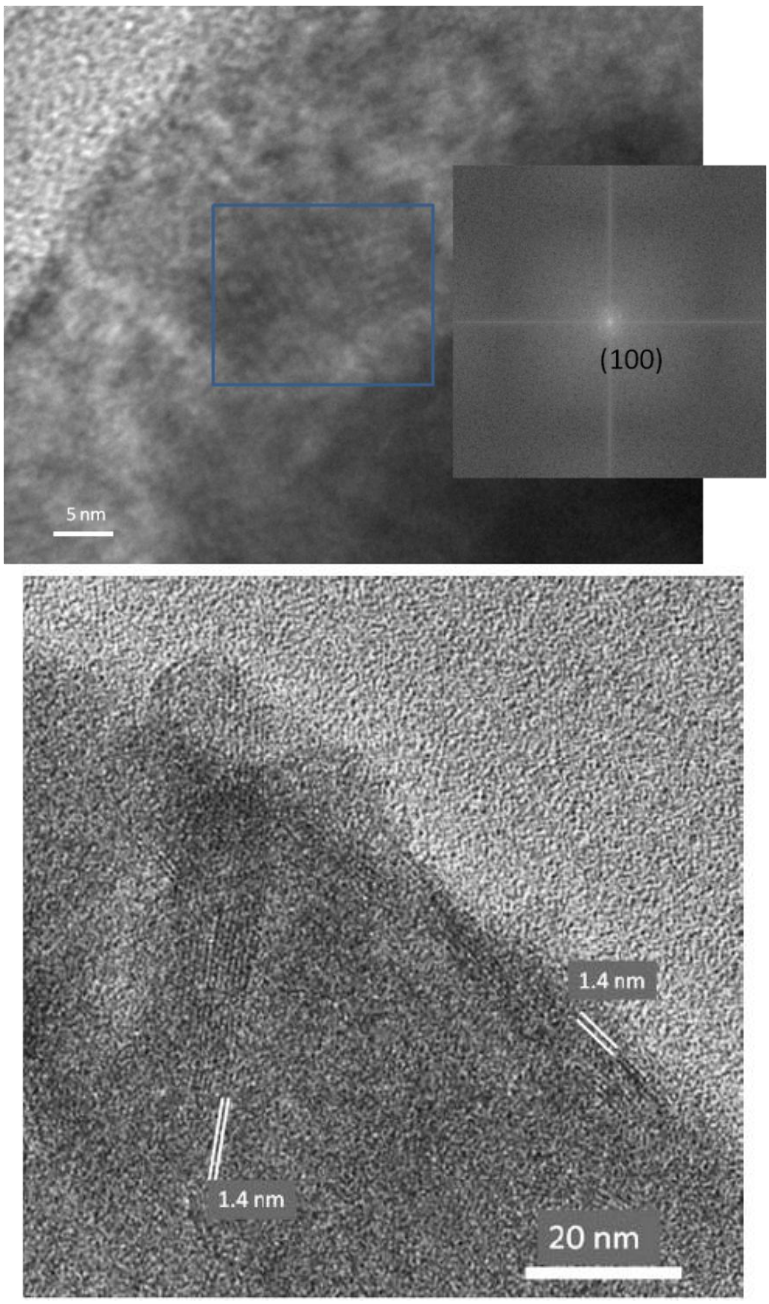

Figure 3.11. Low dose high resolution images of PEDOT PSS in Baytron® P

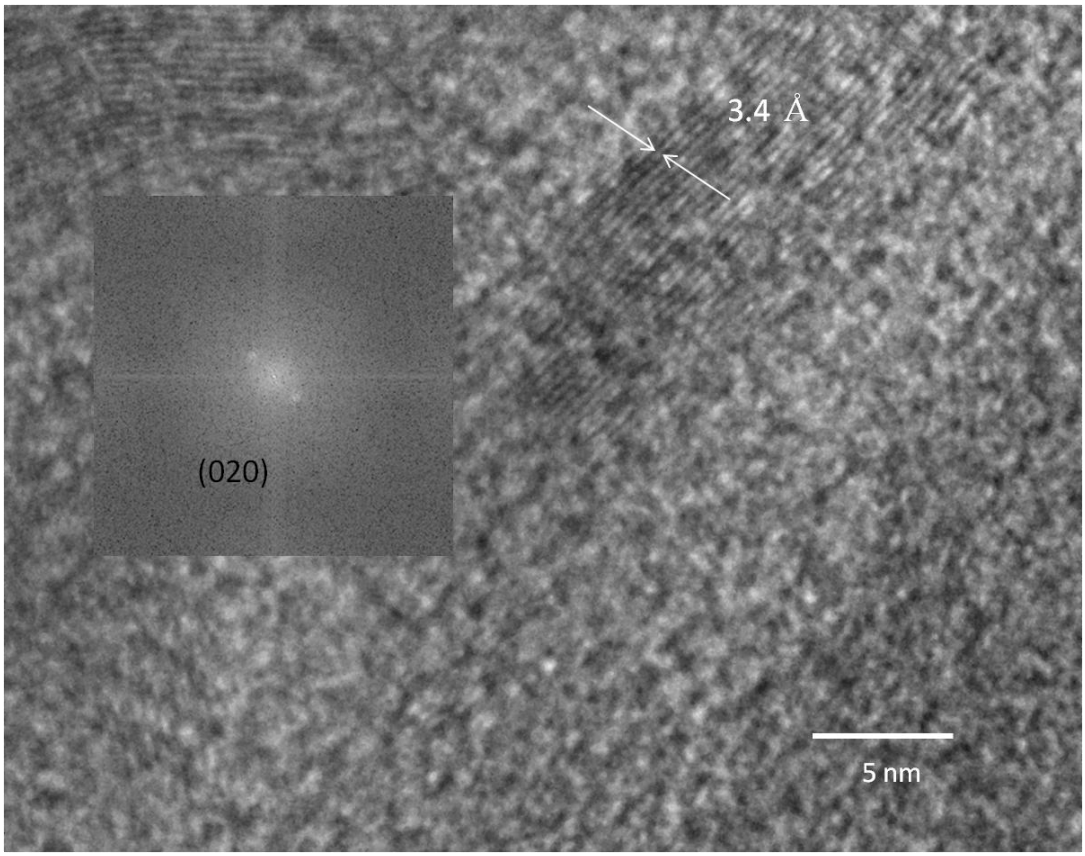

Figure 3.12. High resolution TEM image of Baytron® P showing fringes corresponding to π-π stacking before annealing (FFT analysis indicates small amount of misorientation)

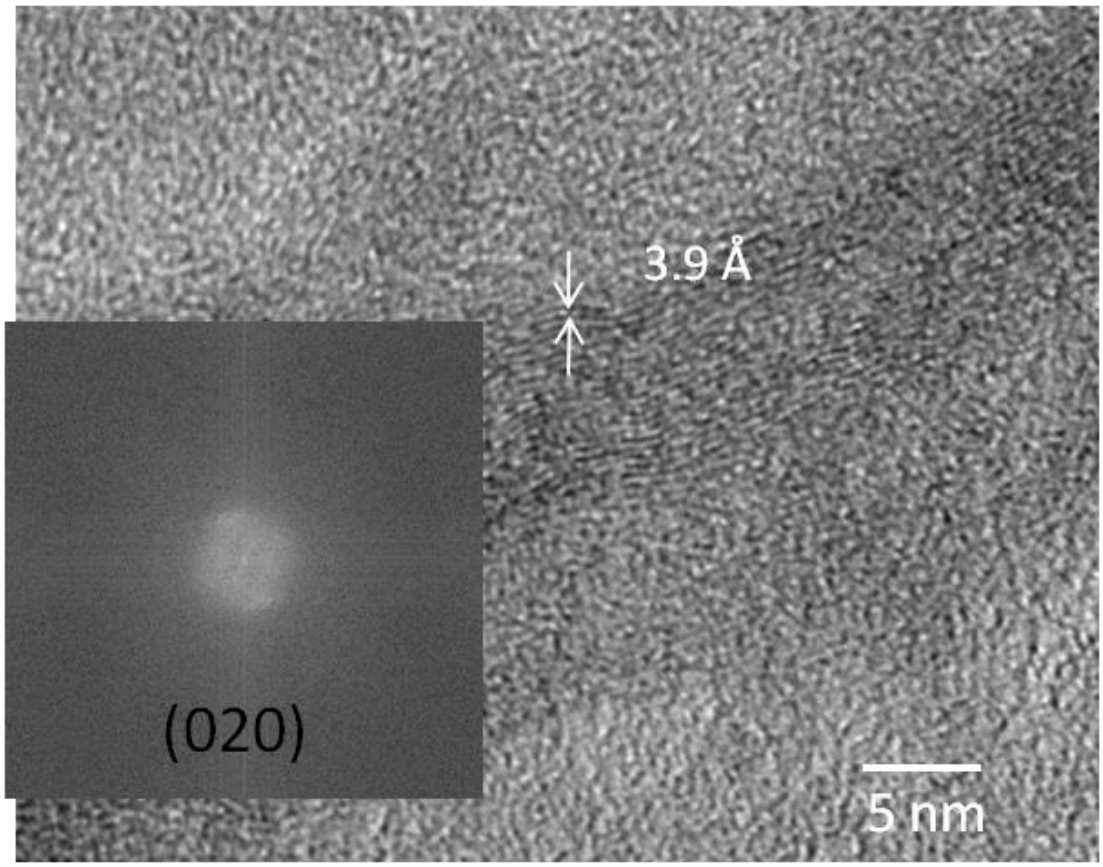

Figure 3.13. High resolution TEM image of Baytron® P showing fringes corresponding to π-π stacking after annealing at 150 °C (FFT analysis indicates lager amount of misorientation comparing to samples before annealing)

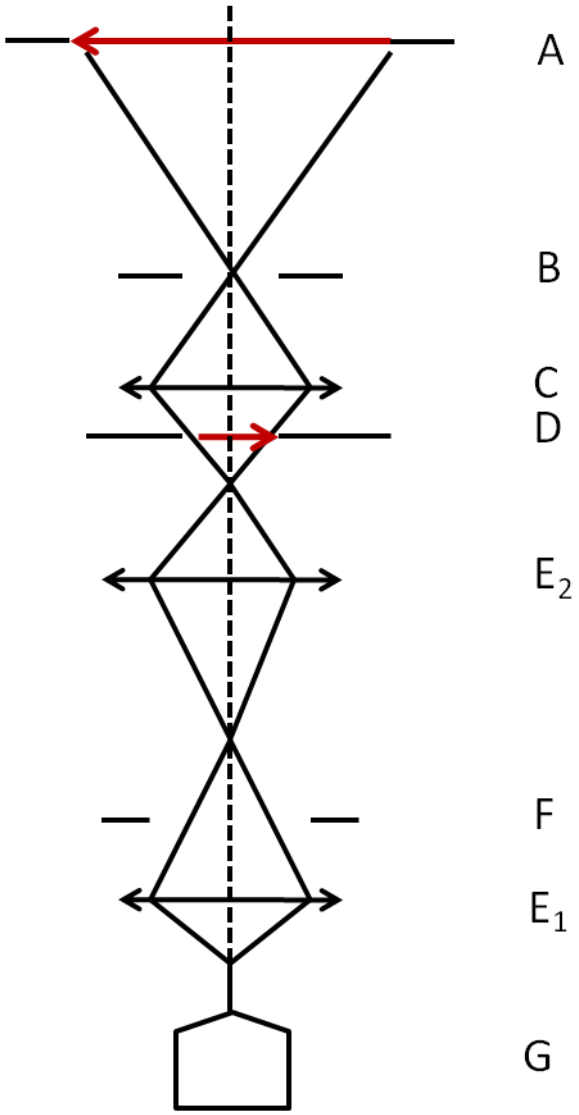

A – *fluorescent screen with magnified image*
B – *objective aperture*
C – *objective*
D – *Sample*
E_1 – *condenser 1*
E_2 – *condenser 2*
F – *condenser aperture*
G – *gun*

a. Schematic diagram of electromagnetic lens under TEM operation mode

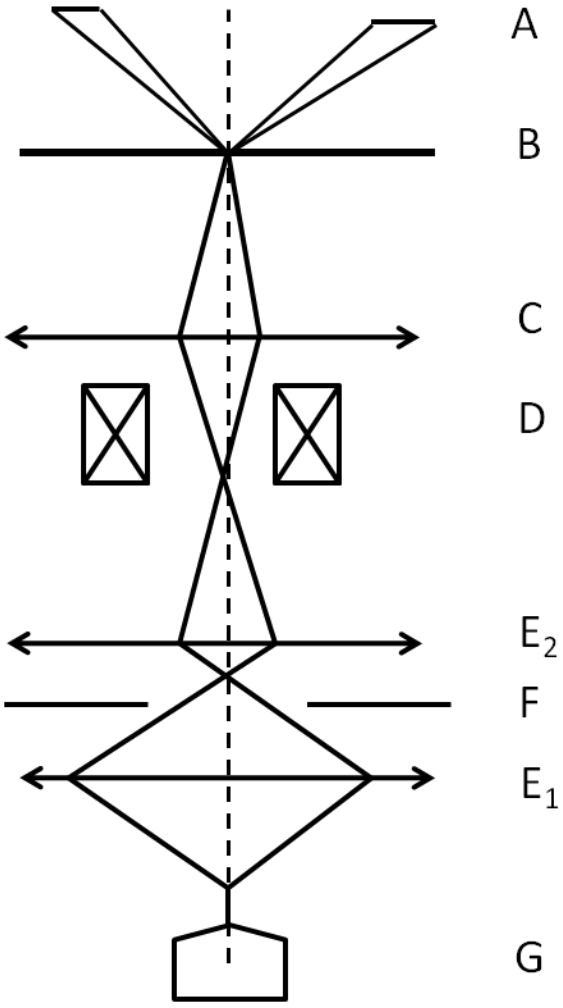

A – STEM detector
B – *sample*
C – *objective*
D – *Scan coils*
E_1 – *condenser 1*
E_2 – *condenser 2*
F – *condenser aperture*
G – *gun*

b. Schematic diagram of electromagnetic lens under STEM operation mode

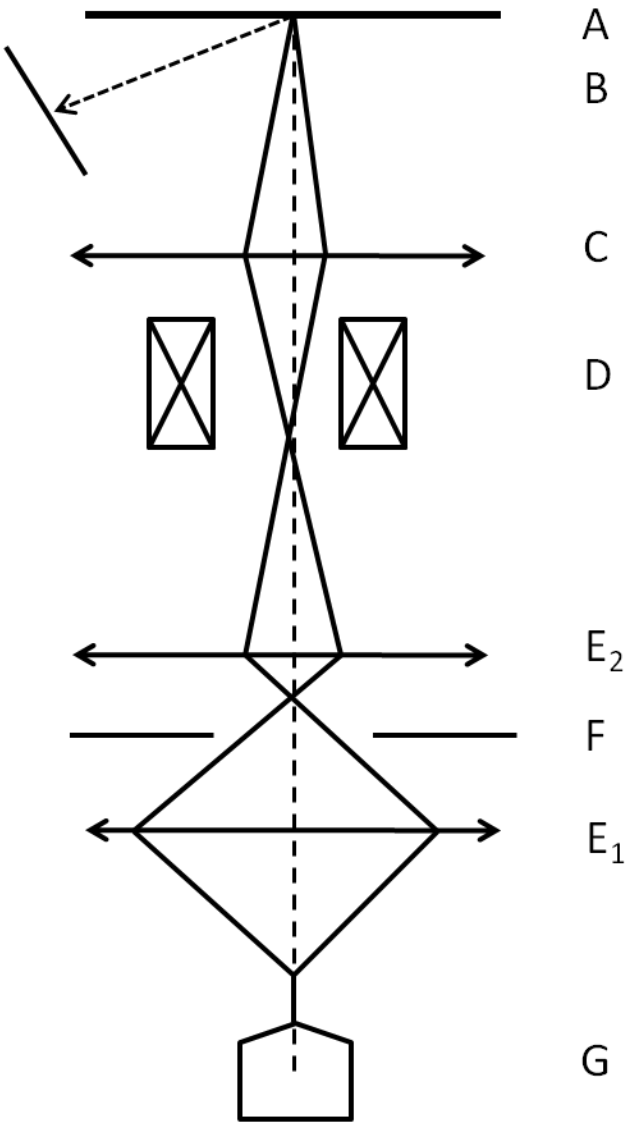

A – *sample*
B – *BSE detector*
C – *objective*
D – *Scan coils*
E_1 – *condenser 1*
E_2 – *condenser 2*
F – *condenser aperture*
G – *gun*

c. Schematic diagram of electromagnetic lens under SEM operation mode

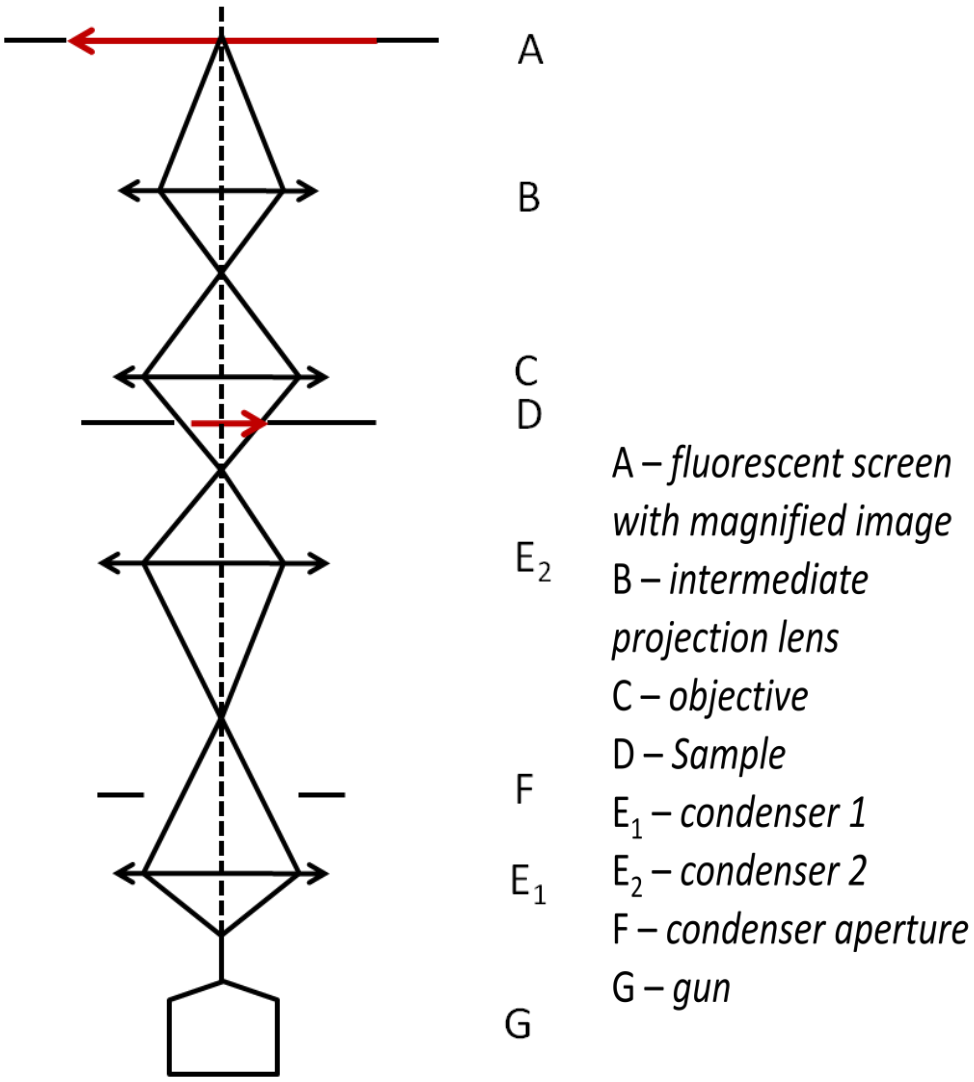

d. Schematic diagram of electromagnetic lens under electron diffraction operation mode

Figure 3.14. Schematic diagram of electromagnetic lens operating under different modes

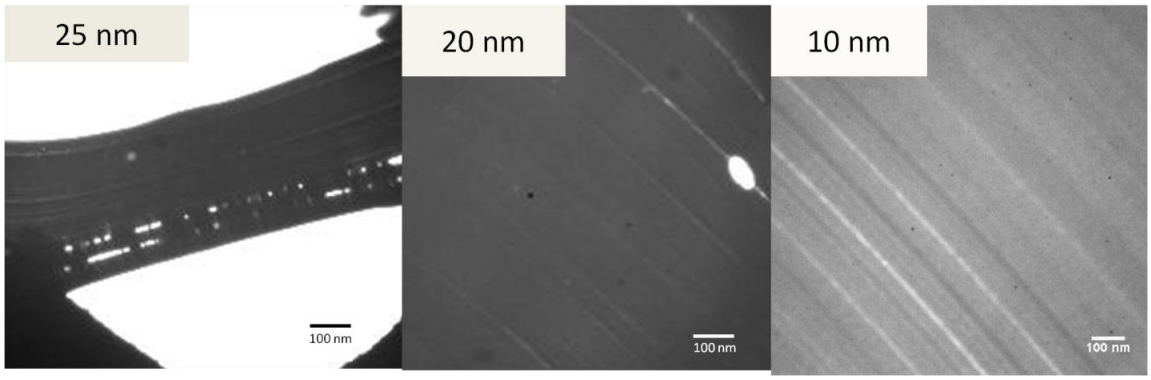

Figure 3.15. LVEM micrographs of microtomed epoxy (density 1.11 g/cm^3) as a function of the nominal thickness (based on instrument settings). These results are consistent with previous studies (Stary & Nebesarova, 2008)calculating that for a material with a density of 1.6 g/cm^3, limited electron transparency is expected for samples thickner than 21 nm

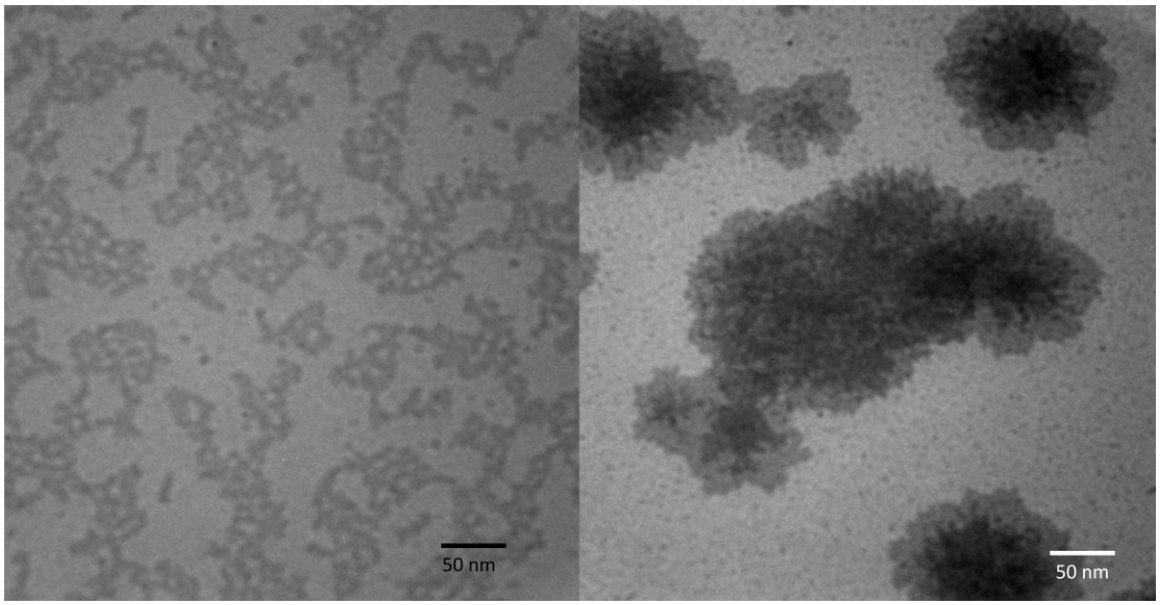

Figure 3.16. LVEM micrograph of PEDOT cubic phases (left: unstained, right: stained with osmium tetroxide): Stained sample does show increased contrast, but fine features appear damaged. Unstained sample shows small features with great contrast (Wu, Shim & Marin, 2010)

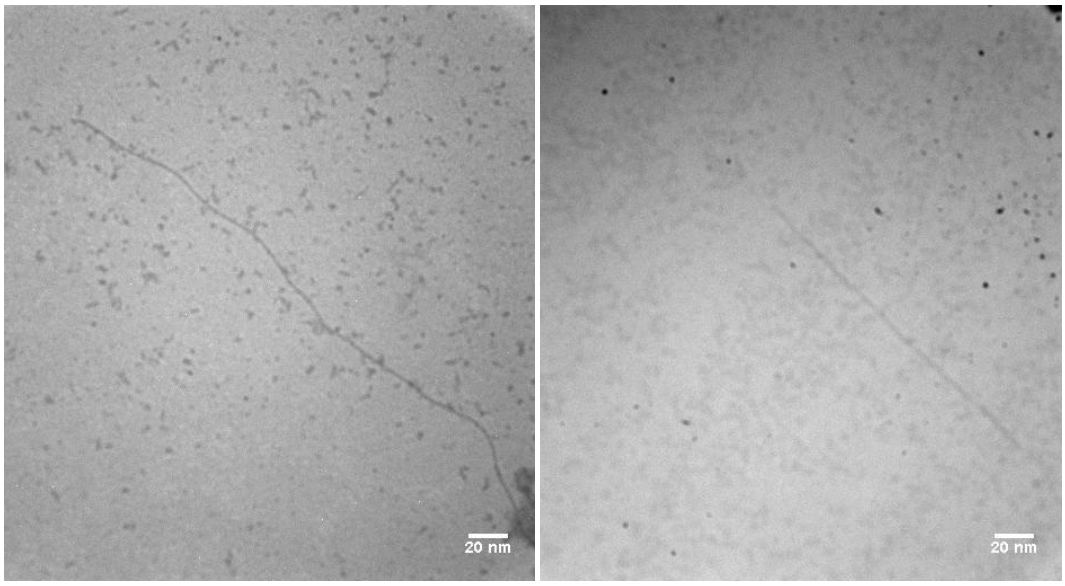

Figure 3.17. LVTEM micrographs of SWCN with diameters around 1 to 2 nm (Left: SWCN dispersed by PSS in water, Right: SWCN dispersed by Nafion® in Ethanol)

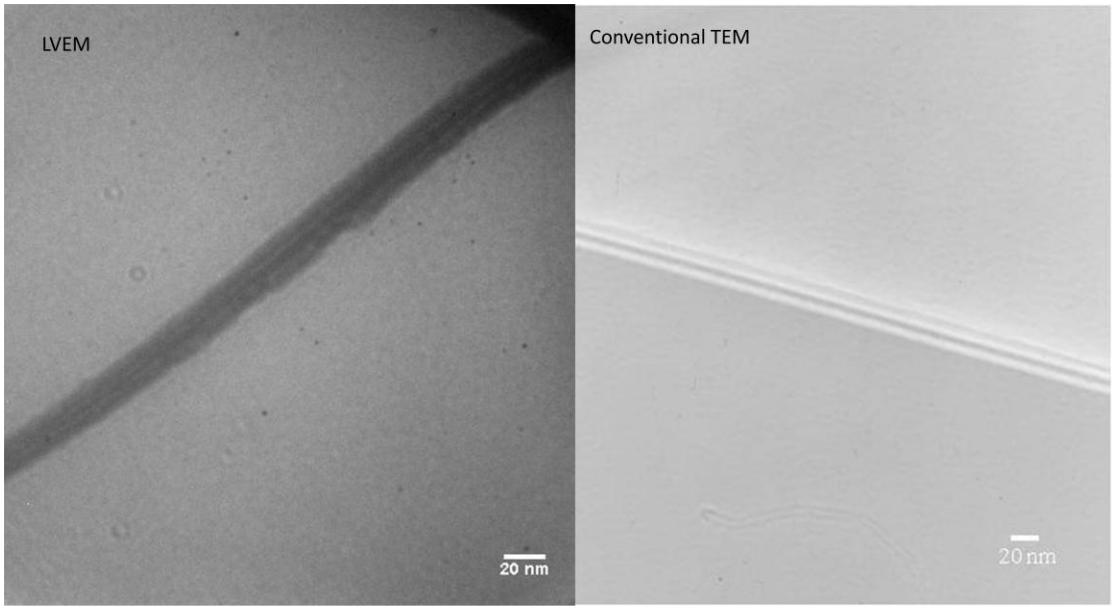

Figure 3.18. Comparison of LVEM micrograph (left) with conventional TEM micrograph (right) of MWCN

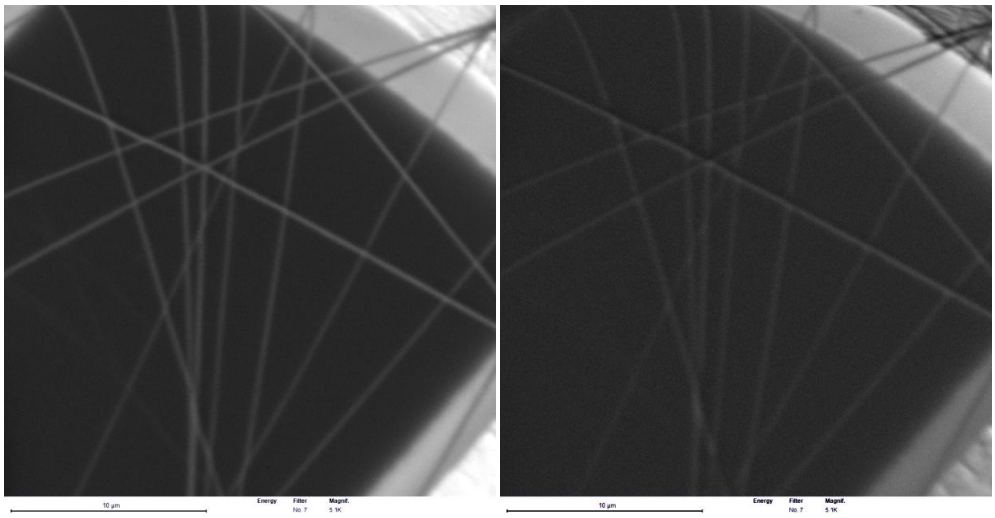

Materials mode Relief modes

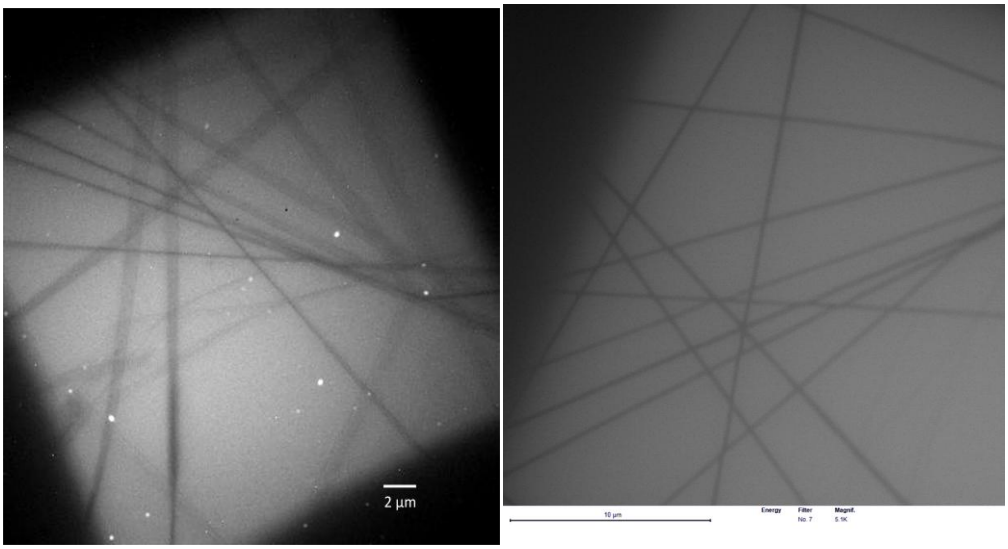

TEM STEM

Figure 3.19. Different image modes of LVEM of the same sample (top left: Materials SEM mode, top right : Relief SEM mode; bottom left: TEM mode, bottom right: STEM mode)

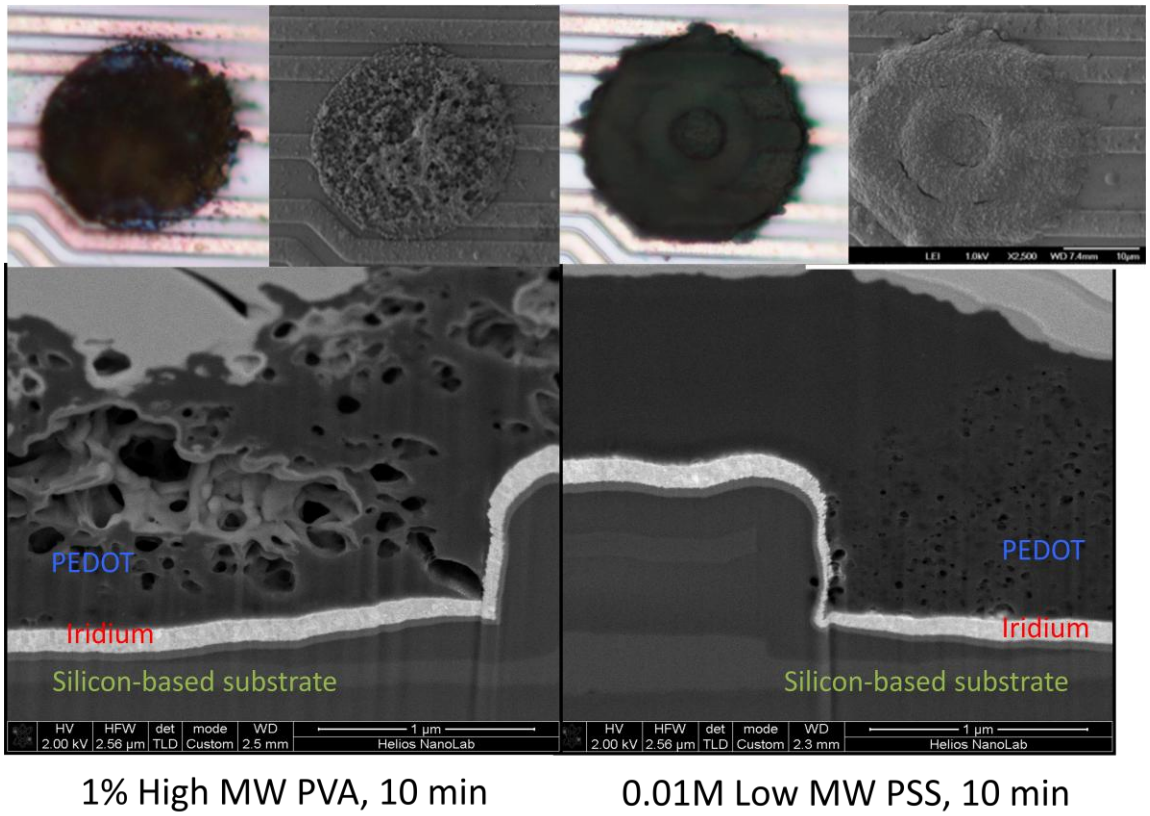

Figure 3.20: FIB/SEM image of PEDOT electrochemically deposited on a microfabricated cortical electrode device. The panel of the images on the left were deposited from a 1% solution of high MW poly(vinyl alcohol) (PVA) for 10 minutes; whereas the panel on right were from a 0.01M solution of low MW PSS for 10 minutes. In each case the upper left image is a top view reflected light optical micrograph, and the upper right is an SEM. The lower image is a secondary electron image of the sample sidewall after FIB sectioning. The PEDOT, iridium electrode, and underlying silicon-based substrate are all readily imaged. The image provides detailed information about the roughness, conformity, and porosity of the various layers. Sectioning through a sample with such large variations in chemistry and mechanical properties is essentially impossible with any other technique.

References

Abidian, M. R; Kim, D.H and Martin, D.C; *Adv Mater*. **18** (2006), 405-409

Adhikari, R. and Michler, G.H; *Journal of macromolecular science, part C: polymer reviews*, **49**, (2009), 141-180

Apgar, P.A. and Yee, K.C., *Acta Crystallogr*. **B34**, (1978), 957

Bellare, J. R., Davis, H. T., Scriven, L. E., & Talmon, Y. *Journal of Electron Microscopy Technique*, **10**, (1988). 87-111.

Bogner, A., Jouneau, P.-H., Thollet, G., Basset, D., & Gauthier, C. *Micron*, **38**, (2007). 390-401.

Bostanjoglo, O., & Otte, D. *Materials Science and Engineering*, **A173**, (1993). 407-411.

Brinkmann, M., Contal, C., Kayunkid, N., Djuric, T., & Resel, R. *Macromolecules*, **43**, (2010). 7604-7610.

Butler, J.H; Joy, D.C; Bradley, G.F and Krause, S.J; *Polymer*, **36**, (1995), 1781-1790

Chen, J and Martin, D.C; *J. Mater. Res.*, **22**, (2007), 1701-1709

Chen J; Subramanian, S; Parkin, S. R; Siegler, M; Gallup, K; Haughn, C; Martin, D.C and Anthony, J.E*; J.Mater. Chem.*, **18**, (2008), 1961-1969.

Corey, J.M., Gertz, C.C., Wang, B., Birrell, L.K., Johnson, S.L., Martin, D.C. and Feldman, E.L., *Acta Biomaterialia* **4**. (2008). 863–875

Drummy, L. F., Farmer, B. L., & Naik, R. R. *Soft Matter*, **3**, (2007). 877-882.

Drummy, L. F., Yang, J., & Martin, D. C. *Ultramicroscopy*, **99**, (2004). 247-256.

Egerton, R. F. *Electron Energy-Loss Spectroscopy in the Electron Microscope* (2nd Edition). New York, NY: Plenum Press. (1986).

Egerton, R. F. Physical Principles of Electron Microscopy: An Introduction to TEM, SEM, and AFM. Springer. (2005).

Evans, J. E., Hetherington, C., Kirkland, A., Chang, L.-Y., Stahlberg, H., & Browning, N. *Ultramicroscopy*, **108**, (2008). 1636-1644.

Fryer, J. R. *Ultramicroscopy*, **11**, (1983). 67-70.

Grubb, D. T. *Journal of Materials Science*, **9**, (1974). 1715-1736.

Haider, M., Braunshausen, G., & Schwan, E. *Optik*, **99**, (1995). 167-179.

Kayunkid, N., Uttiya, S., & Brinkmann, M. *Macromolecules*, **43**, (2010). 4961-4967.

Kim, J. S., LaGrange, T., Reed, B. W., Taheri, M. L., Armstrong, M. R., King, W. E. et al. *Science*, **321**, (2008). 1472-1475.

Kirkland, A., Chang, L.-Y., Haigh, S., & Hetherington, C. *Current Applied Physics*, **8**, (2008). 425-428.

Krivanek, O., Dellby, N., & Lupini, A. R. *Ultramicroscopy*, **78**, (1999). 1-11.

Kübel, C., & Martin, D. C. *Philosophical Magazine A*, **81**, (2001). 1651-1673.

Kübel, C., Mio, M. J., Moore, J. S., & Martin, D. C. *Journal of the American Chemical Society*, **124**, (2002). 8605-8610.

Kumar, S., & Adams, W. W. *Polymer*, **31**, (1990). 15-19.

LaGrange, T., Armstrong, M. R., Boyden, K., Brown, C. G., Campbell, G. H., Colvin, J. D. et al. *Applied Physics Letters*, **89**, (2006). 044105.

Lee, J; Cho, S; Park, Su-Moon; Kim, J; Kim, J; Yu, Jae-Woong; Kim, Y and Russell, T. P. *Nano Lett.*, **8**, (2008), 2315-2320

Liao, J., & Martin, D. C. *Science*, **260**, (1993). 1489-1491.

Liao, J and Martin D.C; *Journal of Materials Research*, **11**, (1996), 2921-2932

Liao, J., & Martin, D. C. *Philosophical Magazine a-Physics of Condensed Matter Structure Defects and Mechanical Properties*, **79**, (1999). 1507-1507.

Libera, M. R., & Egerton, R. F. *Polymer Reviews*, **50**, (2010). 321-339.

Li, J; Qin, F; Li, C; Bao, Q; Chan-Park, M. B; Zhang, W; Qin, J and Ong, B. S; *Chem. Mater.*, **20**, (2008), 2057-2059

Loos, J., Duren, J. K. J. v., Morrissey, F., & Janssen, R. A. J. *Polymer*, **43**, (2002). 7493-7496.

Lovinger, A. J. *Macromolecules*, **18**, (1985). 910-918.

Marko, M., Hsieh, C., Moberlychan, C. A., & Frank, J. *Journal of Microscopy-Oxford*, **222**, (2006). 42-47.

Martin, D. C., Chen, J., Yang, J., Drummy, L. F., & Kübel, C. *Journal of Polymer Science: Physics*, **43**, (2005). 1749-1778.

Martin, D. C., Shen, Y., Wu, J., Povlich, L., Leach, M., Spanninga, S., and Shaw, *PMSE Preprints*, Proceedings of the American Chemical Society Meeting, Salt Lake City, UT, (March 2009).

Martin, D. C., & Thomas, E. L. *Polymer*, **36**, (1995). 1743-1759

Martin, D.C; Wu, J; Shaw, C.M; King, Z; Spannigga, S.A; Rcihardson-Bruns, S; Hendricks, J and Yang, *J; Polymer Reviews*, **50**, (2010), 340–384.

Nam, K. T., Shelby, S. A., Choi, P. H., Marciel, A. B., Chen, R., Tan, L. et al. *Nature Materials*, **9**, (2010). 454-460.

Orth, H., & Fischer, E. W. *Makromol. Chem.*, *88*, (1965). 188.

Rose, H. *Optik*, **84**, (1990). 91-107.

Sawyer, L. C., Grubb, D. T., & Meyers, G. F. Polymer Microscopy (Third Edition). Springer. (2008).

Scherzer, O. *Journal of Applied Physics*, **20**, (1949). 20-29.

Shim,B; Tang. Z; Morabito,M.P; Agarwal, A; Hong, H and Kotov. N. A; *Chem. Mater*. **19**, (2007), 5467-5474

Sijbrandij, S., Thompson, B., Notte, J., Ward, B. W., & Economou, N. P. *J. Vac. Sci. Technol. B*, **26**, (2008). 2103-2106.

Stary, V., & Nebesarova, J. *Journal of Physics: Conference Series*, **126**, (2008). 012062.

Studer, D., & Gnaegi, H. *Journal of Microscopy*, **197**, (2000). 94-100.

Sugiyama, M., & Sigesato, G. *Journal of Electron Microscopy*, **53**, (2004). 527-536.

Texter J; Schwarz, R and Stepan,P; *Polymer Prints*, **48**, (Aug. 2007) 2,

Tosaka, M., Tsuji, M., Cartier, L., Lotz, B., Kohjiya, S., Ogawa, T. et al. *Polymer*, **39**, (1998). 5273-5275.

Voigt-Martin, I. G., Krug, H., & Dyck, D. V. *J. Phys. France*, **51**, (1990). 2347-2371.

White, H., Pu, Y., Rafailovich, M., Sokolov, J., King, A. H., Giannuzzi, L. A. et al. *Polymer*, **42**, (2001). 1613-1619.

Williams, D. B., & Carter, C. B. *Transmission Electron Microscopy: A Textbook For Materials Science.* New York: Plenum Press. (1996).

Wilson, P. M., & Martin, D. C. *Journal of Materials Research*, **7**, (1992a). 3150-3158.

Wilson, P. M., & Martin, D. C. Boston, MA. (1992b).

Wilson, P. M. The University of Michigan, Ann Arbor. (1994).

Wu,J; Shim,B and Martin, D C. *Microscopy and Microanalysis*.**16**, (2010),340-341

Zach, J., & Haider, M. *Nucl. Inst. and Meth. A*, **363**, (1995). 316.

Zhong, S., & Pochan, D. J. *Polymer Reviews*, *50*, (2010). 287-320.

Ziegler, A., Rockel, B., Hegerl, R., Freitag, B., Lücken, U., & Plitzko, J. M. *Journal of Microscopy*, **233**, (2009). 170-177.

Chapter IV

Characterization Of Highly Ordered Electrochemically Deposited 3,4-ethylenedioxythiophene EDOT-Br

Abstract

A highly ordered 3,4-ethylene dioxythiophene EDOT-Br phase was electrochemically synthesized by using bromine as a counterion during deposition. Wide-Angle (WAXS) and Small-Angle (SAXS) X-ray Scattering indicates the formation of highly ordered, crystalline samples. Optical light microscopy, Scanning electron microscopy (SEM) and transmission electron microscopy (TEM) all confirmed the existence of needle-shaped single crystals. Fourier transform infrared spectroscopy (FT-IR), X-ray photoelectron spectroscopy (XPS) and Scanning Electron Microscopy-Energy Dispersive Spectroscopy (EDS) elemental mapping all confirm the existence of chemical bonding similar to that seen in PEDOT.

Introduction

Poly(3,4-ethylene dioxythiophene) (PEDOT) is one of the most promising conductive polymers due to its high thermal, chemical stabilities and transparent properties (Heywang & Jonas, 1992). It has many different applications, such as antistatic layers, electroluminescent displays (Kirchmeyer & Reuter, 2005; Groenendaal, Jonas, Freitag, Pielartzik & Reynolds, 2000), hole injection layers in organic electronic devices (Nguyen, Rendu, Long & De Vos, 2004) and electrode coatings for biomedical devices (Yang & Martin, 2004).

In the EDOT monomer, the alkylenedioxy-substitution on the thiophene ring has two beneficial functions. First substitution in the 3 and 4 positions prevents α,β coupling during polymerization, leading to strictly linear chains. Secondly, the

electron donating oxygen atoms lower the oxidation potential of the thiophene ring enhancing PEDOT stability (Pei, Zucarello, Ahlskog & Inganas, 1994). The rigid backbone conformation of PEDOT facilitates charge transport and favors crystallization, reducing solubility and processability (Lock, Im & Gleason, 2006). Fully undoped soluble PEDOT oligomers have been chemically synthesized from polycondensation of EDOT dihalide. The resulting PEDOT oligomers (2,5-dibromo-3,4-ethylenedioxythiophene) exist in mixtures. This soluble PEDOT opens opportunity to improve its processability (tran-Van, Garreau, Louarn, Froyer & Chevrot, 2001).

The properties of conducting polymers are strongly dependent on their morphology and structure. The degree of crystallinity plays a particularly crucial role in determining the physical properties of the polymer. Charge transport is mostly anisotropic in π-conjugated semi-conductors. Preferential orientation of these semi-conductors is desirable, as charge mobility along the chain is much larger than that perpendicular to it (Jimison,Toney, McCulloch, Heeney & Salleo, 2009; Brinkmann, Contal, Kayunkid, Djuric & Resel, 2010). Highly oriented and nanotextured regioregular π-conjugated polymer poly(3-hexylthiophene) (P3HT) films epitaxially grown on the nanostructured surface of an aromatic substrate potassium 4-bromobenzoate (K-BrBz) has been developed and studied by Brinkmann et, al. The nanotextured P3HT films developed highly oriented crystalline domains connected by amorphous interlamellar zones. The P3HT chains were preferentially oriented along two in-plane directions corresponding to rows of bromine atoms on the surface of the K-BrBz substrate. The growth mechanism involved with the substrate surface reconstruction under proper isothermal crystallization and expitaxial crystallization of the polymer (Brinkmann, Contal, Kayunkid, Djuric & Resel, 2010).

Coupled with grazing incidence diffraction data, Aasmundtveit et al. simulated the structure of PEDOT doped with toluenesulfonate (tosylate) (Aasmundtveit, et al., 1999). They proposed an orthorhombic structure for PEDOT whose lattice parameters

a, b and c are 1.4 nm, 0.68 nm and 0.78 nm respectively. The polymer is flat along c-axis which is also the thiophene backbone. The chains stack along the b-axis forming layers with a stacking distance of b/2. The stacked b-c layers are separated by the dopant along the a-axis. Heating PEDOT up to 200 ℃ increases the crystalline order and expands both lattice parameters a and b. They hypothesized that the conductivity is highest along the c-axis (the backbone direction) and expected that the short stacking distance facilitates conductivity due to orbital overlap.

Peak position and intensities didn't vary with doping and dedoping process by applying voltage to the film but the structural order could be reversibly increased by doping and decreased by dedoping (Aasmundtveit, et al., 2000). They proposed that doping and dedoping process were accomplished by motion of smaller ions between the polymer and the electrolyte.

Reports from previous studies in our group and elsewhere have found that the d-spacing and crystallinity of PEDOT films are highly dependent on the polymerization conditions and doping agents used during synthesis (Martin, et al., 2010). We have found that PEDOT d-spacing can be systematically tailored by changing the counter ions in electrochemical polymerization. Also in previous studies we found that by varying polymerization current, PEDOT crystallinity can be controlled to a certain degree. Different doping counter ions have impacts on PEDOT structure, hence alter the conductivity of PEDOT. Winther-Jensen et al studied the order-disorder transitions of PEDOT doped with different counter ions synthesized by chemical polymerization (Winther-Jensen, et al., 2008). Different counter ions produced different d100 spacing and different conductivity.

The reaction rate of the polymerization increases with the increase of acidification. Strong protic acids and some Lewis acids, including BF_3, $AlCl_3$, $TiCl_4$, $SnCl_4$, $SbCl_5$, *etc.*, existing as catalysts can polymerize EDOT into dimeric or stereoisomeric trimeric compounds without further polymerization (Kirchmeyer & Reuter, 2005).

In the present study, we found a new highly ordered EDOT-Br phase synthesized via facile electrochemical polymerization. The structure and physical properties of the EDOT-Br phase were studied and compared with the less crystalline PEDOT synthesized by chemical or electrochemical polymerization. Polymerization of the highly ordered structure was hypothesized.

Results and Discussion

The EDOT-Br films were grown directly on a conductive substrate out of EDOT alkali bromide (LiBr, NaBr, or KBr) aqueous solutions. The speed of deposition was typically slower than PEDOT doped with other counter-ions. In contrast to the typical blue color of PEDOT film doped with other counter-ions, the films had a silver metallic color after it was soaked in a large quantity of water to remove the excess EDOT monomer and LiBr ions. The EDOT-Br formed highly anisotropic, birefringent films with needle-shaped crystalline domains that were hundreds of microns in size (Figure 4.1).

PEDOT films prepared by chemical or electrochemical polymerization with different counter ions showed different levels of crystallinity with limited orientation and small crystallites (Martin, et al., 2010). Wide angle X-ray diffractions were done on the sample. It has diffraction peaks and d spacings close to PEDOT film (Table 4.1). Normal d100 scattering peaks of PEDOT ranged from 1.12 nm to 1.53 nm depending on the counter ions doped in the PEDOT crystal structure. (Aasmundtveit, et al., 1999; Martin, et al., 2010). When PEDOT counter ions changed from fluoride to chloride, the d_{100} spacing increased from 1.12 nm to 1.39 nm, and the crystallinity increased somewhat but remained essentially a semicrystalline PEDOT polymer. EDOT-Br (Figure 4.2) showed two extremely sharp, strong peaks at d-spacings of 1.11 nm and 1.03 nm. The structure of the crystal had a single crystal texture instead of a semicrystalline polymer. Wide angle X-ray diffraction was also

done on pure LiBr and LiBr hydrate. Neither of these showed any peaks corresponding to a reasonable PEDOT d_{100} spacing, which indicates the scattering peaks at 1.11 nm and 1.03 nm were not contributed either from LiBr or its hydrate.

SEM micrographs were taken after the samples were coated with 10 nm thick gold film. SEM images show local fibrillation within the needle-shaped crystals, oriented perpendicular their long axes, which is presumably their primary growth direction (Figure 4.3). This fibrillation was ~100 nm wide and several microns in length, and is presumably related to the locally anisotropic arrangement of the EDOT-Br oligomers within the needle crystals.

An SEM energy-dispersive X-ray spectroscopy (EDS) elemental map was formed by collecting characteristic X-rays as a function of the position of the beam on the sample I(x,y). The technique is useful to quantitively map out the spatial distribution of different elements in a sample (Williams & Carter, 1996; Crozier, 1995). EDS elemental mapping micrographs of EDOT-Br are shown in Figure 3.4 . The area selected to do the mapping was illustrated on the top SEM images. In the colored elemental mapping images, blue maps out bromine, green maps out oxygen, yellow maps out sulfur and red maps out carbon. Carbon, oxygen and sulfur are contributed by PEDOT. Their concentration and distribution throughout the filament are well correlated. Bromine is the counter ion that should be associated with PEDOT chain. The counter ions are not associated with EDOT repeat unit with one on one basis. It is believed to be one counter ion every 3 or 4 repeat units (Martin et al., 2010), so the concentration of bromine should be lower while the distribution should be correspond to the PEDOT distribution. As seen from Figure 4.4, the bromine counts concentration is lower along the fiber and the distribution matches that of the other three atoms that are contributed by PEDOT chains.

Needle-shaped crystals of EDOT-Br were stripped off the conductive substrate and deposited onto copper grids. The crystals were highly anisotropic and regularly

faceted in the TEM images (Figure 4.5). High-resolution, low dose TEM micrographs of thin samples were taken (Figure 4.6). The fringes in the micrograph had a spacing of 1.03 nm, consistent with the WAXS study. FFT studies showed only small amounts of misorientation, indicating the highly crystalline nature of the crystals.

In previous studies of PEDOT morphology as a function of temperature using DSC coupled with grazing angle x-ray diffraction, it was shown that chemically polymerized PEDOT has a thermodynamic phase transition appearing to begin around 100 ℃ and peak around 140 ℃. This transition corresponds to a loss of the long range π-stacking as the counter ions of the iron salts used in the synthesis were varied. The second thermal spectra obtained immediately after the first run in DSC was shown to be completely featureless indicating the irreversible nature of these thermal transition in normal PEDOT films (Winther-Jensen, et al., 2008).

Figure 4.7. shows the DSC spectra of EDOT-Br film. Two consecutive temperature scans were done from zero to 250 ℃. In the first scan the film showed sharp thermal transition peaks at around 100 ℃ and at 140 ℃. These peaks presumably correspond to the loss of long range π-stacking. The second temperature scan produced completely featureless spectra that are consistent with the thermal transition behaviors of PEDOT films doped with other counter-ions. A series of α,ω-diperfluorohexylsexithiophene (DFH-6T) molecules have been synthesized and studied, the number represents how many thiophene rings are in the molecule. The more thiophene rings in the molecule, the higher the melting temperature starting from 97 ℃ for DFH-2H, to 310 ℃ for DFH-6T (Figure 4.8) (Facchetti, Mushrush, Katz & Marks, 2003). This indicates that the PEDOT-Br might be PEDOT-oligomers.

FT-IR data of EDOT-Br is shown in Figure 4.9. The peak at 641 cm^{-1} corresponds to the vibration of C-S in a cyclic structure. The peak absorptions at 1512, 1415, and 1362 cm^{-1} can be assigned to stretching of the thiophene ring. (Nguyen,

Rendu, Long & De Vos, 2004)

XPS has been utilized to deduce the chemical binding energies of PEDOT to determine information on various counterion bonding (Greczynski, Kugler & Salaneck, 1999; Greczynski, et al., 2001). Br^- acted as a counter-ion in the electrochemically polymerized PEDOT. The S 2p spectrum showed PEDOT peaks at 164.4 eV (S 2p3/2) and 165.6 eV (S 2p1/2) (Figure 4.10). At the same time, the characteristic $PEDOT^+Br^-$ spin-split doublet was observed around 70.7 eV (Br 3d5/2) and 71.7 eV (Br 3d3/2) with a characteristic peak separation around 1.0 eV (Moulder, Stickle, Sobol & Bomben, 1992). To confirm whether the incorporation of Br- as the counter-ion into PEDOT different poly anions including poly (acrylic acid) and PSS were added to EDOT LiBr solution during PEDOT electrochemical polymerization. The XPS signal indicated that the Br- acted as a counter-ion to PEDOT in both systems (Spanninga, 2010).

Trubiez et al. have synthesized and studied a series of EDOT oligomers end-capped with n-hexyl groups. The maxima in absorption spectra of these different EDOT oligomers increased with the increase number of repeating units, from 349 nm for EDOT dimer, to 414 nm for EDOT trimer, and to 459 nm for EDOT tetramer (Turbiez, Frère & Roncali, 2003). UV-Vis spectra can be influenced by the side groups on the thiophene ring. Thiophene oligomers having 3 thiophene rings in the molecule has absorption peaks at 354 has been reported (Havinga, et al., 1991). Figure 4.11. is the UV-Vis spectra of PEDOT-LiBr. It has a distinctive maxima at 354 nm. This indicated that the highly oriented crystalline structure might be formed from EDOT oligomers. Another weak broad, band was seen around 700 nm. For neutral PEDOT, the π-π^* transition maxima normally appeared at around 570 nm while for oxidized PEDOT, oxidative doping peak grows to around 705 nm with the π–π^* transition band decreases in intensity (Łapkowski & Proń, 2000). The oxidative state of the PEDOT films are conductive whereas the neutral state is insulating.

It is possible that the PEDOT oligomers were formed as indicated by the UV-Vis data. Coupled with the data above, the growth mechanism of this highly oriented EDOT-Br crystalline film was proposed as the following three steps (Figure 4.12). In the first step as electrons were injected into the EDOT LiBr aqueous solution, molecular bromine (Br_2) was formed. Bromine has been known to induce bromination of heterocyclic molecules like 2,1,3-Benzothiadiazole (Pilgram, Zupan & Skiles, 1970), so the second step is likely bromination of EDOT monomer forming EDOT with ends capped with bromine. The third step is electrochemical polymerization of EDOT forming dimers and trimers capped by bromine on both ends.

Conclusion

We found a new highly ordered EDOT-Br phase that forms during electrochemical polymerization. This phase shows ordered crystalline domains that are hundreds of microns in size. The structure of the film showed local fibrillation within the needle-shaped crystals that is oriented perpendicular their long axes, which is presumably their primary growth direction. This characteristic fibrillation (forming domains that are ~100 nm wide, and is microns in length) is presumably related to the locally anisotropic arrangement of the PEDOT polymers or oligomers within the needle crystals. The crystals have d-spacings near 1.03 nm, as confirmed both by WAXS and high-resolution TEM. The highly crystalline EDOT-Br film opens possible windows for the detailed study of crystal structure and transport properties in these conductive conjugated EDOT single-crystal films.

Experimental

Synthesis

EDOT (Aldrich) was dissolved in water forming a 0.01 M solution. The alkali halide salts LiBr, NaBr and KBr were purchased from Sigma-Aldrich®, and

dissolved to form a 0.01 M solution. The samples were deposited galvanostatically onto 35 nm gold-palladium thin films that had themselves been evaporated onto glass microscope slides, using a current density of 0.5 mA/cm^2 from an Autolab Potentiostat/Galvanostat model PGSTAT12.

Characterization

Scanning electron microscopy (SEM)

SEM samples were prepared by coating a 10 nm thick gold film on the sample. SEM images and EDS elemental mapping were then studied by a FEI Nova Nanolab Dualbeam Focussed Ion Beam Workstation and Scanning Electron Microscope

Wide angle X-ray Scattering (WAXS)

PEDOT doped with LiBr was made by electrochemical polymerization onto substrates with 35nm thick gold-palladium thin film on them. Wide Angle X-ray Diffraction patterns were acquired with a Bruker D8 Discover system, equipped with a 2D position sensitive wire array detector. Samples were typically oriented in a near grazing incidence geometry, with the film plane horizontal and the Cu Kα X-ray source at an incoming angle of ~2 degrees.

Optical Microscopy (OM)

Optical microscopy was done on a Nikon Optiphot-POL in either transmitted or reflected light. The microscope was also equipped with polarizers and analyzers, and a full wave red filter. Digital images were acquired with a SPOT-RT camera.

Fourier transformed infrared (FT-IR) spectrophotometer

EDOT-Br films were deposited onto an indium tin oxide substrate. FT-IR spectra were conducted on a Jasco FT/IR 4100.

UV-Vis Spectrophotometry

EDOT-Br was grown onto an ITO substrate from EDOT LiBr aqueous solution. UV-Vis spectra were obtained on a Shimadzu UV-Vis-NIR spectrophotometer scanning from 300 nm to 700 nm.

Transmitted electron microscopy (TEM)

TEM samples were prepared by stripping off the film with poly(acrylic acid) (PAA) solution and then drying in an oven at 70 C. The PAA was dissolved in water and the film together with the Au-film was transferred onto a copper grid. Bright field images were taken by a JEOL 3011 300 kV HREM at the University of Michigan EMAL. Low dose, aberration-corrected high resolution TEM micrographs from a EDOT-Br sample were taken at 300 kV on an FEI Titan with an objective lens spherical aberration corrector (no beam corrector).

X-ray Photoelectron spectroscopy (XPS)

The XPS samples were deposited on Au/Pd sputter-coated barbell shaped electrodes (6 mm diameter) on polystyrene (PS) cover slips at 135 μA for 10 minutes. The samples were then rinsed in de-ionized water to remove excess counter-ion from the surface and allowed to air dry. For EDOT-Br, after soaking in de-ionized water for 24 hours, the amount of excess Br- was found to be reduced by at least half. XPS spectra were obtained with a Kratos Axis Ultra DLD X-ray Photoelectron Spectrometer (KratosAnalytical Ltd.,Manchester, UK) with a monochromatic aluminum source at a vacuum pressure of 10-8 to 10-9 Torr. Initial survey scans were run using a pass energy of 160 eV, while characteristic region scans for C 1s, O 1s, S 2p, and Br 3d were also collected utilized pass energy of 20 eV with a step 0.1 eV. All spectra were referenced using the C-C/C-H peak at 285 eV.

Figures

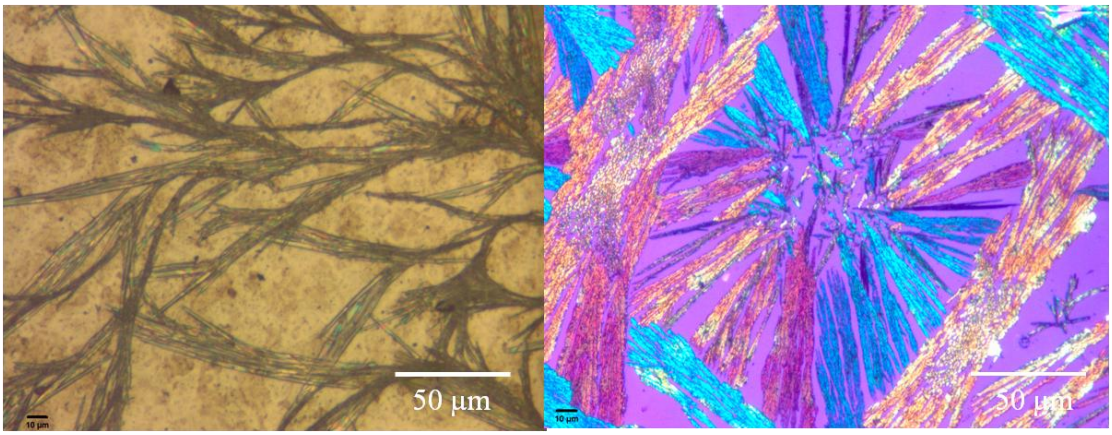

Figure 4.1. Optical micrographs of electrochemically deposited PEDOT film, using bromine as a counterion. Left image: brightfield; Right: polarized light with a full-wave red filter. The films have highly regular, birefringent, faceted crystals that are tens of micrometers in size.

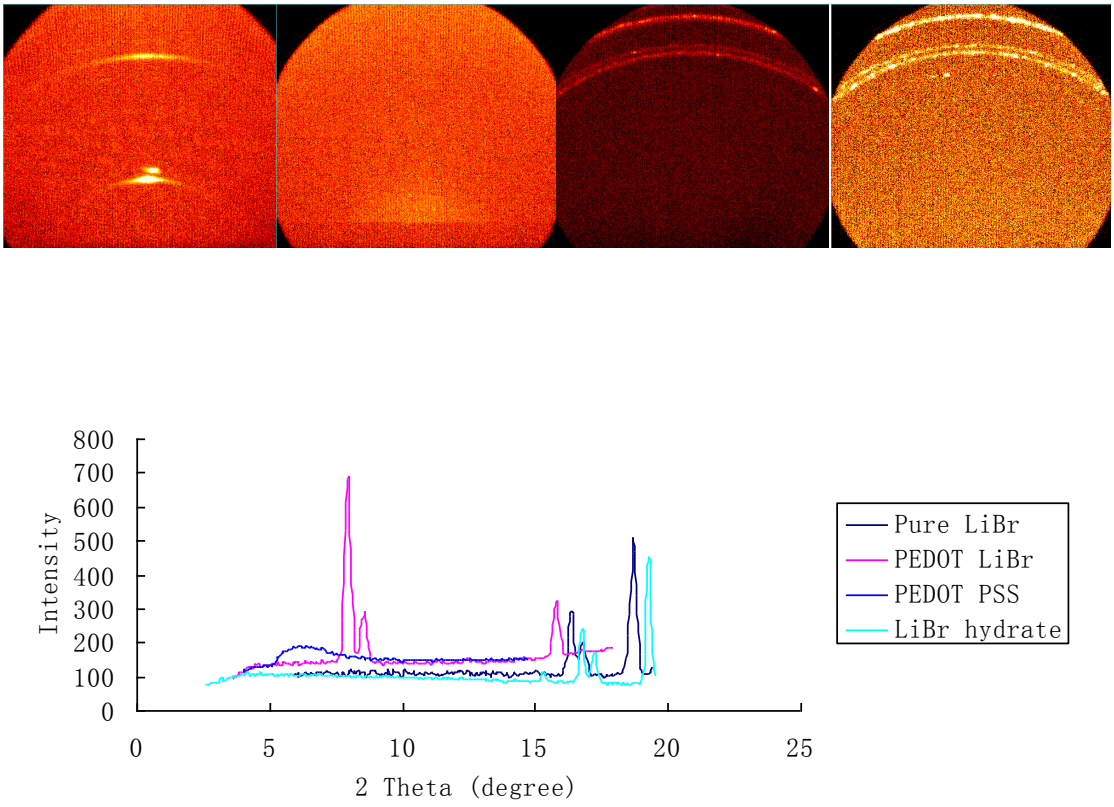

Figure 4.2. WAXD of PEDOT LiBr (left), PEDOT PSS (middle left), Pure LiBr (middle right), LiBr hydrate (right). The films were oriented with the surface normal vertical. Top: 2D WAXS. Bottom: 1D 2 theta scans.

Counter ions	2 theta (degrees)	d100(nm)
Br-	7.95 7.90	1.11 1.03
PSS-	6.05	1.46

Table 4.1. Scattering peaks and calculated d spacings of PEDOT-LiBr from WAXS.

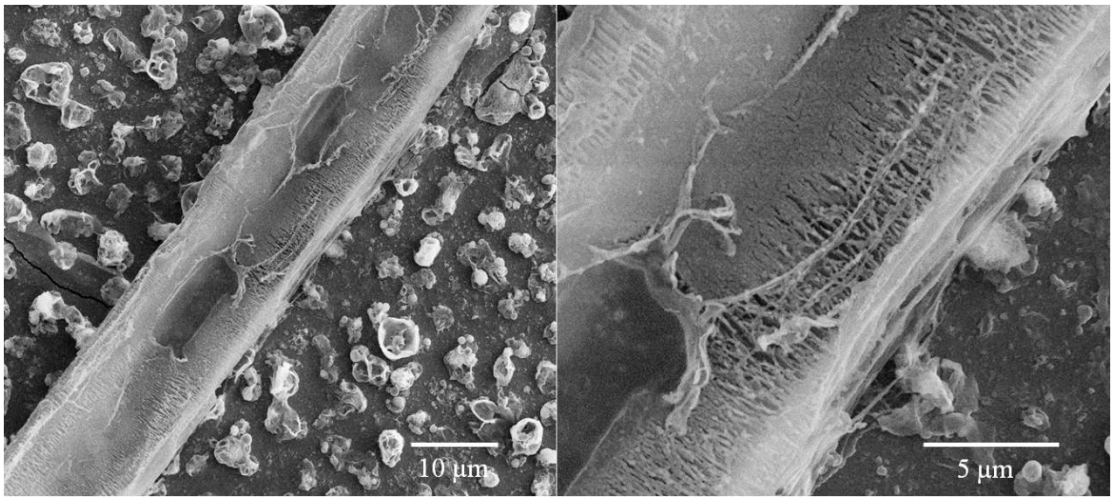

Figure 4.3. SEM images of PEDOT-LiBr showing local fibrillation within needle-shaped crystals. Fibrillation oriented perpendicular to long axes, presumably their primary growth direction. Fibrillation (~100 nm wide, microns in length) presumably related to the locally anisotropic arrangement of the PEDOT polymers or oligomers within the needle crystals.

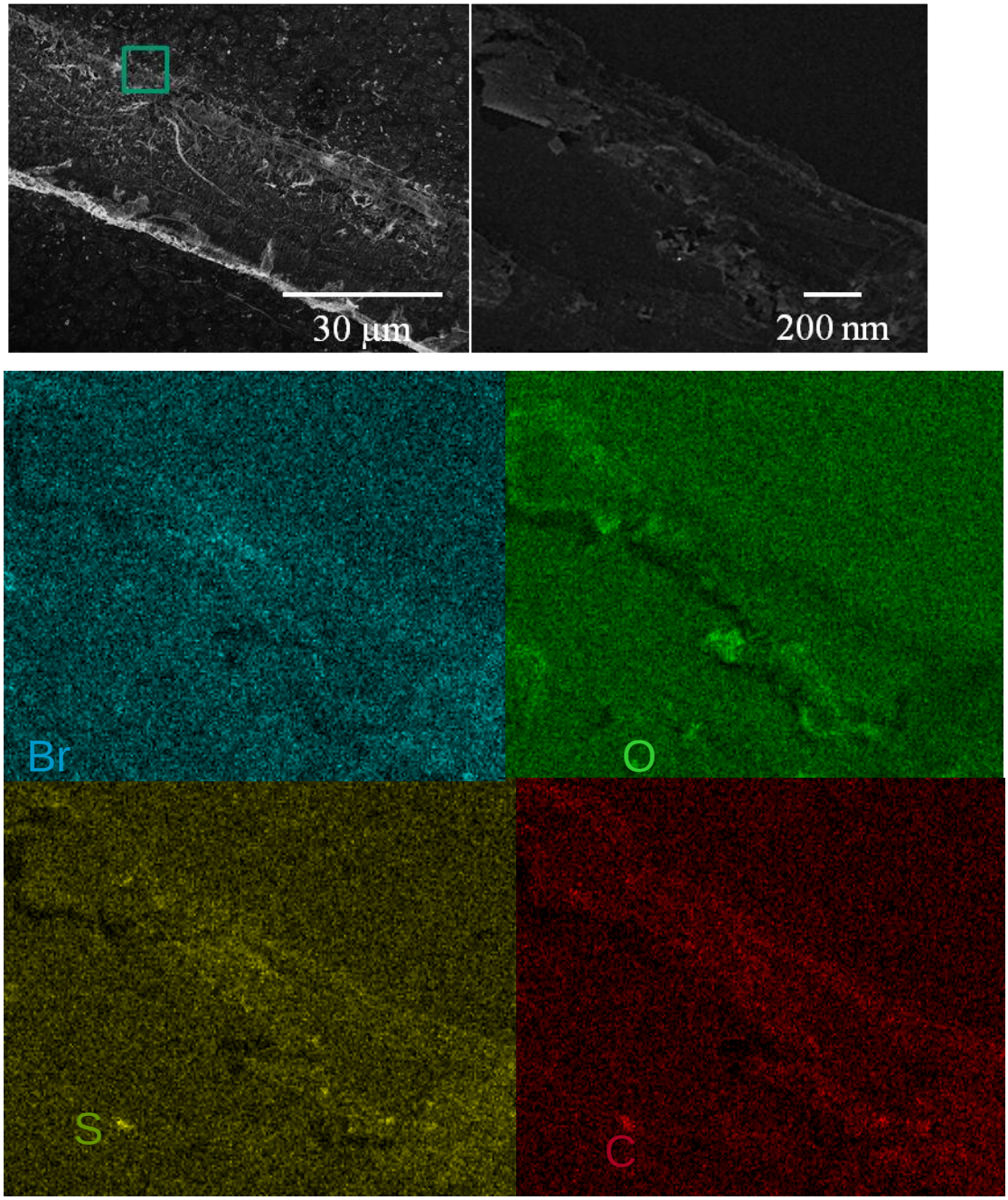

Figure 4.4. SEM EDS elemental mapping micrographs of PEDOT-LiBr. Top: SEM images of the area selected to do the mapping. In the colored elemental mapping images, blue maps out bromine, green maps out oxygen, yellow maps out sulfur and red maps out carbon. Carbon, oxygen and sulfur are contributed by PEDOT. Bromine is roughly associated with sulfur.

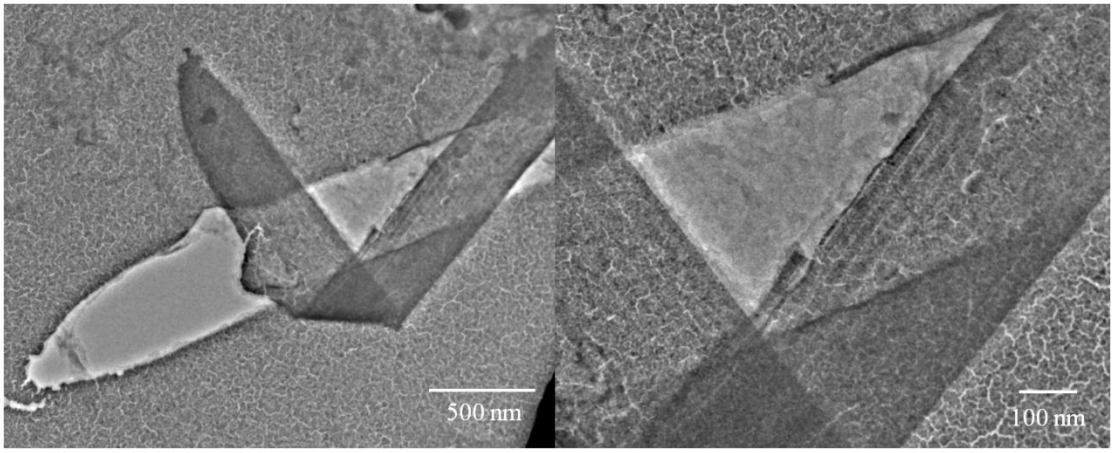

Figure 4.5. Bright field TEM micrographs of PEDOT-LiBr showing a high degree of crystallinity and texturing in the deposited films.

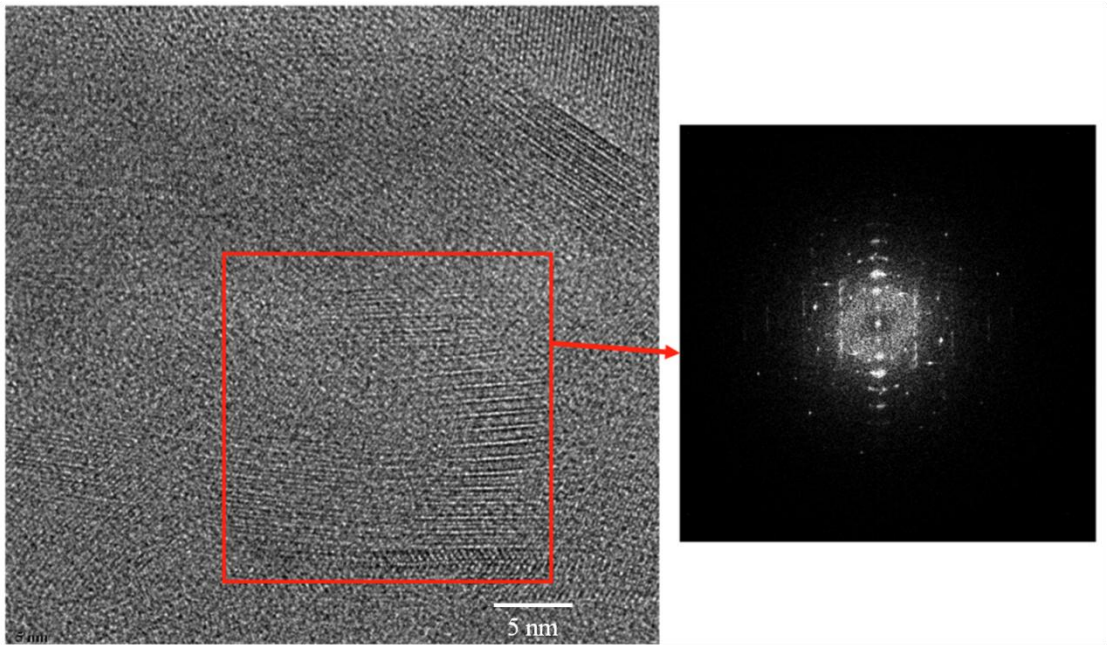

Figure 4.6. High resolution TEM image of PEDOT-LiBr (left). FFT of the selected area showing high crystalline nature of the film with little misorientation (right).

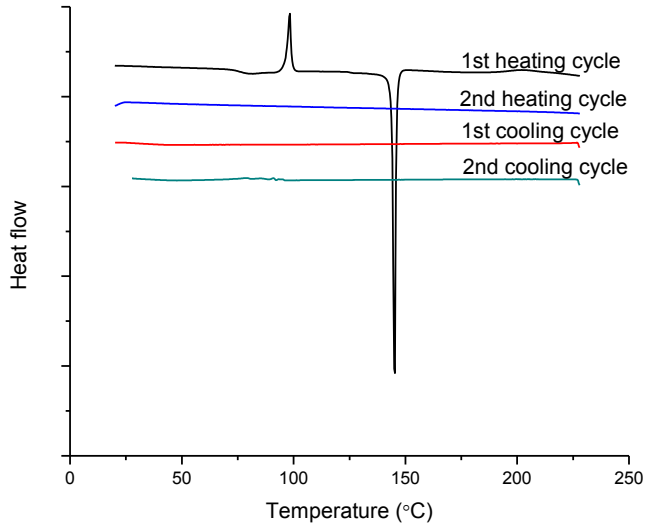

Figure 4.7. DSC spectra of PEDOT-LiBr on two consecutive temperature scans.

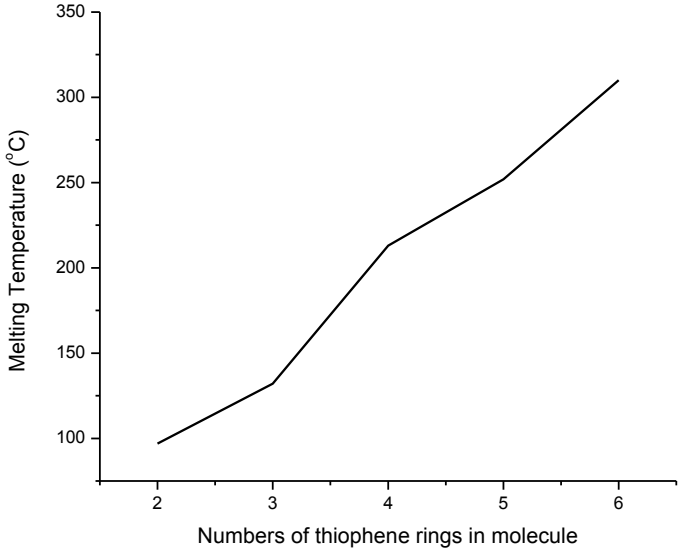

Figure 4.8. Melting temperature of different thiophene oligomers (data from Facchetti, et al., 2003)

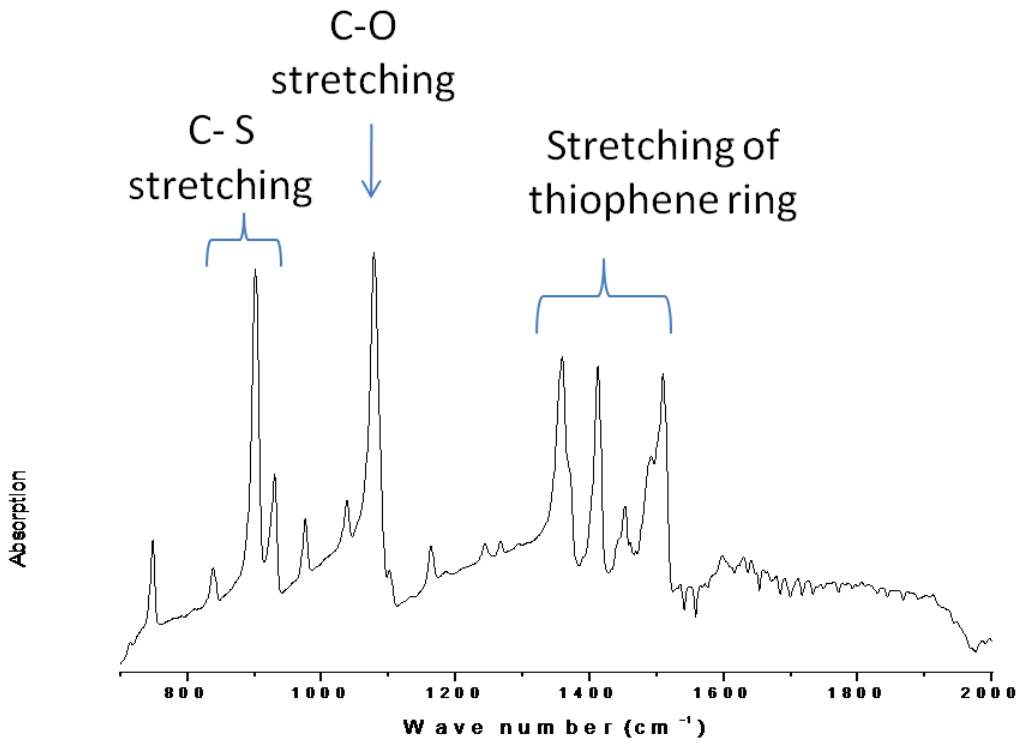

Figure 4.9. FT-IR spectra of PEDOT-LiBr indicating the formation of PEDOT.

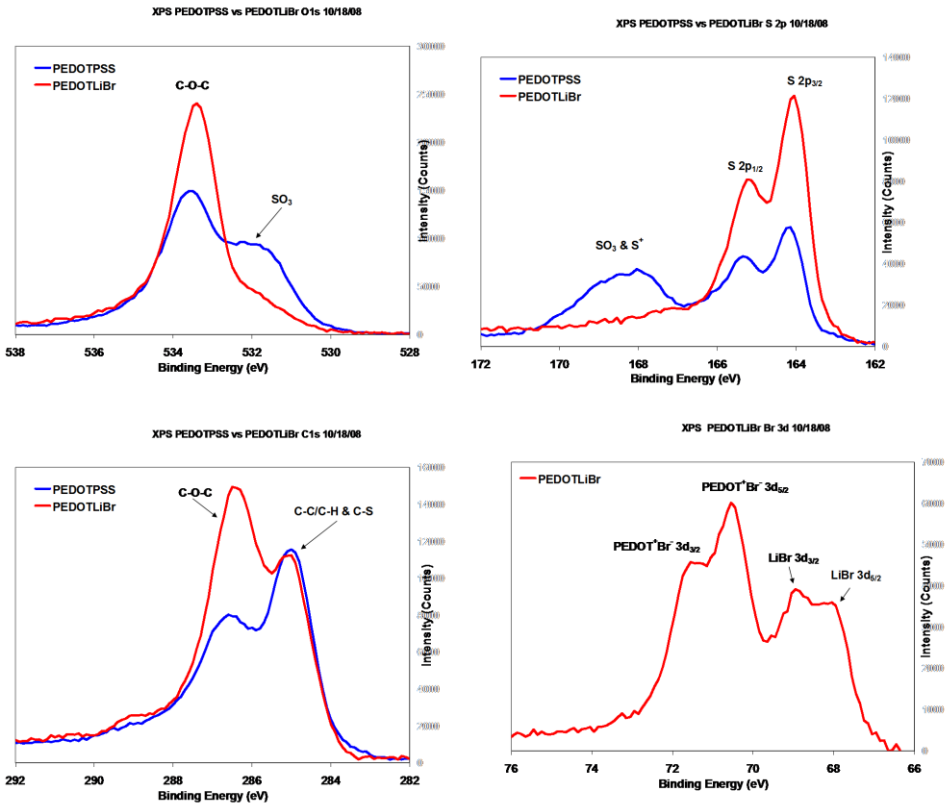

Figure 4.10. XPS spectra of EDOT-Br confirming the existence of PEDOT and Br- acting as counter-ion.

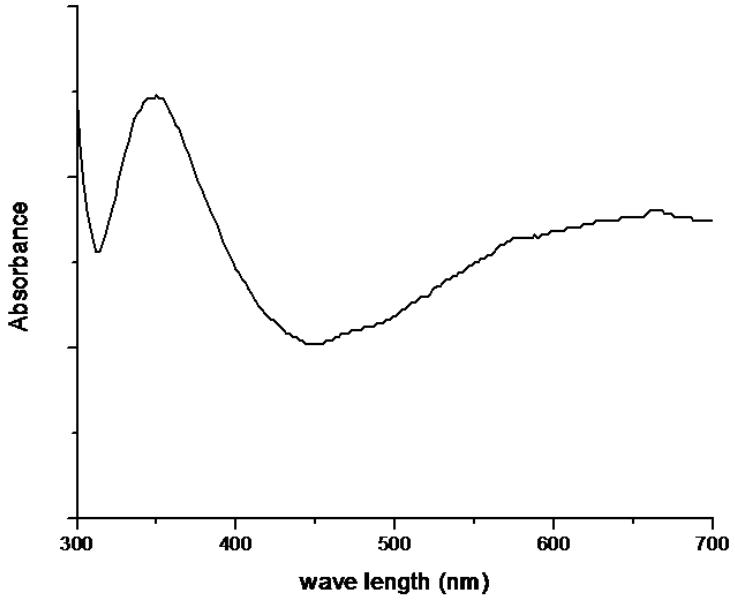

Figure 4.11. UV-Vis spectra of PEDOT-LiBr

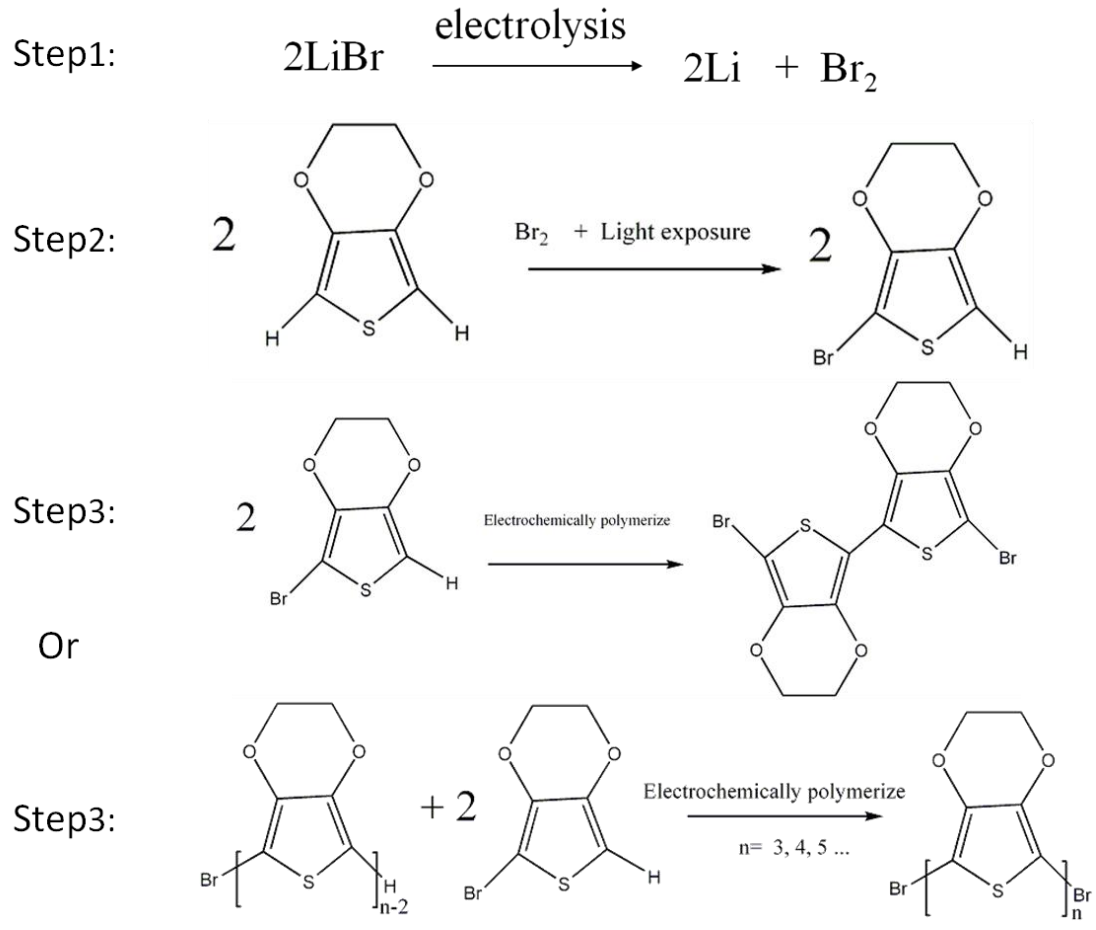

Figure 4.12. Hypothesized growth schematics of highly oriented EDOT-Br.

References

Aasmundtveit, K.E., Samuelsen, EJ., Pettersson, L.A.A., Inganas, O., Johansson, T., Feidenhans'l, R. *Synthetic metals*, **101**, (1999), 561-564.

Brinkmann, M., Contal, C., Kayunkid, N., Djuric, T. and Resel, R. *Macromolecules*, **43**, (2010), 7604-7610.

Facchetti, A., Mushrush, M., Katz, H.E. and Marks, T.J. *Adv. Mater.* **15**, (2003), 33-38.

Greczynski, G.; Kugler, T.; Salaneck, W. R. *Thin Solid Films*, **354**,(1999), 129–135.

Greczynski, G.; Kugler, T.; Keil, M.; Osikowicz, W.; Fahlman, M.; Salaneck, W. R., *Journal of Electron Spectroscopy and Related Phenomena*, **121, (**2001**)**, 1–17.

Groenendaal L., Jonas F., Freitag D., Pielartzik H., Reynolds J.R., *Adv Mater.* **7.** (2000), 481–494.

Havinga, E.E., Rotte, I., Meijer, E.W., Ten Hoeve, W. and Wynber, H. *Synthetic Metals*. **41-43**, (1991), 473-478.

Heywang G. and Jonas, F. *Adv. Mater*., **4**, (1992), 116

Jimison, L. H.; Toney, M. F.; McCulloch, I.; Heeney, M.; Salleo, A. *Adv. Mater.* **21**, (2009), 1568-1572

Kirchmeyer S. & Reuter; K. *J. Mater. Chem*., **15**, (2005), 2077-2088

Łapkowski, M. and Proń, A. *Synthetic Metals.* **110**. (2000). 79–83

Lock, J. P., Im, S. G., Gleason, K. K. *Macromolecules*, **39,** (2006). 5326-5329.

Martin, D.C; Wu, J; Shaw, C.M; King, Z; Spannigga, S.A; Rcihardson-Bruns, S; Hendricks, J and Yang, J; *Polymer Reviews,* **50**, (2010), 340–384.

Moulder, J.F.; Stickle, W.R.; Sobol, P.E.;K.D. Bomben, K.D. *Handbook of X-ray photoelectron spectroscopy: A reference book of standard spectra for identification and interpretation of XPS data*. Physical Electronics: Eden Prairie, MN, (1992).

Nguyen, T P., Rendu, P., Long, P D., De Vos, S A. *Surface and coatings technology*, **180-181**, (2004), 646-649

Pei, Q., Zucarello, G., Ahlskog M., and Inganas, O. *Polymer*, **35**, (1994), 1347.

Pilgram, K., Zupan, M. and Skiles, R. *Journal of Heterocyclic Chemistry*, **7**, (1970), 629-633

Turbiez, M., Frère, P. and Roncali, J. *J. Org. Chem.*, **68**, (2003**)**, 5357–5360

Tran-Van, F ., Garreau, S., Louarn, G., Froyer G. and Chevrot; C. *J. Mater. Chem*., **11**, (2001), 1378-1382

Spanninga, S.A. Ph.D dissertation. The Univeristy of Michigan, (2010)

Williams, D. B., & Carter, C. B. *Transmission Electron Microscopy: A Textbook For Materials Science.* New York: Plenum Press. (1996).

Winther-Jensen, B., Forsyth, M., West, K., Andreasen, W J., Bayley, P., Pas, S., Mackfarlane, D R. *Polymer*, **49**, (2008), 481-487

Yang, J., Martin, D C; *Sensors and Actuators A: physical*, **113**, (2004), 204-211

Chapter V

Bicontinuous Conducting Polymer Cubic Phases

ABSTRACT

This paper describes the synthesis and characterization of poly(3,4-ethylene dioxythiophene) (PEDOT) bicontinuous cubic phases created using non-ionic surfactant templating techniques. 3,4-ethylene dioxythiophene (EDOT) monomer was polymerized in lyotropic bicontinuous cubic phases consisting of poly(oxyethylene)$_9$ nonyl phenol ether (NP-9), octane and aqueous solution. Chemical polymerization of EDOT in the NP-9 cubic phase was accomplished with $AgNO_3$ at an oxidant:monomer molar ratio of 4:1. The samples were characterized using Polarized Optical Microscopy (POM), Small Angle X-ray Scattering (SAXS) and UV-vis spectrophotometry. Both POM and SAXS show that a ternary mixture of NP-9, octane and water forms a bicontinuous cubic phase structure at a concentration of 55:23:22 wt% of surfactant:octane:water. Our data also show that up to 10 wt% EDOT monomer can be introduced into the octane without disrupting the cubic phase. SAXS and OM data from doped samples show that the addition of $AgNO_3$ ($AgNO_3$:EDOT= 4:1) did not cause disruption to the cubic phase structure. UV-vis spectrophotometry and Fourier-transform infrared spectroscopy (FTIR) confirmed the presence of PEDOT in the polymerized sample. Electrochemical impedance spectroscopy (EIS) and Cyclic Voltammetry (CV) of surfactant-ordered films show characteristic electrochemical properties typical of PEDOT films. The porous structure of the polymerized cubic phase PEDOT was observed by transmission electron microscopy (TEM).

INTRODUCTION

There is considerable interest in the use of conducting polymers in a variety of applications such as mechanical actuators and drug delivery systems (Cosnier, 1999; Pernaut & Reynolds, 2000). In particular, they are used as electrode coatings for microelectronic sensors intended for long-term implantation into biological tissues (Xiao, et al., 2003). When implanted in tissue, they are critical in improving the functionality of the biomedical device. These polymers are important in lowering electrode impedance, increasing device sensitivity, and enhancing contact between the device and the surrounding tissue (Xiao, et al., 2003).

Relative to many other polyheterocycles such as polypyrroles or unsubstituted polythiophenes, PEDOT shows improved conductivity and chemical stability (Cosnier, 1999). PEDOT can be oxidatively polymerized either chemically or electrochemically to form soft, low impedance and biologically active films (Xiao, et al., 2003; Yang, et al., 2004). It has been shown that the electrical impedance can be minimized by maximizing the effective surface area of the PEDOT coating (Xiao, et al., 2003). Optimizing the applications of PEDOT in chemical sensors, electrochromic displays and drug carriers also requires the polymer film to have small pore sizes (Pernaut & Reynolds, 2000).

Our group has described several methods to minimize impedance by maximizing the effective surface area (decreasing the pore size) of PEDOT deposited onto microfabricated electrodes. For example, the formation of "nanomushrooms" was achieved by using etched block copolymer thin films as templates (Yang, Xiao & Martin, 2003). We have created "nanofibrils" using certain macromolecular counterions such as poly(acrylic acid) (Yang, Lipkin & Martin, 2007). We have also used polystyrene latex spheres (from 89-490 nm in diameter) to create "nanoporous" films with well-defined hole sizes (Yang & Martin, 2004a; Yang & Martin, 2004b). It is difficult to precisely control the distribution of polymer latex spheres at dimensions less than 100 nm, leading to variations in structure and poorly ordered materials (Yang & Martin, 2004a). This disorder makes it more difficult to establish facile transport from pore to pore, leading to an increase in impedance for the smallest sizes. Thus, it is important to have well

defined, monodisperse holes to obtain the best transport properties.

Certain non-ionic surfactants are able to form bicontinuous mesophases in binary or ternary mixtures with extremely small pore sizes, typically about 4 nm (Qiu & Caffrey, 2000). Surfactants have been used in mesophase-based templating to synthesize inorganic nanoparticles, *e.g.* thin films of bicontinuous cubic mesostructured silica (Hayward, Alberius, Kramer & Chmelka, 2004). Bicontinuous cubic phases are of particular interest as they divide three-dimensional space into two continuous, interconnected domains (Schwarz & Gompper, 1999).

There has been some limited success in the polymerization of other conducting polymers using mesophase-based surfactant templates. For example, Khiew *et al.* have successfully polymerized conducting polyaniline (PANI) in lyotropic bicontinuous cubic phases using the surfactant poly(oxyethylene)$_{10}$ nonyl phenol ether (NP10) (Khiew, Radiman, Huang, Kan & Ahmad, 2004). X-ray diffraction data of the ternary mixture cubic phase exhibited peaks at nearly identical scattering angles as the data for the monomer in the cubic phase, as well as data taken from the resulting surfactant/polymer system after polymerization. Their results were consistent with the direct templating of polyaniline in the cubic lyotropic mesophase (Khiew, Radiman, Huang, Kan & Ahmad, 2004). Hulvat *et al.* have reported directly templating PEDOT from a lyotropic hexagonal phase, in which EDOT monomer was polymerized in a non-ionic surfactant system (Hulvat & Stupp, 2003). They found that the hexagonal LC phase was templated onto the resulting PEDOT polymer but no discussion was made of the formation or polymerization of PEDOT within bicontinuous phases SEM images of these materials showed nanoscale diameter filaments that were somewhat larger than those in the original hexagonal liquid crystal; the individual cylinders formed during the template polymerization had apparently collapsed together into bundles after the surfactant was removed (Hulvat and Stupp, 2003).

In order to make templated conducting polymer coatings on neural prosthetic devices, our group has electrochemically fabricated ordered PEDOT using self-assembled

non-ionic surfactants as a template. Scanning electron microscopy showed that the surfactant-templated PEDOT films formed characteristic defect structures consistent with polymerization within a locally anisotropic mesophase. Transmission electron microscopy images confirmed the local orientation of the templated PEDOT films into textured domains; samples showed circular cracks that highlighted the local anisotropy of the PEDOT films (Yang & Martin, 2004a; Yang & Martin, 2004b). The typical size of the texturing (50-150 nm) was significantly larger than the individual channels in the surfactant mesophase (3-10 nm), again indicating the tendency of the polymerized fibrils to cluster together after surfactant removal, as was seen by Hulvat et al (Yang & Martin, 2004a; Yang & Martin, 2004b; Hulvat & Stupp, 2003).

This paper describes the successful polymerization of PEDOT in bicontinuous cubic phases using surfactant templating. We polymerized EDOT monomer in a lyotropic cubic phase system created from poly(oxyethylene)$_9$ nonyl phenol ether (NP-9), octane and aqueous solution. NP-9 was chosen as the surfactant for our experiments because of its relatively large lattice parameter as well as its ability to form stable ternary mixtures over a relatively large range of composition and temperature, in principle allowing the polymerization of PEDOT.

Surfactant-templated bicontinuous cubic PEDOT may be important for a wide variety of applications. It will be a novel route for making controlled nanoporous materials with monodisperse, interconnected pore spaces. Such materials are expected to be useful for catalysis, chemical sensors, electrochromic display, actuators, drug carriers and filters. Another possible use for such materials with interconnected pores that could be tailored to promote ionic transport would be as electrodes in batteries or fuel cells where both electronic and ionic transport are desired (Winther-Jensen, Winther-Jensen, Forsyth & MacFarlane, 2008). Furthermore, the interconnected pores in bicontinuous cubic phase PEDOT can also presumably be loaded with pharmacologically active agents; applying an external bias manipulates the charge on the conducting polymer phase and therefore controls the release of the pharmacologically active agents (Abidian, Kim & Martin, 2006).

In this study, we incorporated EDOT monomer into bicontinuous cubic mesophases by dissolving the monomer in the aqueous phase. We were able to load up to 10 wt% monomers into the oil phase as discussed in the next chapter which translated into better mechanical stability. As conjugated conductive polymer, PEDOT is a lot more chemically and thermally stable than Polyaniline. PEDOT is not known to be soluble in any of the solvents which makes the resulted PEDOT cubic structure more stable. The resulting microstructure was characterized by Polarized Optical Microscopy (POM) and Small Angle X-Ray Scattering (SAXS). UV-vis spectrophotometry and Fourier-transform infrared spectroscopy (FTIR) were also conducted to determine the presence of PEDOT polymer in the resulting cubic phase.

RESULTS AND DISCUSSION

Characterization of surface structures of ordered PEDOT films

Optical characterization of the structures of ordered PEDOT films showed that surfactant NP-9 exhibits different phases at different compositions of surfactant-water mixtures, including a cubic phase. These phases were readily identified by their textures and characteristic defects.

Figure 5.1 shows the diffusion couple, with the deionized water dropped onto the left part of the glass slide, and NP-9 surfactant dropped on the right region. We observed the transition in physical morphology of the lyotropic crystalline NP-9, from micellar (<30 wt-% NP-9) to hexagonal (32-57wt-%) to cubic (57-65 wt-%) and lamellar (65-77 wt-%) phases as shown in Fig 1a from left to right, with increasing surfactant concentrations. The cubic phases were observed as thin non-birefringent bands between the hexagonal and lamellar phases, which appeared dark under POM. In the cubic phase templated PEDOT we prepared, we selected the nominal concentration of surfactant to octane hydrocarbon to water as 55:23:22 wt%, which corresponds to the center of the region of cubic phase stability.

The key to the concept of "direct-templating" is the formation and retention of the

cubic mesophase throughout the PEDOT polymerization reaction. In our experiments, the problem of phase separation was frequently encountered when EDOT monomers were added into the surfactant system and during the polymerization reactions within the lyotropic mesophase. Therefore, repeated POM and SAXS characterizations were performed on the samples before the addition of EDOT monomer, immediately after the addition of EDOT monomer, and after polymerization of EDOT into PEDOT under UV-initiated polymerization. Structure characterizations were also performed after addition of chemical agent such as $AgNO_3$, after UV-initiated polymerization.

In Figure 5.3, we present the SAXS profiles for the cubic samples only as a representative liquid crystalline phase of the NP-9 surfactant for stability/instability against the templated nano-polymers. In the diffraction plots, the scattering vector $q = \frac{4\pi \sin(\theta)}{\lambda}$ is plotted against intensity. In diffraction experiments, the Bragg peaks of cubic structures are observed at:

$$d_{(hkl)} = \frac{a}{\sqrt{(h^2+k^2+l^2)}} \qquad (1)$$

where $d_{(hkl)}$ is the Bragg spacing, a is the unit cell size (lattice constant) and h, k, and l are the Miller indices. The Miller indices depend on the lattice type and the symmetry of the cubic structure. The above Eq. 1 for a cubic lattice can be combined with the Bragg's diffraction equation:

$$2d_{(hkl)} \sin(\theta) = n\lambda \qquad (2)$$

where theta is the angle of scattering, n is the order of diffraction and Lambda is the wavelength of the X-radiation source. This yields the relation:

$$\sin(\theta) = \frac{\lambda^2}{4a^2(h^2+k^2+l^2)} \qquad (3)$$

Eq. 3 above is used for indexing the observed reflections in our scattering pattern. From

SAXS measurements of undoped, EDOT and monomer doped, as well as polymerized cubic phase samples, Khiew et al. reported the successful polymerization of polyaniline (PANI) in NP-10 cubic phase (Khiew, Radiman, Huang, Kan & Ahmad, 2004). The main peak positions (q values) observed by Khiew et. al. approximately matches the ratio of $\sqrt{16}, \sqrt{24}, \sqrt{32}, \sqrt{38}, \sqrt{50}, \sqrt{60},$ which corresponds closely with the peak positions obtained from a theoretical cubic structure model constructed by Garstecki et al. The spacings would coincide with the following indexing (4 0 0), (4 2 2), (4 4 0), (5 3 2), (5 4 3) and (7 4 3). (Garstecki & Holyst, 2001) By matching their SAXS measurements to simulation results, Khiew et al. determined that they had polymerized PANI in the *Ia*3*d* (cubic Gyroid GX2) space group symmetry (Khiew, Radiman, Huang, Kan & Ahmad, 2004).

Fig. 5.3 below shows SAXS experimental data of cubic phase prepared with NP-9, octane and water, doped with 0.01 M EDOT. Based on our data, we have a simple gyroid strucure. As the data showed, there were two well defined peaks at 0.081 and 0.094 $Å^{-1}$ in Fig 5.3, indexed as (2 1 1) and (2 2 0), matching the Sqrt(8) and Sqrt (6). We did not find the smaller peaks corresponding to GX2 structure found by Khiew et al (Khiew, Radiman, Huang, Kan & Ahmad, 2004).

POM characterizations of 0.01 M EDOT monomer doped NP-9 cubic phase samples indicate that isotropic cubic phase was retained. The SAXS peaks after loading $AgNO_3$ and polymerization shifted right to 0.11 and 0.134 and two more peaks at 0.155 and 0.192 showed up. These peak ratios are consistent with the ratio of Sqrt(16), Sqrt(24), Sqrt(32) and Sqrt(50) corresponding to indexing (400), (422), (440) and (532) which indicates a Ia3d GX2 gyroid structure formed as indexed by Garstecki et al (Garstecki & Holyst, 2001). Thus, addition of UV-initiated polymerization reagent $AgNO_3$ in the aqueous phase according to the same weight ratio as undoped samples produced another form of gyroid structure. The lattice parameter calculated using simple gyroid indexing of the sample before polymerization was 22.0 nm , while after polymerization the lattice parameter calculated using Ia3d GX2 structure was 22.8 nm.

Our choice of $AgNO_3$ as initiator was based on the fact that it caused the least amount of disruption to the cubic phase after it is added into the mixture, compared to other initiators we investigated such as $FeCl_3$. $AgNO_3$ dissolved readily in the aqueous phase and initiated the polymerization of EDOT monomer into PEDOT chains when it is reduced from silver ions to silver metal under the activation by UV radiation. More importantly, $AgNO_3$ dissolved less exothermically in water than $FeCl_3$, helping to insure that the surfactant cubic phase would not be disrupted before EDOT polymerization is initiated, since cubic phases are known to be stable only over a relatively narrow temperature range. Our previous experimental results showed that the highly exothermic solvation reaction of Fe^{3+} ions in aqueous solutions tended to disrupt cubic phase formation.

EDOT polymerized into PEDOT within 24 hours following the UV irradiation that activated the $AgNO_3$ initiator. We visually observed that vials of freshly-prepared cubic phase samples (Fig. 5.6a) were initially colorless, stiff and optically isotropic solid-like substances. The samples changed dramatically in appearance from colorless and optically isotropic to brown (Fig. 5.6b) after 24 hours of polymerization in UV. Within 2 days of polymerization under UV light, the samples in glass vials turned dark brown completely, indicative of the presence of polymerized PEDOT. Control experiments with $AgNO_3$ alone (with no EDOT) showed only a slight amount of darkening, much less than with the EDOT monomer.

SAXS studies showed that the lattice parameter of cubic phase surfactant was not significantly changed after adding $AgNO_3$. The cubic mesophase was not disrupted when EDOT polymerized into PEDOT in 24 hours after UV irradiation is initiated. Slight broadening of the rings was observed, evidently due to the mechanical instability of the resulting PEDOT structure. Fig.5.7 showed that templated PEDOT in cubic phase samples produced a diffraction pattern similar to that obtained from undoped and EDOT-doped NP-9 cubic phases (Fig. 5.5b) after polymerization. The peaks after polymerization shifted right but their q value ratio matched Ia3d GX2 gyroid structure as

found by Khiew et al (Khiew, Radiman, Huang, Kan & Ahmad, 2004). However in some cases, perhaps due to the changes in phase equilibrium as water and organic solvent were lost, the cubic phase structure was disrupted when polymerization was conducted for more than 48 hours (extra peak showed in Figure 5.7). The disruption of the cubic phase structure is observed in Fig.5. 7 as shifting and broadening of the diffraction peaks.

Linear macromolecules synthesized in porous, branched networks, such as PEDOT in these bicontinuous cubic phases, were expected to have chains ending near the strut junctions. (Figure 5.8) The structure can easily collapse during polymerization due to weak mechanical strength.

The chemical composition of the PEDOT polymer film was determined using reflective microfocused FTIR. Fig 5.9 shows the FTIR spectrum of films of PEDOT. The peaks near 830 and 930 cm^{-1} correspond to the vibrations of S-C bonds in polymerized PEDOT chains. The peaks at 1100 and 1160 cm^{-1} are due to the stretching of the C-O-C bonds stretching in the ethylene dioxy group. The peak absorptions at 1250, 1350, 1450 and 1500 cm^{-1} can be attributed to the stretching of the thiophene ring. In the region above 2000 cm^{-1}, the electronic absorption from free charge carriers created from polymerization reaction are seen. The results confirmed the existence of PEDOT, which was in agreement with previous studies (Kvarnstrom, et al., 1999).

UV-Vis Spectra is shown in Fig. 5.10. There is a broad peak at 700 to 800 nm range. Neutral PEDOT has absorptions around 570 nm which is associated with the π-π^* transition of neutral PEDOT (Winther-Jensen & West, 2006). For oxidized PEDOT when conjugation length decreases which indicates the electronic delocalization decreases, the absorption can be around 700 nm (Tran-Van, Garreau, Louarn, Froyer & Chevrot, 2001) to 900 nm which is attributed to bipolaron formation. (Winther-Jensen & West, 2006). $AgNO_3$ absorption spectra showed that there were no peaks in the above 350 nm range.

Electrical properties of ordered PEDOT films

Using EIS (Fig. 5.11), we found that there was as much as two order decrease in the impedance of the cubic-templated PEDOT films as a function of frequency before and after polymerization.

CV was used to test the charge delivery capacity of the surfactant-templated ordered PEDOT films. Fig. 5.12 is a typical CV spectrum of surfactant-templated ordered PEDOT films that showed the intrinsic redox reaction of the films as the potential was swept in a cyclic manner. The switching ability of ordered PEDOT was demonstrated by the graphs. During each cycle, the coated film undergoes oxidation and reduction with corresponding movement of ions into and out of the film. Also, the PEDOT film changed color from light grey to dark grey, which supported the fact that the porous bicontinuous structure made the color change process easier. We noted that a film prepared with only $AgNO_3$ and the solvent in cubic phase without any PEDOT did not show the same color change, therefore eliminating the possibility that color change was attributed to the $AgNO_3$.

TEM of ordered PEDOT films

Low voltage electron microscopy (LVEM) was used to image the unstained PEDOT cubic phases after surfactant was removed (Figure 5.13). The low voltage electron source (5 kV) provided higher contrast to even unstained organic samples. PEDOT cubic phases collapsed into pieces of film with size around tens of nm. Regular pores were found on the collapsed PEDOT cubic phase film with sizes around 3 to 5 nm.

CONCLUSIONS

NP-9 was chosen as the surfactant for our experiments because of its large lattice parameter—indicator of a large pore size—as well as its ability to form ternary mixtures, in principle allowing the polymerization of PEDOT in either the polar or nonpolar phase.

Ordered surfactant templated conducting polymer PEDOT using NP9 was formed via chemical oxidation of EDOT monomer in the lyotropic cubic phase system which consisted of poly(oxyethylene)$_9$ nonyl phenol ether (NP-9), octane and de-ionized water.

We incorporated EDOT monomer into the bicontinuous cubic mesophases by dissolving the monomer in octane and used $AgNO_3$ as the initiator for PEDOT polymerization. The resulting microstructure was characterized by POM and SAXS, and showed that Ia3d cubic phase was obtained although it transited from simple Ia3d gyroid structure to a complex GX2 Ia3d gyroid structure. UV-vis spectrophotometry and FTIR confirmed the presence of PEDOT in the polymerized sample. EIS and CV of surfactant-ordered films showed characteristic electrochemical properties typical of PEDOT films. The collapsed structure of the polymerized cubic phase PEDOT with regular pores was observed in LVEM.

EXPERIMENTAL

Materials

Reagent grade octane (98%) and the non-ionic surfactant poly(oxyethylene)$_9$ nonyl phenol ether (NP10), also known as Tergitol® (NP-9) were purchased from Sigma Aldrich Co. 3,4-ethylenedioxylthiophene (EDOT, >97%) monomer was purchased from H. C. Starck. The oxidative initiator, silver nitrate ($AgNO_3$, reagent, 99+ %), was purchased from Sigma Aldrich Co. The long wave ultraviolet (365 nm) light source used to initiate PEDOT polymerization was a Spectroline model EN-140L purchased from Spectronics Corporation. 1.5 mm diameter XRD glass capillaries were purchased from the Charles Supper Co. The sealed end of the glass capillaries were cut with a pair of scissors before the capillaries were used to contain samples for characterization. J-B WELD Cold Weld with Steel & Hardener (epoxy seal) was mixed in 1:1 ratio before it was applied to seal both ends of XRD capillaries. All samples were prepared by weight in 10 ml glass vials.

Chemical polymerization

1. Diffusion couples

To find the optimal compositions to make cubic phases, diffusion couples was made. A drop of isotropic NP-9 was added adjacent to a drop of water on a glass slide. The sample was then covered with cover slip to prevent water evaporation. Diffusion between the two phases led to the formation of a series of phases as a function of time. The microstructure of the sample was studied under OM.

2. Undoped NP-9 cubic phase samples

Samples were prepared by combining octane, water and NP-9 surfactant in appropriate proportions (determined from the diffusion couple experiments) to produce bicontinuous cubic phases (Cosnier, 1999). Typically 2.0 g of NP-9 surfactant was weighed out and added into a glass vial. The amount of octane and water needed to obtain a final mixture composed of 55 wt-% NP-9, 22 wt-% octane and 23 wt-% DI-water was calculated. Specifically, to the NP-9 surfactant, the calculated amount of octane was added and the mixture vortexed for 1 minute at medium speed. Then the calculated amount of water was added, and vortexed for another 5 minutes.

The cut ends of the XRD capillaries were gently inserted into the sample vial and sample was pushed into capillaries by repeatedly inserting/withdrawing the capillaries. The two cut ends of the capillary were sealed with epoxy. The capillary samples were left for 24 hours to allow the epoxy seals to cure, and for bicontinuous cubic phase to form. A stiff, colorless and optically isotropic solid was formed after 24 hours.

3. NP-9 cubic phase samples doped with EDOT monomer and $AgNO_3$ initiator

The appropriate volume of EDOT monomer was added to deionized water and then stirred for 24 hours to prepare a 0.01M EDOT monomer solution. 1.0 g of the EDOT solution was placed into a clean glass vial and then a measured amount of $AgNO_3$ was dissolved in the EDOT solution to form a 0.04 M $AgNO_3$ doped EDOT solution.

The NP-9, octane and $AgNO_3$ doped EDOT solution were determined and mixed in the same procedure as that for preparing the undoped NP-9 cubic phase samples. The XRD capillaries were also filled in the same manner as the aforementioned procedure.

The capillary samples were shielded from any light source with aluminum foil to prevent PEDOT polymerization from the ambient light and left for 24 hours so that bicontinuous cubic phases would form. A stiff, colorless and optically isotropic solid was observed after 24 hours.

4. NP-9 cubic phase samples with PEDOT polymer

The capillary samples containing NP-9 cubic phase samples doped with 0.01 M EDOT monomer and 0.04 M $AgNO_3$ initiator were exposed to UV light for 24 hours to allow PEDOT polymerization. Under optical examination, the samples appeared stiff, dark brown in color and optically isotropic.

Morphological Characterization

1. Optical Microscopy (OM) and Polarized Optical Microscopy (POM)

Transmission OM and POM were conducted on a Nikon Optiphot POL-2. Images were captured with a Spot RT digital camera. The same capillary samples were used for SAXS characterization.

2. Small Angle X-Ray Scattering (SAXS)

Samples in capillaries were characterized with a Bruker NanoSTAR U X-ray diffractometer system operated at 40 kV and 35 mA. Pressure in the X-ray chamber was maintained in the range of 0.1–1 mbar by opening and closing the air valve. This was done to minimize the risk of rupturing the capillary samples due to the pressure difference between the interior of the capillary and the sample chamber. The Bruker SAXS software was used to analyze diffraction patterns.

3. Transmission Electron Microscopy (TEM)

The PEDOT cubic phase was dissolved in excess amount of ethanol. After the surfactant was removed, PEDOT cubic phase in ethanol suspension was sonicated for 10 minutes and then deposited onto a self-made thin carbon film. The sample was studied by a Delong low voltage electron microscope (LVEM5) with a 5 kV field emission gun.

*4. Fourier transformed infrared (*FT-IR*) spectrophotometer*

A drop of cubic phase PEDOT after the surfactant was removed was deposited on a glass slide. The sample was then studied by a Jasco FT/IR 4100.

5. UV-Vis Spectrophotometry

Cubic phase PEDOT ethanol suspension solution after surfactant was removed was studied by a UV/Vis spectrometer Cary UV50.

Electrical Properties Analysis

1. Electrochemical impedance spectroscopy (EIS)

EIS was performed using an Echochemie Autolab Potentiostat/Galvanostat and the Frequency Response Analyzer (FRA) software. The samples were tested after polymerization before removing the surfactants. Samples were put into a lab made electrodes and covered with a cap.The impedance spectra was recorded at 36 discrete frequencies over a frequency range from 1 Hz to 1 Mhz. The input sine wave had an amplitude of 5 mV; the frequencies utilized were distributed uniformly on log scale.

2. Cyclic Voltammetry (CV)

CV was conducted using an Echochemie Autolab Potentiostat/Galvanostat. The General Purpose Electrochemical System (GPES) software was used for CV. The start and first vertex potentials were -0.6 V and 0.8 V respectively; the scan rate was 1 mV/s.

Figures and Tables

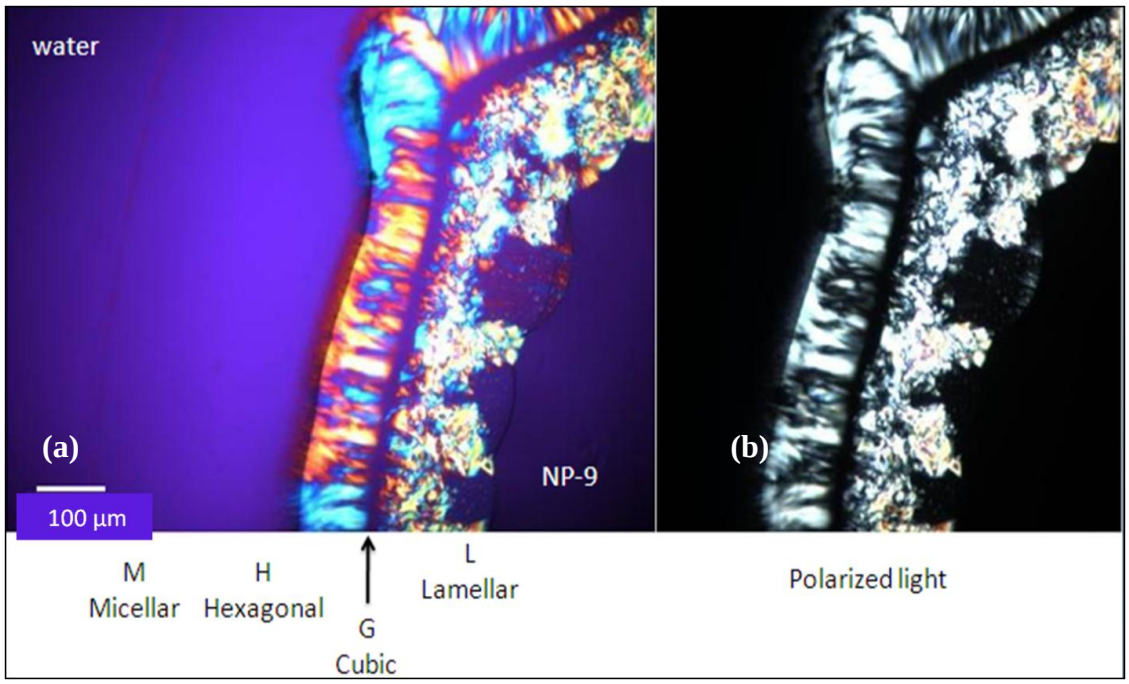

Figure 5.1. Optical micrograph (Fig. 1a) and cross polarized micrograph (Fig 1b) showing diffusion couple of surfactant NP-9 (left portion) in water (right portion on slide).

.

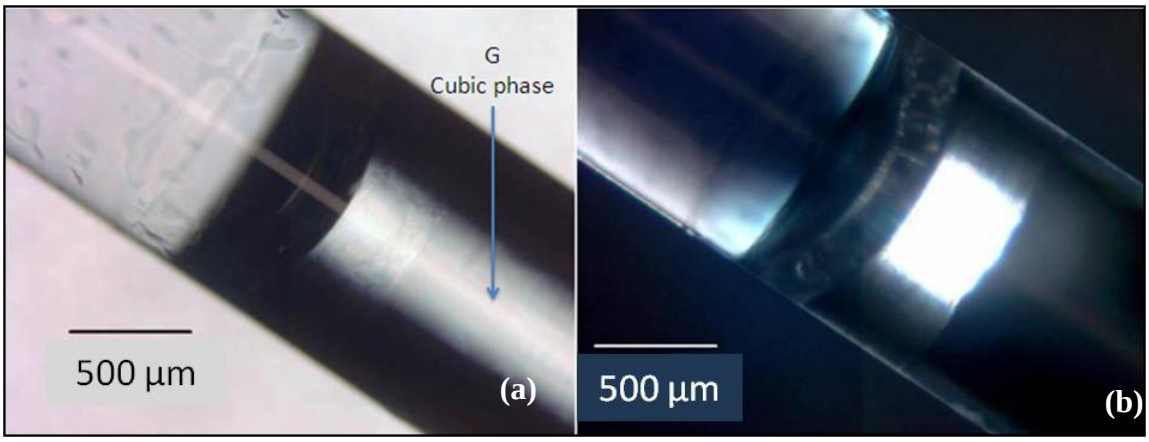

Figure 5.2. OM (Fig 5.2a) and POM (Fig 2b) of pure NP-9 cubic phase samples in 1.0mm glass capillaries. POM (Fig. 5.2b) shows non-birefringent dark bands (right) which are characteristic of surfactant cubic phase. The cubic phases appear optically isotropic and as a solid-like, stiff substance under OM.

.

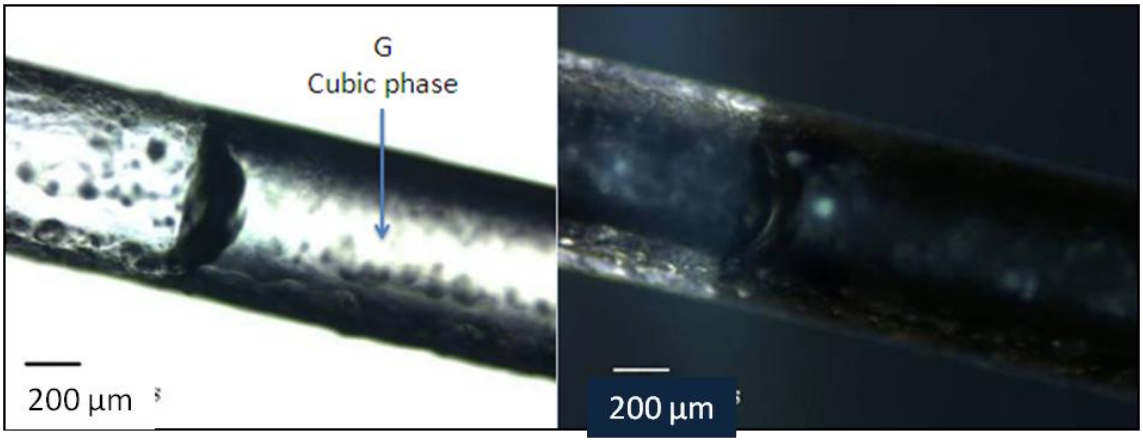

Figure 5.3. OM (Fig. 5.3a) and POM (Fig. 5.3b) of 0.01M EDOT doped NP-9 cubic phase samples in 1.0mm glass capillaries show non-birefringent, dark bands under polarized light, which indicate cubic phase retention after EDOT monomer was added.

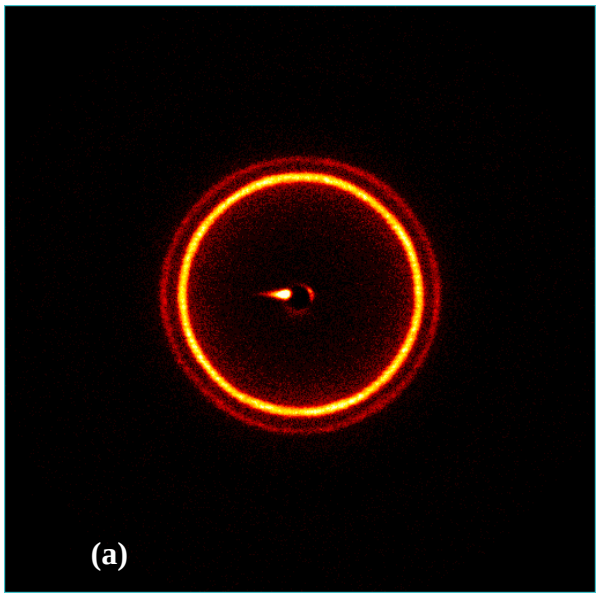

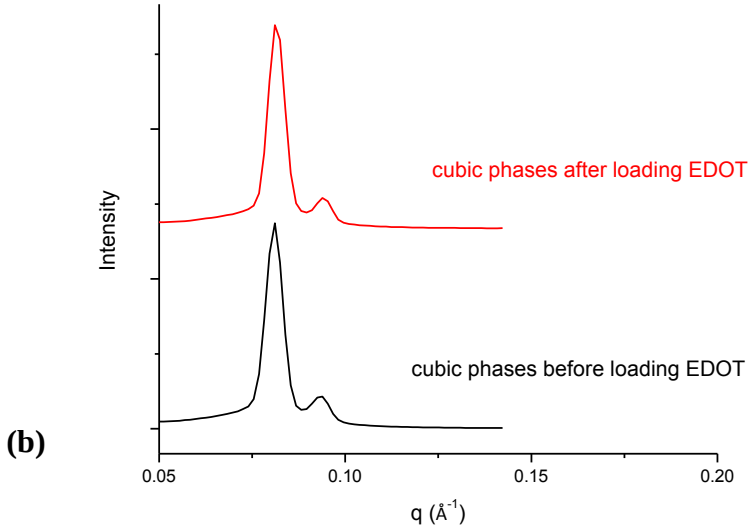

Figure 5.4. SAXS data of .01M EDOT monomer doped NP-9 (Fig. 5.4a) cubic phase samples. There is no significant change in structure of surfactant NP-9 incorporation of EDOT in the lyotropic cubic mesophase(Fig. 5.4b) . Table I displays the q values and corresponding D spacing of the peaks in Fig 5.4(b). Fig. 5.4(b) shows that strongest SAXS peaks correspond to (211), (220) reflections in Ia3d symmetry (G-surface, a=22 nm) in EDOT doped cubic phases (red line), similar to result from undoped cubic phase (black line).

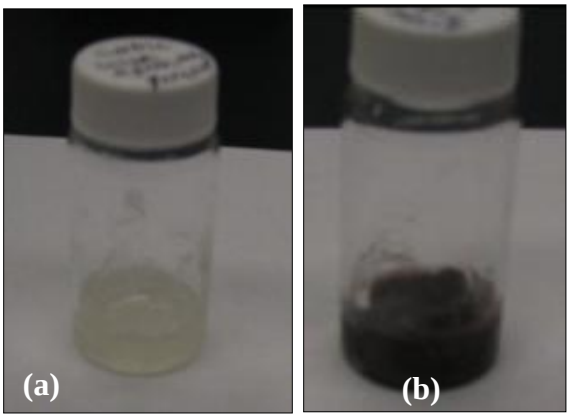

Figure 5.5. Color change in 0.01M EDOT doped NP-9 cubic phases containing AgNO3 initiator, from initially colorless and optically isotropic (Fig. 5.5a) to dark brown (Fig. 5.5b) after 24 hours UV-initiated polymerization.

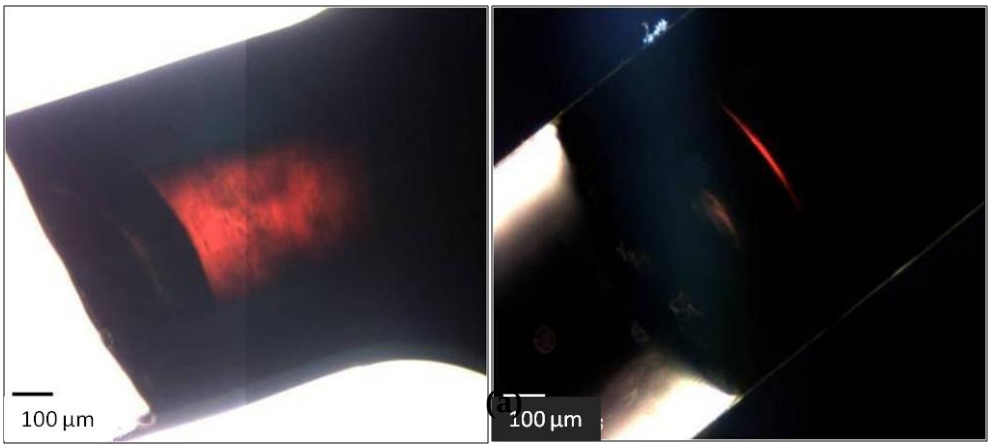

Figure 5.6. OM (Fig. 5.6a) and POM (Fig.5. 6b) of NP-9 cubic phase samples doped with 0.01M EDOT and AgNO3 initiator, after 24 hours UV activated polymerization. Dark bands in POM indicate the presence of cubic phase PEDOT.

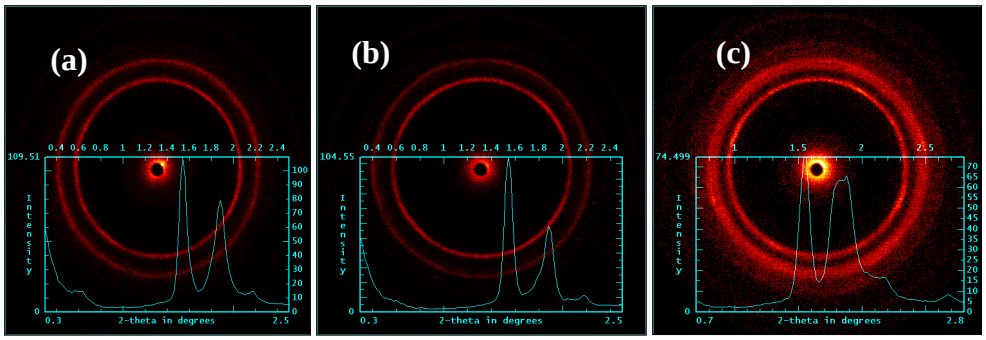

After loading AgNO3 1 day polymerization 2 day polymerization

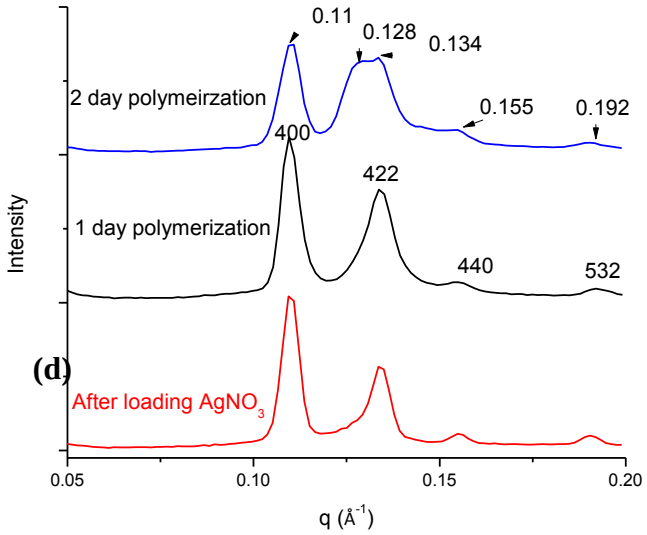

Figure 5.7. SAXS scattering images and plots of NP-9 cubic phase samples doped with 0.01M EDOT and AgNO3 initiator (bottom line) , after 24 hours UV activated polymerization (middle line) and after 48 hours polymerization (top line). (Top: 2-D pattern, Bottom: 1-D plot)

Before polymerization	2-Theta (degrees)	Q value ($Å^{-1}$)	Calculated a (nm) simple gyroid
	1.14	0.081	22.0
	1.32	0.094	
After polymerization	1.56	0.11	Calculated a (nm) GX2
	1.81	0.134	22.8
	2.18	0.155	
	2.70	0.192	

Table 5.1: Lattice parameters of EDOT cubic phases before and after polymerization

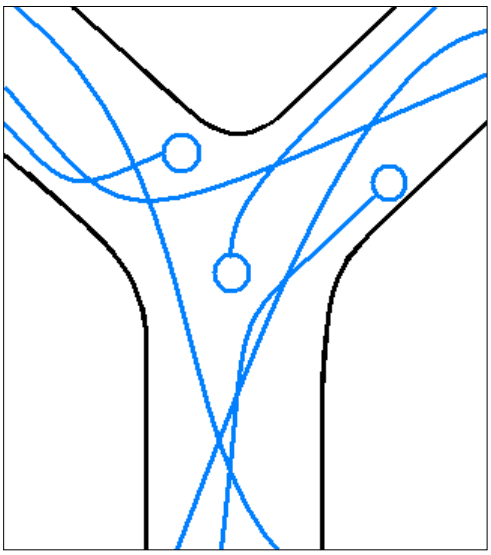

Figure 5.8. Proposed effect of PEDOT cubic structure collapse. (Linear PEDOT macromolecules synthesized in the channels are expected to have chains ending near strut junctions. Note: white circles represent chain ends, black circles are crosslinks.)

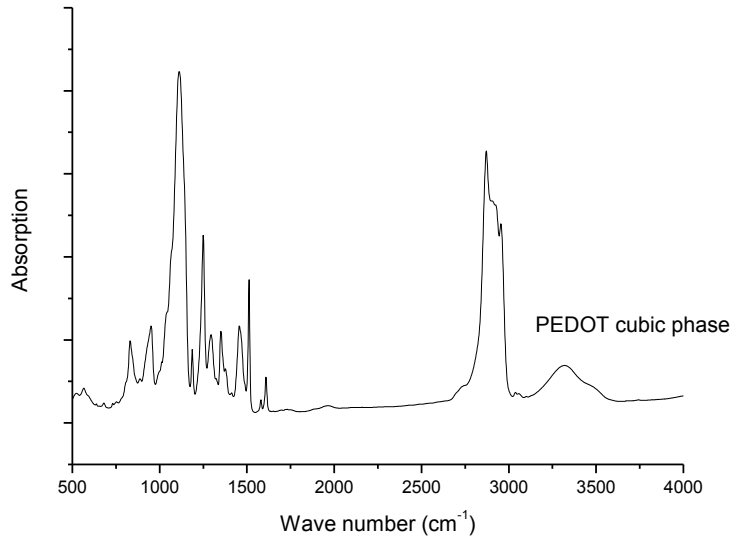

Figure 5.9. FTIR spectrum shows bands that are characteristic of PEDOT films.

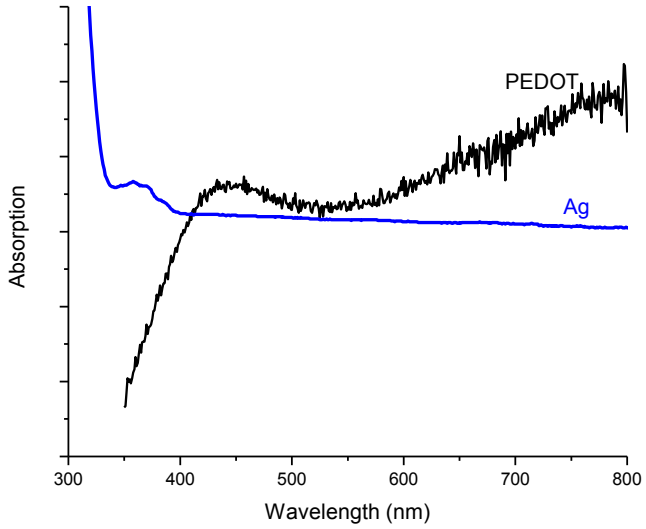

Figure 5.10. UV-vis characterization graph of cubic phase PEDOT (black line) with UV-vis of AgNO3 solution for reference (blue line).

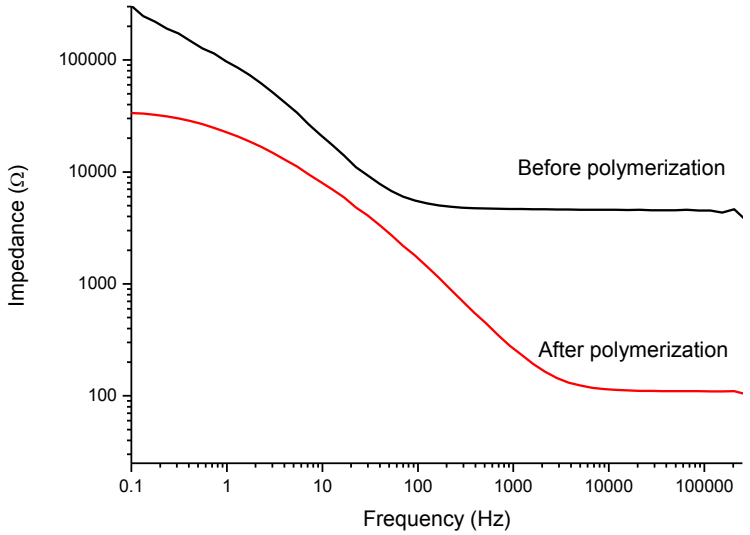

Figure 5.11. Impedance spectroscopy of surfactant-templated ordered PEDOT (red line) film and cubic phase before polymerization (black line) as a function of frequency.

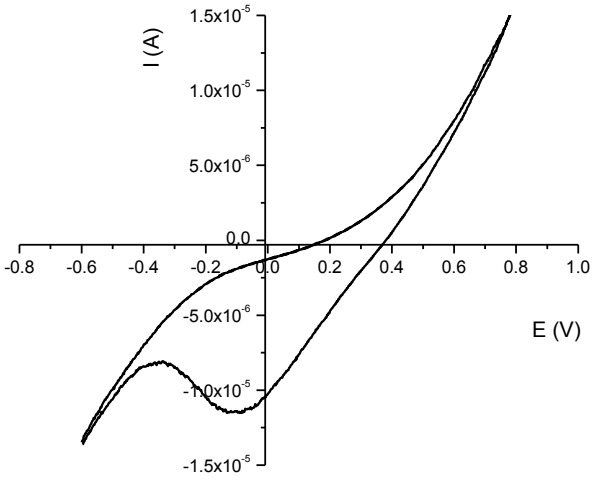

Figure 5.12. CV measurements of surfactant-templated ordered PEDOT films.

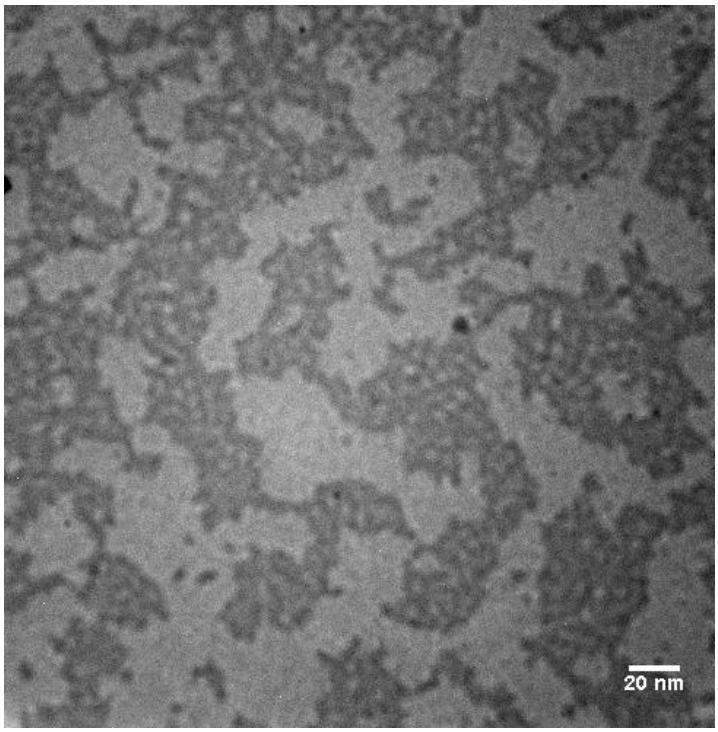

Figure 5.13. LVEM micrographs of PEDOT cubic phases after surfactant removal

.

REFERENCES

Abidian, M.R., Kim, D.H. and Martin, D.C. *A*dvanced Materials, **18**, 4 (2006), 405-409

Cosnier S., *Biosensors and Bioelectronics*, **14,** (1999), 443-456

Garstecki, P. and Holyst, R. *J. Chem. Phys*. **115** (2001), 1095-1099

Groenendaal, L., Zotti, G., Aubert, P.H., Waybright, S.M. and Reynolds, J.R. A*dvanced Materials*, **15,** (2003), 855-879

Hayward, R.C., Alberius, P.C., Kramer, E.J. and Chmelka, B.F. *Langmuir*, **20**, (2004), 5998–6004

Hulvat J.F. and Stupp, S.I. *Angewandte Chemie-International Edition*, **42**, (2003), 778-781

Keszthelyi, T., Grage, M.L., Offersgaard, J.F., Wilbrandt, R., Svendsen, C.,Mortensen, O. S., Pedersen J. K. and Jensen, H. J. A. *J. Phys. Chem. A,* **104** (2000), 2808

Khiew, P.S., Radiman, S., Huang, N.M., Kan, C.S. and Ahmad, S. *Colloids and Surfaces A: Physicochemical and Engineering Aspects*, **247**, 1-3 (2004), 35-40

Kvarnstrom, C., Neugebauer, H., Blomquist, S., Ahonen, H.J., Kankare, J., Ivaska, A. and Sariciftci, N.S. *Synth. Met*. **101**, (1999), 66

Pernaut, J. M., Reynolds, J. R. *J. Phys. Chem. B*, **104**, (2000), 4080–4090

Qiu, H. and Caffrey, M. *Biomaterials*, **21**, (2000), 223-234

Schwarz, U. S. & Gompper, G. *Physical Review E*, **59**, (1999), 5528-5541.

Tran-Van, F., Garreau, S., Louarn, G., Froyer G. and Chevrot,C. *J. Mater. Chem.*, **11,** (2001), 1378-1382

Winther-Jensen, B. and West, K. *Reactive & Functional Polymers*, **66,** (2006), 479-483

Winther-Jensen, B., Winther-Jensen, O., Forsyth, M. and MacFarlane, D. R. *Scence*, **321**, (2008) page 671-674.

Xiao, Y., Cui, X. Hancock, J. M., Bouguettaya, M., Reynolds, J. R. and Martin, D. C. *Sensors and Actuators B: Chemical*, **99**, (2003), 437-443

Yang, J., Lipkin, K. and Martin, D.C. *Journal of Biomaterials Science—Polymer Edition*, **18**, (2007), 1075-1089

Yang, J., Kim, D.H., Hendricks, J.L., Leach, M., Northey, R. and Martin, D.C. *Acta Biomaterialia*, **1**, (2004), 125-136

Yang J. and Martin, D.C. *Sensors and actuators B: Chemical*, **101**, (2004a), 133-142

Yang J. and Martin, D.C. *Sensors and actuators A: Physical*, **113**, (2004b), 204-211

Yang, J., Xiao, Y. and D.C. Martin, D. C., paper presented at the Materials Research Society, Boston, MA, (2003)

Chapter VI

Thermally-induced electrical and microstructural changes in bicontinuous conducting polymer cubic phases

Abstract

We synthesized conducting polymers into bicontinuous cubic structures by template polymerization within an ordered surfactant mesophase (Chapter V). These templated polymers have nanoscale, interconnected, periodic porous microstructures. Transitions of these cubic phase structures can be induced by changing the temperature. The *in-situ* electrical properties of conductive polymer cubic structures have been characterized using impedance spectroscopy as a function of temperature, while structure was simultaneously monitored by Small angle X-ray scattering (SAXS) for the first time.

Introduction

Templating of conductive polymers into bicontinuous cubic phases that divide 3D space into discrete regions that are both continuous and mutually interconnected would provide many other advantages of bulk materials. The high surface area per unit volume or mass would have implications for such as the sensing capabilities of polymer sensors containing embedded enzymes. This ordered, nanoporous microstructure would significantly reduce the required diffusion distances of the analyte and decomposition products into and out of the film (Cassagneau & Caruso, 2002). The performance of drug-releasing polymer systems is also expected to be improved with such small, well-defined, and interconnected channels. Because of the small size of the struts, it is possible that these bioactive proteins could be readily adsorbed and released from the reticulated microstructure of the conducting polymer matrix (Kim, Richardson-Burns, Hendricks, Sequera & Martin, 2006). The small pore

sizes should also increase the loading capacity and release rates for drug delivery systems. The temporal performances of chemical sensors made from conducting polymers depend on diffusion of the analyte, and coupling to the conjugated backbone structure (Swager, 1998; Kim, McQuade, Rose, Zhu & Swager, 2001). A conductive bicontinuous polymer structure opens avenue to significantly reduce the required diffusion distances, and hence increase the response rate.

In electrochromic displays made from conducting polymers, the rate of counterion motion back and forth from the polymer to the surrounding electrolyte is a key limiting performance factor (Argun, Cirpan & Reynolds, 2003). The response of conducting polymer actuators is limited by diffusion of ions in and out of the polymer to effect the desired volumetric shape change (Baughman, 1996; Jager, Smela & Inganas, 2000; Smela, 2003).

The characteristic response time t is expected to scale as l^2/D, where D is a diffusion coefficient controlling the rate of ion exchange from the conducting polymer to the nanoscale ionic network, and l is a characteristic size of the film. Using an estimated value of $D=10^{-7}$ cm^2/s (Cui, Hetke, Wiler, Anderso n& Martin, 2001), gives t=0.1 second for a film with l=1 μm. However reducing the length scale of the material down to 10 nm gives t=10 μsec.

Conductive polymers have been widely used in organic electronics. There is considerable current interest in the use of electrically conducting polymers for a variety of sensors and actuators (Baughman, 1996; Schmidt, Shastri, Vacanti & Langer, 1997; Kuhn & Child,1998; Bar-Cohen, 2001). Nystöm et al,. have made ultrafast all-polymer paper-based batteries using polypyrrole-coated high surface area cellulose fibers of algal to achieve the highest reported charge capacities and charging rates for such batteries (Nystrøm, Razaq, Strømme, Nyholm & Milhranyan, 2009). Establishing a high-surface area boundary among the three active fuel cell layers: air, the eletrolye and the catalyst/conductor is a key requirement for making high performance fuel cells. PEDOT can be used as an O_2 reduction catalyst with enhanced life by coating it onto porous membranes in fuel cells due to its tolerance to CO poisoning (Winther-Jensen, Winther-Jensen, Forsyth & MacFarlane, 2008).

Poly（3，4-ethylene dioxythiophene）(PEDOT or PEDT) is a widely used π-conjugated conductive polymer of interest for several different applications including antistatic layers, electroluminescent devices, hole injection layers in different electronics like organic light emitting diodes and charge transfer layers on neural prosthetic devices. PEDOT reduces the impedance and improves mechanical compatibility (Nguyen, Rendu, Long & De Vos, 2004; Kirchmeyer & Reuter, 2005; Groenendaal, Jonas, Freitag, Pielartzik & Reynolds, 2000; Yang & Martin, 2004a),.

Hulvat and Stupp found that the hexagonal LC phase was templated onto the resulting PEDOT polymer after polymerization in a hexagonal liquid crystalline mesophase of the non-ionic surfactant poly(oxyethylene)$_n$-oleyl ether (n~10) commonly known as Brij 97 (Hulvat & Stupp, 2003; Hulvat & Stupp, 2004). They showed evidence for focal conic defects in the resulting films, although these are more typically associated with smectic phases. They showed SEM images of the nanometer-diameter filaments that had collapsed together into bundles after removal of the surfactant.

In our own laboratory we have been investigating the use of conducting polymers for improving the long-term performance of biomedical devices that are directly implanted into neural tissue (Cui, et al., 2001; Cui, Hetke, Wiler, Anderson & Martin, 2001; Cui & Martin, 2003; Cui, Wiler, Dzaman, Altschuler & Martin, 2003). It is important to create a structure that optimizes the biological interactions with the cells, and maintains facile charge transport. We have found that maximizing the effective surface of the electrode coating makes it possible to minimize the electrical impedance (Winther-Jensen, Winther-Jensen, Forsyth & MacFarlane, 2008).

Our group has developed a number of methods designed to significantly increase the effective surface area of conducting polymers deposited onto the microfabricated electrodes. For example, we have used etched block copolymer films as thin templates, leading to the formation of nanomushrooms (Yang, Xiao & Martin, 2003). We can also create nanofibrils using certain macromolecular counterions such as poly(acrylic acid) (Yang, Lipkin & Martin, 2007). We have used polystyrene spheres ranging from 89 to 490 nm in diameter to create nanoporous films with well-

defined holes (Yang & Martin, 2004a; Yang & Martin, 2004b). Electro-spun nanofibers and nanotubes for drug deliveries and bio-interfacing have been developed and studied (Abidian, Kim & Martin, 2006; Abidian & Martin, 2008; Abidian & Martin, 2009).

Our research in this study is novel in many key respects. By conducting the polymerization within an ordered surfactant phase using surfactant templating techniques, we are able to made bicontinuous structure with pore size an order smaller than that of block copolymers. We loaded these ordered phases with the electropolymerizable monomer EDOT up to 10 wt% while maintaining the bicontinuous cubic structure. The resulting PEDOT film has pores with sizes range from around 3 to 5 nanometers. The templated cubic structure PEDOT obtained in an even more elegant and precisely controlled fashion has provided some improvements in the polymer properties with even higher surface areas. For the first time, *insitu* electrical properties correlating to structures induced by temperature variation and simultaneously monitored by SAXS was recorded.

Results and Discussion

Bicontinuous mesophases with cubic symmetry exist in binary and ternary mixtures of certain surfactants, block copolymers and small molecules (Schwarz & Gompper, 1999). The phases formed in A-B diblock and A-B-C triblock copolymers have pore sizes typically 10-30 nm for block copolymers (Bates & Frederickson, 1999; Matsushita, 2007; Wohlgemuth, Yufa, Hoffman & Thomas, 2001). Although block copolymers like ethylene oxide - propylene oxide have been widely used commercially, they are of limited utility here because the cubic phases are usually only stable over a relatively narrow range of composition (~10 wt%) and temperatures (~6 ℃) (Fairhurst & Holmes, 1997; Funari & Rapp, 1997). Mesophases formed in binary and ternary surfactants containing system are thermodynamically stable equilibrium phases, their pore sizes and geometries are precisely controlled by the chemistry, composition, and temperature of the system. The typical dimensions for the pores are ~4 nm for surfactant phases (Qiu & Caffrey, 2000).

Poly(oxyethylene)$_{10}$ nonyl phenol ether (NP10) (Figure 6.1) is a commercial available non-ionic surfactant. It forms various liquid crystal phases with different amount of water component containing micellar, hexagonal, cubic, lamellar and reversed micellar phases (Figure 6.2).

Diffusion couples between the different components of water and NP 10 were created by placing a drop of surfactant adjacent to a drop of water or monomer aqueous solution to more rapidly explore the water-surfactant-monomer ternary phase diagram.

The optical textures and their characteristic defects as a function of composition that developed as water or saturated monomer aqueous solution diffused into the surfactant can be readily indentified as micellar, hexagonal, cubic, lamellar and reversed micellar phases from left to right (Figure 6.3).

Small angle X-ray scattering (SAXS) monitors the structure before and after loading monomer into the hydrophobic phase (Figure 6.4). The two strongest peaks are approximately matching to indexing (2 1 1) and (2 2 0) of a simple Ia3d gyroid structure (Garstecki, & Holyst, 2001). Cubic phase is stable after loading up to 10 wt% monomer with little q value variations. After polymerization, all the peaks shifted to the right indicating cubic structure contracting from ~22 to ~18-19 nm (Table 6.1).

Temperature stabilities of cubic phase structure with 10 wt% monomer in the hydrophobic cores before and after polymerization were monitored by SAXS (Figure 6.5). The structure is stable up to 30 ℃ before polymerization. The structure collapsed above 40 ℃ into lamella crystalline phase at 70 ℃ and returned to cubic phase after dropping the temperature from 70 ℃ to 20 ℃ again due to the easy mobility of monomer in the mixture.

Cubic phase structure after polymerization was only stable up to 20 ℃ and collapsed above 20 ℃ into lamellar crystalline phase. Lamellar crystalline phase structure was then collapsed above 60 ℃. The structure transformation was not reversible after dropping from 70 ℃ to 20 ℃ due to the collapse of PEDOT cubic phase structure and the incapability of PEDOT chains diffuse back into the cubic structure.

The temperature induced structure transition is similar to the pressure induced phase transition in Ia3d bicontinuous cubic phases. Previous study has shown that Ia3d bicontinuous cubic phase formed in monoolein water system went through a phase transition to the Lamellar Lα phase and then to lamellar crystalline phase with the increase of pressure (Mariani, Pisani, Ferrero, Cunsolo & Narayanan, 2000).

The *insitu* impedance spectroscopy was conducted throughout the temperature induced structure transformation. This experimental technique utilized a home-made sample holder which temperature control and electrical properties measurement can be realized at the same time while monitoring the phase change in SAXS (Figure 6.6). The impedance for the monomer-containing cubic phases was very high as there were no conductive substances in the sample (Figure 6.7). It initially decreased a little as the temperature increased with the increased mobility of ions in the mixture and had no consistent changes around further temperature variations. The phase plot of the impedance spectroscopy shows that phase angles increased from around 20 ℃ to at frequencies of 0.1 Hz, reached to around 80 ℃ at around 10 Hz and dropped to 0 ℃ starting around 1000 Hz, indicating that the electrode is primarily functioning as a capacitor at 10 Hz and a pure resistor at 1000 Hz and above.

Effect of temperature induced structure change on impedance of 10 wt% PEDOT cubic after polymerization was showed in Figure 6.8. The impedance dropped from 30000 to 20 Ω with increasing temperatures comparing that of little change in the monomer state of the cubic phases. The relative flat impedance curves at 70 ℃ and cool back to 20 ℃ indicated that the cubic structure collapsed and remain collapsed even the temperature decreased to 20 ℃ again. The nanoparticles formed percolation threshold in the collapsed structure and formed a short circuit in the test cell. The impedance dropped more than two orders of magnitude across the frequencies ranges tested of all the different amount of monomer loaded (Figure 6.9). The more EDOT loaded in octane phase before polymerization, the higher impedance at low frequencies after polymerization. The impedance dropped dramatically after the temperature induced structure transformations.

The phase plot of the impedance spectroscopy reveals phase angles of around 10 ° for the polymerized PEDOT cubic phase structure indicating a more resistive nature as opposed to capacitive of the sample. The phase angle reached at a maximum at 70 ° at around 300 Hz, acted more capacitive, and dropped along the increase of frequency from 300 Hz and on. The flat phase angle curves at 70 ℃ and after cooling back to 20 ℃ again indicated that short circuit was formed by the silver nanoparticles.

To confirm that the impedance change was largely due to structure transformation, impedance spectroscopy of dry Clevios® P was studied while the temperature swept from 20 ℃ to 70 ℃ and back to 20 ℃ (Figure 6.10). The sample was made by depositing Clevios® P into an O ring of the sample holder and let it dried. 0.027 g of dry PEDOT PSS was studied. The impedance dropped more than two times from 20 ℃ to 70 ℃ and did not go back to the original value after the sample was recycled back to 20 ℃ again. The phase angles dropped a little as the temperature increased across the frequency range indicating a little bit higher resistive capability at higher temperature.

Hence the impedance dropping of PEDOT cubic phases were a combination of structure collapse and temperature increase effects.

The isotropic Ia3d cubic phase of EDOT loaded sample was transparent as EDOT monomer has very light color (Figure 6.11). After the polymerization, the sample turned to uniform dark color which indicated the forming of PEDOT as it absorbs blue light in the visible range. The surfactant and oil template were removed by exchanging them out using excess amount of acetone below 20 ℃. There were black particles left in the acetone solution as seen from Figure 6.11, SAXS indicated that cubic structure is destroyed in the template removing process. The structure changes involved in the PEDOT cubic structure collapse induced by temperature change or template removal is shown in Figure 6.12. Up to 10 wt% of EDOT was loaded into the oil phases which translated into up to 2 wt% PEDOT produced in the final sample and PEDOT is brittle in nature. All these factors contributed to the mechanical instability in the PEDOT cubic structure which can easily collapse upon applied forces.

FT-IR was used to confirm PEDOT existence (Figure 6.13). The peak at 822 and 922 cm^{-1} corresponds to the vibration of C-S in a cyclic structure. The peak at 1100 corresponds to carbon oxygen carbon stretching in the ethylene dioxy group. The peak absorptions at 1610, 1512, 1450, 1290 and 1240 cm^{-1} can be assigned to stretching of the thiophene ring. In the region above 2000 cm^{-1}, the electronic absorption from free charge carriers created from polymerization reaction are seen. Thus confirms PEDOT existence. This is consistent with a typical n-doped PEDOT spectra (Kvarnström, Neugebauer, Ivaska & Sarciciftci, 2000).

A drop of the suspension solution was deposited onto a copper grid with 30 nm thick amorphous carbon film and stained with osmium tetroxide for 30 minutes. The sample was then looked under a JEM 2000 FX with a 200 kV-LaB6 gun (Figure 6.14). The size of the clusters ranged from 50 to 500 nm. This explains the low angle SAXS scattering after polymerization. Pores are uniformly distributed with sizes around 3 to 5 nm. The lattice fridges were around 7.8 nm, which possibly corresponded to the (211) in simple Ia3d gyroid planes.

A drop of the suspension solution after ultra sound sonication was deposited onto a copper grid with home-made thin amorphous carbon film (< 10 nm) and then studied by a 5 kV Delong Low Voltage Electron Microscope (LVEM) (Figure 6.15). The low gun acceleration potential gives enhanced contrast to low atomic number materials. A PEDOT films having size ranging from 20 nm to a couple of hundred nm were distributed with relatively regular pores in it. The pore sizes are around 3 to 5 nm. LVEM micrographs also showed that the normal clusters size were around 50 to 200 nm which were cubic structure corpses left after surfactant removal. The LVEM data is consistent with our proposal that PEDOT cubic structures can easily collapse due to phase transitions induced either by temperature change or surfactant removal.

Conclusion

As a result of our work we are able to create highly ordered conducting polymer structures of interest for a wide variety of applications. This is a novel route

for making controlled nanoporous PEDOT with monodisperse, interconnected pore spaces. The insitu electrical properties of PEDOT bicontinuous cubic structure were studied while structure transformation was induced by temperature with SAXS monitoring the structure change at the same time. The impedance of these bicontinuous cubic structures dropped more than two orders in magnitude before and after polymerization. Thermal stability study showed that PEDOT bicontinuous cubic structure was less stable than when it was in monomer state possibly due to the better mobility of the small monomer molecules. As the structure of PEDOT bicontinuous cubic phases collapsed, the impedance dropped more than 5 orders of magnitude. This was due to a combination of structure collapse and electrical property change of PEDOT film under different thermal conditions. The PEDOT cubic structure was mechanically unstable due to the little amount of PEDOT polymer doped in the system. It collapsed induced by either thermal ramping or surfactant removal and the process was not reversible which indicates the immobile nature the PEDOT polymer. The collapsed pieces of PEDOT bicontinuous cubic structure produced a PEDOT film with regular 3 to 5 nm pores on them. This gave the film extremely large surface area and can possibly be useful for rapid response times when used as sensors and actuators. They should also be useful as both electronic and ionic conductors, and for controlled drug delivery, and filters (Baughman, 1996; 2000; Smela, 2003).

Experimental

Materials

Reagent grade Octane (98%) and the other non-ionic surfactant poly(oxyethylene)$_{10}$ nonyl phenol ether (NP10), also known as Tergitol® (NP-10) were purchased from Sigma Aldrich Co. 3,4-Ethylenedioxylthiophene (EDOT, >97%) monomer was purchased from Clevios P®. The initiator, Silver Nitrate ($AgNO_3$, reagent, 99+ %), was purchased from Sigma Aldrich Co. The long wave Ultraviolet

(365nm) source used to initiate PEDOT polymerization was Spectroline model EN-140L purchased from Spectronics Corporation.

Chemical Polymerization

Diffusion couple

To find the optimal compositions to make cubic phases, a diffusion couple was made. A drop of isotropic NP-10 was added adjacent to a drop of water on a glass slides. The sample was then covered with cover slip to prevent water evaporation. After the mixture was well mixed, the sample was studied under OM.

NP-10 cubic phase samples—Samples were prepared by combining octane, water and NP-10 surfactant in appropriate proportions to produce bicontinuous cubic phases. EDOT monomers were dissolved in octane forming solutions with different amount of monomer concentration. The amount of surfactant, monomer octane solution and water needed to obtain a final mixture composed of 55 wt-% NP-10, 22 wt-% Octane and 23 wt-% DI-water was calculated.

To the NP-10 surfactant, add the calculated amount of EDOT Octane solution and vortex the mixture for 1 min with vortex speed set to medium. Next, add the calculated amount of de-ionized water to the mixture of NP-10 and Octane, then vortex for about 5 min. The mixture was then put in refrigerator for 1 day to stabilize into a clear transparent gel. 4 EDOT molar times of AgNO3 was added into the gel and let it diffuse into the mixture for a week. Uv light was then illuminating the sample at 4 ℃ for a week to make PEDOT fully polymerized.

Characterization

Optical Microscopy (OM) and Polarized Optical Microscopy (POM)—Transmission OM and POM were conducted on a Nikon Optiphot POL-2. Images were captured with a Spot RT digital camera.

Small Angle X-Ray Scattering (SAXS)—Samples were capped in a self-made sample holder with aluminum foils as electrodes.

SAXS data were collected on a Regeico SAXS operated at 50 kV and 40 mA with temperature control functions on the sample.

Impedance spectroscopy was monitored by a Princeton Applied Research 2273 Galvanostat with Frequency Response Analysis.

Transmission Electron Microscopy (TEM)

The PEDOT cubic phase was dissolved in excess amount of acetone. After the surfactant was removed, a drop of cubic phase PEDOT in acetone was deposited onto a copper grid with carbon films on it. The sample was then stained under osmium tetroxide for 15 minutes to enhance the contrast. The sample was then studied under a JEOL 2000 FX.

PEDOT cubic structure suspension in acetone was sonicated and then deposited onto a copper grid with self made thin carbon film (<10 nm) on it. The sample was then studied under a 5 kV table top LVEM which gives enhanced contrast to the unstained organic sample.

Fourier transformed infrared (FT-IR) spectrophotometer

A drop of cubic structure PEDOT after the surfactant was removed was deposited on a glass slides. The sample was then studied by a Jasco FT/IR 4100.

Figures and Tables

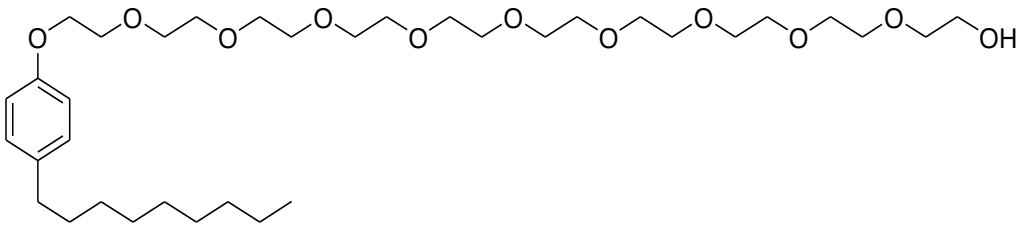

Figure 6.1. Molecular structure of Tergitol® NP-10

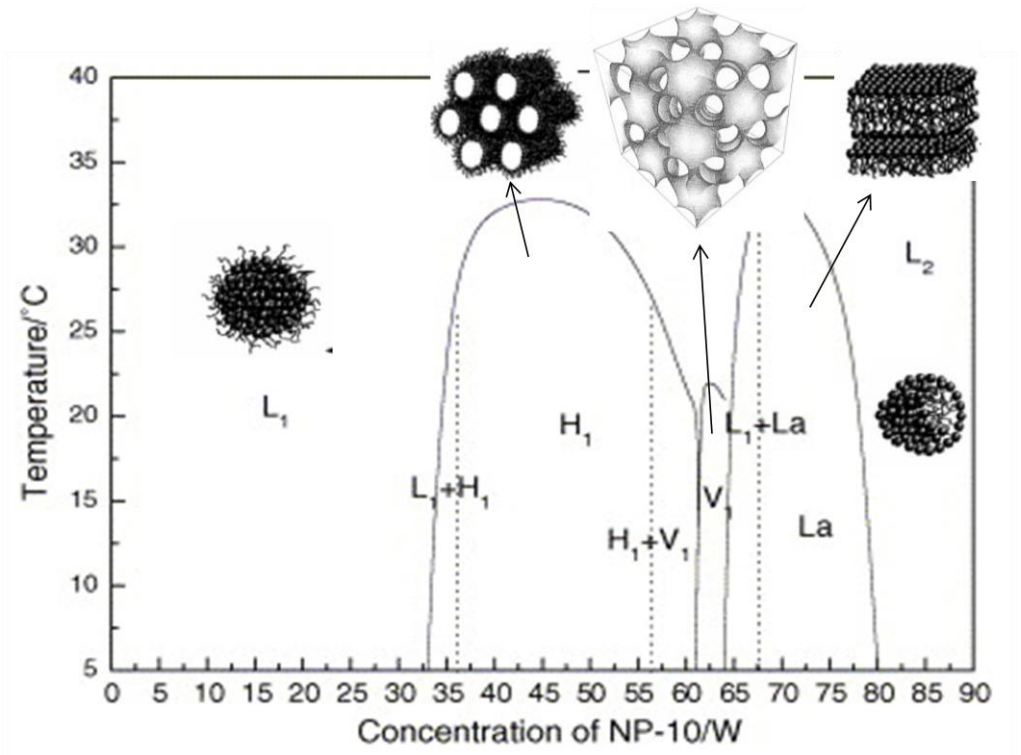

Figure 6.2. NP-10 – Water binary phase diagram (Wang, Zhang, Feng & Xie, 2005)
L1: micelles, H1: hexagonal phase; V1: bicontinuous cubic phase; La: lamellar phase; L2: reversed micelles

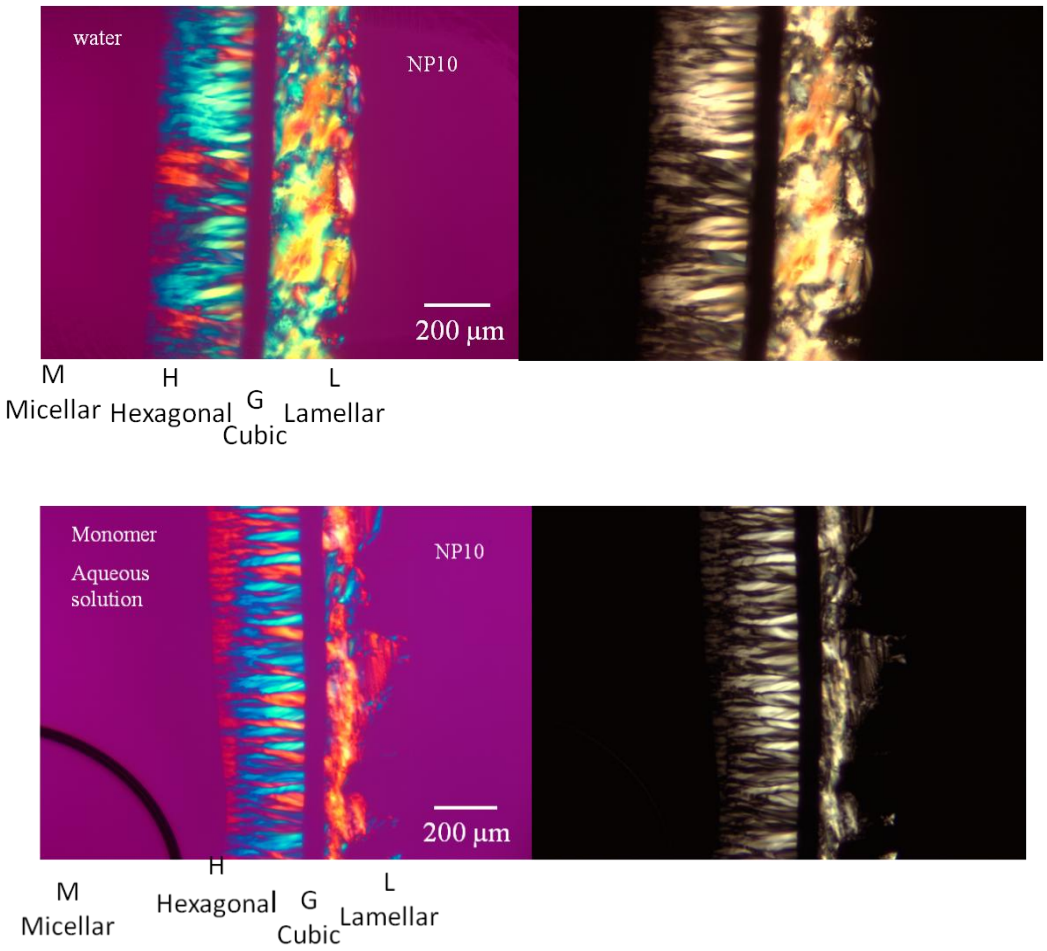

Figure 6.3. Diffusion couple of NP10 and water before and after adding monomers (Top: NP10 water, Bottom: NP10 water after adding EDOT)

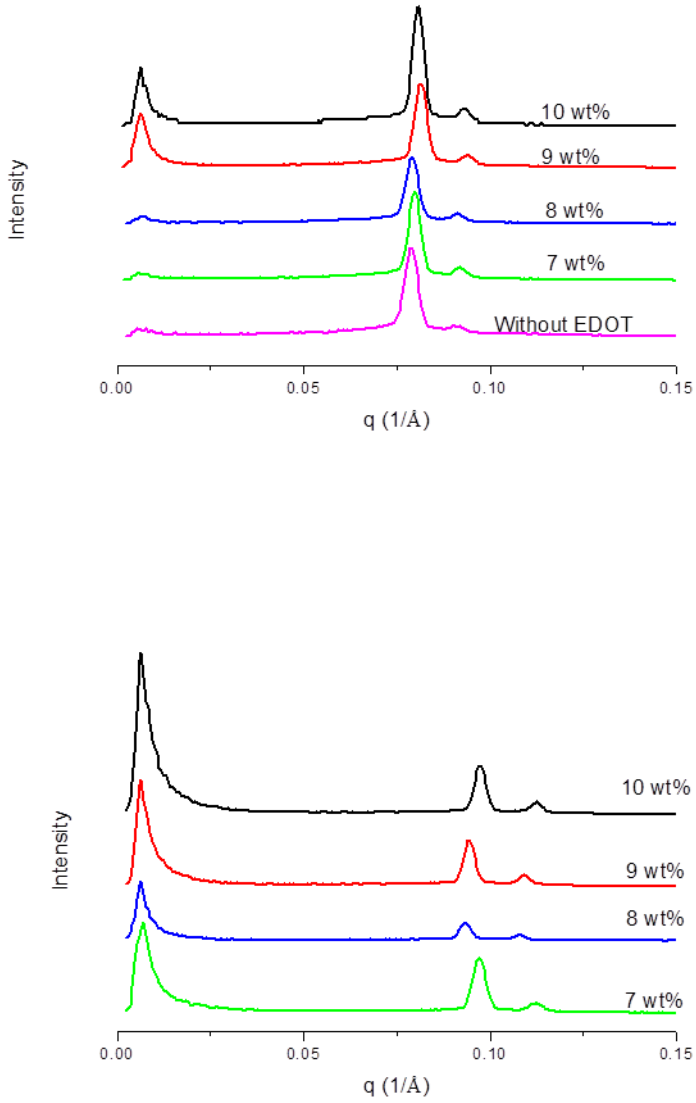

Figure 6.4. SAXS of Cubic structure with different EDOT monomers loaded in oil phase (Top: before polymerization, Bottom: after polymerization)

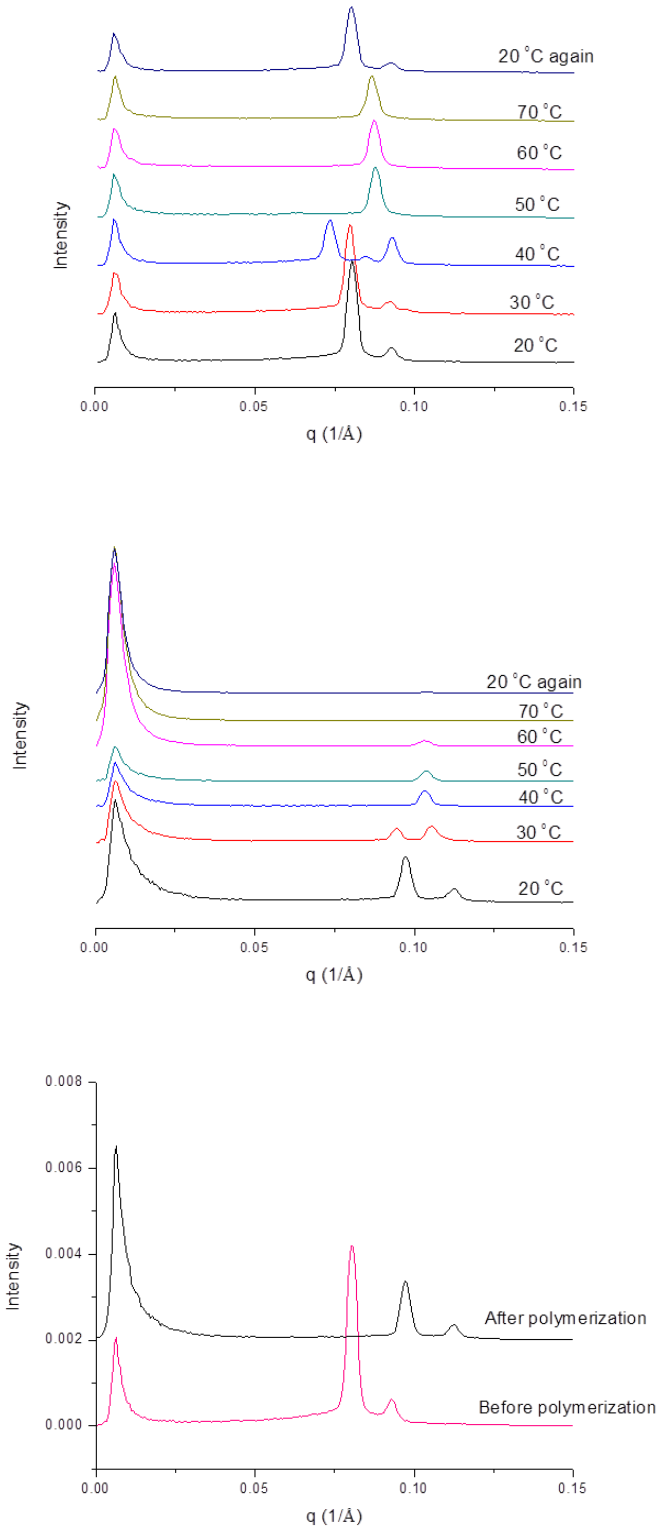

Figure 6.5. SAXS monitoring cubic phase (10 wt% EDOT monomers in oil phase) transitions induced by temperature changing from 20 C to 70 C before and after polymerization. (Top: before polymerization, Middle: after polymerization, Bottom: Comparing the structure at 20 ℃ before and after polymerization)

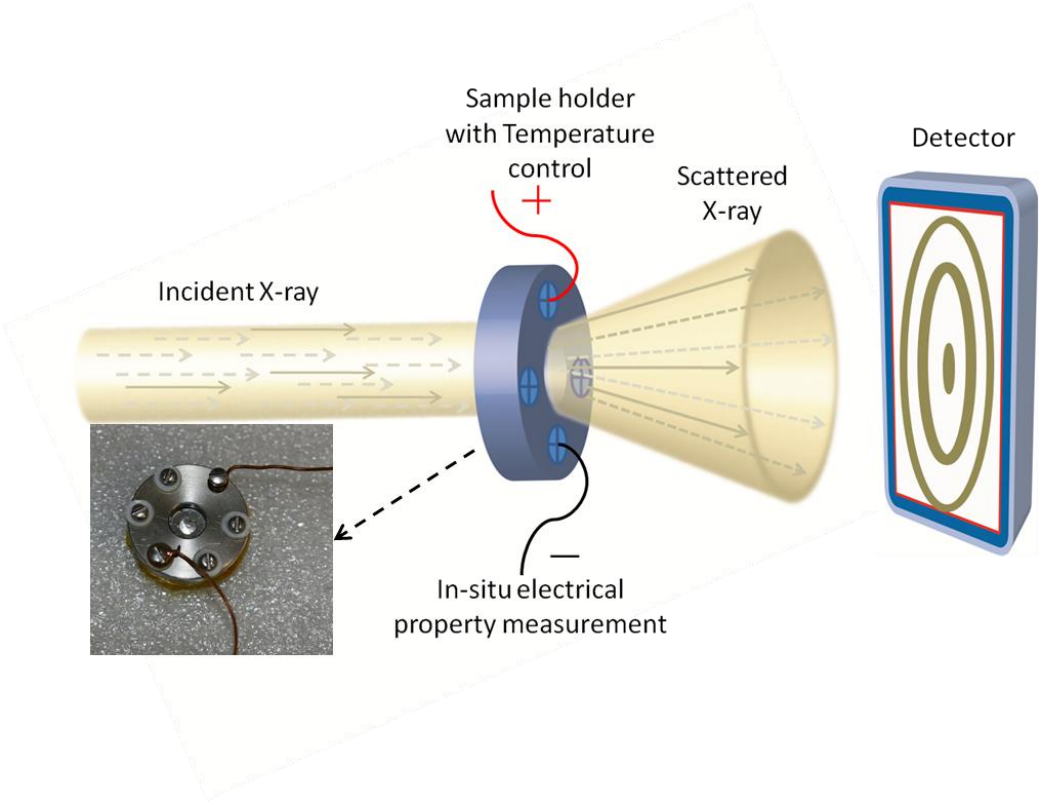

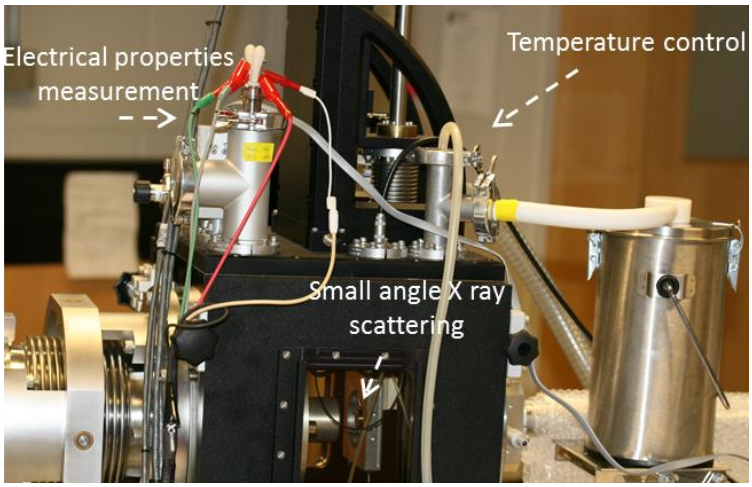

Figure 6.6. Schematics of In-Situ impedance spectroscopy of phase transformations induced by changing temperature with real pictures of the sample holder and SAXS chamber shown at the bottom.

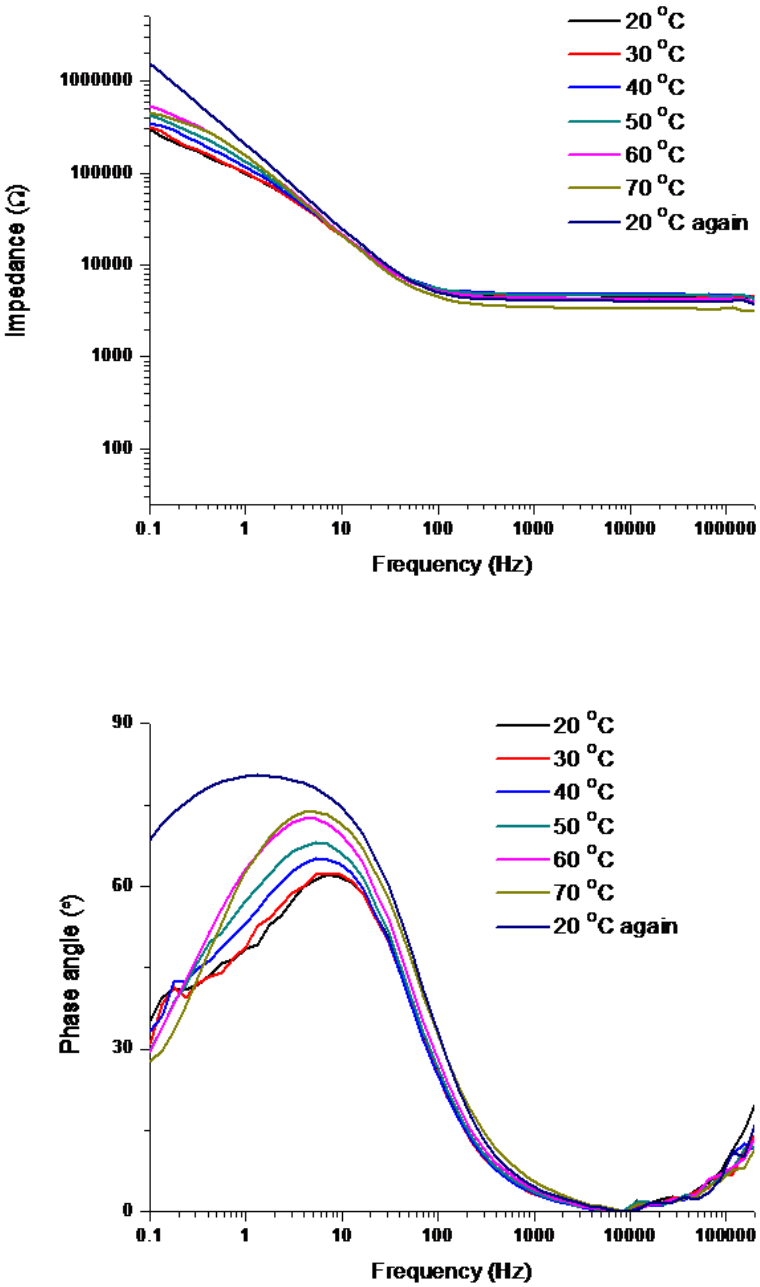

Figure 6.7. EIS of 10 wt% PEDOT cubic phase before polymerization (Top: Impedance plot, Bottom: Phase angle plot)

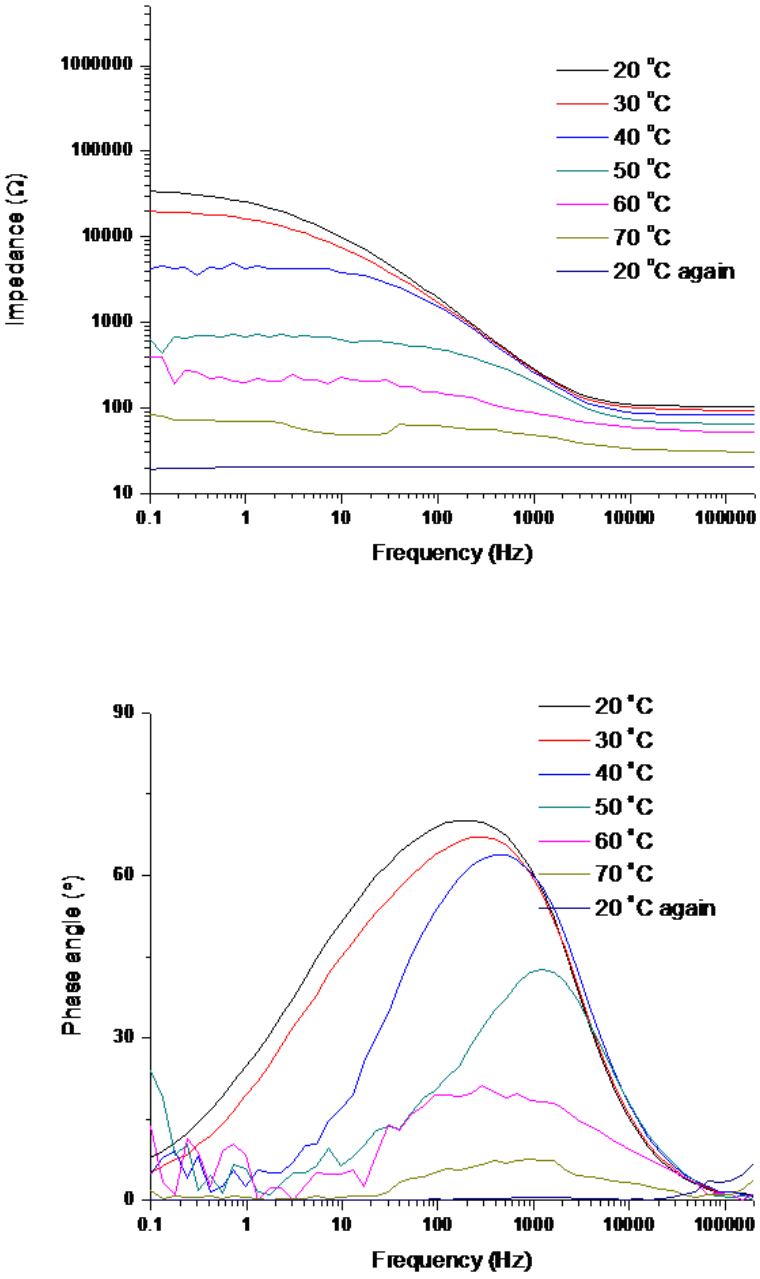

Figure 6.8. EIS of 10 wt% PEDOT cubic phase After polymerization (Top: Impedance plot, Bottom: Phase angle plot).

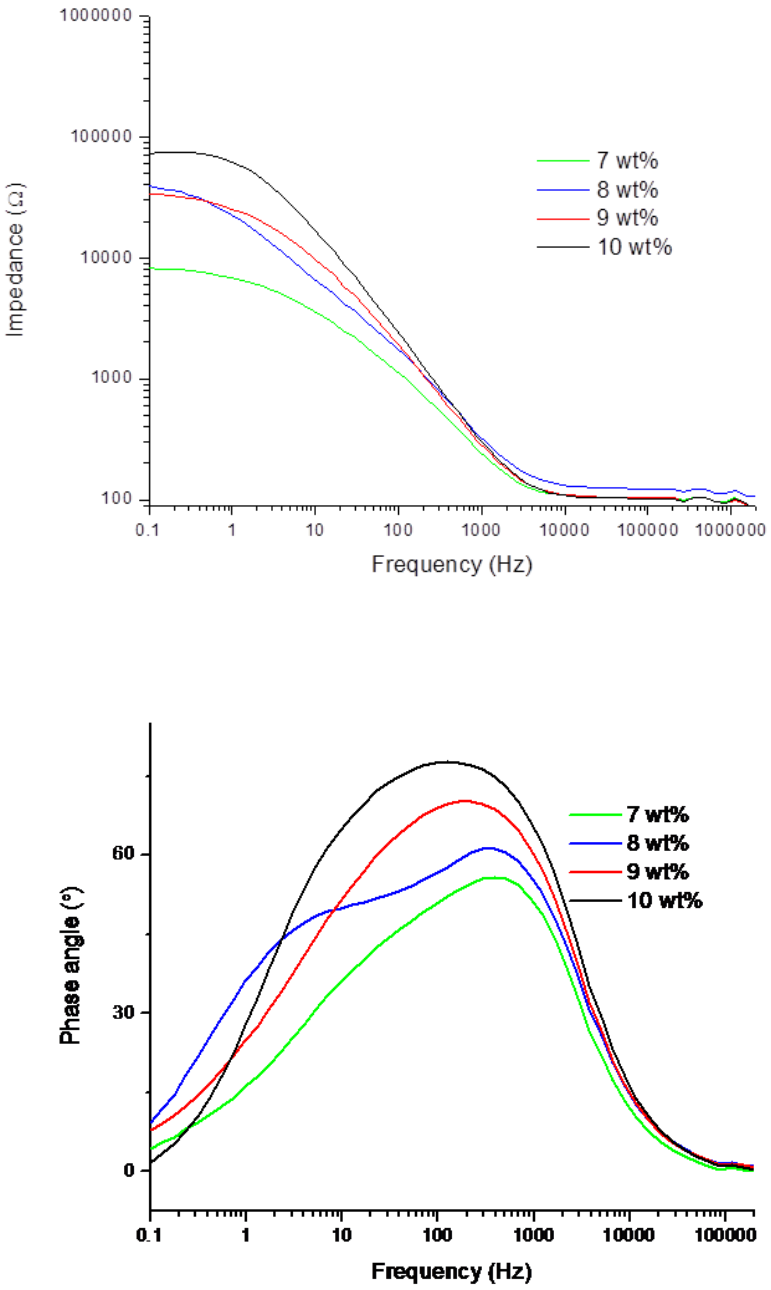

Figure 6.9. EIS of cubic phase with different amount of EDOT monomers loaded in the oil phase after polymerization (Top: Impedance plot, Bottom: Phase angle plot).

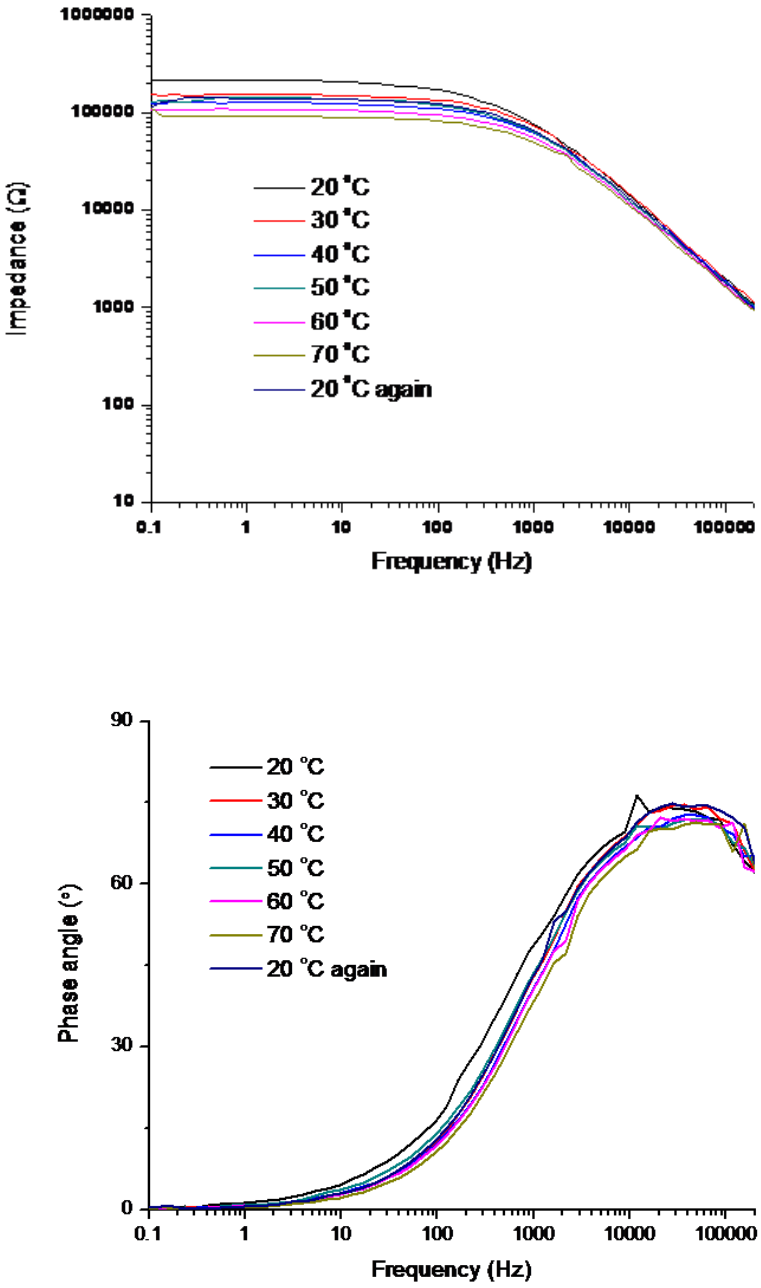

Figure 6.10 . EIS of dry Clevios P (Top: Impedance plot, Bottom: Phase angle plot).

Figure 6.11. 10 wt% PEDOT cubic phase polymerization process (left: before polymerization, middle: after polymerization, right: after surfactant removed)

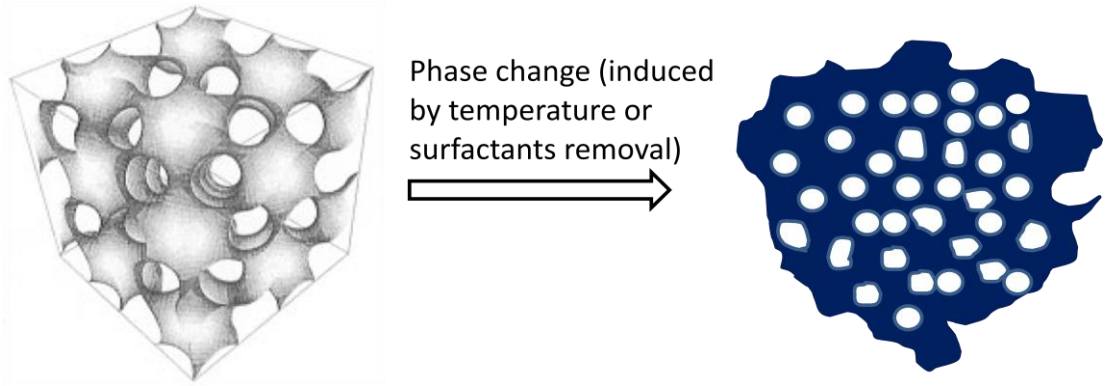

Figure 6.12. Schematic of PEDOT cubic structure collapse during phase transformation

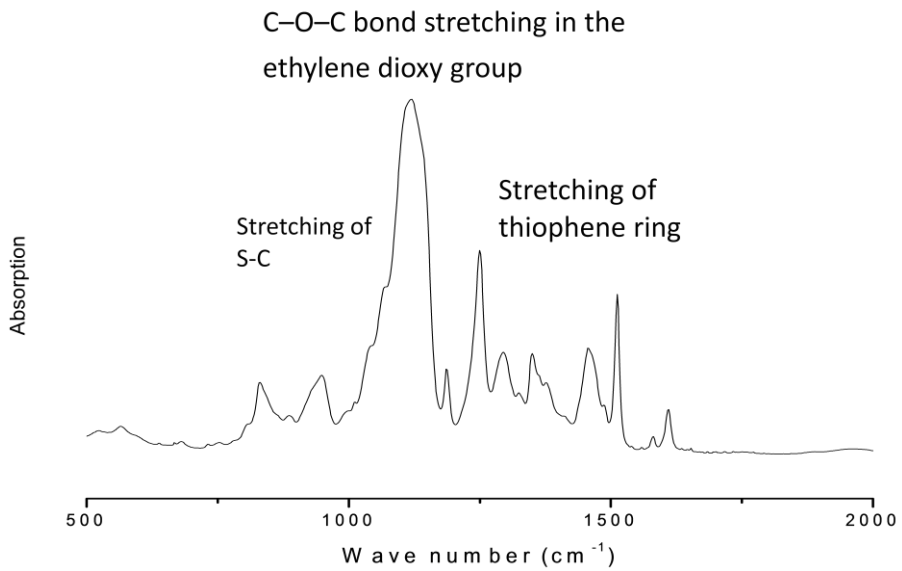

Figure 6.13. FT-IR spectra of PEDOT cubic phase

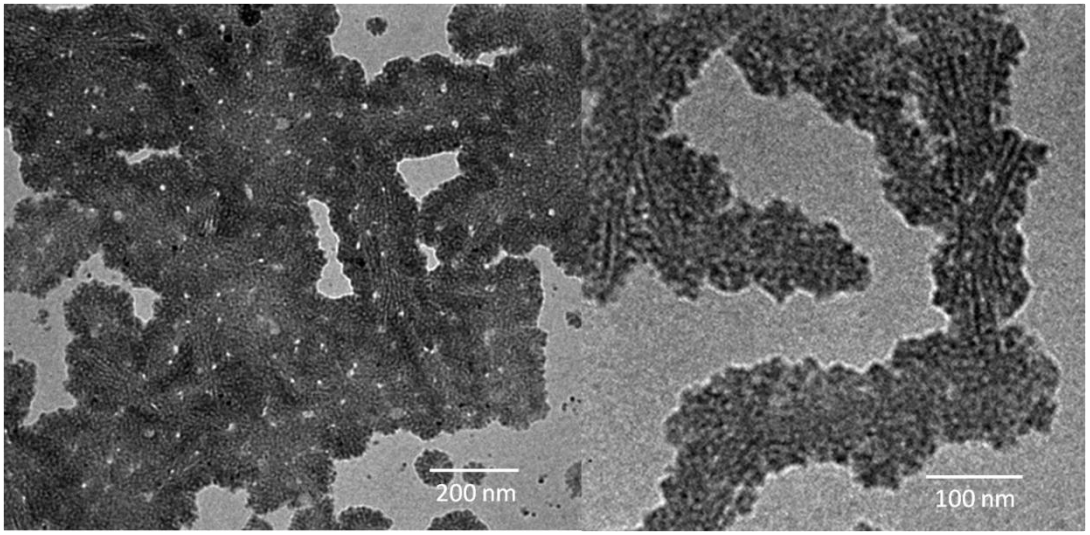

Figure 6.14. TEM micrographs of stained PEDOT cubic phase after surfactant removal

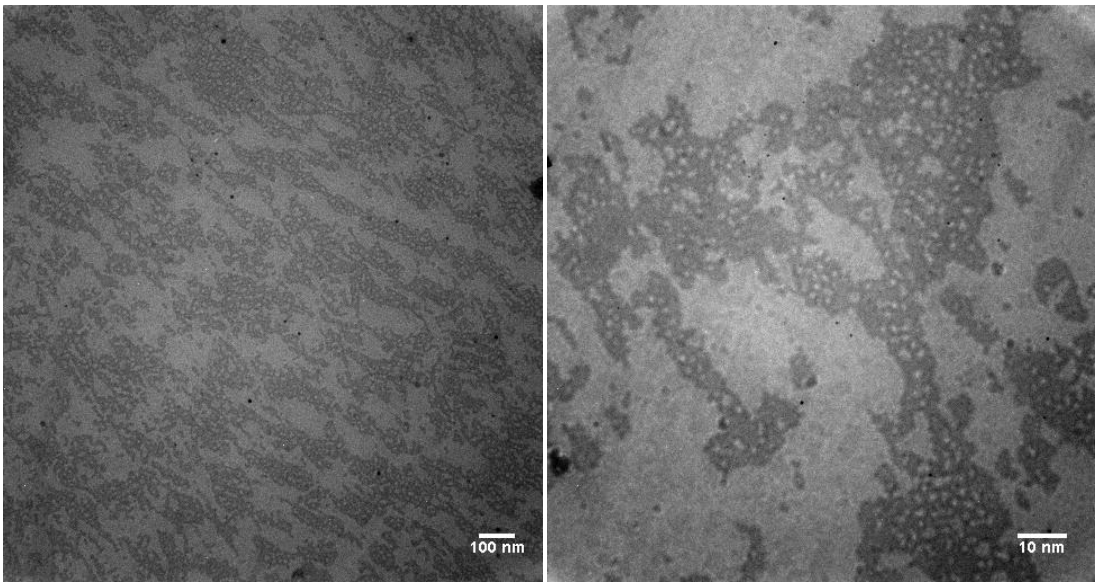

Figure 6.15. LVEM micrographs of PEDOT cubic phase after surfactant removal

Amount of monomers in octane	q_{211} ($Å^{-1}$)	q_{220} ($Å^{-1}$)	Calculated as simple gyroid (nm)
7 wt%	**0.0797**	**0.0917**	**22.3**
8 wt %	**0.0791**	**0.091**	**22.5**
9 wt%	**0.0809**	**0.0924**	**22.0**
10 wt %	**0.0802**	**0.0928**	**22.2**
0 wt%	**0.079**	**0.0906**	**22.5**

Amount of monomers in octane	q_{211} **($Å^{-1}$)**	q_{220} **($Å^{-1}$)**	**Calculated as simple gyroid (nm)**
7 wt%	**0.097**	**0.113**	**18.3**
8 wt %	**0.093**	**0.107**	**19.1**
9 wt%	**0.094**	**0.109**	**18.9**
10 wt %	**0.097**	**0.113**	**18.3**

Table 6.1. Calculated lattice parameters of cubic phases with different amount of EDOT monomers loaded in oil phase before and after polymerization (Top: before polymerization, Bottom: after polymerization)

Reference:

Abidian, M.R. and Martin, D.C. *Biomaterials*, **29**, (2008), 1273-1283.

Abidian, M.R. and Martin, D.C. *Advanced Functional Materials*, **19**, (2009), 573-585.

Abidian, M.R., Kim, D.H.and Martin, D. C. *Advance materials*. **18**, (2006), 405–409.

Argun, A. A., Cirpan, A., & Reynolds, J. R. *Advanced Materials*, **15**, (2003). 1338-1341.

Bar-Cohen, Y. Bellingham, Wash.: SPIE Press. (2001).

Bates, F. S. & Frederickson, G. H. *Physics Today*, **52**, (1999). 32-38.

Baughman, R. H. *Synthetic Metals*, **78**, (1996). 339- 353.

Cassagneau, T. & Caruso, F. *Advanced Materials*, **14**, (2002). 1837-1841.

Cui, X., Hetke, J. F., Wiler, J. A., Anderson, D. J., & Martin, D. C. *Sensors and Actuators A:Physical*, **93**, (2001). 8-18.

Cui, X., Lee, V. A., Raphael, Y., Wiler, J. A., Hetke, J. F., Anderson, D. J. *Journal of Biomedical Materials Research*, **56**, (2001). 261-272.

Cui, X. & Martin, D. C. *Sensors and Actuators B: Chemical*, **89**, (2003). 92-102.

Fairhurst, C. E. & Holmes, M. C. *Langmuir*, **13**, (1997). 4964-4975.

Funari, S. S. & Rapp, G. *J. Phys. Chem. B*, **101**, (1997). 732-739.

Garstecki, P. and Holyst, R. *J. Chem. Phys*. **115**. (2001). 1095.

Groenendaal L., Jonas F., Freitag D., Pielartzik H., Reynolds J.R., *Adv Mater.* **7**. (2000), 481–494.

Hulvat, J. F. & Stupp, S. I. *Angewandte Chemie-International Edition*, **42**, (2003). 778-781.

Hulvat, J. F. & Stupp, S. I. *Advanced Materials*, **16**, (2004). 589-592.

Jager, E. W. H., Smela, E., & Inganas, O. *Science*, **290**, (2000). 1540-1545.

Kim, D.-H., Richardson-Burns, S. M., Hendricks, J., Sequera, C., & Martin, D. C. *Advanced Functional Materials*, **17**, (2006). 79-86.

Kim, J. S., McQuade, D. T., Rose, A., Zhu, Z. G., & Swager, T. M. *Journal of the American Chemical Society*, **123**, (2001). 11488-11489.

Kirchmeyer, S., Reuter, K. *Journal of Materials Chemistry*. **15**, (2005), 2077-2088.

Kuhn, H. H. & Child, A. D. Electrically Conducting Textiles. In T. A. Skotheim, R. L. Elsenbaumer, & J. R. Reynolds (Eds.), *Handbook of Conducting Polymers(Second Edition).* New York: Marcel Dekker, Inc. (1998). 993-1013.

Kvarnström, C., Neugebauer, H. Ivaska, A. and Sarciciftci, N.S. *J. Mole. Struct*. **521**, (2000), 271-277.

Mariani, P., Pisani, M., Ferrero, C., Cunsolo A. and Narayanan, T. *ESRF newsletter*, **10**, (2000), 21-23

Matsushita, Y. *Macromolecules*, **40**, (2007). 771-776.

Nguyen, T P., Rendu, P., Long, P D., De Vos, S A. *Surface and coatings technology*, **180-181**, (2004), 646-649.

Nyström, G., Razaq, A., Strømme, M., Nyholm L.and Milhranyan, A. *Nanoletters*, **9**, (2009), 3635–3639

Qiu, H. & Caffrey, M. *Biomaterials*, **21**, (2000). 223.

Schmidt, C. E., Shastri, V. R., Vacanti, J. P., & Langer, R. *Proc. Natl. Acad. Sci. USA*, **94**, (1997). 8948-8953.

Schwarz, U. S. & Gompper, G. *Physical Review E*, **59**, (1999). 5528-5541.

Smela, E. *Advanced Materials*, **15**, (2003). 481-494.

Swager, T. M. *Accounts of Chemical Research*, **31**, (1998). 201-207.

Wang, H., Zhang, G., Feng, S. and Xie, X. *Colloids and Surfaces A: Physicochem. Eng. Aspects.* **256**, (2005) 35-42.

Winther-Jensen, B., Winther-Jensen, O., Forsyth, M. and MacFarlane, D. R. *Scence*, **321**, (2008) page 671-674.

Wohlgemuth, M., Yufa, N., Hoffman, J., & Thomas, E. L. *Macromolecules*, **34**, (2001). 6083-6089.

Yang, J., Martin, D C; *Sensors and Actuators A: physical*, **113,** (2004a), 204-211.

Yang, J. & Martin, D. C. *Sensors and Actuators B: Chemical*, **101**. (2004b). 133- 142.

Yang, J., Lipkin, K., & Martin, D. C. *Journal of Biomaterials Science -- Polymer Edition*, **18**, (2007). 1075-89.

Yang, J., Xiao, Y., & Martin, D. C. *Materials Research Society,* Boston, MA. (2003).

Chapter VII

Facile methods for fabricating aligned electrospun poly(3,4-ethylene dioxythiophene) (PEDOT) nanofibers and nanotubes

Abstract

Two efficient methods for fabricating aligned PEDOT nanofibers and nanotubes are presented. Electrospinning was used to created aligned assemblies of poly(lactide-co-glycolide) (PLGA) or poly(caprolactone) (PCL) polymers that have been heavily loaded with polymerizable EDOT monomer. The alignment was created by a rotating wheel or an insulating gap between conductive metallic strips. The non-conductive polymer / EDOT monomer blend fibers were converted to PEDOT nanofibers or nanotubes by exposure to an oxidative catalyst. These methods made it possible to efficiently create large assemblies of aligned nanofibers and nanotubes. The aligned fiber assemblies have been shown to direct neural cell growth in vitro.

Introduction

Materials with well-defined structures on the nanometer scale have unique properties including higher charge/discharge capacities, faster response times and higher sensing capabilities (Cho & Lee, 2008; Li, Martin & Scrosati, 2000; Cassagneau & Caruso, 2002). Among the different nanostructured shapes that are possible to create, fibers and tubes have attracted special attention due to their potentially anisotropic transport and optical properties (Aleshin,2006; Law, Goldberger & Yang, 2004). Conductive polymers such as polyaniline have been templated into 1-D nanoscale structures using a so-called hard-template-assisted technique (Wu & Bein, 1994).

Poly(3,4-ethylene dioxythiophene）(PEDOT) is a π-conjugated polymer that has received wide interest for many different applications (Kirchmeyer & Reuter, 2005;

Groenendaal, Jonas, Freitag, Pielartzik & Reynolds, 2000; Yang & Martin, 2004a). The rigid, linear conformation of PEDOT facilitates charge transport and favors crystallization that reduces its solubility and processability (Lock, Im & Gleason, 2006). PEDOT can be polymerized both chemically and electrochemically. Details of the morphology of PEDOT have been recently reviewed (Martin, et al., 2010).

PEDOT nanowires and nanotubes have been developed by electrochemical polymerization in a porous alumina template (Xiao, Cho, Liu & Lee, 2007). The complicated process involved polymerizing in a home-made gold-coated alumina template with a certain pore diameter and then both the alumina template and gold film were removed. This produced a mixed polymer fiber and tubular structure and would not likely be a cost-effective way to produce conductive polymer fibers and tubes.

PEDOT nanofibers as thin as 10 nm in diameter were chemically synthesized by soft template assisted self-assembly techniques that involve chemically polymerizing EDOT monomer loaded in cylindrical surfactant micelles or reverse microemulsions (Han & Foulger, 2006; Zhang, et al., 2006). Although the PEDOT nanofibers produced by these techniques showed enhanced electrical conductivity, the fibers segregate into randomly oriented fiber mats after surfactant template removal. This made it hard to process these fibers because of the insoluble nature of PEDOT polymer.

Wet-spinning techniques have been used to make aligned PEDOT-PSS fibers from aqueous suspension. The electrical properties of these fibers were comparable to that of PEDOT cast films (Takahashi, Ishihara & Okuzaki, 2005). A dip-treatment in ethylene glycol was used to improve the conductivity and mechanical strength of these fibers, presumably due to the removal of the more electrically insulating PSS from the surfaces of the PEDOT/PSS grains and crystallization of PEDOT in the microfibers (Okuzaki, Harashina & Yan, 2009). The diameters of these fibers were relatively large, ranging from 5-11 μm in diameter.

Electrospinning is another convenient way to make polymer fibers and tubes with diameters ranging from below 30 nm to 100 μm (Zhou, et al., 2003; Huang, Zhang, Kotaki.& Ramakrishna, 2003). Dorsal root ganglia neurite growth has been shown to be

directed by aligned electrospun fibers (Corey, et al., 2007). Different PEDOT morphologies coated on electrodes have been shown to have potential for improving the communication between bionic devices and living tissue (Cui & Martin, 2003; Yang, et al., 2004; Yang & Martin, 2004b; Xiao, Martin, Cui & Shenai, 2006; Yang, Lipkin & Martin, 2007). Electrospun PEDOT fibers and tubes have been deposited onto gold electrode surfaces to improve electrical properties and control drug release (Abidian, Kim & Martin, 2006; Abidian & Martin, 2008; Abidian & Martin, 2009). The fibers formed by electrospinning were mostly randomly oriented forming non-woven mats. However, there are ways to produce aligned electrospun fibers. A grounded rotating wheel has been used to draw the electrospun fibers into an aligned form as the fibers are spun (Theron Zussman & Yarin, 2001). Electrospun polymer fibers can also be directed by electrostatic interactions into uniaxially aligned arrays using a collector composed of two conductive strips separated by an insulating gap of variable width or simply placing a rectangular frame structure under the spinning polymer jet (Li, Wang & Xia, 2004; Zhang, et al., 2006).

Previously we have shown that aligned assemblies of PEDOT nanotubes can be created by subsequent electrochemical polymerization around and through oriented PLGA electrospun nanofibers. However this method is slow and relatively inefficient, since it requires a conductive electrode. Furthermore, much of the PEDOT does not come in contact with the PLGA template and thus remains untemplated, and it is only possible to make relatively thin films. Nevertheless, these oriented assemblies have been previously shown to direct the regeneration of neural cells and deliver biologically active agents (Abidian et al., 2010). Here, two efficient methods for fabricating aligned PEDOT nanofibers and nanotubes are presented. Electrospinning was used to create aligned assemblies of PLGA or PCL polymers that have been heavily loaded with polymerizable EDOT monomer. The alignment was created by using either a rapidly rotating wheel or by an insulating gap between conductive metallic strips. The non-conductive polymer / EDOT monomer blend fibers were then converted to PEDOT nanofibers or nanotubes by exposure to an oxidative catalyst. These methods made it possible to efficiently create

large assemblies of aligned nanofibers and nanotubes. The aligned fiber assemblies have been shown to direct neural cell growth in vitro.

Results and Discussion

EDOT monomer was mixed into solutions of the biocompatible polymers PLGA and PCL (Li, Laurencin, Caterson, Tuan & Ko, 2002; Abidian, Kim & Martin, 2006; Yoshimoto, Shin, Tera i& Vacanti, 2003). Fibers could be aligned from 10 wt% to 30 wt% solutions with mass ratios of EDOT to PLGA or PCL ranging from 10:1 to 3:2. In the first approach, a rotating mandrel (~1 cm in diameter) was used to align the fibers (Figure 7.1). As the fibers were collected onto the surface of the rotating beam, they were oriented circumferentially. The second method used to align the polymer fibers was by collecting them onto a conductive substrate with a gap of controlled size (Figure 7.2). A bundle of well-aligned fibers were suspended over the void. The length of the fibers could be controlled by varying the width of the gap from 0.5 cm to 3 cm. These oriented fibers became stacked into multi-layer structures after sufficiently long collecting times. This gap alignment technique works well as long as the material in the gap is a good insulator. It has been argued that the driving force for this alignment is the electrostatic interactions between the conductor and dielectric in the gap. The alignment improved somewhat as collection time increased, evidently due to electrostatic repulsions between deposited fibers (Li, Wang & Xia, 2004).

The aligned fibers were exposed for 24 hours to an aqueous solution of $FeCl_3$ oxidant in order to polymerize the EDOT monomer mixed into them. After polymerization, residual $FeCl_3$ was removed by soaking the fibers in an excess amount of water for an extended period of time. Figure 7.3 shows the micrographs of the fibers after polymerization. The overall alignment of fibers was well preserved after polymerization. The color of the fibers turned to light blue for thinner samples and to dark color for thick samples indicating PEDOT formation as PEDOT absorbs blue light in the visible light range. The aligned fibers on the rotating beam were cut off and then polymerized. The fibers became stiff and rigid. An optical micrograph and SEM micrograph of a bundle of

aligned PEDOT/PLGA fibers is shown in Figure 7.4. While PEDOT is insoluble in most organic solvents, PLGA and PCL can easily be removed by soaking the fibers into their respective solvents such as acetone and chloroform.

After the PLGA and PCL template were removed from the fibers, well-aligned conductive PEDOT tubes were formed. A typical SEM micrograph of these tubes is shown in Figure 7.5. The tubes maintained the fiber alignment and the surface morphology of the precursor fibers indicating that EDOT monomers had been continuously distributed. The amount of PEDOT formed in the aligned nanofibers was mechanically stable enough to withstand the template removal without significantly collapsing or reorganizing.

The PEDOT nanofibers and nanotubes were collected onto copper grids with amorphous carbon support films and studied under TEM (Figure 7.6). The smallest diameter of the fibers and tubes was ~ 150 nm; fibers thinner than that were not mechanically stable enough to remain intact during sample preparation (Li, Wang & Xia, 2004). TEM micrographs of PEDOT nanofibers taken before removing the PLGA or PCL core (Figure 7.7) shows a uniform relatively dark fiber. After removal of the internal template the TEM clearly shows the tubular structure of the resulting PEDOT nanotube.

The effects of concentration of oxidizer were studied. SEM and TEM micrographs of PEDOT-PLGA fibers polymerized with different oxidizer concentration were shown in Figure 7.8. The roughness of the fiber surfaces were dependent on the concentrations of $FeCl_3$ aqueous solution; the higher the concentration, the rougher the surface. From both TEM and SEM images, we can see that the surfaces of the fiber becomes rougher from sample a through sample c with the corresponding oxidizer concentration being 30 wt% , 50 wt% and 60 wt% respectively.

The tubular structure formed probably due to the fast polymerization rate in the higher concentrated oxidizer solution which produced a relatively dense PEDOT wall that prevented the oxidizer diffusing into the fiber to polymerize the remaining EDOT monomer inside. Inside the tube, PLGA and left over EDOT can be washed away by an

excess amount of acetone. PEDOT tubes were left since PEDOT does not dissolve in acetone. The conductive PEDOT tubes were well aligned, uniform and their mechanical strength was strong enough to hold themselves together through the washing process. A schematic of this process is shown in Figure 7.9. The thickness of the wall was unrelated to the diameters of the tubes. They were all around 500 nm. This might be the effective thickness of the wall that prevents $FeCl_3$ from diffusing into inside over the time frame of the oxidative polymerization. In some cases, two or more well-aligned fibers could be polymerized together forming a multiwall nanotube structures (Figure 7.10)

At low concentrations of oxidizer solution, fibers instead of tubes were formed, as shown in sample c from Figure 7.8. This might due to the slow polymerization rate near the surface which lets the oxidizer diffuse into the core of the fiber and polymerize the EDOT inside.

The diameters of the aligned fibers could be controlled by adding different amounts of EDOT monomer into the precursor polymer solution. We determined that the diameters dropped from around 8 μm, to around 4 μm and then to around 2 μm when the EDOT to PLGA weight ratios changed from 10% to 30% and then to 50% (Figure 7.11).

The resistance of the fibers was measured by using a two point probe (Table 7.1). The diameter was measured by SEM micrographs. The conductivity of a single 8 μm diameter fiber was then calculated to be 2.2 mS/cm. This is comparable to the conductivities of PEDOT chemically polymerized by $FeCl_3$ (Corrandi & Armes, 1997).

All the samples with diameter were spun within the same time length with the same rotation speed, so the number of fibers in any bundle was the same. Resistivity of a bundle of 8 μm fibers was 2.2k Ω, 4 μm fibers was 4 k Ω, and 2 μm fibers was 7.8 kΩ. After normalized by conductivity of 8 μm fibers, conductivity of sample 2 was 2.3 mS/cm, and conductivity of sample 3 was 2.5 mS/cm. There was not much difference in the conductivities between the three samples, which indicates that the diameter of the fibers has little effect in varying the conductivity of PEDOT fibers along the fiber direction.

The resistivity of fibers polymerized by 50 wt% $FeCl_3$ was 13 kΩ and fibers polymerized by 30 wt% $FeCl_3$ was 50 kΩ. After normalized by fibers polymerized by 60 wt% $FeCl_3$, conductivity of fibers polymerized by 50 wt% $FeCl_3$ was 0.75 mS/cm and fibers polymerized by 30 wt%was 0.2 mS/cm. Conductivity of PEDOT was not affected by the concentration of oxidizer ($FeCl_3$) (Corradi & Armes, 1997). The difference in conductivity is determined by the amount of PEDOT formed in the outer shell of the PEDOT/PLGA fibers and tubes. With lower concentrations of oxidizer, less amount of PEDOT was formed, thus producing fibers with lower conductivity. This is consistent with the TEM studies which showed that less concentrated oxidizer produced thinner PEDOT walls.

Raman spectrum (λ=532 nm) is shown in Figure 7.12. The peaks at 436 and 574 cm^{-1} are contributed by C-O-C deformation. The peak at 858 and 990 cm^{-1} are assigned to O-C-C deformation and oxyethylene ring deformation respectively. Both peaks at 1228 and 1264 cm^{-1} are due to C-C inter-ring stretching in plane modes. The peaks at 1061, 1370, 1429 and 1508 cm^{-1} correspond to C-O stretching, C-C stretching in plane modes, C=C stretching in plane modes (symmetric) and C=C stretching in-plane modes (antisymmetric) respectively. This is consistent with calculated and experimental frequencies from other research groups (Table 2) (Nguyen, Rendu, Long & De Vos, 2004; Xu & Czernuszka, 2008; Tran-Van, Garreau, Louarn, Froyer & Chevrot, 2001).

FT-IR spectra were also used to monitor the PEDOT formation within the aligned fibers. Figure 7.13 shows FT-IR spectra of aligned fibers using PCL as a template. There were distinctive peaks before and after polymerization. The CH_2 stretchings of the oxyethylene ring at around 2800-3000 cm^{-1} showed up in both spectra. Characteristic PEDOT peaks showed up after polymerization. The peaks near 837 and 920cm^{-1} corresponded to the vibrations of S-C bonds in polymerized PEDOT chains. The peaks at about 1055 and 1155 cm^{-1} was due to the stretching of the C-O-C bonds stretching in the ethylene dioxy group. The peak absorptions at around 1250, 1307, 1467 and 1517 cm^{-1} can be attributed to the stretching of the thiophene ring. This is consistent with former FT-IR studies (Nguyen, Rendu, Long & De Vos, 2004; Kvarnström, Neugebauer, Ivaska & Sarciftci, 2000).

As can be seen from Figure 7.14, EDOT did not have absorption peaks over 300 nm in its UV-Vis spectrum. A sample of 5 wt% $FeCl_3$ absorbed light below 400 nm. There is a broad absorption band from 550 nm to 600 nm in the PEDOT fibers. Neutral PEDOT has an absorption at ~ 570 nm in the visible range corresponding to the π-π^* transition (Winther-Jensen & West, 2006). This also confirms the PEDOT existence as FT-IR and Raman spectra.

The thermal behavior of the aligned fibers was investigated by thermogravimetric analysis (TGA) in a nitrogen environment (Figure 7.15). The thermal decomposition of PLGA occurred at 200–300 ℃, inducing a significant weight loss. PLGA was almost burned off after the heating cycle (Xu & Czernuszka, 2008). The major thermal decomposition of PEDOT occurred from 280-400 ℃. There was around 40 wt% carbon left at 500 ℃ after PEDOT was burned off (Zhan, et al., 2008). The top plot showed that thermal deposition of all samples with different diameter and different PEDOT/PLGA ratio started around 200 ℃. Based on the left over weight after the fibers were burned off, 8 μm fibers produced the least residue which indicates the lowest PEDOT/PLGA ratio in the fiber. From the TEM we can tell the wall thickness of the fibers was essentially independent of the EDOT/PLGA ratio. 8 μm fibers had a larger diameter, and the thickness of the PEDOT shell was fixed, thus produced lower PEDOT/PLGA ratio. 2 μm fibers had the highest PEDOT/PLGA ratio in the fiber. From the bottom plot, fibers polymerized by the lowest oxidizer concentration produced the lowest amount of residue which indicates the lowest PEDOT/PLGA in the fiber. This confirms that lower concentration of $FeCl_3$ produced lower amount of PEDOT in the fiber.

Dorsal root ganglia (DRG) were plucked from the spinal cords of embryonic 15-day rats and placed on the fiber bundles. Confocal micrographs (Figure 7.16) showed guided neuron, DNA and glia outgrowth from primary nervous tissue on aligned electrospun nanofibers. This was consistent with former studies of guided dorsal root ganglia neurite growth by electro-spun PLLA fibers. The conductive polymer PEDOT inside the fiber may facilitate signal recording and stimulation in the aligned neural tissue.

Conclusion:

Aligned electro-spun PEDOT fibers and tubes templated by biocompatible polymers were developed using two facile alignment approaches. Spectroscopic techniques including Raman, FT-IR and UV-Vis all confirmed the PEDOT formation in the fibers/tubes.

The diameters of the PEDOT-PLGA/PCL electrospun fibers could be controlled from 150 nm to 20 μm by varying the EDOT concentrations in the blend solution, with higher concentration producing fibers with smaller diameters. The final thickness of the wall was determined only by the concentration of EDOT monomer and oxidizer concentration, not the precursor filament diameter. The conductivities of the fibers were not influenced by the amount of PLGA/PCL in them.

Higher oxidizer produced rougher fiber/tube surfaces. The lowest oxidizer concentrations produced fibers instead tubes after template removal. The conductivities were lower when the fibers or tubes were produced in a less concentrated oxidizer solutions because there was less PEDOT formed.

These oriented PEDOT nanofibers and nanotubes were efficient in guiding the alignment of both neurons and glia cells. They may provide signal recording and stimulation while directing the regeneration of nerve tissues. PEDOT nanotubes can also be applied to targeted drug delivery at neural interfaces (Abidian, Kim & Martin, 2006; Abidian & Martin, 2008; Abidian & Martin, 2009).

Experimental:

Electro-spinning

The solvent for EDOT/PLGA we used was a mixture of chloroform and DMF with a volume ratio of 80/20. PLGA to solvent weight ratio was fixed at 31 to 100. The solvent for EDOT/PCL is THF.

For collecting the fibers on rotating beam, 2kV to 5 kV potentials were applied onto the electro-spinning apparatus. Diameter of the glass beam with thin layer of gold palladium deposited was 9mm. Distance between tip of needle and beam was 6cm. All

the fibers were made with a rotating speed at196-204 rpm for 10 minutes. The fibers were soaked in $FeCl_3$ solution for 24 hours. $FeCl_3$ was washed away by excess amount of water.

For fibers collecting onto the conductive substrate with a gap void, 10 to 15 kV potentions were applied. The collecting substrates were made by aluminum foil or carbon film. The size of the gaps ranges from 0.5 cm to 3 cm.

EDOT/PLGA ratio control

Samples with 8 μm diameter, 4 μm diameter and 2 μm diameter were produced from solutions containing different EDOT/PLGA weight ratios, 10%, 30% and 50 % respectively. All three samples were soaked under a 60 wt% $FeCl_3$ aqueous solution for 24 hours.

Oxidizer concentration control

Three samples of 8 μm thick fibers were produced from a 30 wt% EDOT/PLGA solution and soaked in different concentrations of $FeCl_3$, 60 wt %, 50 wt% and 30 wt% respectively, for 24 hours. $FeCl_3$ was then washed away by excess amount of water

Characterization

TEM sample preparation

Copper grids were put on scotch tape for 5 minutes and then taken off. Fibers were then stuck onto the copper grids with the remaining glue. The fibers were examined in a JEOL-2000FX with a 200 kV LaB_6 gun.

SEM images were coated with a 10 nm thick evaporated layer of gold and then studied in a JSM-7400F at 3 kV.

Raman spectroscopy of PEDOT fiber was obtained on a lab made apparatus (in the Rabolt laboratory at the University of Delaware) with a green laser (532 nm) having a power of 2 mW on the sample.

The PEDOT/PCL fibers were sonicated in water forming a suspension. UV-Vis spectra were obtained on a Shimadzu UV-Vis-NIR spectrophotometer scanning from 250 nm to 800 nm.

FT-IR spectroscopy was done on the fibers as they were made by a Perkin-Elmer spectrum 100 FT-IR spectrometer.

Conductivity of the fibers was measured using two point probe measurement with a fiber length of 0.48 cm. A single fiber with diameter of 8 μm was determined by SEM. The resistance of the fiber was determined by the two point probe and conductivities calculated from it. The conductivities of the other fibers were normalized by comparison with this sample since the number of fibers in each bundle was fixed by using the same rotation speed and electrospinning time.

TGA was done on a Perkin-Elmer Thermogravimetric Analyzer in a nitrogen environment heating up to 500 ℃ at a scan rate of 20 ℃/min.

Figures and Tables:

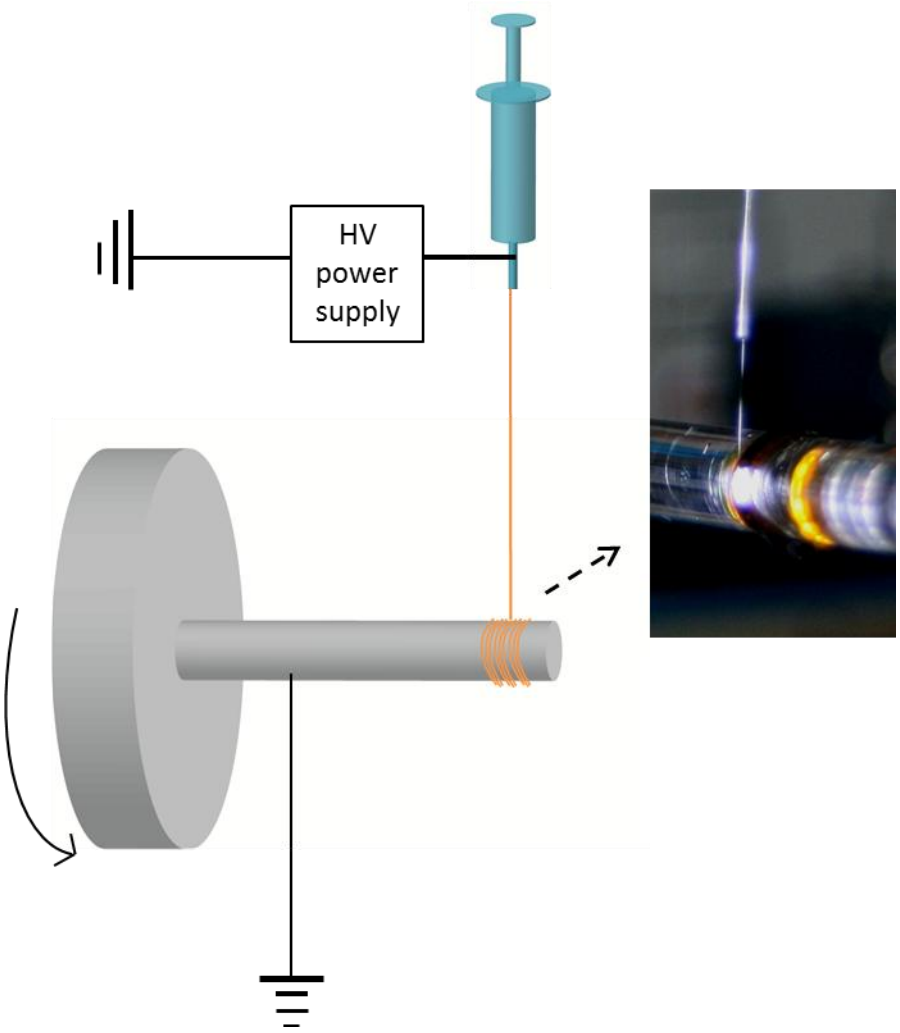

Figure 7.1. Schematics of aligned electrospun EDOT PLGA or PCL fibers with a rotating beam. An optical micrograph of the polymer fibers as they were collected onto the rotating beam is shown on the right.

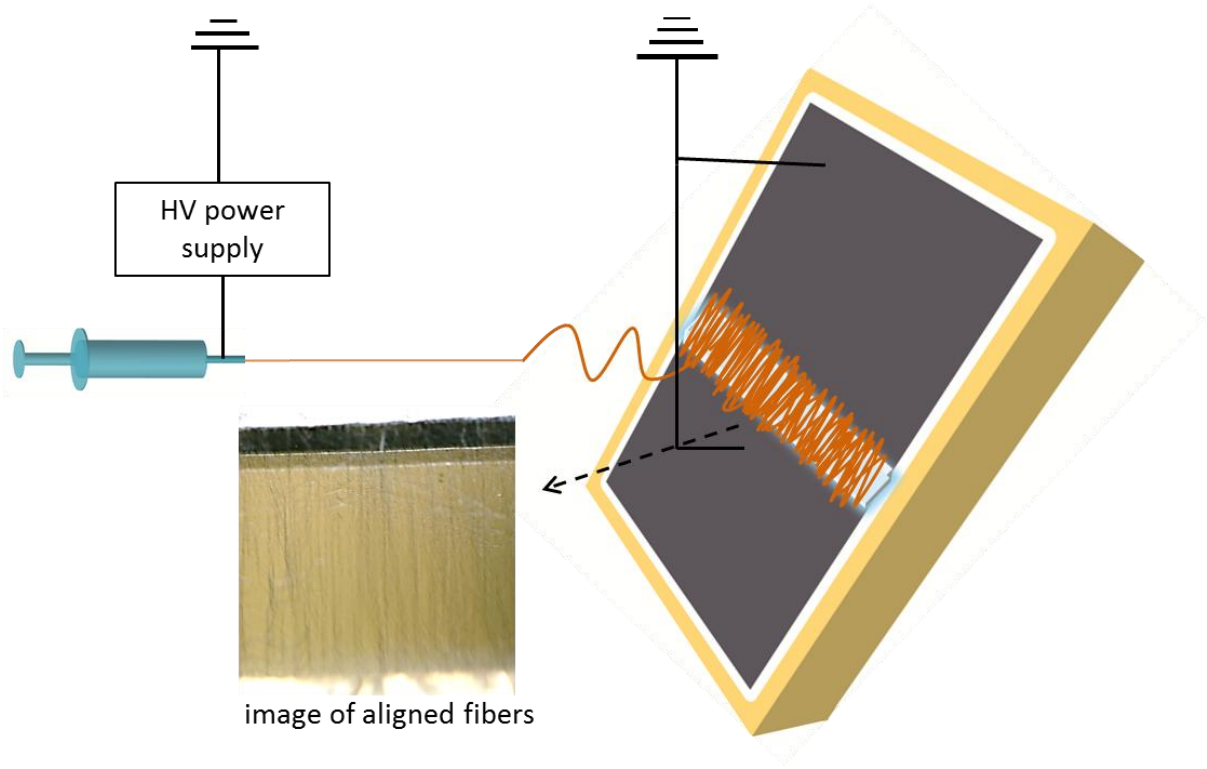

Figure 7.2. Schematic illustration of aligned electrospun EDOT PLGA or PCL fibers using a conductive substrate with a gap void with an optical micrograph of the aligned fibers (gap is 1 cm wide)

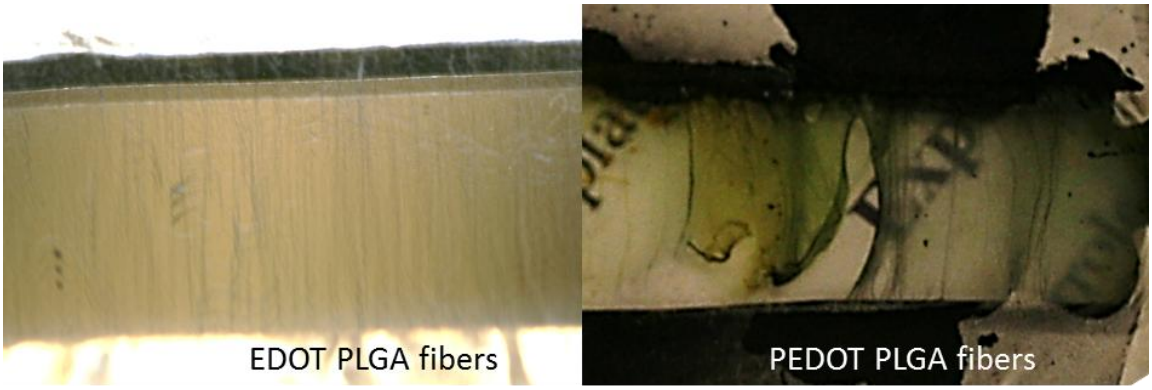

Figure 7.3. Optical micrographs of aligned fibers before and after polymerization (left: EDOT/PLGA fibers, Right: PEDOT/PLGA fibers).

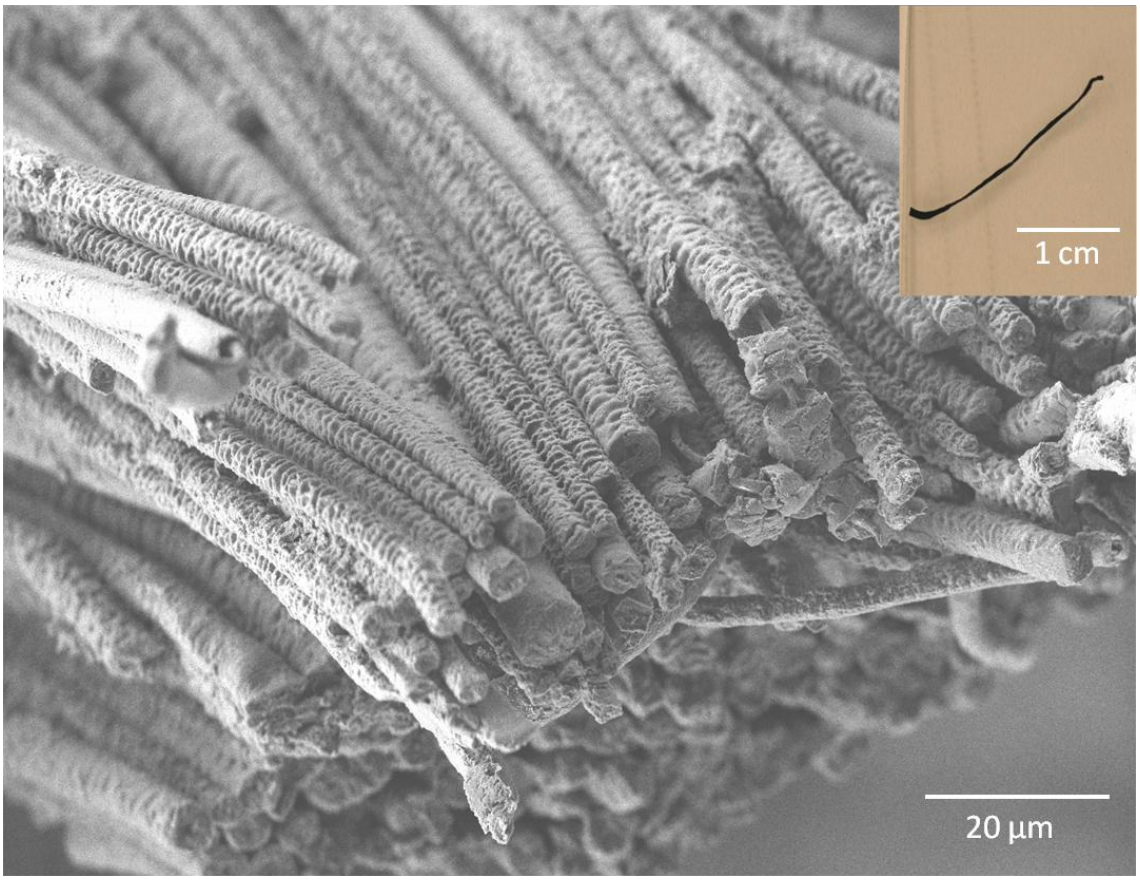

Figure 7.4. SEM micrograph and optical micrograph (embedded image) of aligned PEDOT/PLGA fibers.

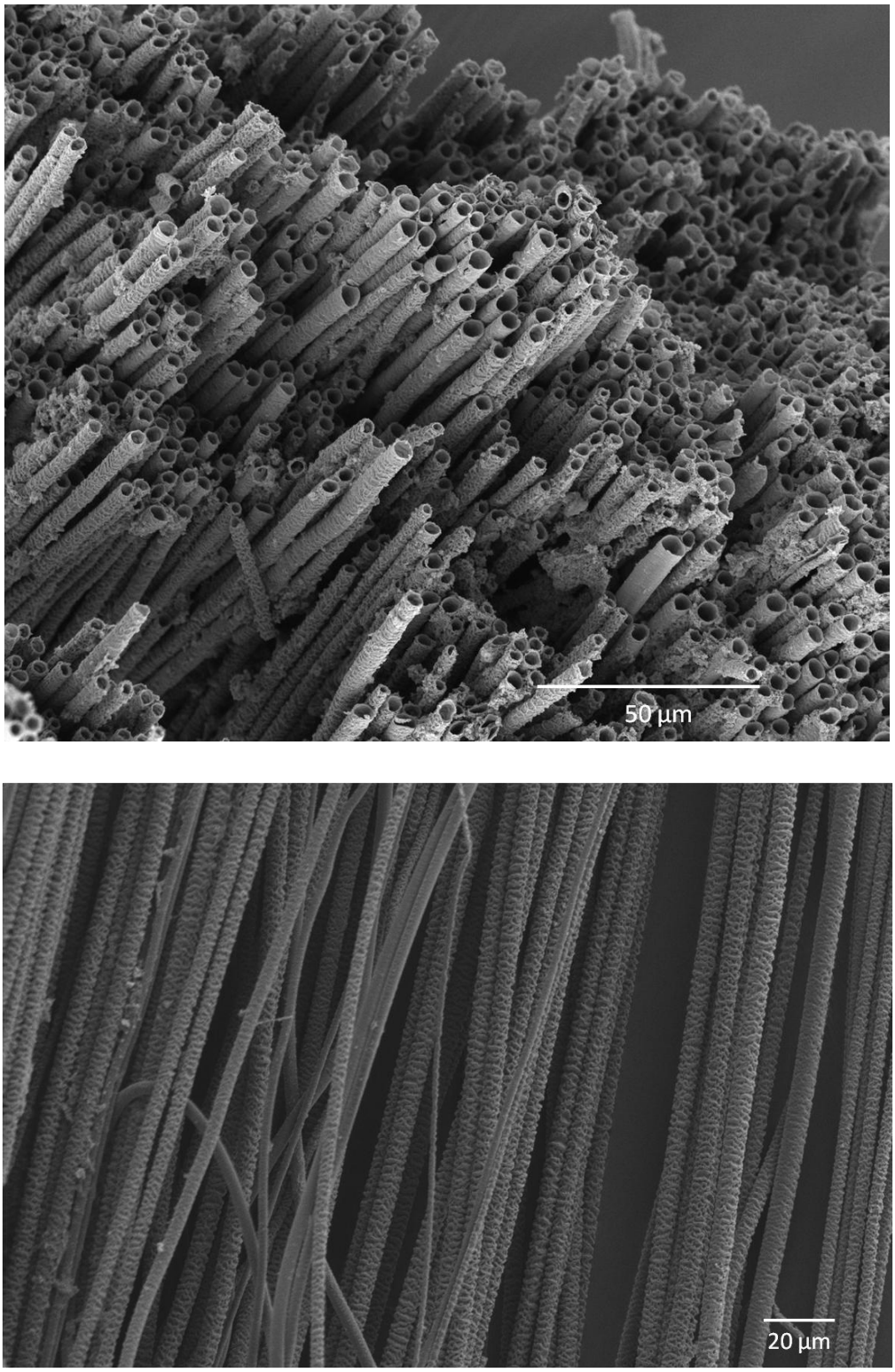

Figure 7.5. SEM micrographs of PEDOT tubes after PLGA/PCL template removal (Top: side view, Bottom: Plan view)

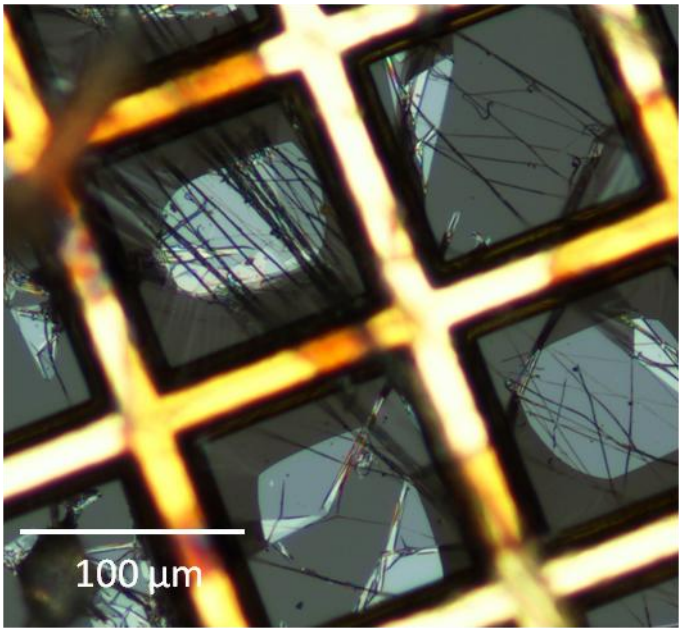

Figure 7.6. An optical micrograph of a typical TEM sample of PEDOT PCL fibers

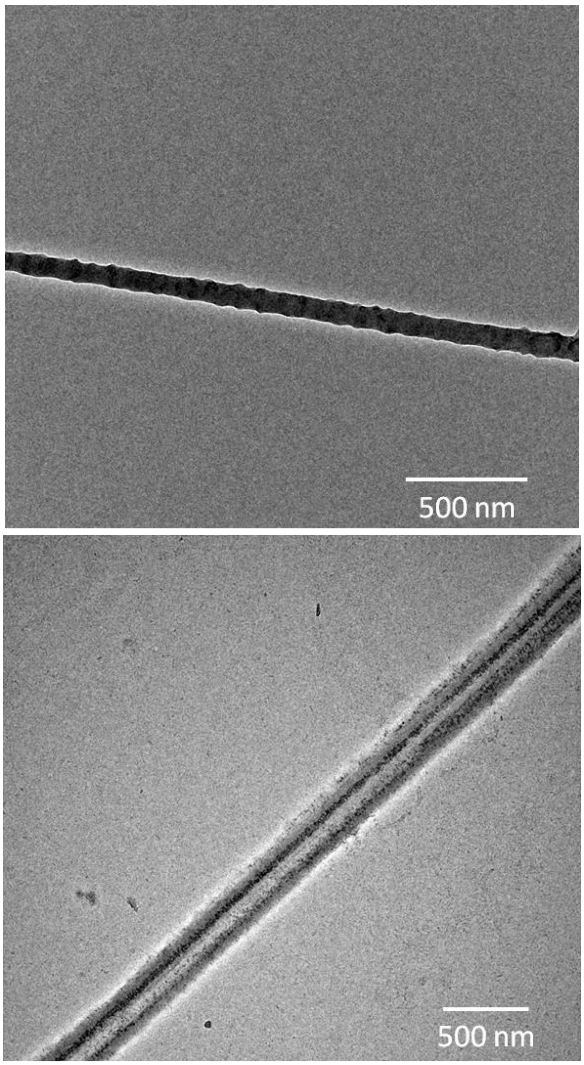

Figure 7.7. TEM micrographs of PEDOT PCL fibers before and after PCL template removal (Left: PEDOT PCL fiber, Right: PEDOT tube).

SEM

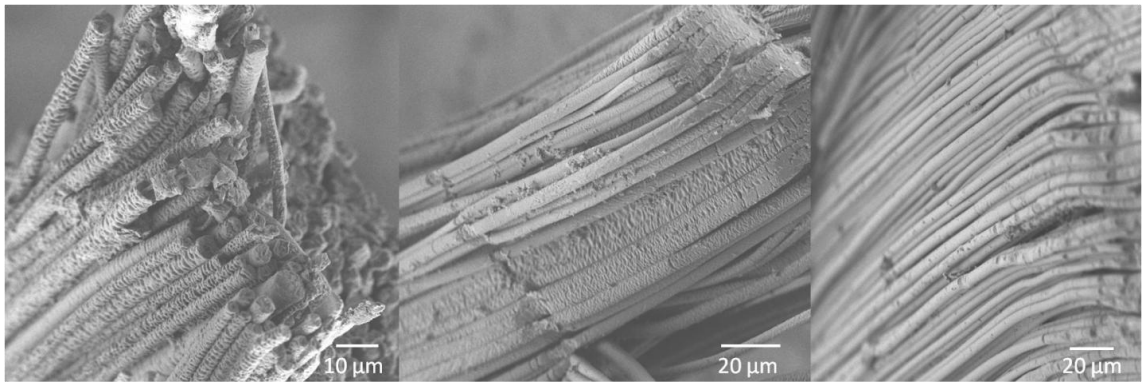

TEM

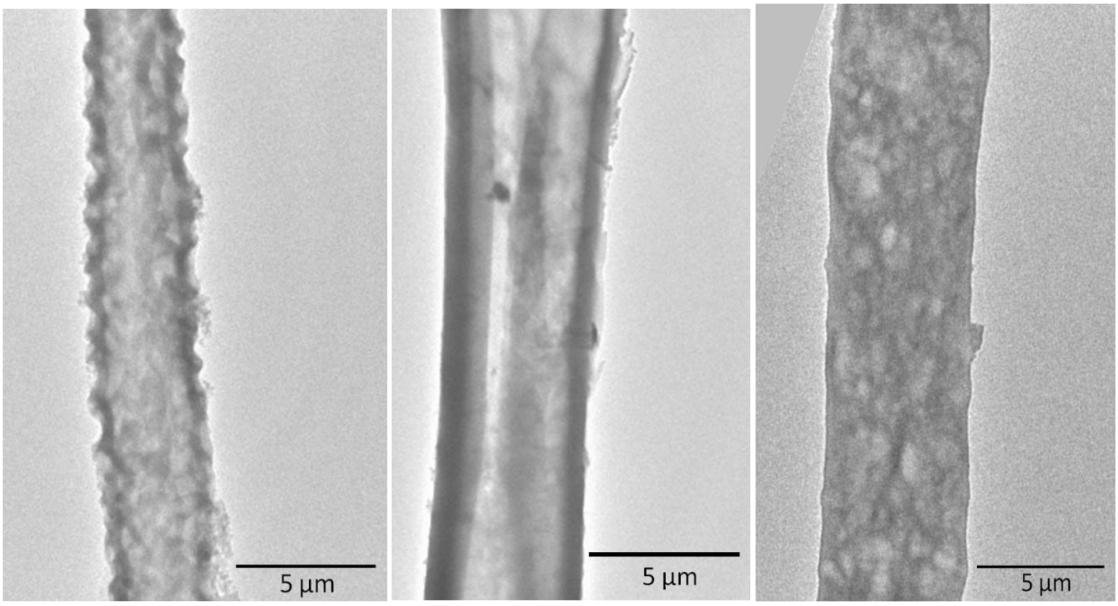

Figure 7.8. SEM and TEM micrographs of PEDOT fibers showing surface morphology control by varying oxidizer concentration (Left: Fibers polymerized by 60 wt% $FeCl_3$ solution , Middle: fibers polymerized by 50 wt% $FeCl_3$, Right: fibers polymerized by 30 wt% $Fecl_3$ soltuion)

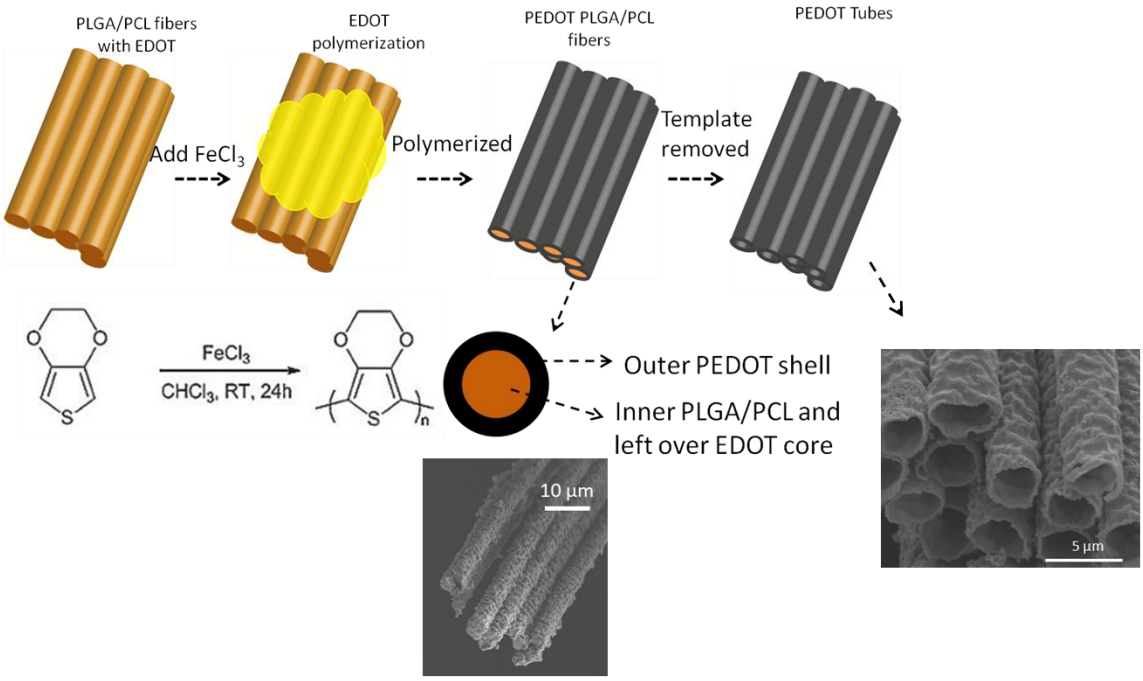

Figure 7.9. Schematic illustration of PEDOT tubes formation with real sample images.

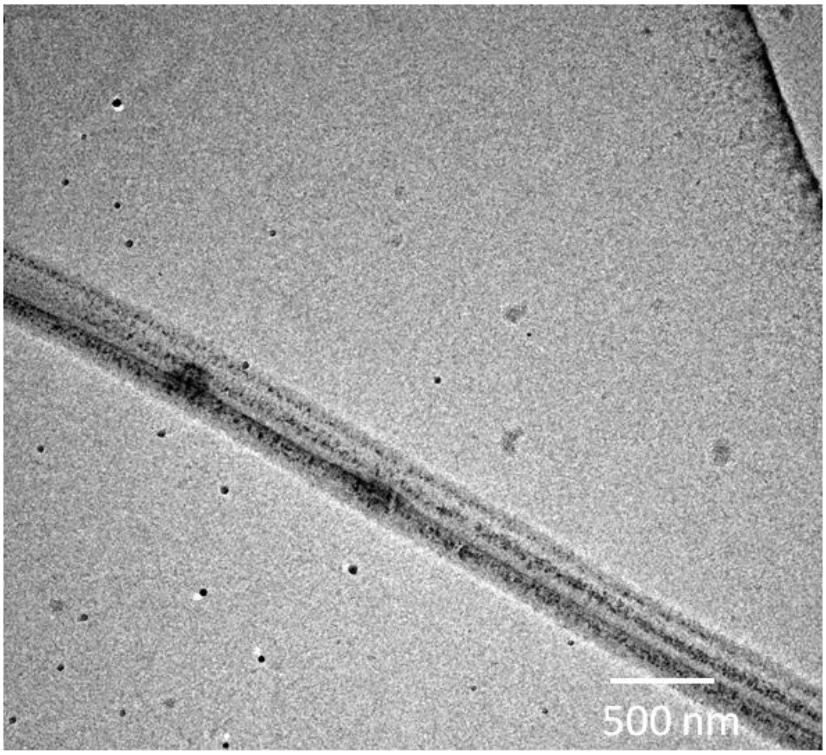

Figure 7.10. Two aligned fibers polymerized together forming PEDOT tube similar to multiwall nanotube structure.

SEM

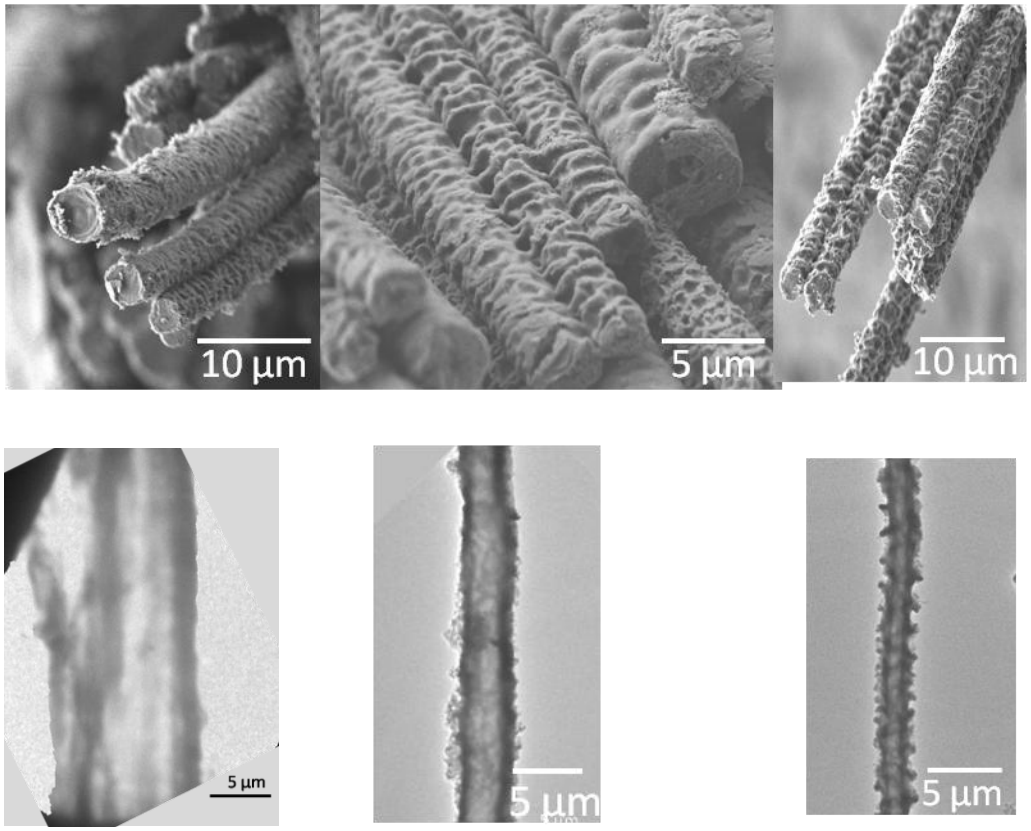

Figure 7.11. SEM and TEM micrographs of PEDOT fibers showing size control by varying monomer/template ratio (Left: 8 µm fibers with EDOT/PLGA ratio of 1:10, Middle: 4 µm fibers with EDOT/PLGA ratio of 3:10, Right: 2 µm fibers with EDOT/PLGA ratio of 5:10)

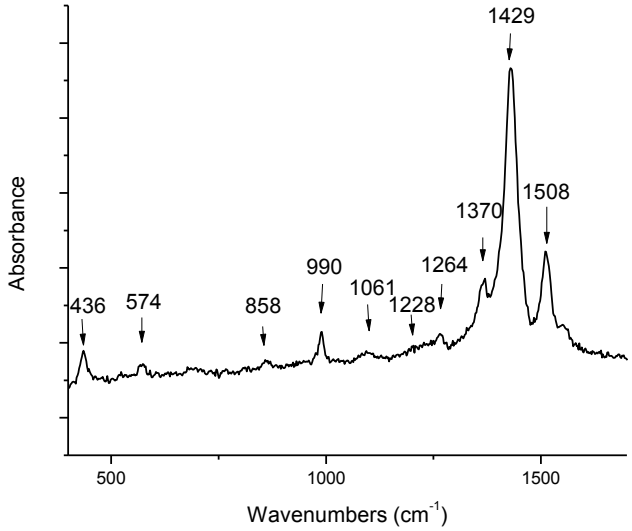

Figure 7.12. Raman spectroscopy of PEDOT/PLGA fiber

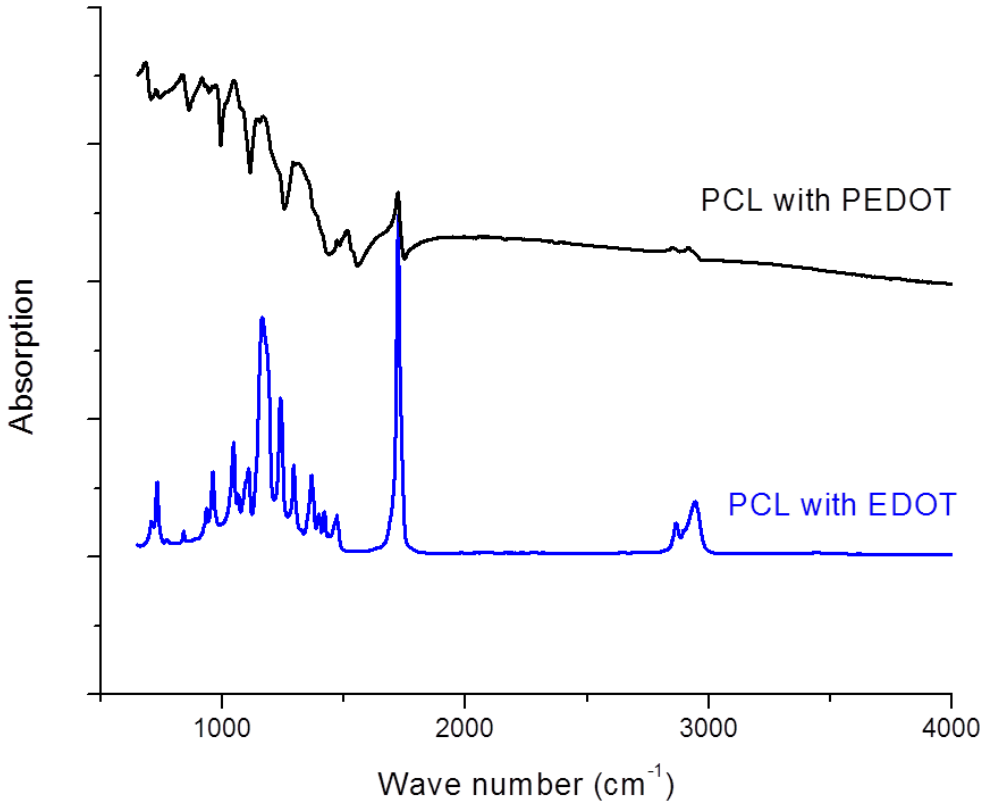

Figure 7.13. FT-IR spectra of aligned PEDOT fibers using PCL as a template.

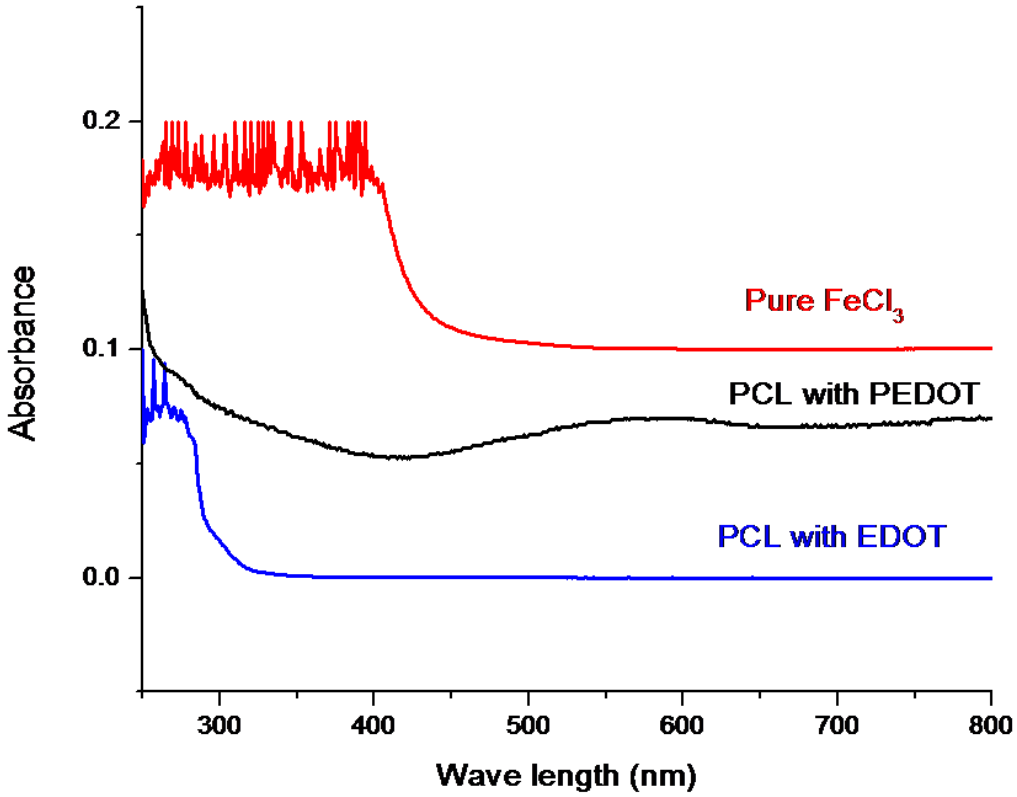

Figure 7.14. UV-Vis spectra of PEDOT fibers using PCL as a template showing distinctive PEDOT peak around 570 nm (blue line: PCL fibers with EDOT, Black line: PCL fibers withPEDOT, Red line: 5wt% $FeCl_3$ aqueous solution for reference).

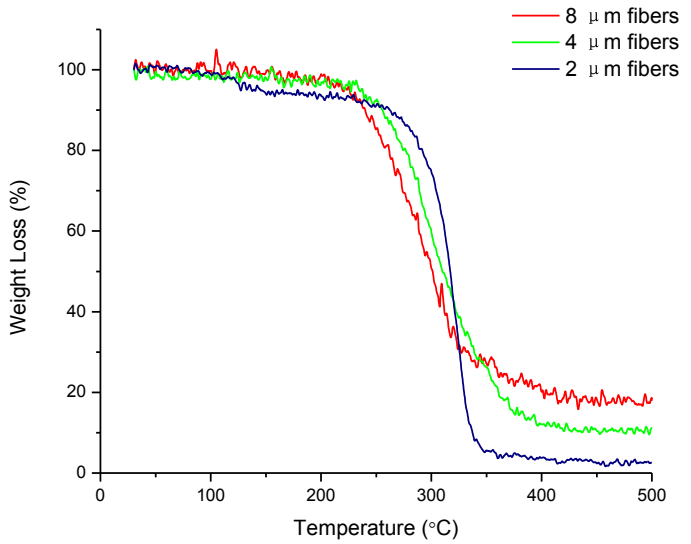

a) TGA of PEDOT/PLGA fibers with different diameters. (Red line: 8 μm fibers with EDOT/PLGA ratio of 1:10, Green line: 4 μm fibers with EDOT/PLGA ratio of 3:10, Blue line: 2 μm fibers with EDOT/PLGA ratio of 5:10)

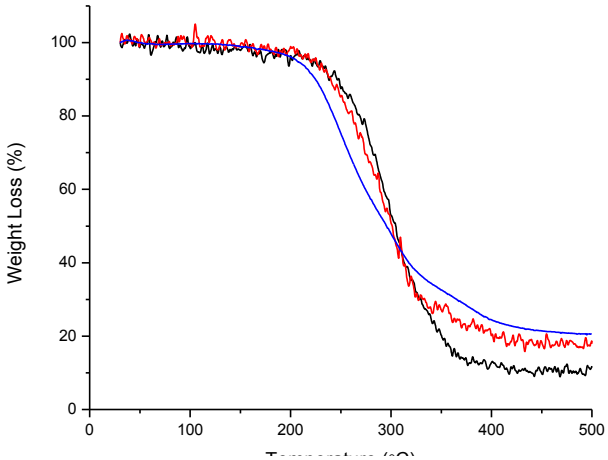

b). TGA of PEDOT/PLGA fibers polymerized with different concentration of oxidizer solutions (Black line: Fbiers polymerized by 60 wt% $FeCl_3$ solution , Red line: Fibers polymerized by 50 wt% $FeCl_3$ solution, Blue line: Fibers polymerized by 30 wt% $Fecl_3$ soltuion)

Figure 7.15. TGA of PEDOT/PLGA fibers.

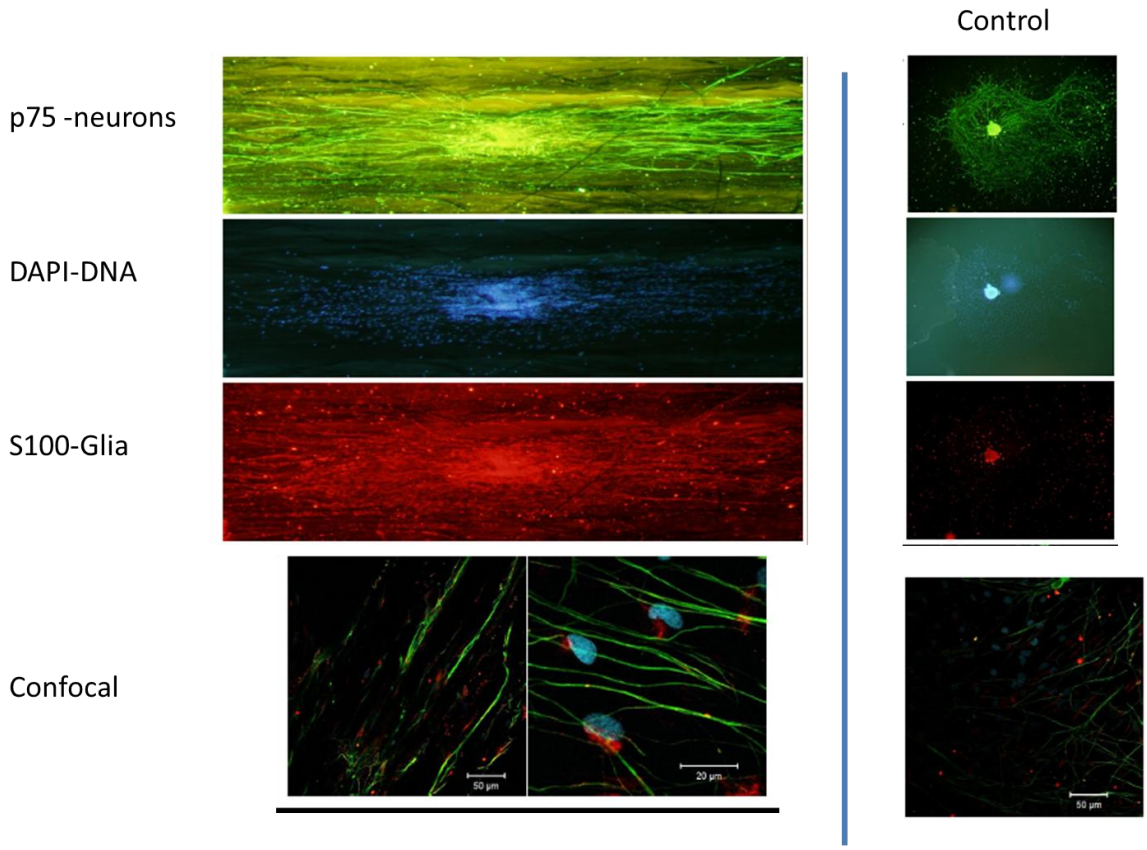

Figure 7.16. Confocal images of aligned PEDOT/PLGA nanofibers guide regenerating peripheral nervous tissue

Sample	Resistance (k Ω)	Conductivity (mS/cm)
8 µm fibers polymerized by 60 wt% $FeCl_3$	2.2	2.2
4 µm fibers polymerized by 60 wt% $FeCl_3$	4	2.3
2 µm fibers polymerized by 60 wt% $FeCl_3$	7.8	2.5
8 µm fibers polymerized by 50 wt% $FeCl_3$	13	0.75
8 µm fibers polymerized by 30 wt% $FeCl_3$	50	0.2

Table 7.1. Conductivity of different PEDOT/PLGA fibers (8 µm fibers were spun from sample with EDOT/PLGA ratio of 1:10, 4 µm fibers were spun from sample with EDOT/PLGA ratio of 3:10 and 2 µm fibers were spun from sample with EDOT/PLGA ratio of 5:10)

Experimental Frequencies (cm^{-1})	Calculated frequencies (cm^{-1}) (Tran-Van, Garreau, Louarn, Froyer & Chevrot, 2001)	
1508	1509	C=C strecthing in plane modes (antisym.)
1429	1444	C==C stretching in plane modes(sym.)
1370	1366	C-C stretching in plane modes
1264	1267	C-C inter-ring stretching in plane modes
1228	1228	C-C inter-ring stretching in plane modes
1061	1061	C-O stretching
990	988	oxyethylene ring deformation
858	865	O-C-C deformation
574	565	C-O-C deformation
436	440	C-O-C deformation

Table 7.2. Peaks in PEDOT/PLGA Raman spectra

References:

Abidian, M.R. and Martin, D.C. *Biomaterials*, **29**, (2008), 1273-1283.

Abidian, M.R. and Martin, D.C. *Advanced Functional Materials*, **19**, (2009), 573-585.

Abidian, M.R., Kim, D.H.and Martin, D. C. *Advance materials*. **18**, (2006), 405–409.

Aleshin, A. N. *Advanced Materials*, **18**, (2006), 17-27.

Cassagneau, T. & Caruso, F. *Advanced Materials*, **14**, (2002). 1837-1841.

Cho, S. and Lee, S.B. *Acc. Chem. Res*., **41**, (2008), 699–707.

Corrandi, R. & Armes, S.P. *Synthetic Metals*, **84**, (1997), 453-453

Corey, J.M., Lin, D.Y., Mycek, K.B., Chen, Q., Samuel,S., Feldman, E. L.and Martin,D.C. *Journal of Biomedical Materials Research Part A*, **83A**, (2007), 636-645.

Corradi, R. and Armes, S. P., *Synthetic metals*, **84,** (1997), 453-454.

Cui, X., Martin, D. C. *Sensors and Actuators B:Chemical*, **89**, (2003). 92-102.

Groenendaal L., Jonas F., Freitag D., Pielartzik H., Reynolds J.R., *Adv Mater* **7** (2000), 481–494.

Han, M.G. and Foulger, S.H. *Small*. **2**. (2006), 1164-1169.

Huang, Z.; Zhang, Y.; Kotaki, M.and Ramakrishna,S. *Composites Science and Technology* **63** (2003) 2223–2253.

Kirchmeyer, S., Reuter, K. *Journal of materials chemistry*., **15, (**2005), 2077-2088.

Kvarnström, C., Neugebauer, H. Ivaska, A. and Sarciciftci, N.S. *J. Mole. Struct*. **521**, (2000), 271-277.

Law, M., Goldberger, J., Yang, P. *Annu. Rev. Mater. Res*. **34,(** 2004), 83–122.

Li, D.; Wang, Y. and Xia, Y. *Advanced Materials*, **16**, (2004), 361-366.

Li,N.; Martin, C.R.; Scrosati, B. *Electrochem. Solid-state let.* **3**, (2000), 316-318.

Li, W., Laurencin, C. T., Caterson, E. J., Tuan, R. S. and Ko, F. K. *Journal of biomedical materials research.* **60**, (2002), 613-621.

Lock, J. P., Im, S. G., Gleason, K. K. *Macromolecules*, **39**, (2006). 5326-5329.

Martin, D.C; Wu, J; Shaw, C.M; King, Z; Spannigga, S.A; Rcihardson-Bruns, S; Hendricks, J and Yang, J; *Polymer Reviews*, **50**, (2010), 340–384.

Nguyen, T.P., Rendu, P.L., Long, P.D. and De Vos, S.A. *Surface and Coatings Technology*, **180-181**, (2004), 646-649.

Okuzaki, H., Harashina, Y., Yan. H., *European Polymer Journal.* **45** (2009) 256–261.

Takahashi, T., Ishihara, M. and Okuzaki, H. *Synthetic Metals*. **152** (2005) 73–76.

Theron A, Zussman E, Yarin A.L. *Nanotechnology.* **12**. (2001); 384–90.

Tran-Van, F., Garreau, S., Louarn, G., Froyer G. and Chevrot,C. *J. Mater. Chem.*, **11,** (2001), 1378-1382.

Winther-Jensen, B. and West, K. *Reactive & Functional Polymers*, **66**, (2006), 479-483.

Wu, C. G. and Bein, T. *Science.* **264**, (1994), 1757–1759.

Xiao, R.; Cho, S II.; Liu, R. and Lee, S.B. *J. AM. Chem. Soc.* **129**, (2007), 4483-4489.

Xiao, Y., Martin, D. C., Cui, X.,and Shenai, M. Applied Biochemistry and Biotechnology, **128**, (2006). 117-129.

Xu, Q. and Czernuszka,J. T. *Journal of Controlled Release*. **127**, (2008), 146–153.

Yang, J., Martin, D C; *Sensors and Actuators A: physical*, **113**, (2004a), 204-211.

Yang, J. and Martin, D.C. *Sensors and actuators. B Chemical*, **101**, (2004b).1-2

Yang, J., Kim, D.H., Hendricks, J.L., Leach, M., Northey, R.and Martin, D.C. *Acta Biomaterialia*, **1**, (2004).

Yang, J; Lipkin, K and Martin, D C. *Journal of biomaterials science-Polymer edition*, **18**, (2007), 1075-1089.

Yoshimoto, H., Shin, Y. M., Terai, H. and Vacanti, J. P. *Biomaterials*. **24**, (2003), 2077-2082.

Zhan, L., Song, Z., Zhang, J., Tang, J., Zhan, H., Zhou, Y., Zhan, C. *Electrochimica Acta*, **53**, (2008), 8319–8323.

Zhang, X.; Lee, J.S.; Lee, G.S.; Cha, D.K.; Kim, M. J.; Yang, D. J. and Manohar, S. K. *Macromolecules* **39**, (2006), 470-472.

Zhou, Y., Freitag, M., Hone, J., Staii, C., Johnson, A. T., Pinto, N. J. Jr., MacDiarmid, A. G. *Appl. Phys. Lett*. **83,** (2003), 3800.

Chapter VIII

Conclusions and suggestions for future research

Conclusions

In this dissertation the morphology of PEDOT has been studied and controlled at different length scales from nanometers to micrometers.

On the nanoscale, it was found that different counter-ions of the dopants produce PEDOT crystals with different d_{100} spacing (from 1.15-1.52 nm) (Martin et al., 2010). Simple inorganic counter-ions typically produce smaller d_{100} spacings than complex polymeric counter-ions. The cations of the dopants have no significant effect on the d_{100} spacing. The deposition current density plays a significant role in the degree of crystallinity of PEDOT with higher current density producing higher crystalline PEDOT films but no significant effect on the size of d100 spacing. Cross sections of electrochemically deposited PEDOT were studied by TEM and EDS mapping. The initial growth of PEDOT film is dense and smooth and become porous and fuzzy as the film grows thicker; this is consistent with our previous finding that the impedance of electrochemically deposited PEDOT films dramatically decreases initially and then slowly increases after reaching a minimum (Chapter II).

A highly ordered PEDOT-Br phase was formed during electrochemical deposition in the presence of bromine counterions. This phase shows highly ordered crystalline domains that are hundreds of microns in size. SEM images of the crystals showed local fibrillation within the needle-shaped crystals and oriented perpendicular their long axes, which is presumably their primary growth direction. This fibrillation (~100 nm wide, several microns in length) is presumably related to the locally anisotropic arrangement of the PEDOT polymers or oligomers within the needle crystals. The crystals have d spacing at 1.03 nm which was confirmed both by WAXS and high-resolution TEM. These highly crystalline PEDOT or PEDOT oligomer films open possible windows for the detailed

study of the microstructure and transport properties of conductive conjugated polymers (Chapter IV).

On the tens of nanometers scale, non-ionic surfactants were used to template PEDOT into bicontinuous cubic phases. We were able to create highly ordered conducting polymer structures of interest for a wide variety of applications. We found that AgNO3 was an appropriate oxidant for this process because of its low heat of solution and relatively slow reaction rate. The impedance of these bicontinuous cubic phases dropped more than two orders in magnitude before and after polymerization. The PEDOT cubic phases were more thermally stable than the precursor cubic phases with only EDOT monomer. As the structure of PEDOT bicontinuous cubic phases collapsed, the impedance dropped by more than 5 orders of magnitude. The PEDOT cubic phase collapsed irreversibly after thermal ramping or surfactant removal. Fragments of the PEDOT bicontinuous cubic phases of 10-20 nm in size were imaged by LVEM, revealing regular 3 to 5 nm pores. These PEDOT bicontinuous cubic films have extremely large specific surface areas (with a surface area to volume ratio around 1.3×10^9 m^2/m^3 if the pore size was 3 nm (Pang et al. 2004)) and may be useful for rapidly responding sensors and actuators. They should also be useful as simultaneous electronic and ionic conductors, controlled drug delivery, and filters (Chapter V and Chapter VI).

On the micrometer scale, aligned PEDOT fibers and tubes were prepared by electrospinning blends of PLGA and EDOT monomer onto a rotating wheel or a dielectric gap in a metal substrate. The diameters of the fibers can be controlled from 2 μm to 20 μm changing the EDOT concentration in the solution, with higher EDOT concentrations producing fibers with smaller diameters. PEDOT was formed by exposing the PLGA/EDOT monomer fibers to $FeCl_3$ oxidant. The result was a region of PEDOT formed near the surface, with a thickness that was independent of fiber diameter. Higher oxidizer concentrations produced rougher fiber/tube surfaces. Very low oxidizer concentration produced PEDOT/PLGA fibers instead of tubes. Growth direction of neural cells had been directed by these well aligned PEDOT/PLGA fibers (Chapter VII).

Future work

The composition, unit cell structure, and growth mechanisms of the highly oriented PEDOT-Br crystals should be explored by electron diffraction and molecular simulations. It could be of interest for applying them into active layers with a nano-structured bulk heterojunction morphology used in organic solar cells.

The amount of EDOT in non-polar phase of the bicontinuous cubic phase ternary systems has been increased up to 10 wt%. This oily phase accounts for 20 wt% of the ternary system giving a overall effective concentration of EDOT of 2 wt% in the ternary system. This relatively low amount of PEDOT after polymerization is likely the source of mechanical instability of the bicontinuous cubic phases. EDOT derivatives with long alky side chains should be explored to replace the oil phase in the ternary system which hopefully can contain up to 20 wt% of the monomer and thus increases the mechanical stability of the structure after polymerization. Now that a reproducible means of forming these ordered, porous conducting polymers has been found, the applications of these porous PEDOT with extremely high effective surface area should be explored.

Solution-processable conjugated polymers formed from new functionalized thiophene monomers have recently been developed in our group. These monomers are based on 3,4-propylene dioxythiophene (ProDOT), and are functionalized using thiol-ene chemistry. These ProDOT monomers have side groups designed to create conjugated polymers that can be dissolved in common solvents. Electrospun fibers using these soluble polymers may be well aligned. Studies of the detailed organization of these electrospun polymer nanofibers at the molecular level would make it possible to explore the anisotropy of charge transport, providing fundamental information about the relationship between chemical structure, morphology, and macroscopic properties of conjugated polymers. This may also make it possible to extract information about the relative role of both electron/hole transport (along the oriented molecular backbone) and ionic transport (in the interstices between chains).

References

Martin, D.C; Wu, J; Shaw, C. M.; King, Z; Spanninga, S.A; Richardson-Burns, S; Hendricks, J and Yang, J; *Polymer Reviews*, **50**, (2010), 340–384.

Pang, J., Hampsey, E. J., Hu, Q., Wu, Z., John, V. T. and Lu, Y. *Chem. Commun.*, (2004), 682-683